Mechanical characterization and numerical modeling of aortic valve tissues

Colin Laville

▶ **To cite this version:**

Colin Laville. Mechanical characterization and numerical modeling of aortic valve tissues. Materials. Université Paris sciences et lettres, 2017. English. NNT : 2017PSLEM069 . tel-02127058

HAL Id: tel-02127058
https://pastel.hal.science/tel-02127058

Submitted on 13 May 2019

HAL is a multi-disciplinary open access archive for the deposit and dissemination of scientific research documents, whether they are published or not. The documents may come from teaching and research institutions in France or abroad, or from public or private research centers.

L'archive ouverte pluridisciplinaire **HAL**, est destinée au dépôt et à la diffusion de documents scientifiques de niveau recherche, publiés ou non, émanant des établissements d'enseignement et de recherche français ou étrangers, des laboratoires publics ou privés.

THÈSE DE DOCTORAT

de l'Université de recherche Paris Sciences et Lettres
PSL Research University

Préparée à MINES ParisTech

MECHANICAL CHARACTERIZATION AND NUMERICAL MODELING OF AORTIC VALVE TISSUES

CARACTÉRISATION MÉCANIQUE ET MODÉLISATION NUMÉRIQUE DES TISSUS DE VALVE AORTIQUE

École doctorale n°364

SCIENCES FONDAMENTALES ET APPLIQUÉES

SPÉCIALITÉ MÉCANIQUE NUMÉRIQUE ET MATÉRIAUX

COMPOSITION DU JURY :

M. Stéphane Avril
MINES Saint–Étienne, Président du jury

Mme Valérie Deplano
Université Aix–Marseille II, Rapporteur

M. Laurent Delannay
Université catholique de Louvain, Rapporteur

M. François Bay
MINES ParisTech, Examinateur

M. Yannick Tillier
MINES ParisTech, Examinateur

Soutenue par Colin Laville
le 13 septembre 2017

Dirigée par Yannick Tillier

MINES ParisTech

PSL RESEARCH UNIVERSITY PARIS

MINES ParisTech
Centre de Mise en Forme des Matériaux (CEMEF)
CNRS UMR 7635
1 rue Claude Daunesse, CS 10207, 06904 Sophia Antipolis Cedex, France
http://cemef.mines-paristech.fr

Remerciements

Mes premiers remerciements vont aux différents membres de mon jury qui ont accepté de relire et d'examiner mon travail. Je remercie Stéphane Avril d'avoir bien voulu présider ce jury. Un grand merci également aux rapporteurs, Valérie Deplano et Laurent Delannay, ainsi qu'aux examinateurs, François Bay et Yannick Tillier, pour l'intérêt qu'ils ont manifesté et la discussion pertinente qu'ils ont su apporter à mes travaux. Je tiens tout particulièrement à remercier Yannick, mon directeur de thèse, pour m'avoir accordé sa confiance à travers une grande liberté de travail, mais aussi pour son soutien et sa disponibilité.

Je tiens ensuite à exprimer mes remerciements envers Christophe Pradille pour avoir rendu possible la réalisation de cette machine de traction indispensable à ma thèse, ainsi que pour ses conseils et son aide notamment en corrélation d'images et en analyse inverse. J'aimerais également remercier les différents membres du groupe MEA, Christelle Combeaud pour s'être impliquée dans le développement de la machine, Francis Fournier pour en avoir réalisé la conception, Arnaud Pignolet pour le développement du logiciel de contrôle et Marc Bouyssou pour l'usinage des différentes pièces. Merci aussi à Sélim, Carole et Hallen du groupe SCS pour le temps qu'ils ont consacré à la résolution de mes problèmes informatiques, et à Thomas Olivier du laboratoire Hubert Curien à Saint–Étienne, pour m'avoir permis d'utiliser le microscope confocal et pour son aide précieuse lors de la campagne expérimentale. Je tiens également à remercier chaleureusement le personnel administratif du laboratoire, Marie–Françoise et Sylvie, toujours de bonne humeur et disponibles pour aider les étudiants.

Je me dois enfin de remercier mes collègues doctorants et post–doctorants sans qui ces années de thèse auraient été beaucoup moins enrichissantes. Merci à Florian et Daniel pour avoir patiemment répondu à mes questions parfois naïves, à Xavier pour avoir pris le temps de me guider dans la découverte du code source de FORGE®, à Modesar pour son aide très précieuse notamment en algorithmique, à mes collègues de bureau Fabien et Christophe pour nos discussions et le soutien mutuel, mais aussi à Ziad, Ali, Mehdi, Antoine, Luis, Romain, Grégoire, Pierrick, Abdel, Stéphanie, Benjamin, Danai et les autres. Un grand merci à tous pour les bons moments passés ensemble.

Pour finir, je voudrais remercier mes proches et tout particulièrement mes parents, pour leur soutien sans faille pendant toutes ces années.

Contents

General Introduction **1**

1 Aortic valve tissues **7**
1.1 Introduction . . . 8
1.2 Mechanical characterization . . . 11
1.2.1 Specimen preparation . . . 11
1.2.2 Biaxial device . . . 11
1.2.3 Digital image correlation method . . . 13
1.2.4 Experimental protocol . . . 13
1.3 Fibers orientation measurement . . . 15
1.3.1 Specimen preparation . . . 15
1.3.2 Confocal laser scanning microscopy and experimental setup . . . 16
1.3.3 Experimental protocol . . . 17
1.4 Experimental results . . . 18
1.4.1 Biaxial tensile tests results and discussion . . . 18
1.4.2 Confocal laser scanning microscopy results and discussion . . . 29
1.5 Summary of Chapter 1 . . . 34
1.6 Résumé en français . . . 35

2 Mechanical framework and models **37**
2.1 Introduction . . . 38
2.2 Continuum mechanical framework . . . 39
2.2.1 Kinematics . . . 39
2.2.2 Stress and objectivity . . . 43
2.2.3 Hyperelastic framework . . . 45
2.3 Lagrangian variational formulations of the problem . . . 48
2.3.1 Boundary conditions . . . 49
2.3.2 Weak formulation of balance equations . . . 50
2.3.3 Total Lagrangian formulation . . . 52
2.3.4 Updated Lagrangian formulation . . . 52
2.3.5 Quasi–incompressiblility . . . 55

2.4 Finite element discretization . . . 56
2.4.1 Spatial discretization . . . 56
2.4.2 Temporal discretization . . . 62
2.5 Material models . . . 65
2.5.1 Fiber distribution . . . 65
2.5.2 Strain–energy functions . . . 68
2.5.3 Polyconvexity . . . 76
2.5.4 Fibers orientation . . . 76
2.6 Solver validation . . . 79
2.6.1 Convergence and stability . . . 79
2.6.2 Models implementation . . . 81
2.6.3 Fibers orientation algorithm . . . 85
2.7 Summary of Chapter 2 . . . 87
2.8 Résumé en français . . . 88

3 Inverse analysis procedure **89**
3.1 Introduction . . . 90
3.2 Inverse analysis approach . . . 91
3.2.1 Generalities on inverse analysis . . . 91
3.2.2 Inverse analysis method . . . 93
3.2.3 Fibers dispersion and concentration parameters . . . 93
3.2.4 Numerical setup and inverse analysis procedure . . . 94
3.3 Inverse analysis results . . . 99
3.3.1 Models comparison . . . 99
3.3.2 Influence of input data . . . 101
3.3.3 Limitations of the inverse analysis procedure . . . 105
3.4 Summary of Chapter 3 . . . 105
3.5 Résumé en français . . . 106

4 Toward fluid–structure interaction **107**
4.1 Introduction . . . 108
4.2 Governing equations . . . 109
4.2.1 Navier–Stokes equations for incompressible flows . . . 109
4.2.2 Boundary conditions . . . 110
4.3 SPH : method and implementation . . . 111
4.3.1 Generalities on SPH . . . 111
4.3.2 SPH interpolation . . . 112
4.3.3 First order differential operators . . . 114
4.3.4 Second order differential operator . . . 116
4.3.5 Accuracy of SPH differential operators . . . 116
4.3.6 Definition of the kernel function . . . 117

4.3.7 Fluid discretization . . . 120
4.3.8 Incompressible SPH . . . 122
4.3.9 Boundary conditions treatment . . . 125
4.3.10 Time–stepping and numerical stability . . . 127
4.3.11 Reduction of the computational time . . . 127
4.4 SPH–FE coupling . . . 129
4.4.1 FSI algorithm . . . 129
4.4.2 Interface coupling . . . 130
4.5 Solver validation . . . 131
4.5.1 SPH implementation validation . . . 131
4.5.2 SPH–FE coupling validation . . . 134
4.6 Summary of Chapter 4 . . . 137
4.7 Résumé en français . . . 137

Conclusions and outlook **139**

Appendix A Device protocol **143**
A.1 Introduction . . . 143
A.2 Protocol . . . 143

Appendix B Material models derivatives **145**
B.1 Introduction . . . 145
B.2 Weisbecker model . . . 145
B.3 Holzapfel Gasser Ogden model . . . 146
B.4 Modified Holzapfel Gasser Ogden model . . . 147

References **149**

List of Figures

1 Heart circulation diagram 2
2 Examples of prosthetic AVs 3
3 AV replacement surgery with a mechanical prosthesis 4

1.1 Microscopy images of some constituents 8
1.2 Illustration of the AV displaying the leaflet structure 9
1.3 Porcine AV leaflet excised 11
1.4 The biaxial tensile device 12
1.5 Example of subset tracking during deformation 13
1.6 Sample mounted on the biaxial tensile devise 14
1.7 Example of subset choice on 3D–VIC™ 15
1.8 Confocal microscope Leica TCS SP2 SE form Hubert Curien Laboratory (Saint–Étienne, France) 16
1.9 Optical system and objective 17
1.10 Scheme of the observation areas positions (mm) on both samples 17
1.11 Scheme of an excised AV leaflet 18
1.12 Averaged thickness of the samples with dispersion for each valve 19
1.13 (1 : 1) curves at be beginning and at the end of a complete loading protocol on a sample 19
1.14 3D–DIC error measurement on an immersed plate submitted to a rigid body motion 20
1.15 Example of nominal strain evolution function of the smoothing area for a subset size of 21 px 21
1.16 Example of averaged strain on a frozen sample on three different areas . . 24
1.17 Example of averaged strain on a fresh sample on three different areas . . . 24
1.18 Tension–strain results for the (1 : 1) loading condition on six frozen samples for both circumferential and radial axes 25
1.19 Tension–strain results for the (1 : 1) loading condition on six fresh samples for both circumferential and radial axes 25
1.20 Example of superposition of the tension–strain results for a representative frozen (blue) and fresh (red) sample using (1 : 1) loading condition 25

1.21 Tension curves on one representative frozen sample for the seven loading conditions of the experimental protocol . . . 26
1.22 Tension curves on one representative fresh sample for the seven loading conditions of the experimental protocol . . . 27
1.23 Collagen fibers (channel 1) and elastin fibers and cells (channel 2) in the arterialis . . . 30
1.24 Superposition of channel 1 and channel 2 . . . 30
1.25 Pictures of collagen fibers . . . 31
1.26 Four pictures of collagen fibers from a total stack of 140 µm depth . . . 31
1.27 Illustration of angles measurements with respect to the picture frame . . . 32
1.28 Examples of principal orientation identification issues encountered while processing confocal images . . . 32
1.29 Angles (°) interpolated on a real scale grid (mm) for the square sample . . . 33
1.30 Angles (°) interpolated on a real scale grid (mm) for the whole leaflet . . . 33

2.1 Lagrangian description of the motion . . . 40
2.2 Traction vectors acting on infinitesimal surface elements . . . 45
2.3 Illustration of the different types of boundary conditions . . . 49
2.4 $P1^+/P1$ tetrahedron element with velocity (left) and pressure (right) degree of freedom . . . 58
2.5 Decomposition of the $P1^+/P1$ element into 4 sub–tetrahedrons . . . 59
2.6 Illustration of the Newton–Raphson algorithm where $x_0 = x_n$ is the initial (known) solution at t and $x_k = x_{n+1}$ is the converged solution at $t + \Delta t$ . . . 63
2.7 Characterization of the fiber direction vector in the tree–dimensional Cartesian coordinate system $\{E_1, E_2, E_3\}$ . . . 66
2.8 Examples of probability density functions ρ_r for $1 < \lambda_r < 1.5$ . . . 71
2.9 Relation between κ and b according to equation (2.135) . . . 74
2.10 Three–dimensional graphical representation of the collagen fibers orientation for several κ values . . . 74
2.11 Two–dimensional representation of the distribution $\rho(\theta)$ of the collagen fibers for several κ values . . . 75
2.12 Illustration of the projection of a fiber direction (in red) from a 2D measurement to a 3D geometry . . . 76
2.13 Illustration of the Djikstra's algorithm on a 2D mesh to compute a minimum distance d between the reference and current elements . . . 77
2.14 Illustration of the projection method from a 3D geometry into a plane . . . 78
2.15 Pressure applied on one–fourth of the geometry . . . 79
2.16 Pressure field in the quasi–incompressible case without and with stabilization 80
2.17 Pressure field in the incompressible case without and with stabilization . . . 80
2.18 Evolution of the normalized volume with compression in incompressible and quasi–incompressible formulations . . . 81

2.19 Isotropic models validation on uniaxial tension tests 81
2.20 Circular fiber arrangement on one–eighth of a spherical balloon (arrows indicate the orientation of the fibers) 82
2.21 Inflation of the spherical balloon submitted to internal pressure with $\kappa = 0.333$, $\kappa = 0.2$ and $\kappa = 0$ from top to bottom (the norm of the displacement field $\|\boldsymbol{d}\|$ is shown) 83
2.22 Energy conservation on a bending test (the norm of the displacement field $\|\boldsymbol{d}\|$ is shown) 84
2.23 Energy conservation during an indentation test on one–fourth of the deformable cube (the norm of the displacement field $\|\boldsymbol{d}\|$ is shown) 85
2.24 Example of sinusoidal θ (°) interpolation and projection corresponding to fiber orientation vectors 85
2.25 Orientation projection on a complex 3D geometry of prosthetic valve (from left to right : top, side and bottom views) 86
2.26 Example of random κ interpolation and projection 86
2.27 κ on a complex 3D geometry of prosthetic valve (from left to right : top, side and bottom views) 87

3.1 Evolutionary algorithm diagram 92
3.2 Interpolation of measured fibers directions on the undeformed finite element mesh 94
3.3 Interpolation on the sample of the local concentration and dispersion parameters 95
3.4 Illustration of the modeled area at the initial and deformed states 95
3.5 Scheme of an excised AV leaflet with radial and circumferential axes definition 96
3.6 Superposition of displacements from all the experimental loading conditions on a representative fresh sample (DIC measurements) 96
3.7 Superposition of forces from all the experimental loading conditions on a representative fresh sample 96
3.8 Displacements from DIC measurements imposed on the modeled geometry 97
3.9 Forces from experimental measurements to be compered to computed results 98
3.10 Forces from experimental (1 : 1) result (blue) and inverse analysis results (red) for each model 100
3.11 Forces from experimental (blue) and inverse analysis (red) results with fixed angles 102
3.12 Forces from experimental results (blue), 7 loadings identification (red), 5 loadings identification (green), 3 loadings identification (cyan) and 1 loading identification (magenta) 103
3.13 Forces from experimental (blue) and inverse analysis (red) results with free angles 104

3.14 Comparison of the experimental (blue) and numerical (red) tension curves for a (1 : 1) loading condition 105

4.1 Illustration of the different boundary conditions 111
4.2 Example of bell–shaped function 117
4.3 Neighbors of a particle i with its kernel support 118
4.4 Plot of the non–normalized 5^{th} order Wendland kernel and its derivative . 120
4.5 Illustration of three classic wall boundary conditions with from left to right : ghost particles, repulsive force and dynamic particles boundaries . 125
4.6 No–slip and free–slip wall boundary conditions from left to right 126
4.7 Illustration of k–d tree algorithm functioning in 2D where l_i represents the splitting lines and p_i the particles 128
4.8 2D illustration of FSI interface with fluid particles (blue) and dynamic boundary particles generated from finite element nodes (gray) 130
4.9 Illustration of the hydrostatic pressure in a water column (dynamic boundary particles are represented in transparent gray) 131
4.10 Evolution of the hydrostatic pressure versus time for $z = 10$ mm 132
4.11 Evolution of the pressure along the vertical direction 132
4.12 Illustration of a Poiseuille flow for Re = 0.5 (dynamic boundary particles are represented in transparent gray) 133
4.13 Evolution of the maximum Poiseuille velocity flow along E_3 versus time for Re = 0.5 133
4.14 Velocity profiles for a Poiseuille flow at several Re and comparison with the theoretical solution 134
4.15 Representation of the initial configuration with blood particles in blue and dynamic boundary particles in transparent gray 135
4.16 FSI illustration at $t = 0.4$ s (longitudinal cutting plane view) 135
4.17 FSI illustration at $t = 0.6$ s (longitudinal cutting plane view) 136
4.18 Fluid–structure interface issues 136

A.1 Leaflet excision and application of the ink 143
A.2 Positioning of the sample on the support device 144
A.3 Mounting of the sample on the biaxial device 144
A.4 Sample mounted on the biaxial device 144

List of Tables

1.1 Nominal strain and norm of the planar displacement field at the end of several loading conditions on a frozen leaflet 22
1.2 Nominal strain and norm of the planar displacement field at the end of several loading conditions on a fresh leaflet 23

2.1 Some penalty functions of the literature 55

3.1 Sets of parameters identified by inverse analysis on the $(1:1)$ experiment 100
3.2 Modified HGO model parameters identification depending on the number of experimental loading conditions used 101
3.3 Modified HGO model parameters identification with unknown fibers orientation 103

List of Algorithms

1 FE implementation of the Weisbecker model 72
2 Initial anisotropy directions from experimental data 78
3 ISPH solver at increment n 122
4 EISPH solver at increment n 124
5 SPH–FE weak coupling 130

Nomenclature

Abbreviations

AI	Angular Integration
ALE	Arbitrary Lagrangian–Eulerian
ASGS	Algebraic Subgrid Scale
AV	Aortic Valve
CPU	Central Processing Unit
DIC	Digital Image Correlation
EISPH	Explicit Incompressible SPH
FE	Finite Element
FSI	Fluid—Structure Interaction
GAG	Glycosaminoglycan
GST	Generalized Structure Tensors
HGO	Holzapfel Gasser Ogden
IBM	Immersed Boundary Method
IPM	Immersed Particle Method
ISPH	Incompressible SPH
MOOPI	MOdular software dedicated to Optimization and Parameters Identification
OSGS	Orthogonal Subgrid Scale
PG	Proteoglycan
SALS	Small Angle Light Scattering

SPH	Smoothed Particle Hydrodynamic
SUPG	Streamline–Upwind Petrov–Galerkin

Notations

A, a	Scalar values
$\boldsymbol{A}$	Vector defined in the material description
$\boldsymbol{a}$	Vector defined in the spatial description
$\mathbf{A}$	Second order tensor defined in the material description
$\mathbf{a}$	Second order tensor defined in the spatial description
$\mathbb{A}$	Fourth order tensor defined in the material description
$\mathbb{a}$	Fourth order tensor defined in the spatial description

General Introduction

Scientific background and motivation

The heart has four chambers, the left atrium, the left ventricle, the right atrium and the right ventricle, and four valves that ensure unidirectional blood flow during the cardiac cycle. A cardiac cycle consists of two phases : diastole and systole. In the diastole phase, heart ventricles are relaxed and atria and ventricles fill with blood. In the systole phase, the ventricles contract and eject blood into the arteries. Throughout the cardiac cycle, blood pressure increases and decreases.

Valves are passive tissues that open and close under blood pressure forces. Anatomically, they are divided into two types, the semilunar (pulmonary and aortic) and the atrio–ventricular (mitral or bicuspid and tricuspid) valves. The semilunar valves are circular and composed of three similarly sized leaflets. Leaflets are attached to the wall at the so–called basal attachment and move freely on their opposite edge. The highest points of the basal attachment meet the other leaflets to form commissures. The atrio–ventricular valves are more complex from a morphological point of view, with unsymmetrical geometries. The mitral valve is composed of two leaflets whereas tricuspid valve is composed of three leaflets, all with different shapes and sizes and continuous basal attachment all around the valves. To prevent the valves from turning over, leaflets are attached to the inner walls of the ventricles by wired structures called chordae tendineae. Semilunar valves prevent the reverse blood flow into the ventricles during diastole while the atrio–ventricular valves prevent the reverse blood flow from ventricles to the atria during systole. The loading cycle of the valves is repeated every second so that, during a lifetime period, they will open and close nearly three billion times [Sacks et al. 2009]. A heart blood flow diagram is shown on fig. 1.

In the USA in 2010, the number of deaths directly attributable to valvular heart diseases was 23 141 [Roger et al. 2012]. Taking into account valvular diseases as underlying cause of the death or being otherwise mentioned on the death certificate, the mortality number increases to 47 830. From two studies on 16 501 and 11 911 participants, the prevalence of any valve diseases adjusted to the entire US population range from 1.8 to 2.5%. This

prevalence also increases with ages : 0.3–0.7% from 18 to 44 years, 0.4–0.7% from 45 to 54 years, 1.6–0.9% from 55 to 64 years, 4.4–8.5% from 65 to 74 years and 11.7–13.3% over 75 years.

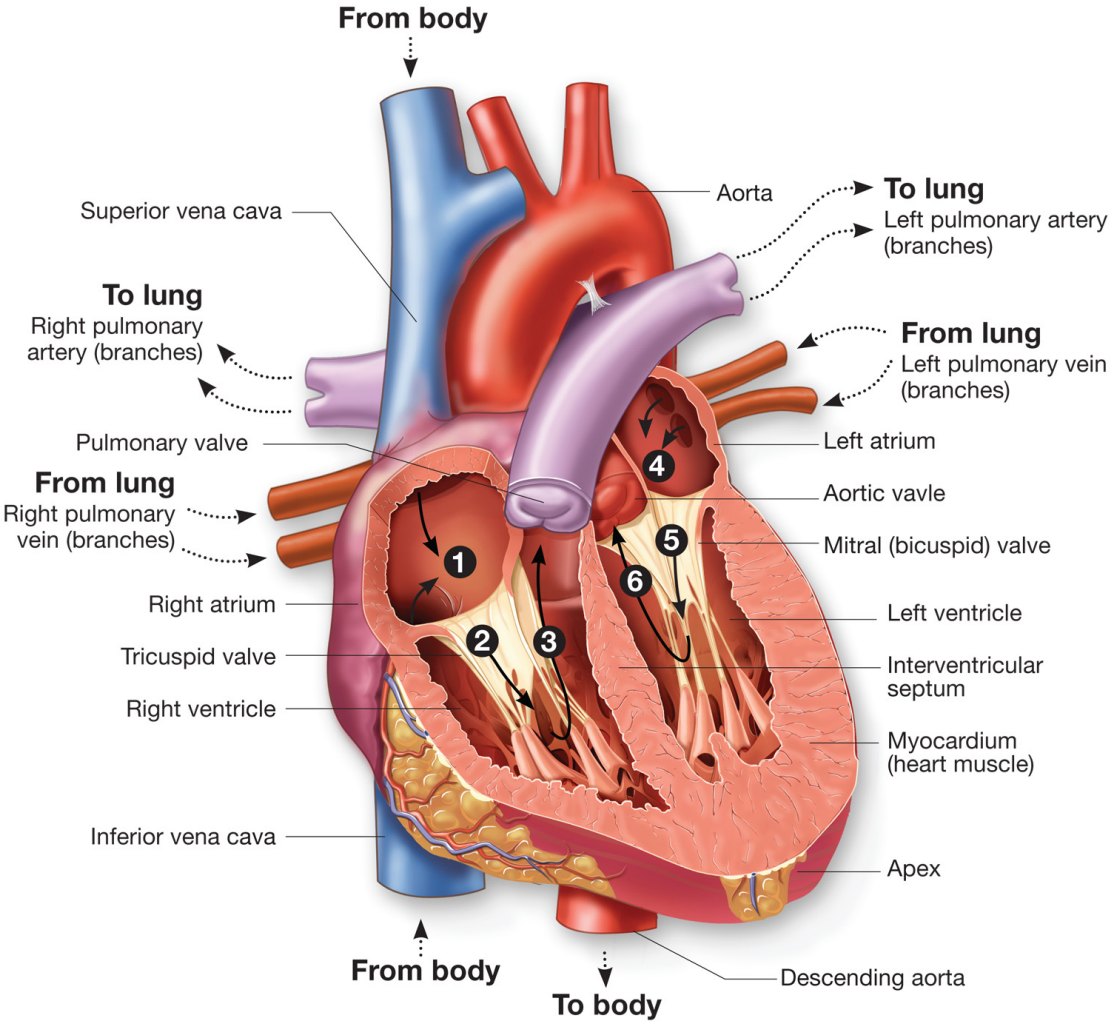

Fig. 1 – Heart circulation diagram : ❶ deoxygenated blood returns from the body to fill the right atrium of the heart creating a pressure against the tricuspid valve ; ❷ contracting the right atrium blood pressure forces the ticuspid valve to open filling the right ventricle ; ❸ contracting the right ventricle the pressure forces the tricuspid valve to close and the pulmonary valve to open sending deoxygenated blood toward the lungs ; ❹ oxygenated blood returns from the lungs and fills the left atrium creating a pressure against the mitral valve ; ❺ contracting the left atrium blood pressure forces the mitral valve to open filling the left ventricle ; ❻ contracting the left ventricle the pressure forces the mitral valve to close and the aortic valve to open sending oxygenated blood toward the body (retrieved from http://biology-forums.com)

Two kinds of diseases can affect heart valves : insufficiency (or regurgitation) when the valve does not close completely, allowing a blood leak backward, and stenosis, which is more dangerous, when the tissues become stiffer (due to calcification for instance) preventing the complete opening of the valve. Depending on the severity, treatment

may be with medication but often involves valve repair or replacement with an artificial valve. More than 280 000 prosthetic valves are implanted annually worldwide [Pibarot et al. 2009] and this number will drastically increase in the next decades with population growth and aging.

We subsequently focus on the Aortic Valve (AV). Among the different valves, AV presents indeed the highest mortality. Aortic valvular diseases were directly responsible of 15 576 deaths in 2010 in the USA and considered as an underlying cause of death in 31 746 cases [Roger et al. 2012]. When valvular replacement is needed, two artificial solutions are currently available : the mechanical and the biological prostheses (fig. 2). They are designed to mimic the function of natural valves.

(a) Mechanical model **(b)** Biological model

Fig. 2 – Examples of prosthetic AVs (retrieved from http://ctsurgerypatients.org)

Mechanical prostheses Three basic types of mechanical valve design exist : bileaflet, monoleaflet and caged ball (no longer implanted) valves. They are entirely manufactured from artificial materials. Modern prostheses are made of pyrolytic carbon or titanium coated with pyrolytic carbon. The sewing ring used to suture the valve to the walls is usually made of Teflon (polytetrafluoroethylene) or polyester. Mechanical prostheses have a good durability (usually much greater than 20 years). However, they suffer from major issues. They produce a unphysiological flow that requires a lifelong anticoagulation treatment. Their rigid leaflet structure can also be responsible of cavitation leading sometimes to failure. Finally, the implantation requires an open–heart surgery. A picture of the suture of a mechanical prosthesis is shown on fig. 3.

Biological prostheses Unlike mechanical prostheses, bioprostheses mimic the anatomy of the native valves. They are made of treated (glutaraldehyde) porcine valvular tissues or bovine pericardium mounted on a supporting structure or stent. Biological prostheses offer a better biocompatibility. Due to their improved hemodynamics, the risk of thrombus formation is low and usually does not require the use of anticoagulant drugs. However, their durability is limited. They last between 10 to 15 years, sometimes less, and clinical follow–ups indicate that more than 50% of patients develop complications within 10 years

[Mohammadi et al. 2011]. Indeed, as bioprostheses lack living cells, degenerative processes induced by mechanical fatigue, enzymes, and calcium deposition slowly deteriorate the structural components and lead to progressive valve degeneration [Simionescu 2004]. The implantation often requires an open–heart surgery but percutaneous implantation also exists when the patient is considered to be at high or prohibitive operative risk. In that case, a percutaneous transfemoral approach is usually chosen. Nowadays, approximately 55% of the implanted prostheses are mechanical and 45% are biological [Bezuidenhout et al. 2013]. Autografts and allografts which are natural valves respectively obtained from the patient or a cadaver donor, represent together a small percentage due to their limited availability and specific surgical skills. In order to prevent or minimize the impact of the implantation, Pibarot et al. [2009] worked on a patient specific optimal selection method of the prosthesis.

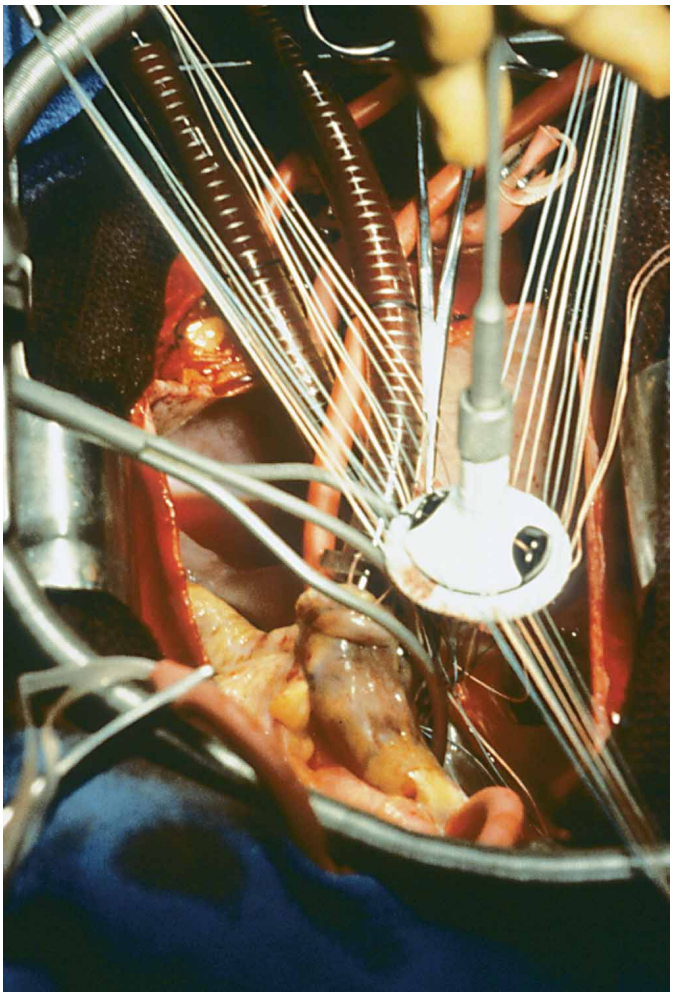

Fig. 3 – AV replacement surgery with a mechanical prosthesis (retrieved from `http://biology-forums.com`)

Context

The heart valves research and development area is of particular importance and currently, none of the mechanical or biological solutions are optimal. Thus, for several decades soft tissues biomechanical research has been focused on tissues mechanical characterization and numerical modeling for a better understanding of their physiological and pathological behaviors. One of the main purpose of these studies was the design of engineered soft tissues with mechanical properties as close as possible to those of natural ones. Readers can refer for instance to Mohammadi et al. [2011] for a review on the modeling and design of prosthetic aortic heart valves. Among others, Amoroso et al. [2012], Rong Fan et al. [2013] and Courtney et al. [2006] worked on scaffold for tissue engineering.

Polymeric prostheses represent a promising alternative. They can have a similar geometry to natural valves since they are made of flexible polymer films. This design ensure the ability to closely reproduce natural hemodynamics and generally do not require anticoagulant treatment. It is also expected that polymeric biomaterials can be treated to improve their biocompatibility, mainly hemocompatibility (minimum of inflammation and thrombogenicity) and biostability (resistance to oxidation and hydrolysis). However, polymeric prostheses currently suffer from insufficient material properties to be suitable for long–lasting implantation. After 40 years of development, results are still unsatisfactory. No polymeric valve has been clinically successful yet to be permanently implanted. They remain relegated to use in temporary ventricular assist devices for bridging heart failure to transplantation [Bezuidenhout et al. 2013]. Improving durability while keeping a good biocompatibility would allow polymeric prosthetic valves to become a clinical reality for surgical implantation and suitable for minimally invasive use (transfemoral approach for instance). Bezuidenhout et al. [2013] propose a review of the different types of polymeric replacement heart valves currently available and identify the needs to provide longterm durability and biocompatibility. A vast literature exists on biocompatibility of polymeric materials. Reader can refer for instance to Ghanbari et al. [2009] and Kidane et al. [2009] for recent advances and emerging hopes in polymers, nanomaterials and surface modification techniques that can lead together to the emergence of novel biomaterials for prosthetic heart valves with improved biocompatibility and biostability. In addition, progresses in manufacturing techniques can be expected and could lead to acceptable material durability.

Objectives and outlines of the document

The design of polymeric valves may be split into a structural design and material problem. This work is part of a Carnot M.I.N.E.S (Méthodes InNovantes pour l'Entreprise et la Société) project which aims to develop polymeric biomaterials for prosthetic heart

valves following a biomimetic approach. Biomimetism is a promising approach in the field of tissue engineering in order to obtain better mechanical properties from complex polymeric materials inspired from real valvular tissues. Engineered polymer materials should tend toward natural tissues mechanical properties. Thus, the objectives of this PhD thesis were essentially focused on the material problem, namely the mechanical characterization of reference natural tissues and their finite element modeling at the tissue level using relevant material models, since the development of new implants can greatly benefit from finite element modeling coupled with relevant experimental results. Due to the difficulty to obtain healthy human AV, we worked on porcine tissues.

This document consists of four chapters. Chapter 1 is dedicated to the mechanical characterization of porcine valvular tissues through biaxial tensile tests. For the purpose of this study, a custom biaxial tensile device has been designed and built at Cemef MINES ParisTech (Centre de Mise en Forme des Matériaux). The device is coupled with a digital image correlation system. Mechanical tests are performed on both frozen and fresh samples. The microstructure which is responsible for the mechanical behavior of the tissues is also studied using confocal microscopy. Chapter 2 is devoted to the numerical modeling and the implementation of three material models of the literature in a custom laboratory version of the finite element software FORGE® NXT[1]. A phenomenological approach is chosen in order to represent the tissue at the macroscopic level. However, selected models are able to take into account some structural information through angular integration or generalized structure tensor approaches. Hence, an algorithm is developed in order to transpose experimentally observed microstructural information into finite element models. From numerical models of chapter 2 and experimental results of chapter 1, a material model parameters identification is carried out in chapter 3. An inverse analysis approach using a metamodel–assited evolutionary algorithm developed at Cemef MINES ParisTech is chosen. This allows to select the most accurate model for predicting the mechanical behavior of the tissues with its associated set of material parameters. Finally, in chapter 4, firsts elements of a fluid–structure interaction model in FORGE® are introduced. The fluid part is intended to model bloodstream and interactions between blood and valvular tissues. A smoothed particle hydrodynamic method is chosen for its relative simplicity and its Lagrangian formulation. The implemented fluid solver is then weakly coupled with the finite element solver used for the solid material. The last part of the document summarizes the main developments and achievements of the current work. Suggestions of improvement and future work are also presented.

[1] http://transvalor.com

Chapter 1

Aortic valve tissues

Contents

1.1 Introduction 8
1.2 Mechanical characterization 11
1.2.1 Specimen preparation 11
1.2.2 Biaxial device 11
1.2.3 Digital image correlation method 13
1.2.4 Experimental protocol 13
1.3 Fibers orientation measurement 15
1.3.1 Specimen preparation 15
1.3.2 Confocal laser scanning microscopy and experimental setup . . 16
1.3.3 Experimental protocol 17
1.4 Experimental results 18
1.4.1 Biaxial tensile tests results and discussion 18
1.4.2 Confocal laser scanning microscopy results and discussion . . . 29
1.5 Summary of Chapter 1 34
1.6 Résumé en français 35

1.1 Introduction

Soft tissues consist of protein fiber networks and cells immersed into a ground substance. They can grow and remodel reacting to their environment (*i.e.* chemical and mechanical changes). Protein fibers refer to collagen and elastin while the ground substance includes all the other components of the extracellular matrix, mainly water and glycosaminoglycans (GAGs). Collagen is the main structural protein, responsible for the tissue stiffness and cohesion. It consists of multiple tropocollagen molecules that form collagen fibrils via crosslinks. Multiple fibrils form fibers, which create a network. Several types of collagen can be defined depending on the arrangement of the protein molecules. Elastin is a highly elastic protein that contributes to the tissue cohesion and confer its elasticity. These elastic properties result from the ability of proteins to unfold reversibly allowing the tissue to go back to its original shape after stretching or contracting. Elastin is synthesized and secreted in the extracellular matrix during the growth period. With aging, the amount of available elastin decreases and is gradually replaced by collagen, making the tissue stiffer. Glycosaminoglycans consist of long unbranched polysaccharides, usually attached to a protein to form proteoglycans (PGs). Highly hydrated, they may facilitate the diffusion of nutrients and oxygen across tissues. Microscopy images of some constituents that can be found in soft tissues are shown on fig. 1.1.

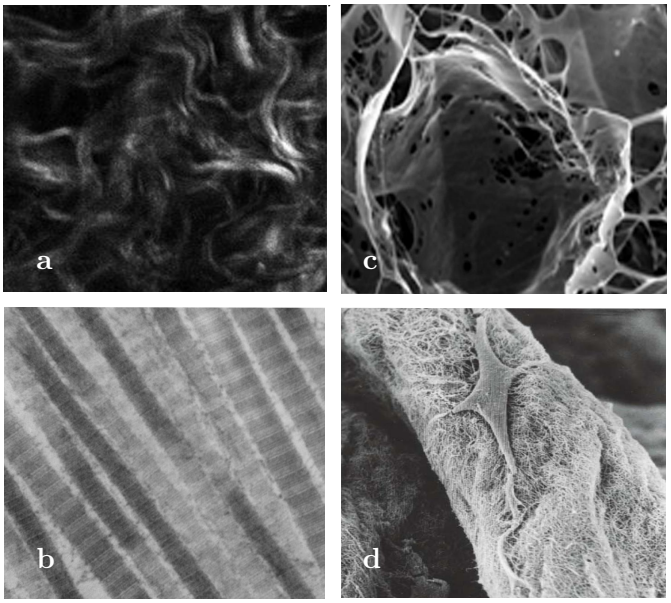

Fig. 1.1 – Microscopy images of some constituents : (a) confocal image of wavy collagen fiber bundles ; scanning electron microscopy images of (b) individual type I collagen fibers (c) elastin structure isolated from AVs using NaOH digestion [Vesely 1997] (d) AV interstitial cell on collagen fiber showing long cellular extensions [Taylor et al. 2003]

AV leaflets are tri–layered structures mostly composed of wavy type I collagen, elastin and GAGs [Sacks et al. 2009]. They contain about 50% of collagen and 13% elastin on

a dry weight basis. Stella and Sacks worked on the characterization of the mechanical properties of the layers [Stella and Sacks 2007] and Buchanan and Sacks on the interlayer micromechanics [Buchanan et al. 2013]. From these studies, the fibrosa which constitutes the upper part of the leaflet, appears to be the main layer regarding the mechanical behavior. The fibrosa is the thickest layer ($\sim$ 40% of the total thickness) and is essentially composed of undulated and strongly oriented collagen fibers. This layer is composed of 50% collagen (from which 90% of type I collagen) and 10% elastin on a dry weight basis [Mohammadi et al. 2011]. The fibrosa is considered to be the primary structural layer due to its amount of collagen organized into large fibers. The bottom layer ($\sim$ 30% of the total thickness) is called ventricularis. Mainly composed of elastin (20%) and collagen fibers (almost 50%) this layer is highly elastic and appears to assist in reducing large radial strains [T. C. Lee et al. 2001; Vesely 1997]. Because of its high elastin concentration, the ventricularis carries slight compressive preload on the fibrosa layer at rest [Vesely 1997]. The central spongiosa layer contains a high concentration of GAGs. Its physiological function is believed to be a damping of the leaflet structure and to lubricate the fibrosa and ventricularis as they shear and deform [Eckert et al. 2013; Lovekamp et al. 2006]. The presence of collagen and elastin fibers confer to the spongiosa a good resistance to delamination through collagen fiber interconnections between the fibrosa and the ventricularis layers. Some authors distinguish a fourth layer, the lamina arterialis, closely related to the fibrosa and located on the outflow side of the leaflet (fig. 1.2). A population of interstitial cells with characteristics of myofibroblasts also resides in AV tissues [Mulholland et al. 1997]. Their role is to maintain tissue structural integrity through protein synthesis and enzymatic degradation. Being attached to the surrounding matrix, they transmit load at the cellular level but does not contribute significantly to the leaflet mechanical behavior [Merryman et al. 2006].

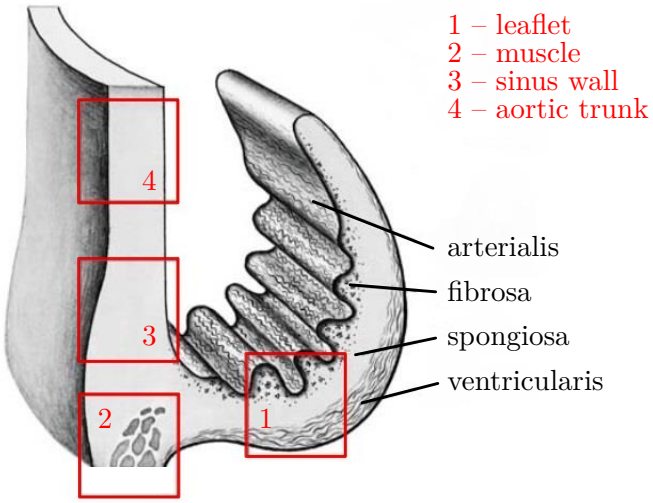

Fig. 1.2 – Illustration of the AV displaying the leaflet structure [Schenke-Layland et al. 2009]

During a cardiac cycle AV cusps are submitted to three physiological loading modes : tension, shear and flexure. However, for feasibility issues, most of the characterization work that can be found in the literature are carried out on tension testing. Biaxial tensile tests are usually performed for valve leaflets because uniaxial loadings are known to lead to non–physiologic deformation due to fibers rotations allowed by the unconstrained specimen edges. Also, the small strain domain of uniaxial tensile tests may lead to non–unique solutions during inverse analysis procedure. In order to estimate relevant material parameters numerous experiments over a wide range of mechanical solicitations are commonly made [Sacks 1999]. Billiar et al. [2000b] have studied the multi–protocol biaxial mechanical behavior of AV fresh and glutaraldehyde–treated cusps (chemical treatment of biological tissues widely used for bioprosthetic heart valves). The leaflets time–dependent mechanical properties were investigated by Stella, Liao, et al. [2007] and Borghi et al. [2013]. AV tissues appears to be quasi–elastic materials under physiological planar biaxial loading states, with negligible time-dependent effects, unlike most of soft tissues that exhibit vicoelastic behavior. The authors speculate that this specific behavior results from the interactions between the collagen fibers and the surrounding matrix at the molecular level, especially the stabilizing effect of glycosaminoglycans. However, as the study of soft biological materials presents many theoretical and practical difficulties especially due to their highly heterogeneous structure, optical techniques are occasionally used to measure two– or three–dimensional angular fiber distributions. For instance, Billiar and Sacks developed a method using Small Angle Light Scattering (SALS) on a tensile device to quantify the fiber kinematics of tissues under biaxial stretching [Billiar et al. 1997; Billiar et al. 2000b].

As biological soft tissues usually present significant regional heterogeneity due to their local fibers arrangement, local composition and their geometrical non–uniformity, they remain challenging to be accurately characterized. Thus, the use of non–invasive video analysis systems for local full–field surface measurements, widely used in engineering research, seems to have a great potential. However, the reported biomechanical applications of these methods are still rather limited. Among them, the most popular technique is the Digital Image Correlation (DIC). This is an optical method which uses high resolution cameras to measure surface strain fields and displacements by tracking grey level intensity values on the sample surface during the deformation. D. Zhang et al. [2004] present the fundamentals of DIC with advanced applications to biological materials. Among examples of DIC use for biomechanical applications Deplano et al. [2016], for instance, used biaxial tensile tests and three–dimensional DIC (3D–DIC or stereoscopic DIC) on porcine ascending aorta. Badel et al. [2012] used 3D–DIC coupled with a material model for the mechanical identification of layer–specific properties of mouse carotid arteries. Sutton, Ke, et al. [2008] used a microscopic 3D–DIC system for strain field measurements on mouse carotid arteries. Luyckx et al. [2014] studied human tendon tissue using 3D–DIC,

and Boyce et al. [2008], bovine cornea through inflation tests.

In this chapter a mechanical characterization of porcine AV leaflet tissues was performed using biaxial tensile experiments coupled with DIC measurements. The mechanical behavior of soft tissues being closely related to their fibrous architecture, confocal microscopy was also used to obtain local planar angular collagen fiber distributions in the fibrosa layer. These material and structural information will allow to accurately calibrate valvular tissue models through inverse analysis procedures (see chapters 2 and 3). In section 1.2 we introduce the biaxial device and the experimental protocol used for the mechanical characterization of the tissues. The structural characterization, with local collagen fiber orientations measurements using confocal microscopy is detailed in section 1.3. Finally, results are presented and discussed in section 1.4. A summary concludes the chapter (section 1.5).

1.2 Mechanical characterization

In this section we present the mechanical characterization of AVs through biaxial tensile tests coupled with full–field surface measurements. Due to the difficulty to obtain healthy human AV samples, we have worked on porcine tissues.

1.2.1 Specimen preparation

Two frozen (stored at −20 °C) and two fresh porcine hearts (about 5 months, 80 kg) were obtained from a local provider. AV leaflets were excised using a bistoury (fig. 1.3). For each specimen, one square sample of about 10 mm side length was isolated from the central (lower belly) region of the leaflet. Similarly to Billiar et al. [2000b], samples were stored into 0.9% isotonic saline (NaCl) at room temperature during the preparation of the experiment.

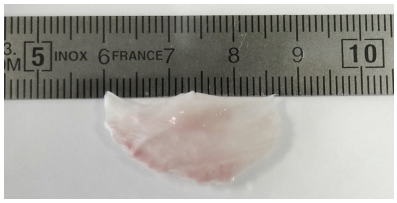

Fig. 1.3 – Porcine AV leaflet excised

1.2.2 Biaxial device

A custom biaxial tensile test device, funded by MAT XPER[1] company, was designed and built in our laboratory for the purpose of this study (fig. 1.4). The device is equipped

[1] http://mat-xper.com

with four synchronized motorized arms, allowing a maximum displacement of 25 mm each and a minimum step of 0.05 µm. Speed ranges from 0.07 µm/s to 26 mm/s. Each arm comprise a 50 N load cell with a sensitivity of 0.001 N. Following Sun et al. [2005] who studied the effect of boundary conditions on the estimation of the planar biaxial mechanical properties of soft tissues, specimens are maintained with a rake of five hooks on each side (at initial distance of 1 mm from each other). These boundary conditions appear to provide a better stress uniformity than clamps. The minimum area between the hooks is 7×7 mm^2. Two cameras are placed above the specimen in order to measure full–field surface strain using a high contrast speckle pattern and 3D–DIC software. It consists of 5 Mp resolution PIKE® cameras from Allied Vision Technologies[1], with a maximum acquisition frequency of 14 fps. Low distortion fifty millimeter Schneider–Kreuznach[2] photographic lenses are mounted. In order to constantly and uniformly illuminate the sample's surface, two coherent light sources are placed above. Arms are controlled in displacement with a custom LabVIEW software (National Instruments[3]). Each axis stops independently when imposed force threshold is reached in order to prevent tissue degradation. During the experiment, samples are immersed into a bath of 0.9% isotonic saline at room temperature. See appendix A for further information.

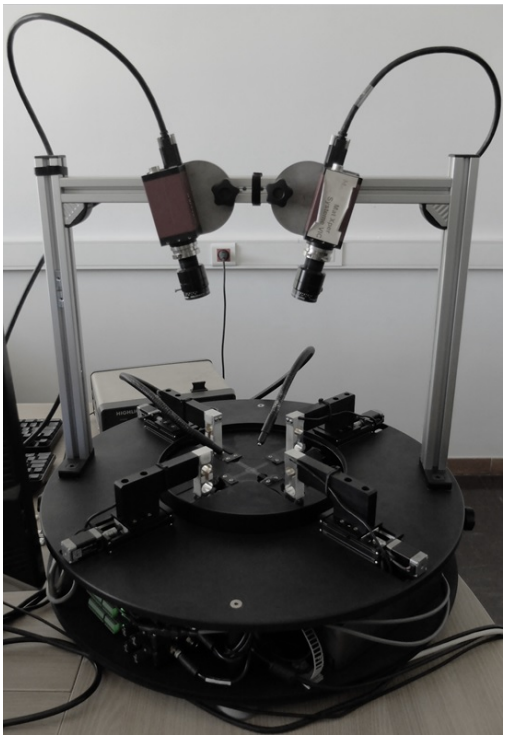

Fig. 1.4 – The biaxial tensile device

[1] http://alliedvision.com
[2] http://schneiderkreuznach.com
[3] http://ni.com

1.2.3 Digital image correlation method

As stated in the introduction, DIC is an non–invasive optical technique that uses image recognition to analyze and compare grey levels of pixels from digital images of the sample's surface. The basic principle is to build a displacement field from pictures in the initial and a deformed configurations by tracking similar points in both images (fig. 1.5). In practice, its a local collection of pixel values (called "subset") with a signature that maximizes a similarity function which is tracked. The subset displacements and deformations are tracked by checking possible matches at several locations. Each location is graded depending on a similarity score calculated using a correlation function (classically a sum of squared differences of the pixel values). High resolution and low noise cameras need to be used to take pictures of the sample during deformation. In order to make the tracking procedure possible, the surface of the sample has to be randomly and highly contrasted. If the surface does not naturally allow tracking, a high contrast speckle pattern (paint, ink, powder, ...) is usually applied. The method has a large number of applications for two– and three–dimensional deformation measurements for a large size of scales and a large range of time scales. To have more detailed information, the reader is highly encouraged to refer to the book written by Sutton, Orteu, et al. [2009].

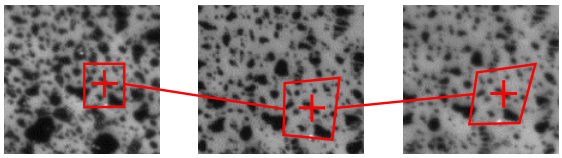

Fig. 1.5 – Example of subset tracking during deformation

1.2.4 Experimental protocol

First of all, the 3D–DIC system was set up. The focus of each camera was made using the maximum aperture size. Then the opening of the aperture was reduced in order to increase the depth of field during image recording. The depth of field is important to maintain focus in case of out–of–plane displacements. The system was calibrated using a standard calibration grid (a panel with a regular points grid) provided with the DIC system. The accuracy of the whole procedure is highly dependent of the quality of the calibration which ensures the dimensional coherence of the system. During this process the distance from the system to the sample and the orientation of the cameras are determined. We used the VIC–3D™ software from Correlated Solutions[1] for the image acquisition and the DIC processing over a selected finite area of observation.

In order to capture local strain using full–field surface measurement, a speckle pattern was made on the samples surfaces. We experienced many difficulties to find a paint

[1] http://correlatedsolutions.com

or ink able to adhere to the tissue ones immersed into the isotonic saline. In order to preserve there mechanical properties, AV tissues, which contain a lot of water, have to remain moist during the application time of the paint. However, the moisture of the leaflet surface prevents a fast drying of the paint.

After several attempts, we selected the black "Bombay India ink", suggested in Genovese et al. [2011], which is a waterproof and quick–drying ink. Moreover, following the same authors, this ink appears to not affect the tissue mechanical behavior. To facilitate the application of the ink, the surface of the sample was quickly dried with a jet of compressed air at room temperature. Then, the ink was sprayed over the sample using an airbrush at low pressure (0.5 bar with a 0.5 mm pipe) until the speckle pattern uniformly covers the surface. The specimen dried for less than five minutes at ambient air before being mounted on the biaxial device and immersed into isotonic saline (fig. 1.6).

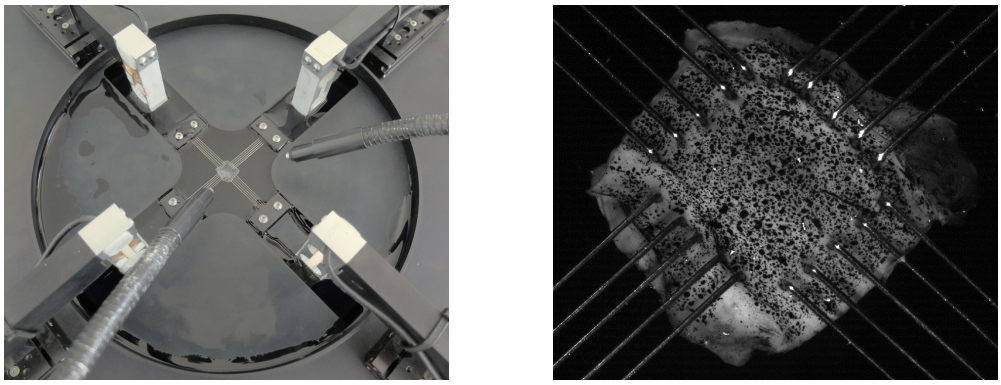

(a) Sample immersed **(b)** Speckle pattern

Fig. 1.6 – Sample mounted on the biaxial tensile devise

A small pre–load of 0.01 N was initially applied to slightly stretch the samples. From this loading state, specimens were preconditioned[1] for three monotonic loadings at 0.01 mm/s with a force threshold of 0.5 N on each axis. Samples were submitted to seven loading conditions $(F_x : F_y) = \{(1:1), (1:0.5), (1:0.25), (1:0.1), (0.1:1), (0.25:1), (0.5:1)\}$ at 0.01 mm/s, where the couple $(F_x : F_y)$ represents the force threshold ratio on each axis depending on the loading protocol. The maximum force threshold is fixed to 0.5 N. This value was chosen to correspond to the *in vivo* membrane tension peak of 60–80 N/m which occurs during diastole [Sacks et al. 2009]. This means for instance that for a $(1:0.5)$ loading $F_x = 0.5$ N and $F_y = 0.25$ N. Thus, each axis stops independently when it reaches its own force threshold. As aortic leaflet tissues showed negligible sensitivity to strain rates ranging from quasi–static to physiologic [Stella, Liao, et al. 2007], only one displacement velocity was used for the experiments. Finally, once the sample has been

[1] Preconditioning is usually essential in biomechanics is order to stabilize the mechanical response of the tissue (softening) and tend toward the *in vivo* mechanical behavior.

removed five thickness measurements at different locations were made using a micrometer (with a resolution of 2 µm) and averaged. Thickness measurements were made after the experiment in order to avoid damaging of the tissues and to take into account the loss of water induced by the deformation.

For the post–processing on the 3D–VIC™ software, subset size and subset overlapping (in px) were chosen with respect to the speckle pattern size, distribution and contrast (fig. 1.7) in order to obtain the best compromise between accuracy and analysis time [Candau et al. 2016]. Note that the equivalence is of about 73 px for 1 mm. Three virtual extensometers were placed and averaged on each axis in order to measure real displacements of the sample's boundaries. Strain was averaged in the central area of the specimen. The preconditioned state was used as reference state for strain computation.

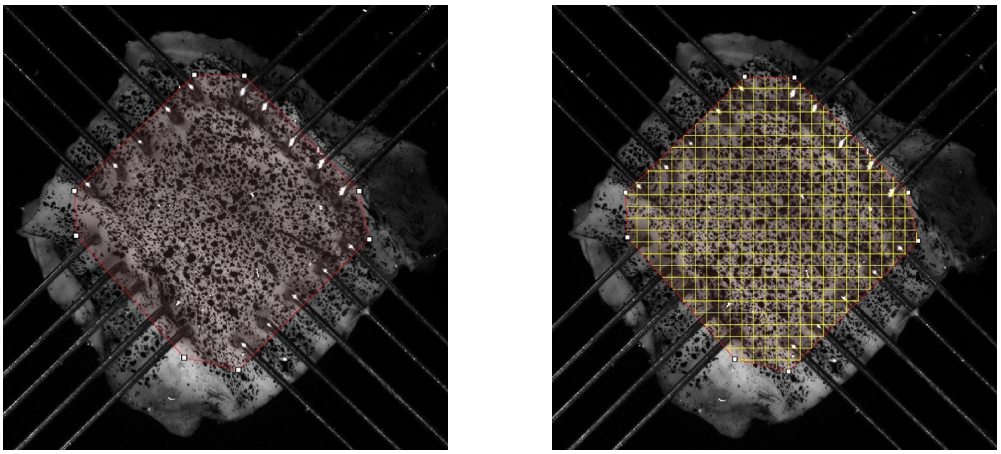

(a) Selection of the area of interest **(b)** Subset grid size (29 px)

Fig. 1.7 – Example of subset choice on 3D–VIC™

1.3 Fibers orientation measurement

In this section we study the collagen network structure in the fibrosa layer of porcine AVs. The objective was to get information on local fibers orientation.

1.3.1 Specimen preparation

Two fresh samples were observed using confocal laser scanning microscopy. The first sample was a square excised from the central (lower belly) region and previously tested on the biaxial tensile device. The second sample was a whole leaflet which did not undergo any *ex vivo* mechanical loading. The surface of the samples was carefully dried with a fabric in order to stuck them in a Petri dish, in their undeformed state, using a cyanoacrylate adhesive. The glue was applied on the ventricularis side so that the fibrosa

layer can be observed. Finally, the Petri dish was filled with 0.9% isotonic saline and fixed on the microscope stage. After a few minutes, the tissue was rehydrated and stabilized.

1.3.2 Confocal laser scanning microscopy and experimental setup

Confocal microscopy is based on the fluorescence principle, usually with a laser as light source. The laser beam goes through a pinhole, is reflected by a mirror and is finally focused on the specimen thanks to an objective lens. The surface of the specimen is scanned by moving the pinhole in an optically conjugate plane in front of a detector. Thus, only light produced by fluorescence coming from the focal plane can be detected and participates to the image formation. Out–of–focus light is optically eliminated by the confocal pinhole. Moreover, confocal microscopy allows to reconstruct three–dimensional data by recording a stack of two–dimensional images taken at successive focal planes through the sample. This is called "optical sectioning". Readers may refer for instance to the work of Laurent et al. [1992] for further information on the working principle of confocal microscopes.

The experiments were made at the Hubert Curien laboratory (Saint–Étienne, France) on a Leica TCS SP2 SE confocal microscope (fig. 1.8). The laser used was a Chameleon Vision from COHERENT®. A $\times 40$ water immersion objective was mounted on the microscope and the zoom was set to $\times 1.7$ to get closer to the optimal pixel size (fig. 1.9). Resulting images were 12–bit images with a total size of 220×220 µm^2 and a pixel resolution of 1024×1024. In order to excite collagen fibers in all directions, a laser beam of circularly polarized light at 830 nm was used.

Fig. 1.8 – Confocal microscope Leica TCS SP2 SE form Hubert Curien Laboratory (Saint–Étienne, France)

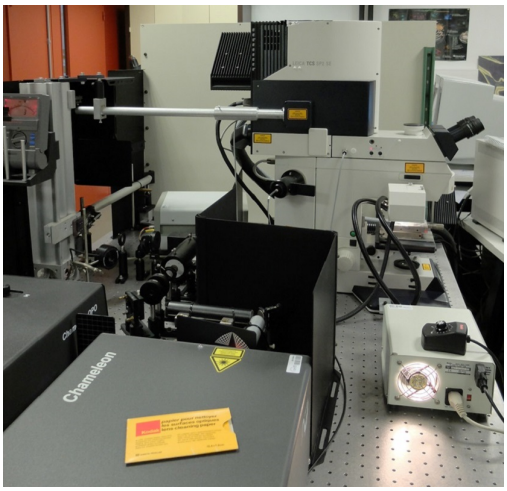

(a) Laser and optical system

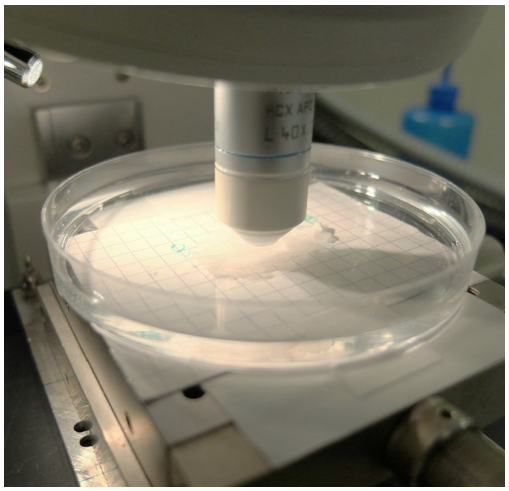

(b) Water immersion objective (×40)

Fig. 1.9 – Optical system and objective

1.3.3 Experimental protocol

For both samples, the reference point was taken on a grid placed below the Petri dish aside from the sample. From this point, a series of images were made knowing the planar coordinates of each measurement and displacements were applied using a micrometric xy travel stage. Due to the waviness of the samples' surfaces and the spacing between successive acquisitions, the focus had often to be made manually making the overall protocol time consuming.

On the squared sample, images acquisitions were made each millimeter in the circumferential direction and half millimeter in the radial direction (fig. 1.10). An area of 5×5 mm^2 located at the center of the sample was scanned. On the leaflet sample, images acquisitions were made with a measuring interval of 2 millimeters in both directions (fig. 1.10). An area of approximately 26×12 mm^2 was scanned.

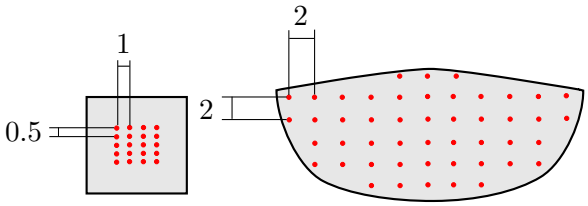

Fig. 1.10 – Scheme of the observation areas positions (mm) on both samples

1.4 Experimental results

In this section we present experimental results obtained from biaxial tensile tests with full–field surface measurements and collagen fibers observations from confocal images of AV samples. Local fiber orientations information provided by confocal images and the mechanical response of the tissue will be later use for the identification of material models parameters using inverse analysis procedures (chapter 3). To the best of our knowledge, 3D–DIC has not previously been applied to the measurement of local biomechanical properties of AVs.

1.4.1 Biaxial tensile tests results and discussion

Conventions

Hereinafter, we define the radial and circumferential axes of tension as stated on fig. 1.11. They respectively correspond to the direction of the radius from the center of the valve and the direction following the circumference.

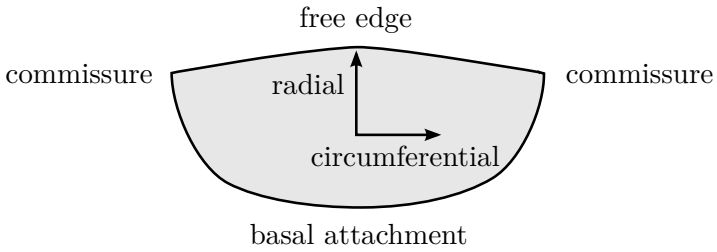

Fig. 1.11 – Scheme of an excised AV leaflet

Thickness measurements

The averaged thickness measurements of the samples are presented on fig. 1.12. Each bar of the histogram represents the averaged thickness of the three leaflets of a valve with the maximum and minimum dispersion of leaflets' averaged thickness from the mean. No significant dispersion between the valves samples was found, with an average value of 0.525 mm. The dispersion between the average thickness of each sample of a valve ranges from 45 to 97 µm difference with the mean value.

However, this measurements should be taken with caution due to the difficulty to obtain accurate and repeatable thickness values using a micrometer for practical reasons (softness of the tissues, heterogeneous thickness, ...).

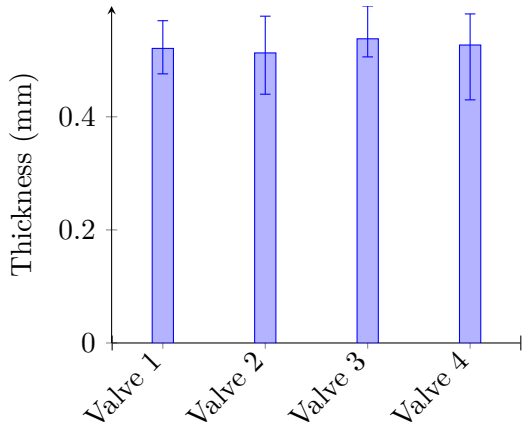

Fig. 1.12 – Averaged thickness of the samples with dispersion for each valve

Tissue preservation

In order to ensure that the tissue was stabilized after preconditioning and did not yet damaged during the experiments, a $(1:1)$ loading was repeated after the complete loading protocol. In fig. 1.13, the first $(1:1)$ loading condition of the protocol and the last one are superimposed for one sample. No significant differences in the mechanical response were found.

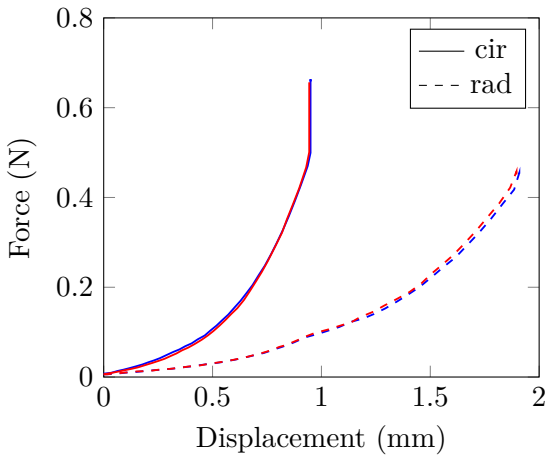

Fig. 1.13 – $(1:1)$ curves at be beginning and at the end of a complete loading protocol on a sample

3D–DIC measurements on immersed samples

The sample being immersed, the 3D–DIC measurements can be affected by optical refraction at the interface between the media (*i.e.* isotonic saline for the sample and air for the cameras). A few people have studied this effect. In Sutton and McFadden [1999], the

authors showed that increasing errors are introduced as the angle between the optical axis and the optical interface changes. They conclude that carefully control of the rotation angle between the specimen and the viewing system during underwater experiments is sufficient to minimize the effects of orientation variations on full–field surface measurements. Results also indicated that slow fluid motion does not significantly affect these measurements. However, some authors have developed optimization–based or correction methods to calibrate cameras. This is the case for instance for Ke et al. [2008] who present a stereo vision and calibration methodology improving 3D–DIC measurements accuracy on submerged objects.

No correction were applied to our correlation system. However, to be sure of the measurements accuracy despite of the isotonic saline bath, a 3 mm displacement rigid body motion of a steel plate was captured. The strain field was measured and the displacement from DIC and the device arm were compared (fig. 1.14). No significant differences were observed between the device and the DIC measurements of the displacement. Strain fields had also negligible noise showing that results are not significantly affected by the samples immersion.

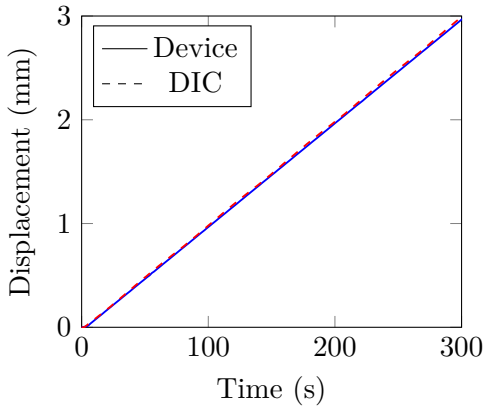

(a) Displacements comparison

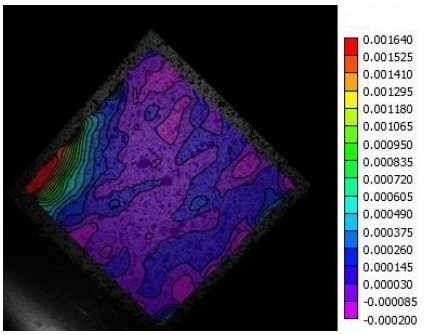

(b) Nominal strain ε_{xx}

Fig. 1.14 – 3D–DIC error measurement on an immersed plate submitted to a rigid body motion

3D–DIC strain fields

Correlation parameters can significantly affect the strain field. In order to chose relevant parameters, the influence of the subset size, subset overlapping (or its opposite "step") and filter size values was evaluated. The filter size corresponds to the number of data points used to interpolate the deformation gradient. Hence, the smoothing area is of dimension step $\times$ filter size pixels.

It is known that small subset size associated with large step values results in a strong

underestimation of the calculated strain [Candau et al. 2016]. Moreover, low step values improve the strain estimation but also significantly increase the analysis time, and too low filter size can lead to noisy strain flied. Thus, choosing a subset value adapted to the speckle pattern size and distribution, it is mandatory to select a suitable combination of step and filter size. On fig. 1.15, an example of evolution of the averaged strain in a small area as a function of the smoothing area is presented for a subset size fixed to 21 px. The step ranges from 1 to 13 px and the filter size from 9 to 25. It appears that the calculated strain decreases drastically when the smoothing area increases, with a significant loss of information. A combination of step and filter size product giving the same result also give equivalent estimation of the strain. Hence we placed at the beginning of the decreasing slope with a step of 3 px and a filter size of 9 in this example. This area offers the best compromise between accuracy of the results and analysis time.

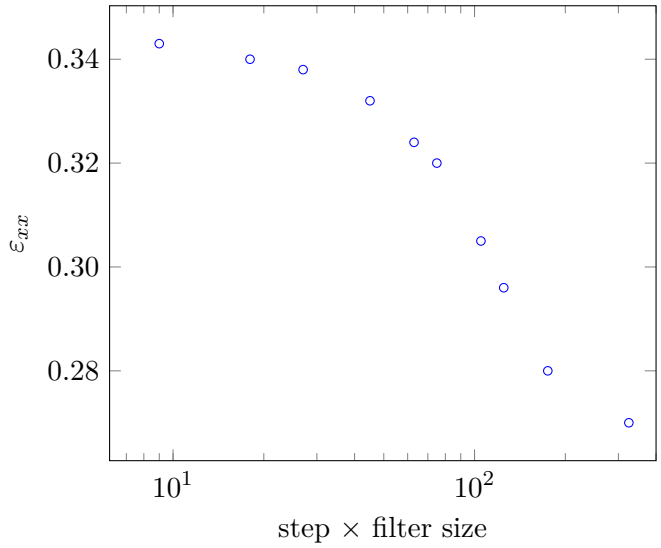

Fig. 1.15 – Example of nominal strain evolution function of the smoothing area for a subset size of 21 px

Examples of 3D–DIC strain fields ε on frozen and fresh samples are presented respectively on tab. 1.1 and tab. 1.2. On those pictures, the strain in the radial direction corresponds to ε_{xx} and the strain in the circumferential direction corresponds to ε_{yy}. Nominal strain was used. On both frozen and fresh samples, results showed highly heterogeneous strain fields in all directions (with also shear) for all loading conditions. Local strain concentrations generated by the boundary conditions can be observed around the rakes and at the sample's corners. However, these local strain concentrations appear to not strongly affect the 25% central area. Indeed, the boundary conditions used do not allow large shear deformations resulting in a relatively uniform load distribution. Due to the anisotropic mechanical behavior of the tissue and the high tensile stiffness of the collagen fibers, circumferential direction deforms less than the radial direction.

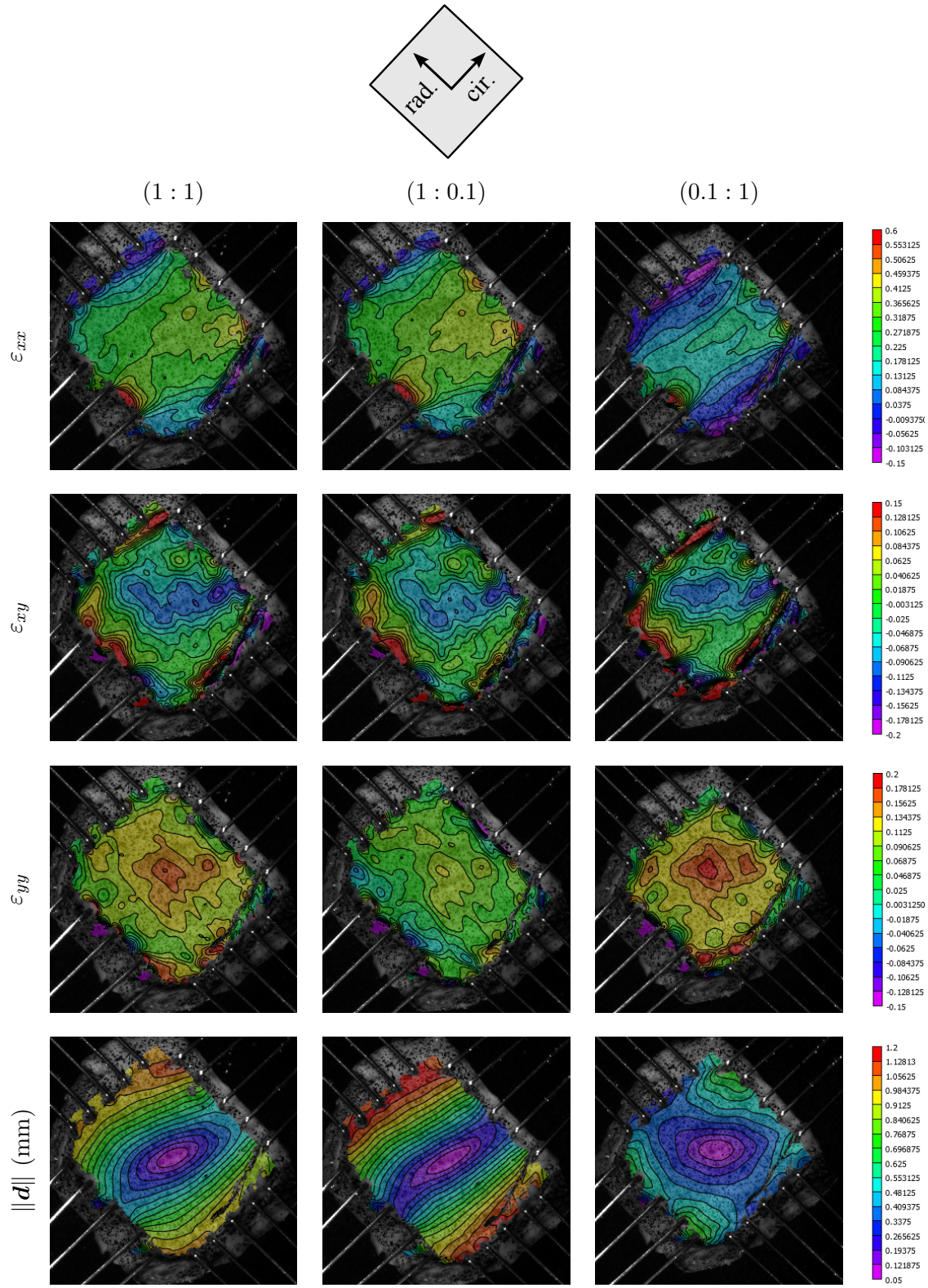

Tab. 1.1 – Nominal strain and norm of the planar displacement field at the end of several loading conditions on a frozen leaflet

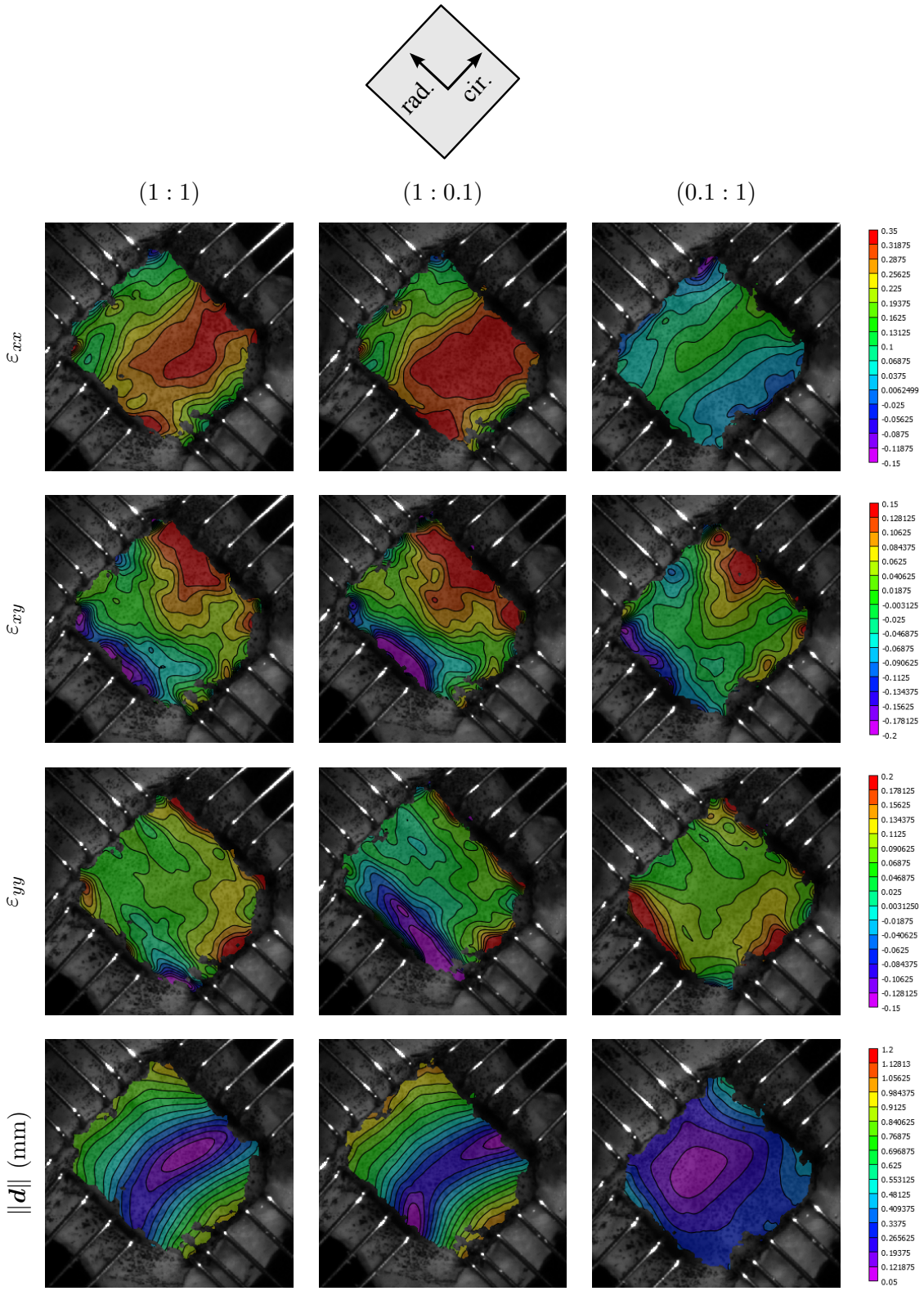

Tab. 1.2 – Nominal strain and norm of the planar displacement field at the end of several loading conditions on a fresh leaflet

Tension–strain data

As samples are thin, a plane stress state is assumed. The classic membrane stress (or tension) in N/m was used in order to avoid the use of ambiguous thickness measurements in the stress calculations as for instance in Billiar et al. [2000b]. The strain along each direction was averaged in a circular area at sample's center. An example of the influence of the size of this area on the strain value is shown on fig. 1.16 and fig. 1.17 respectively for frozen and fresh tissues. In both cases, the averaged strain increases with the surface area getting closer to the boundary conditions. However, in the 25% central region the effect of the surface area on the measurements remains low. Tension–strain results for frozen and fresh samples are shown on fig. 1.18 and fig. 1.19 for a single loading. A significant dispersion of the results in both, radial and circumferential directions can be observed. Furthermore, fresh samples present meaningful differences in their mechanical response in comparison to frozen samples, such as lower strain and stress levels and a stronger coupling between the tension axes (fig. 1.20). In order to avoid the ambiguous calculation of an averaged behavior, one representative sample for each frozen and fresh tissues was chosen to present results of a full loading protocol respectively on fig. 1.21 and fig. 1.22.

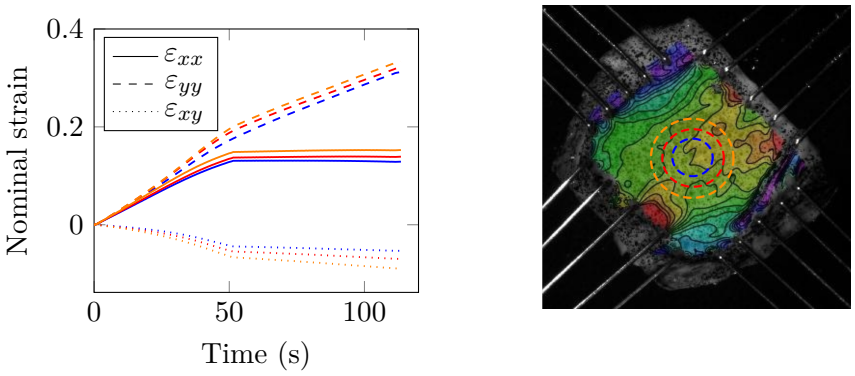

Fig. 1.16 – Example of averaged strain on a frozen sample on three different areas

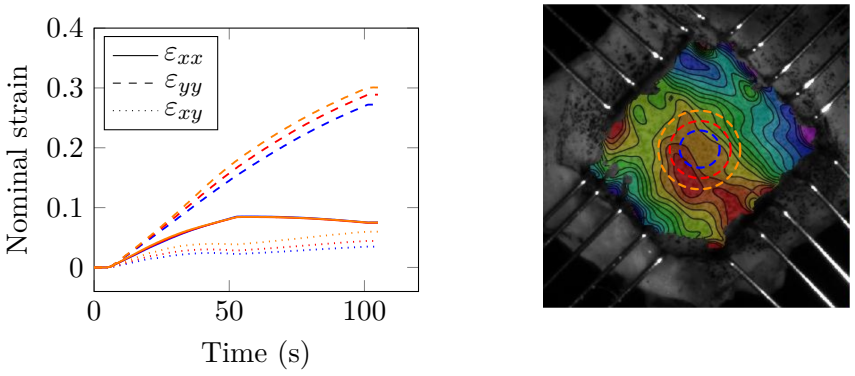

Fig. 1.17 – Example of averaged strain on a fresh sample on three different areas

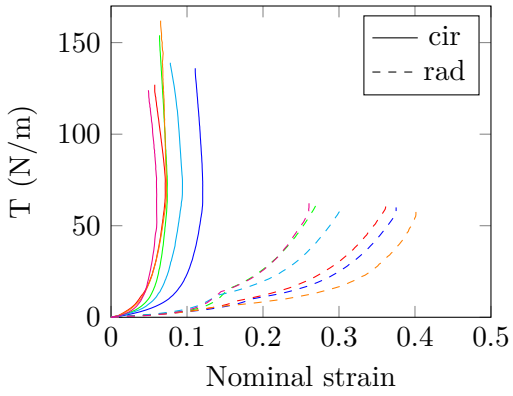

Fig. 1.18 – Tension–strain results for the (1 : 1) loading condition on six frozen samples for both circumferential and radial axes

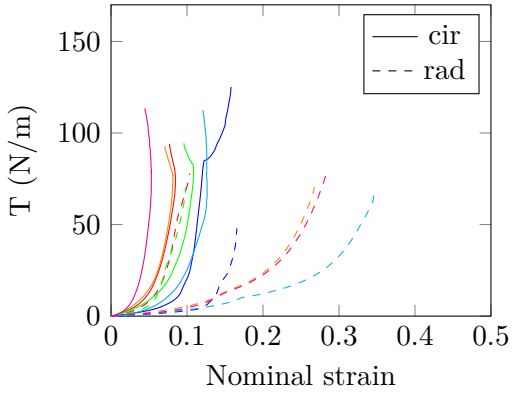

Fig. 1.19 – Tension–strain results for the (1 : 1) loading condition on six fresh samples for both circumferential and radial axes

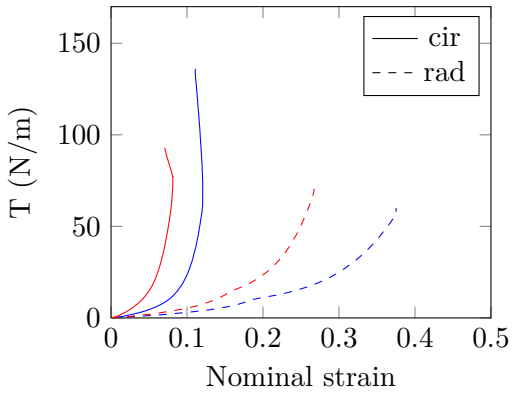

Fig. 1.20 – Example of superposition of the tension–strain results for a representative frozen (blue) and fresh (red) sample using (1 : 1) loading condition

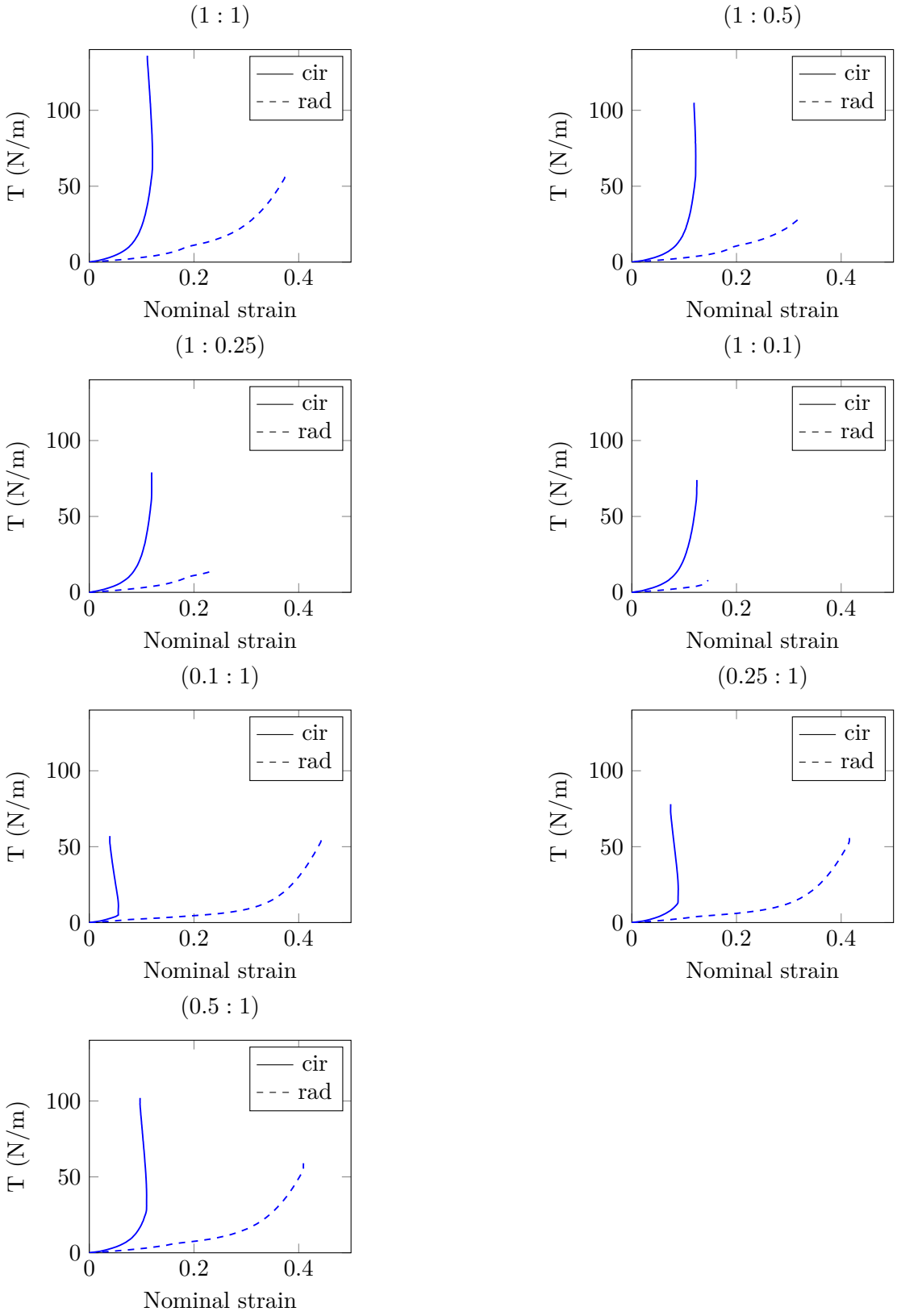

Fig. 1.21 – Tension curves on one representative frozen sample for the seven loading conditions of the experimental protocol

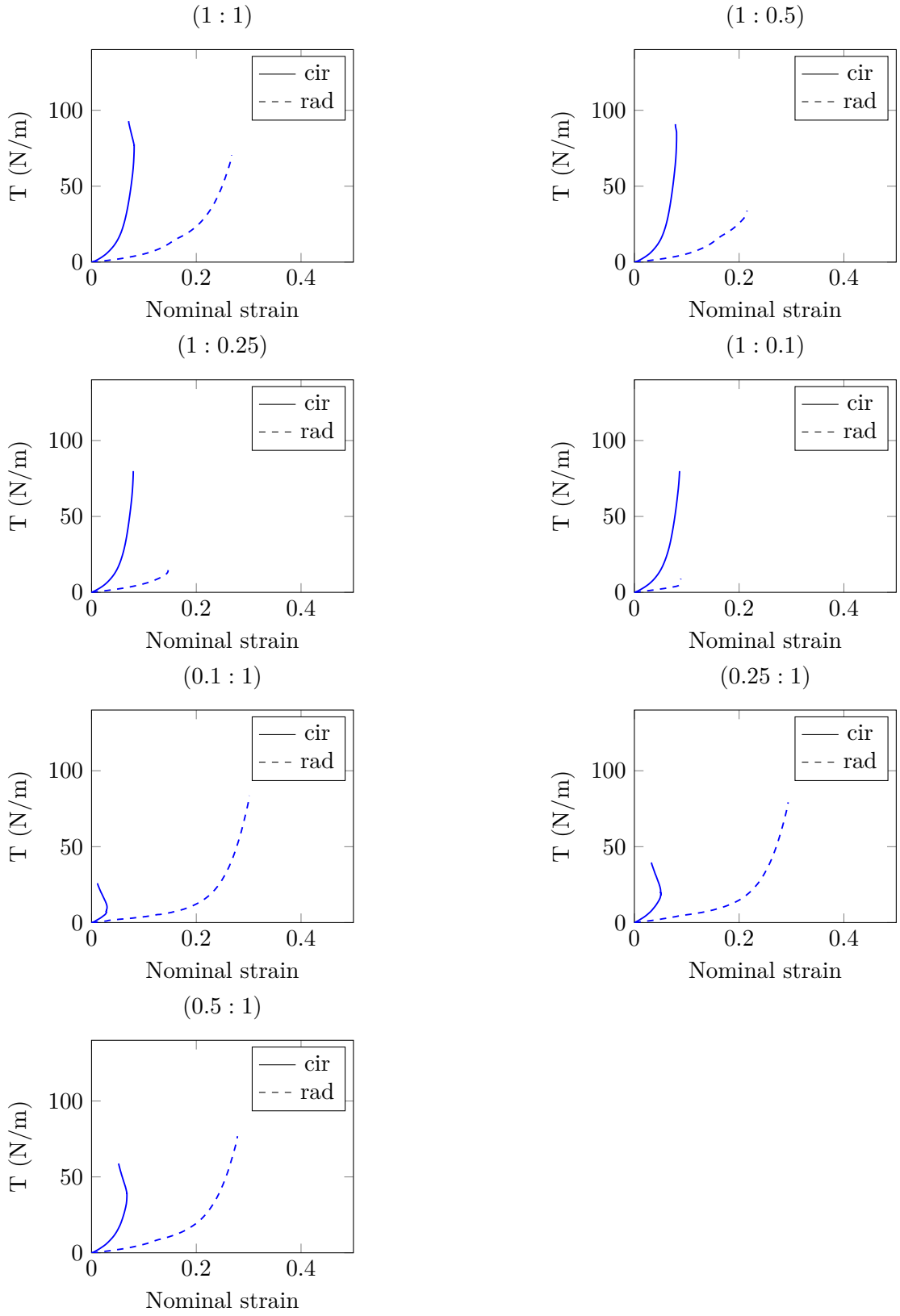

Fig. 1.22 – Tension curves on one representative fresh sample for the seven loading conditions of the experimental protocol

Discussion

Like most soft tissues, the AV tissue structure with a collagen fibers network embedded in an elastin matrix is responsible for their anisotropic behavior. Results presented above are consistent with literature data, highlighting the well–known highly non–linear mechanical behavior of these tissues. This behavior is imputable to the increasing number of initially crimped collagen fibers which are activated with deformation, starting to carry a load. Liao et al. [2007] have investigated the relation between collagen fibril kinematics (rotation and stretch) and tissue–level mechanical properties of mitral valves tissues under biaxial loading using SALS. According to their findings, collagen fibrils remain in their unstrained configuration until the beginning of the highly non–linear region of the tissue–level stress–strain curve. From tension–strain curves (fig. 1.21 and fig. 1.22), it can be clearly observed that the tissue is much more compliant in the radial direction than in the circumferential one, inducing large extensibility disparities. This mechanical response has to be compared to the fibrous structure. However, from an histology point of view it is known that collagen fibers in the fibrosa are mainly oriented in the circumferential direction (fig. 1.11), making the tissue very stiff. In the fibrosa, elastin plays a minor role and is only predominant in terms of mechanical response at low stretch, when most of the collagen is crimped. In the ventricularis, elastin fibers are predominately oriented in the radial direction. According to Vesely [1997], in this layer elastin participates equally with collagen during initial circumferential stretches but dominates the radial behavior, making the tissue response more compliant. This radial extensibility is important during valve closure phase, in order to prevent retrograde flow by ensuring leaflets' co–adaptation.

For both, frozen and fresh samples 3D–DIC measurements showed highly heterogeneous strain fields (tab. 1.1 and tab. 1.2). Thus, a complete inverse procedure on the force–displacement is required to exploit the experimental results. However, the strain and stress levels were significantly lower for fresh tissues. A strong coupling between the axes can also be observed. When one axis stops moving, the displacement on the other axis is responsible for fibers rotations. These fibers rotations induce significant realignments and decreasing strains can occur on the immobile axis. Thus, decreasing strain appears in the circumferential direction for conditions with low circumferential strain and large radial strain ($(0.1:1)$ for instance). This phenomenon is much more visible on fresh samples showing that the freezing of the tissue probably damages the fibrous structure. Experimental results showed an important scattering of the mechanical response between the samples, for both fresh and frozen conditions, but no significant difference between the leaflets of a same valve (or from different valves) was observed. The last observation should be taken with caution due to the limited number of specimens. For instance, in a recent study on the mechanical properties of aged human cardiac valves (70.1 ± 3.7 years old) some differences between non–coronary, left coronary and right coronary aortic leaflets' mechanical response were highlighted [Pham et al. 2017]. A good agreement was

found when superposing (1 : 1) loading conditions at the beginning and at the end of the protocol showing that the overall protocol did not affect the mechanical properties of the samples, *i.e.* tissue integrity is preserved during the experiments and the mechanical behavior is repeatable after preconditioning (fig. 1.13). Thus, the scattering observed does not likely come from sample deterioration during the experiment. However, it can be related to tissue variability, and more importantly to the alignment of the sample with respect to the stretch axes. Indeed, small misalignment errors could significantly modifies fibers reorientation and stretch which consequently affect the overall mechanical response of the tissues. However, the conservation time after excision (from 0 to 48 hours depending on the test) is variable from one leaflet to another and could also affect the tissue behavior. As significant change in the mechanical behavior between frozen and fresh tissues was observed, we will subsequently focus our work on fresh samples, especially for the inverse analysis procedure (see chapter 3).

Limitations

We have limited our study to *in vitro* experiments of planar biaxial tensile tests that cannot be directly compared to the complex loading encountered by the leaflets *in vivo*. Tension experiments only partially reproduce diastole loading, but not systole. Moreover, tensile results were obtained in the central region of the leaflet and should not be generalized to all areas. Other regions, like commissural regions for instance, probably exhibit a very different mechanical behavior due to their specific fiber arrangement. Regarding the DIC measurements, the speckle pattern quality varies from one sample to another due to the difficulty of applying the ink on the surface of AV and may affect the full–field surface measurements. Moreover, variability induced by the positioning of the sample with respect to the stretch axes makes the interpretation of mechanical data harder, as well as the heterogeneous strain field averaged in the central region. Finally, this study was carried out on porcine tissues that may differ significantly from human ones. Indeed, it is known that aged human AV tissues exhibit a higher level of stiffness than young porcine AV tissues [Stephens et al. 2009; Martin et al. 2012; Oomen et al. 2016; Pham et al. 2017]. However, both thickness and stiffness increase with age and the literature lacks of experimental data on the mechanical behavior of young human AV tissues to be compared to the results presented above.

1.4.2 Confocal laser scanning microscopy results and discussion

Histological observations

From an histological point of view a distinct layer above the fibrosa, also highlighted by some authors [Schenke-Layland et al. 2009], can be observed. This layer, called arterialis, is composed of a sparse network of heterogeneously oriented collagen and elastin fibers as well as cells. These microconstituants were observed using two detectors. The channel 1

with a wave lengths $\lambda = 830$ nm revealed specifically collagen fibers, whereas the channel 2 detecting all the wave lengths between 530 nm and 700 nm showed elastin fibers and cells (fig. 1.23). A superposition of the two channels is shown on fig. 1.24 with channel 1 in green and channel 2 in red. However, this layer is not considered as meaningful regarding the overall mechanical behavior of the tissue and will not be considered hereafter.

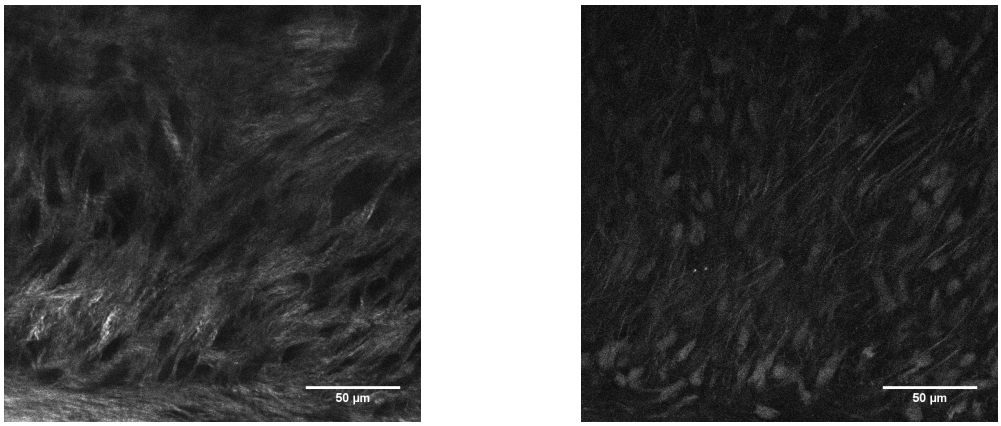

(a) Channel 1 with $\lambda = 830$ nm **(b)** Channel 2 with $530 < \lambda < 700$ nm

Fig. 1.23 – Collagen fibers (channel 1) and elastin fibers and cells (channel 2) in the arterialis

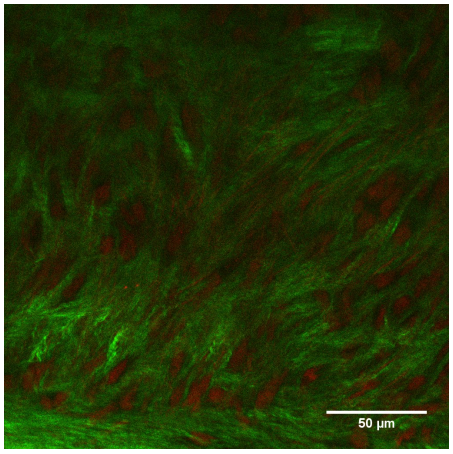

Fig. 1.24 – Superposition of channel 1 and channel 2

Confocal microscopy results showed that collagen fibers orientations considerably evolve with depth in the first ∼100 µm from the surface. From a randomly oriented state close to the surface, collagen fibers changes to an highly aligned state in the fibrosa layer (fig. 1.25). An example of images from a stack of 140 µm depth is shown on fig. 1.26. Once the fibrosa layer is reached, the orientation of the collagen fibers becomes quite stable with small orientation changes between 110 and 140 µm depth. Moreover, fibers are mainly oriented in the focal plane. Thus, assuming negligible orientations change, a single image was taken in the fibrosa layer for each location instead of a stack.

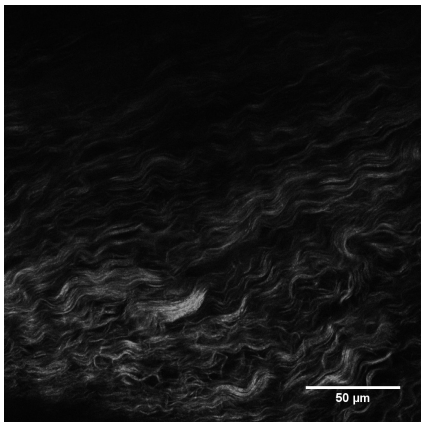

(a) Close to the surface

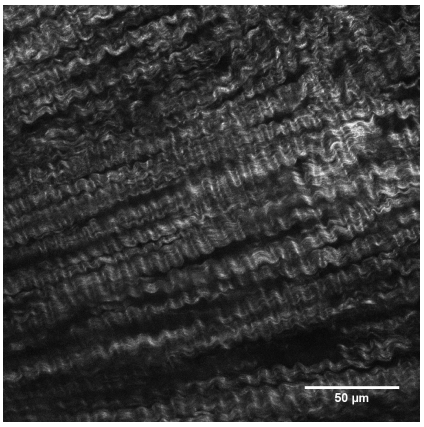

(b) In the fibrosa

Fig. 1.25 – Pictures of collagen fibers

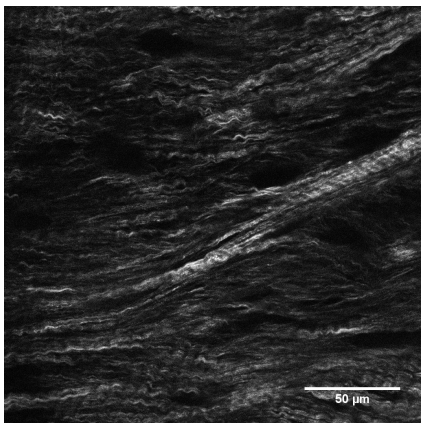

(a) 50 µm depth

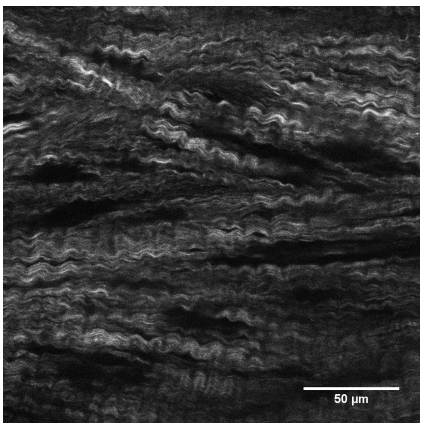

(b) 80 µm depth

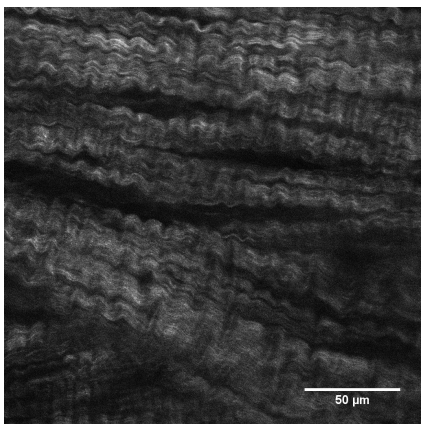

(c) 110 µm depth

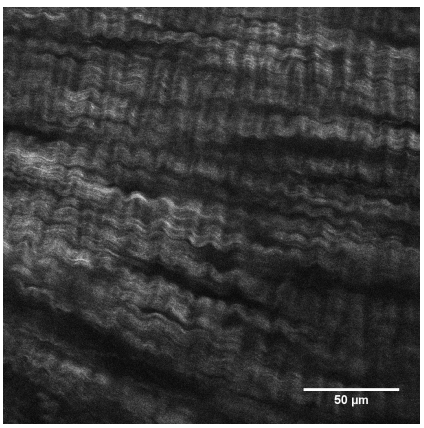

(d) 140 µm depth

Fig. 1.26 – Four pictures of collagen fibers from a total stack of 140 µm depth

Identification of the collagen orientations

Due to the specific collagen fibers structure of the fibrosa layer, the identification of the local fiber orientations in an automated way presents many practical difficulties. The quasi–continuous structure of uniformly crimped fibers makes very challenging the use of a segmentation algorithm to identify the preferred fibers orientations (see an example fig. 1.28a). Thus, the orientation measurement was made manually using ImageJ[1] software. Ten measured angles were averaged on each confocal image in order to obtain a local principal fiber direction (fig. 1.27). Despite the low number of measurements, the highly aligned fibrous structure in the fibrosa makes them relatively accurate. Moreover, this method allows to only select the fibers in fibrosa layer without pre–treatment when two layers are visible on an confocal image (fig. 1.28b).

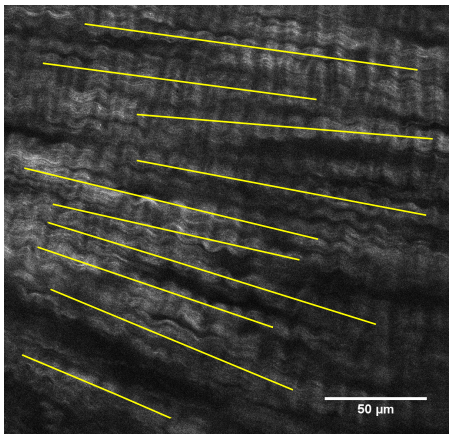

Fig. 1.27 – Illustration of angles measurements with respect to the picture frame

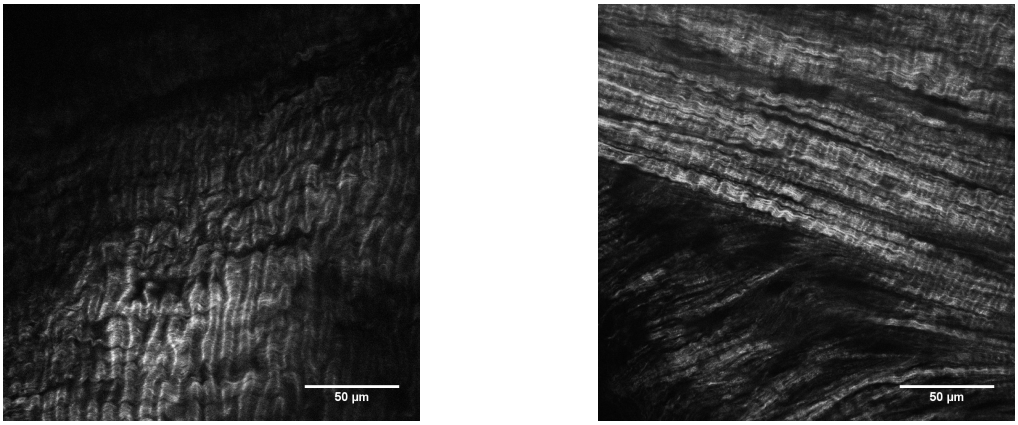

(a) Example of dense fibrous structure **(b)** Example of layers transition

Fig. 1.28 – Examples of principal orientation identification issues encountered while processing confocal images

[1] http://imagej.net

Locally averaged angles were then interpolated on a fine regular grid using cubic spline (a Python script presented subsection 2.5.4 was developed to interpolate or extrapolate angle values on the whole sample). Results are respectively presented on fig. 1.29 for the square sample and fig. 1.30 for the whole leaflet. Preferred fiber directions were mainly oriented in the circumferential direction $0 \pm 10°$. However, regional disparities can be observed with maximum angles of approximately $\pm 50°$.

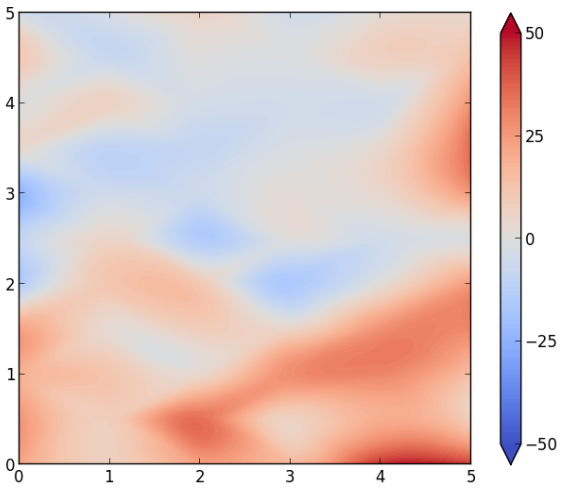

Fig. 1.29 – Angles (°) interpolated on a real scale grid (mm) for the square sample

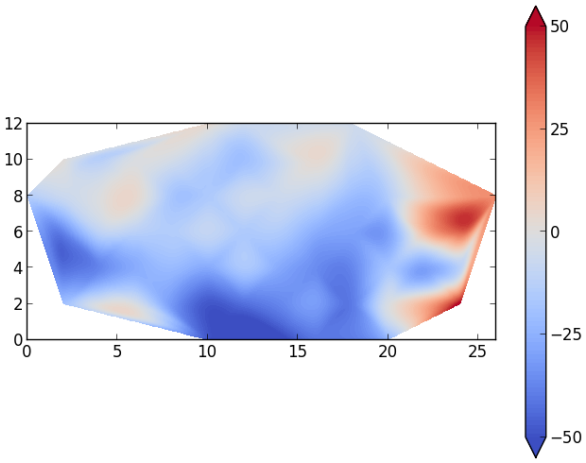

Fig. 1.30 – Angles (°) interpolated on a real scale grid (mm) for the whole leaflet

Discussion

Histological observations showed a thin superficial layer on the outlet side of the leaflet. This layer, the lamina arterialis, reported in the literature by several authors [Schenke-Layland et al. 2009; Misfeld et al. 2007; Gross et al. 1931] is mainly composed of a sparse network of collagen fibers with interstitial cells. However, there is some confusion about the nomenclature of the layers and only three main layers are usually distinguished : the fibrosa, the spongiosa and the ventricularis.

On the outlet side of the leaflet, collagen fibers evolve from approximately randomly oriented close to the surface to highly aligned in depth. In agreement with the literature, we found collagen fibers mainly oriented in the circumferential direction ($\pm 10°$) in the fibrosa layer. However, interpolated results of the local principal angle measurements (fig. 1.29 and fig. 1.30) showed heterogeneously distributed regional variations from $-50°$ to $+50°$ maximum around the circumferential direction.

Limitations

Due to the important spacing between the images in comparison to the size of the measurement area, the continuity of the local angular information is not ensured. Thus, the cubic interpolation on the samples' surface is a rough approximation and may not accurately capture angles evolution, especially discontinuities. The highly heterogeneous samples' geometry also induced difficulties. The large variations of the thickness did not allow to acquire images at a constant depth. Moreover, the image quality was affected by the relief of the samples' surface. The laser beam can be partially blocked by the relief of the tissue surrounding the measurement area, in a valley for instance. In that case, images were usually not usable to identify fibers orientations. Finally, despite the precautions taken, the angle measurement can be affected by the positioning of the sample on the microscope stage.

1.5 Summary of Chapter 1

The mechanical characterization of soft tissues often require the use of biaxial tensile tests, especially in the case of anisotropic behavior. Hence, a biaxial tensile device was designed and built in the laboratory for the purpose of this study. The mechanical tests were associated with DIC in order to allow full–field surface measurements. The experimental protocol consist of a preconditioning stage followed by seven force loadings carried out with a constant velocity. Four porcine valves, two frozen and two fresh, were used for mechanical tests. Samples were excised in the central region of the leaflets and kept hydrated in a 0.9% isotonic saline bath during the experiments. Observed strain fields are highly heterogeneous for both, frozen and fresh samples. However, these het-

erogeneities are mainly localized around the gripping system. Experimental results show an anisotropic hyperelastic behavior with a strong mechanical coupling between the tensile axes. Moreover, meaningful differences in the mechanical behavior of the two type of samples is observed, with higher stress and strain levels for the frozen tissues. The freezing having a detrimental effect on the mechanical properties of the leaflets, we focus hereinafter on fresh tissue behavior.

In order to determine the local principal collagen fibers direction, the main layer from a mechanical point of view, the fibrosa, was observed using a confocal microscope. The study was made at the Hubert Curien laboratory (Saint–Étienne, France) on two fresh samples. One sample was previously mechanically tested and the other one is an entire leaflet never tested. A series of images were taken at several locations on the samples' surface, allowing for each picture to extract a principal fibers direction. Measurements were then interpolated on the whole sample's surface. Results show that collagen fibers in the fibrosa are mainly oriented along the circumferential direction with large local disparities.

1.6 Résumé en français

La caractérisation mécanique des tissus mous nécéssite souvent de recourir à des essais de traction biaxiale, en particulier lorsque ces tissus présentent un comportement anisotrope. Ainsi, une machine de traction biaxiale a été conçue et construite au laboratoire pour les besoins de cette étude. Les essais mécaniques ont été associés à un système de corrélation d'images numériques afin de mesurer les champs de déplacements surfaciques des éprouvettes. Le protocole expérimental comporte un préconditionnement suivi de sept chargements en force effectués à vitesse de déplacement constante. Quatre valves de porc, deux congelées et deux non–congelées, ont ainsi été testées. Les éprouvettes ont été excisées dans la région centrale du feuillet et maintenues hydratées dans un bain de solution saline à 0.9% pendant toute la durée de l'essai. Les champs de déformations observés sont fortement hétérogènes pour les deux types d'éprouvettes. Ces hétérogénéités sont néanmoins principalement concentrées proche des zones d'attache des échantillons. Les résultats expérimentaux montrent un comportement hyperélastique anisotrope et un fort couplage mécanique entre les directions de traction. En outre, d'importantes différences de comportement entre valves congelées et non–congelées sont observées, avec des niveaux de contraintes et de déformations significativement plus élevés dans le cas des tissus congelés. La congélation ayant un effet néfaste sur le comportement mécanique des feuillets, on se concentrera pour la suite uniquement sur les résultats des tissus non–congelés.

Afin de connaître les orientations préférentielles locales des fibres de collagène, la prin-

cipale couche au regard du comportement mécanique, la fibrosa, a été observée à l'aide d'un microscope confocal. L'étude a été réalisée au laboratoire Hubert Curien (Saint–Étienne, France) sur deux échantillons de tissus non–congelés, l'un étant une éprouvette préalablement testée mécaniquement, l'autre un feuillet complet non testé. Une série d'images a été prise sur la surface des échantillons, permettant pour chacune d'entre elles d'extraire une direction principale. Les différentes mesures ont ensuite été interpolées sur la totalité de la surface des échantillons. Les résulats montrent que les fibres de collagène dans la fibrosa sont principalement orientées suivant la direction circonférentielle avec néanmoins d'importantes disparités locales.

Chapter 2

Mechanical framework and models

Contents

2.1 Introduction 38
2.2 Continuum mechanical framework 39
2.2.1 Kinematics 39
2.2.2 Stress and objectivity 43
2.2.3 Hyperelastic framework 45
2.3 Lagrangian variational formulations of the problem 48
2.3.1 Boundary conditions 49
2.3.2 Weak formulation of balance equations 50
2.3.3 Total Lagrangian formulation 52
2.3.4 Updated Lagrangian formulation 52
2.3.5 Quasi–incompressiblility 55
2.4 Finite element discretization 56
2.4.1 Spatial discretization 56
2.4.2 Temporal discretization 62
2.5 Material models 65
2.5.1 Fiber distribution 65
2.5.2 Strain–energy functions 68
2.5.3 Polyconvexity 76
2.5.4 Fibers orientation 76
2.6 Solver validation 79
2.6.1 Convergence and stability 79
2.6.2 Models implementation 81
2.6.3 Fibers orientation algorithm 85
2.7 Summary of Chapter 2 87
2.8 Résumé en français 88

2.1 Introduction

A large literature exists on the numerical modeling of soft tissues which are known to be non–homogeneous multiphased highly non–linear materials (see chapter 1). Regarding cardiovascular soft tissues, aortic and valvular tissue modeling has been widely studied through several approaches, from macroscopic phenomenological approach to multi–scale approach using homogenization methods. A lot of current studies are based on the work of Lanir [Lanir 1979; Lanir 1983] on a general theory for the constitutive modeling of fibrous connective tissues. This theory assumes that the overall tissue response is the sum of contributions of its constituents, such as collagen and elastin fibers. In the initial configuration, collagen fibers are wavy and soft while elastin is pre–stretched. Upon deformation the fibers rotate and stretch gradually, until they are completely stretched and oriented in the direction of the deformation. Several other major assumptions are made : each fiber is perfectly flexible, has no compressive strength and deforms affinely with the macroscopic deformation.

From this work, many constitutive models were introduced. Among the macroscopic phenomenolocical models with statistical distribution of collagen fibers, one can cite the work of Gasser et al. [2006] (based on Holzapfel, Gasser, et al. [2000]) and extended in Holzapfel, Niestrawska, et al. [2015] to non–symmetric collagen fiber dispersion (see also Pandolfi et al. [2012] or Freed et al. [2005] for instance). As collagen fibers do not support compressive load, Holzapfel and Ogden discussed the tension–compression switch in soft fibrous solids in Holzapfel and Ogden [2015] showing that the mechanical response is often significantly overestimated by not excluding all the fibers under compression. To describe the change between the free and deformed configuration of collagen fibers during deformation, Grillo et al. [2014] studied the remodelling in statistically oriented fiber–reinforced materials. One can also refer to Karšaj et al. [2009] and Kuhl et al. [2007]. Recently, a lot of efforts have been undertaken to improve models accuracy with structurally motivated material models considering several scales. One can refer for instance to Billiar et al. [2000a], Sacks [2003] or Martufi et al. [2011] and Weisbecker et al. [2015] taking into account fiber recruitment and fiber distribution density functions.

Since the mechanical behavior of soft collagenous tissue depends primarily on the response of its constituents, their structure and the nature of the crosslinks that affect constituents interactions play a very important role in constitutive modeling. Thus, small scale modeling that can capture microstructural changes during the deformation is becoming increasingly popular. Recently, W. Zhang et al. [2015] presented a meso–scale layer–specific structural constitutive model of the mitral heart valve leaflets and Oren et al. [2013] proposed an analytical and numerical micromechanics–motivated approach for soft fibrous connective tissues modeling using homogenization methods. Moreover,

Pence et al. [2012] explore the connection between transversely isotropic and mixture theory models for fiber reinforced hyperelastic materials. However, these models are still not able to reproduce the overall response of a tissue at the organ level, mainly for computational efficiency reason as well as for the difficulty to accurately define representative elementary volumes.

In this study, since the whole AV has to be modeled, a phenomenological approach was chosen for numerical modeling. The tissue was assumed to be a monolayer material structurally close to the fibrosa, with a strongly oriented network of collagen fibers responsible for the leaflet hyperelastic and anisotropic behavior (see chapter 1). Thus, non–linear transverse isotropic constitutive equations with statistical fiber distribution were used, assuming macroscopically identifiable preferred fiber directions. In section 2.2 we recall some important concepts and definitions of the continuum mechanics, and especially the hyperelasticity framework. The implemented Finite Element (FE) variational formulation of the mechanical problem is then presented in section 2.3 as well as the space and time discretizations and the problem resolution (see 2.4). The material models implemented are detailed in section 2.5. Finally, in section 2.6, the solver implementation is discussed and validated. A short summary concludes the chapter (2.7).

2.2 Continuum mechanical framework

In this section some basics of the general continuum mechanical framework of elasticity are introduced with subsequently used notations. We focus on important mechanical concepts for hyperelastisity mainly referring to Holzapfel [2006b].

2.2.1 Kinematics

Description of motion

We define the stress free reference configuration Ω_0 initially occupied by a deformable body $\mathcal{B}$ and Ω its current configuration (fig. 2.1). Following standard notations we consider the function χ which is a bijection of Ω_0 on Ω. The deformation $\chi : \Omega_0 \longrightarrow \mathbb{R}^3$ transforms a reference point $\boldsymbol{X} \in \Omega_0$ at time t_0 into a material point $\boldsymbol{x} = \chi(\boldsymbol{X}, t) \in \Omega$ at time t. The new particle position is then described by the vector $\boldsymbol{x}(\boldsymbol{X}, t)$ and the displacement vector $\boldsymbol{U}(\boldsymbol{X}, t)$ links the initial position to the current one :

$$\boldsymbol{U}(\boldsymbol{X}, t) = \boldsymbol{x}(\boldsymbol{X}, t) - \boldsymbol{X}. \tag{2.1}$$

In index notation, $U_i = x_i - X_I$ with $i = 1, 2, 3$ and $I = 1, 2, 3$. The Cartesian coordinate system E_I, $I = 1, 2, 3$ is used.

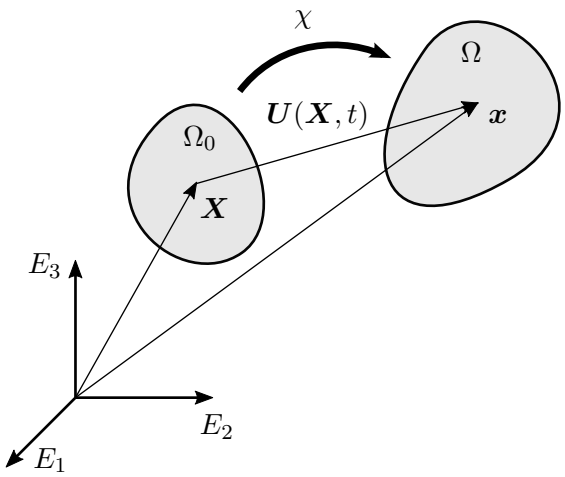

Fig. 2.1 – Lagrangian description of the motion

With this approach, the motion of a material point of $\mathcal{B}$ is totally defined by its initial and current states as translation, rotation and deformation are included in $\boldsymbol{U}$. If the motion of $\mathcal{B}$ is described using X_I coordinates, the description is said to be Lagrangian or material[1]. In contrast, if the motion of $\mathcal{B}$ is described with respect to the current position using x_i coordinates, the description is said to be Eulerian or spatial[2]. In that case we define the displacement vector $\boldsymbol{u}(\boldsymbol{x},t) = \boldsymbol{x} - \boldsymbol{X}(\boldsymbol{x},t)$ of a particle at time t. Both descriptions are equivalent and it is possible to switch from one to another by means of the motion χ. Hence, by change of variables,

$$\boldsymbol{U}(\boldsymbol{X},t) = \boldsymbol{U}(\chi^{-1}(\boldsymbol{x},\boldsymbol{t}),t) = \boldsymbol{u}(\boldsymbol{x},t). \tag{2.2}$$

During a motion χ, the material velocity is defined by

$$\boldsymbol{V}(\boldsymbol{X},t) = \frac{\partial \chi(\boldsymbol{X},t)}{\partial t}, \tag{2.3}$$

where $\boldsymbol{X}$ is fixed. The material velocity represents the time rate of change of the position of a particle $\boldsymbol{X}$ at time t. The spatial velocity of a fixed location $\boldsymbol{x}$ at time t is given by

$$\boldsymbol{v}(\boldsymbol{x},t) = \boldsymbol{V}(\chi^{-1}(\boldsymbol{x},\boldsymbol{t}),t) = \boldsymbol{V}(\boldsymbol{X},t). \tag{2.4}$$

To make the notations less cluttered, time is omitted hereinafter.

Deformation

We introduce deformation tensors, which describe the transformation of a body $\mathcal{B}$ from the reference configuration to the current one, and strain tensors, which describe the relative displacement between particles excluding rigid–body motions.

[1] Uppercase letters are used for Lagrangian notations
[2] Lowercase letters are used for Eulerian notations

An infinitesimal length $\mathrm{d}\boldsymbol{X}$ in the initial configuration is transformed into an infinitesimal length $\mathrm{d}\boldsymbol{x}$ in the current configuration following

$$\mathrm{d}x_i = \frac{\partial x_i}{\partial X_J}\mathrm{d}X_J, \tag{2.5}$$

thus

$$\mathrm{d}\boldsymbol{x} = \mathbf{F}\cdot\mathrm{d}\boldsymbol{X}, \tag{2.6}$$

where $\mathbf{F} = \partial\boldsymbol{x}/\partial\boldsymbol{X} = \mathbf{I} + \nabla_X\boldsymbol{U}$[1] ($F_{iI} = \partial x_i/\partial X_I$ with indicial notations) quantifies the local deformation gradient. $\mathbf{I}$ is the identity tensor in $\mathbb{R}^3$. The deformation gradient is always invertible. Notice that $\mathbf{F}^{-1} = \partial\boldsymbol{X}/\partial\boldsymbol{x} = \mathbf{I} - \nabla\boldsymbol{u}$. We define J as the (strictly positive) Jacobian determinant of $\mathbf{F}$. J represents the infinitesimal volume ratio which characterizes the volume change between the current and the reference configurations respectively, $\mathrm{d}v = \det(\mathbf{F})\mathrm{d}V$ therefore $J = \det(\mathbf{F}) = \mathrm{d}v/\mathrm{d}V > 0$ ($J = 1$ for incompressible materials). The relation between the deformed and the initial volume is given by

$$\mathrm{d}v = J\mathrm{d}V. \tag{2.7}$$

We define the boundary $\partial\Omega_0 \subset \mathbb{R}^2$ of Ω_0, and similarly the boundary $\partial\Omega \subset \mathbb{R}^2$ of Ω, and we consider a deformed body element surface $\mathrm{d}a \subset \partial\Omega$ and the normal unit vector $\boldsymbol{n}$ of $\mathrm{d}a$ ($\mathrm{d}\boldsymbol{a} = \boldsymbol{n}\mathrm{d}a$). Just like for (2.7), $\mathrm{d}a$ can be linked with the element surface $\mathrm{d}A \subset \partial\Omega_0$ of normal unit vector $\boldsymbol{N}$ ($\mathrm{d}\boldsymbol{A} = \boldsymbol{N}\mathrm{d}A$) using Nanson's formula

$$\boldsymbol{n}\mathrm{d}a = J\mathbf{F}^{-T}\cdot\boldsymbol{N}\mathrm{d}A, \tag{2.8}$$

where $(\bullet)^T$ denotes the transpose of a tensor. We also define the surface Jacobian J_s as the area ratio between the current and the reference configurations

$$\mathrm{d}a = J_s\mathrm{d}A = J\left\|\mathbf{F}^{-T}\cdot\boldsymbol{N}\right\|. \tag{2.9}$$

Thus, the evolution of the normal vector in the current configuration can be rewritten

$$\boldsymbol{n} = \frac{J}{J_s}(\mathbf{F}^{-T}\cdot\boldsymbol{N}). \tag{2.10}$$

Following Holzapfel [2006b] we consider the well known multiplicative decomposition

$$\mathbf{F} = J^{\frac{1}{3}}\bar{\mathbf{F}} \tag{2.11}$$

of the deformation gradient into a volumetric (or spherical) part $\hat{\mathbf{F}} = J^{\frac{1}{3}}\mathbf{I}$ and an isochoric (or unimodular) part $\bar{\mathbf{F}} = J^{-\frac{1}{3}}\mathbf{F}$, with $\det(\bar{\mathbf{F}}) = 1$. This decomposition comes

[1] $\nabla_X(\bullet)$ denotes derivative with respect to the reference configuration X_i while $\nabla(\bullet)$ denotes derivative with respect to the current configuration x_i

from the determinant properties applied to $\mathbf{F}$, such as $\det(\mathbf{F}) = \det(\hat{\mathbf{F}}) \cdot \det(\bar{\mathbf{F}})$ and $\det(\hat{\mathbf{F}}) = \det(\alpha\mathbf{I}) = \alpha^3$ with $\alpha > 0$. Finally, one can obtain $\alpha = J^{\frac{1}{3}}$. According to Weiss et al. [1995], the decomposition allows a separate numerical treatment of the dilational and deviatoric parts of the deformation gradient which tends to prevent numerical difficulties like ill–conditioning of the tangent stiffness matrix due to the larger contributions from the dilational stiffness on the diagonal, or incorrect pressures and locking of the mesh due to overconstrainted displacement field (see section 2.4).

We introduce the right and left Cauchy–Green tensors, respectively $\mathbf{C} = \mathbf{F}^T \cdot \mathbf{F}$ and $\mathbf{b} = \mathbf{F} \cdot \mathbf{F}^T$ as a deformation measure respectively in the Lagrangian and Eulerian description. Following the same decomposition we have

$$\begin{aligned} \mathbf{C} &= J^{\frac{2}{3}}\bar{\mathbf{C}} \quad \text{with} \quad \bar{\mathbf{C}} = \bar{\mathbf{F}}^T \cdot \bar{\mathbf{F}}, \\ \mathbf{b} &= J^{\frac{2}{3}}\bar{\mathbf{b}} \quad \text{with} \quad \bar{\mathbf{b}} = \bar{\mathbf{F}} \cdot \bar{\mathbf{F}}^T. \end{aligned} \tag{2.12}$$

Notice that $\mathbf{C}$, $\mathbf{b}$ and their multiplicative decomposition are positive definite and symmetrical tensors, unlike $\mathbf{F}$, respectively for each $\boldsymbol{X} \in \Omega_0$ and $\boldsymbol{x} \in \Omega$. According to the polar decomposition theorem, the deformation gradient $\mathbf{F}$ can also be decomposed using symmetrical dilatation tensors $\mathbf{U}$, $\mathbf{v}$ and a rotational tensor $\mathbf{R}$. This decomposition is unique. Thus, $\mathbf{F} = \mathbf{R} \cdot \mathbf{U} = \mathbf{v} \cdot \mathbf{R}$, where $\mathbf{U} = \mathbf{R}^T \cdot \mathbf{v} \cdot \mathbf{R}$ and $\mathbf{v} = \mathbf{R} \cdot \mathbf{U} \cdot \mathbf{R}^T$. $\mathbf{U}$, $\mathbf{v}$ are positive definite and $\mathbf{R}$ is orthogonal, so that $\det(\mathbf{R}) = 1$, $\mathbf{R} \cdot \mathbf{R}^T = \mathbf{I}$. From equations (2.12) we can write

$$\mathbf{C} = \mathbf{U}^2, \quad \mathbf{b} = \mathbf{v}^2. \tag{2.13}$$

Notice that $\mathbf{U}$ and $\mathbf{v}$ tensors can also be written as functions of $\mathbf{F}$:

$$\mathbf{U} = \sqrt{\mathbf{F}^T \cdot \mathbf{F}}, \quad \mathbf{v} = \sqrt{\mathbf{F} \cdot \mathbf{F}^T}. \tag{2.14}$$

We finally define the (Lagrangian and symmetric) Green-Lagrange strain tensor $\mathbf{E}$

$$\mathbf{E} = \frac{1}{2}(\mathbf{C} - \mathbf{I}) = \frac{1}{2}(\nabla_X \boldsymbol{U} + \nabla_X \boldsymbol{U}^T + \nabla_X \boldsymbol{U}^T \cdot \nabla_X \boldsymbol{U}), \tag{2.15}$$

and the linearised strain tensor

$$\boldsymbol{\varepsilon} = \frac{1}{2}(\nabla_X \boldsymbol{U} + \nabla_X \boldsymbol{U}^T). \tag{2.16}$$

This last tensor is an approximation that implies the small perturbation assumption, $\|\nabla_X \boldsymbol{U}\| \ll 1$. In that case, geometrical non–linearities are neglected. Notice that $\mathbf{E}$ (and $\boldsymbol{\varepsilon}$) vanishes for rigid–body motions ($\mathbf{C} = \mathbf{I}$ and $\nabla_X \boldsymbol{U}$ is null), *i.e.* motions which preserve angles and lengths.

Deformation rate

We define below some Eulerian tensors which depend on the velocity, and in particular, the deformation rate tensor. These tensors can be useful in the context of mechanical law with a rate sensitivity.

The spatial velocity gradient is the derivative of the spatial velocity $\boldsymbol{v}$ with respect to the spatial coordinates :

$$\nabla \boldsymbol{v} = \frac{\partial \boldsymbol{v}}{\partial \boldsymbol{x}}. \tag{2.17}$$

The material velocity gradient is the material time derivative of the deformation gradient $\mathbf{F}$, which gives :

$$\dot{\mathbf{F}} = \frac{\partial \boldsymbol{V}}{\partial \boldsymbol{X}} = \nabla_X \boldsymbol{V}. \tag{2.18}$$

They are both generally non–symmetric second–order tensors. One can notice that $\nabla \boldsymbol{v} = \dot{\mathbf{F}} \cdot \mathbf{F}^{-1}$. The spatial velocity gradient can be additively decomposed into a symmetric and an antisymmetric part according to

$$\nabla \boldsymbol{v} = \mathbf{d} + \mathbf{w}, \tag{2.19}$$

where

$$\mathbf{d} = \frac{1}{2}\left(\nabla \boldsymbol{v} + \nabla \boldsymbol{v}^T\right) = \mathbf{d}^T, \tag{2.20}$$

$$\mathbf{w} = \frac{1}{2}\left(\nabla \boldsymbol{v} - \nabla \boldsymbol{v}^T\right) = -\mathbf{w}^T. \tag{2.21}$$

Notice that in the small perturbation assumption, $\mathbf{d} \approx \dot{\boldsymbol{\varepsilon}}$ is the (symmetric) Eulerian deformation rate tensor. In index notation,

$$\dot{\boldsymbol{\varepsilon}}_{ij} = \frac{1}{2}\left(\frac{\partial v_i}{\partial x_j} + \frac{\partial v_j}{\partial x_i}\right). \tag{2.22}$$

2.2.2 Stress and objectivity

Stress tensors

The concept of stress is used to describe mathematically surface forces acting on a body. They can be boundary or internal forces. We denote $\mathrm{d}\boldsymbol{f}$ an element force acting on the element surface $\mathrm{d}a$ defined above, and similarly the fictive element force $\mathrm{d}\boldsymbol{F}$ initially acting on the element surface $\mathrm{d}A$ following the relation $\mathrm{d}\boldsymbol{F} = \mathbf{F}^{-1} \cdot \mathrm{d}\boldsymbol{f}$. We subsequently present several second–order stress tensors.

The Cauchy stress tensor $\boldsymbol{\sigma}$ is defined following

$$\frac{\mathrm{d}\boldsymbol{f}}{\mathrm{d}a} = \boldsymbol{\sigma} \cdot \boldsymbol{n}. \tag{2.23}$$

$\boldsymbol{\sigma}$ represents the state of stress at a material point in the deformed configuration Ω (Eulerian tensor). If the continuum body is in static equilibrium, according to the principle of conservation of linear and angular momentum, it can be demonstrated that $\boldsymbol{\sigma}$ is symmetrical, so that $\boldsymbol{\sigma} = \boldsymbol{\sigma}^T$ and in index notation $\sigma_{ij} = \sigma_{ji}$.

However, in large deformations (also called finite deformations) the deformed surface $\mathrm{d}a$ is usually unknown due to geometry variations over time. Tensors defined in the reference configuration Ω_0 are then more appropriate. We define the first Piola–Kirchhoff stress tensor $\mathbf{P}$ which relates forces in the current configuration to areas in the reference configuration as

$$\frac{\mathrm{d}\boldsymbol{f}}{\mathrm{d}A} = \mathbf{P} \cdot \boldsymbol{N}, \tag{2.24}$$

and the second Piola–Kirchhoff stress tensor $\mathbf{S}$ which relates forces transposed in the reference configuration to areas in the reference configuration as

$$\frac{\mathrm{d}\boldsymbol{F}}{\mathrm{d}A} = \mathbf{S} \cdot \boldsymbol{N}. \tag{2.25}$$

The (generally not symmetric) tensor $\mathbf{P}$ describes the configuration of the body in both current or reference states. This is neither a Lagrangian nor an Eulerian tensor. In comparison, the (symmetric) tensor $\mathbf{S}$ has no physical meaning but is Lagrangian, and thus very useful. From these three tensors we can write the relations

$$\mathbf{P} = J\boldsymbol{\sigma} \cdot \mathbf{F}^{-T}, \tag{2.26}$$

$$\mathbf{S} = \mathbf{F}^{-1} \cdot \mathbf{P} = J\mathbf{F}^{-1} \cdot \boldsymbol{\sigma} \cdot \mathbf{F}^{-T}, \tag{2.27}$$

$$\boldsymbol{\sigma} = J^{-1}\mathbf{P} \cdot \mathbf{F}^T = J^{-1}\mathbf{F} \cdot \mathbf{S} \cdot \mathbf{F}^T. \tag{2.28}$$

Finally, for every elementary surface $\mathrm{d}\boldsymbol{f} = \boldsymbol{t}\mathrm{d}a = \boldsymbol{T}\mathrm{d}A$, $\boldsymbol{t}$ and $\boldsymbol{T}$ respectively represent the Cauchy (or "true") and first Piola–Kirchhoff (or "nominal") traction vectors and are defined as (fig. 2.2) :

$$\begin{aligned} \boldsymbol{t} &= \boldsymbol{\sigma} \cdot \boldsymbol{n}, \\ \boldsymbol{T} &= \mathbf{P} \cdot \boldsymbol{N}. \end{aligned} \tag{2.29}$$

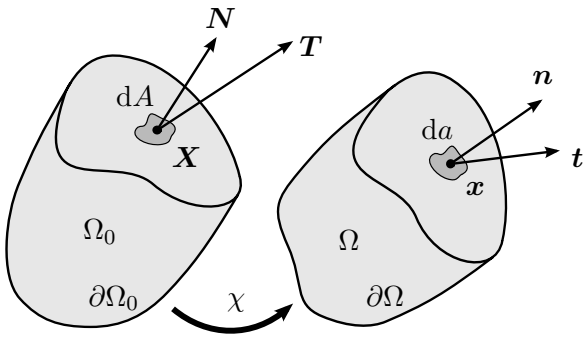

Fig. 2.2 – Traction vectors acting on infinitesimal surface elements

Objectivity

Objectivity (or frame indifference) is a very important concept in mechanics. The macroscopic mechanical behavior of a material does not depend on the observer and thus, the mathematical representation of this behavior must be invariant by referential changing. Therefore, distances between arbitrary points in space and time intervals are preserved with a change of observer. If this principle is not observed, constitutive equations are affected by rigid–body motions. The description of the motion depends on the observers which can be located at different places and move at different velocities. Consequently, time derivatives like velocity or acceleration are generally not–objective. Because they are defined in the reference frame, Lagrangian quantities are naturally objective. In the case of Eulerian quantities, referential changes formula, which can be interpreted as rigid–body motions, must be used. The reader can refer to Holzapfel [2006b] for further details.

2.2.3 Hyperelastic framework

Hyperelasticity

We subsequently focus on the phenomenological approach, relative to the macroscopic behavior of material as continua. This approach is widely used and particularly successful in solid mechanics. It consists in using mathematical equations which are fitted to reproduce an experimentally observed behavior. However, phenomenological modeling does not take into account the physical microscopic mechanisms responsible for the transformation.

For our purpose, we use the non–linear constitutive theory of hyperelasticity. This theory is suitable to describe a wide range of physical phenomena, especially for materials which undergo large strains. A material is hyperelastic if several criteria are achieved :

1. existence of a stress–free reference configuration (no residual stress) ;

2. no energy dissipation ;

3. the material behavior is described by an Helmholtz free–energy function W defined per unit of reference volume, depending on the strain and the temperature.

This strain–energy function vanishes in the reference configuration. This can be expressed with the normalization condition

$$W = W(\mathbf{I}) = 0. \tag{2.30}$$

Another physical requirement is that the strain–energy function increases with deformation, thus

$$W = W(\mathbf{F}) \geqslant 0. \tag{2.31}$$

The strain–energy function is assumed to have only one global minimum for $\mathbf{F} = \mathbf{I}$, with no other stationary point.

Stress and elasticity tensors

For hyperelastic materials, the second Piola–Kirchhoff stress tensor $\mathbf{S}$ and the (fourth–order) material elasticity tensor $\mathbb{C}$ derives from the strain–energy function W with respect to the Green–Lagrange strain tensor $\mathbf{E}$ (or right Cauchy–Green tensor $\mathbf{C}$)

$$\mathbf{S} = \frac{\partial W}{\partial \mathbf{E}} = 2\frac{\partial W}{\partial \mathbf{C}}, \quad \mathbb{C} = \frac{\partial \mathbf{S}}{\partial \mathbf{E}} = \frac{\partial^2 W}{\partial \mathbf{E}^2} = 4\frac{\partial^2 W}{\partial \mathbf{C}^2}. \tag{2.32}$$

The Cauchy stress $\boldsymbol{\sigma}$ and the spatial elasticity tensor $\mathbb{c}$ are obtained from equations (2.32) by mean of a push–forward operation denoted $\chi^\star(\bullet)$, times a factor J^{-1}. This transformation, called "inverse Piola transform", is a correspondence between vector and tensor fields respectively defined over the reference and the deformed configuration. In return, we denote $\chi^{\star^{-1}}(\bullet)$ the pull–back operation and $J\chi^{\star^{-1}}(\bullet)$ the Piola transform. Therefore

$$\boldsymbol{\sigma} = J^{-1}\chi^\star(\mathbf{S}), \quad \mathbb{c} = J^{-1}\chi^\star(\mathbb{C}), \tag{2.33}$$

and using index notations

$$\sigma_{ij} = J^{-1}F_{iI}F_{jJ}S_{IJ}, \quad c_{ijkl} = J^{-1}F_{iI}F_{jJ}F_{kK}F_{lL}C_{IJKL}. \tag{2.34}$$

The elasticity tensor $\mathbb{C}$ (and equally for $\mathbb{c}$ in the Eulerian description) always possesses minor symmetries for elastic materials. These minor symmetries directly result from the symmetries of the second Piola–Kirchhoff and right Cauchy–Green (or Green–Lagrange) tensors. Thus,

$$C_{IJKL} = C_{JIKL} = C_{IJLK}. \tag{2.35}$$

Additionally, for hyperelasticity, $\mathbb{C}$ also possesses the major symmetries $\mathbb{C} = \mathbb{C}^T$, or in index notation

$$C_{IJKL} = C_{KLIJ}. \tag{2.36}$$

The condition (2.36) is necessary and sufficient for a material to be hyperelastic. The number of independent tensor components at each strain state is reduced from 36, after minor symmetries, to 21.

We adopt the classical decoupled form of the elastic strain–energy function into a purely volumetric part $W_{vol}(J)$ and an isochoric contribution $W_{iso}(\bar{\mathbf{C}})$:

$$W(J, \bar{\mathbf{C}}) = W_{vol}(J) + W_{iso}(\bar{\mathbf{C}}). \tag{2.37}$$

This formulation is only appropriate for incompressible or nearly incompressible materials. From this decoupled potential, the second Piola–Kirchhoff stress can be split into its volumetric and deviatoric parts

$$\mathbf{S} = \mathbf{S_{vol}} + \mathbf{S_{iso}} \quad \text{with} \quad \mathbf{S_{vol}} = 2\frac{\partial W_{vol}}{\partial \mathbf{C}}, \quad \mathbf{S_{iso}} = 2\frac{\partial W_{iso}}{\partial \mathbf{C}}. \tag{2.38}$$

One can notice that $\det(\mathbf{C}) = J^2$, so that $\dfrac{\partial J}{\partial \mathbf{C}} = \dfrac{1}{2} J\mathbf{C}^{-1}$ after developments. From the standard results that can be found for example in Holzapfel [2006b],

$$\mathbf{S_{vol}} = -pJ\mathbf{C}^{-1}, \quad \mathbf{S_{iso}} = J^{-\frac{2}{3}}\mathbb{P} : \bar{\mathbf{S}}, \tag{2.39}$$

where $p = -\partial W_{vol}/\partial J$ is the hydrostatic pressure (which is an indeterminate Lagrange multiplier in the incompressible case), $\mathbb{P} = \mathbb{I} - \dfrac{1}{3}(\mathbf{C}^{-1} \otimes \mathbf{C})$ is the physically correct deviatoric operator in the Lagrangian description (so that $[\mathbb{P} : (\bullet)] : \mathbf{C} = 0$) and $\bar{\mathbf{S}} = 2\partial W_{iso}/\partial \bar{\mathbf{C}}$ the fictitious second Piola–Kirchhoff stress tensor. We define $\mathbb{I}$ the symmetric fourth–order identity tensor defined in index notation as

$$\mathbb{I}_{IJKL} = \frac{1}{2}(\delta_{IK}\delta_{JL} + \delta_{IL}\delta_{JK}), \tag{2.40}$$

δ being the Kronecker delta. The inverse Piola transform of equation (2.39) leads to the decoupled Cauchy stress tensor form

$$\boldsymbol{\sigma} = \boldsymbol{\sigma_{vol}} + \boldsymbol{\sigma_{iso}} \quad \text{with} \quad \boldsymbol{\sigma_{vol}} = -p\mathbf{I}, \quad \boldsymbol{\sigma_{iso}} = J^{-\frac{2}{3}}\mathbb{p} : \bar{\boldsymbol{\sigma}}, \tag{2.41}$$

where $\mathbb{p} = \mathbb{I} - \dfrac{1}{3}(\mathbf{I} \otimes \mathbf{I})$ is the physically correct deviatoric operator in the Eulerian description (so that $[\mathbb{p} : (\bullet)] : \mathbf{I} = 0$) and $\bar{\boldsymbol{\sigma}} = J^{-1}\chi^{\star}(\bar{\mathbf{S}}) = 2J^{-1}\mathbf{F}(\partial W_{iso}/\partial \bar{\mathbf{C}})\mathbf{F}^T$ the fictitious Cauchy stress tensor. The material elasticity tensor may also be written in the decoupled form $\mathbb{C} = \mathbb{C}_{\text{vol}} + \mathbb{C}_{\text{iso}}$ with $\mathbb{C}_{\text{vol}} = 2\partial \mathbf{S_{vol}}/\partial \mathbf{C}$ and $\mathbb{C}_{\text{iso}} = 2\partial \mathbf{S_{iso}}/\partial \mathbf{C}$. The

details of the derivatives can be found in Holzapfel [2006b]. However, we remind below its inverse Piola transform which defines the decoupled form of the spatial elasticity tensor $\mathbb{c} = \mathbb{c}_{\text{vol}} + \mathbb{c}_{\text{iso}}$ with

$$\mathbb{c}_{\text{vol}} = \tilde{p}(\mathbf{I} \otimes \mathbf{I}) + 2p\mathbb{I}, \tag{2.42a}$$

$$\mathbb{c}_{\text{iso}} = J^{-\frac{4}{3}}\mathbb{p} : \bar{\mathbb{c}} : \mathbb{p} + \frac{2}{3}\left[J^{-\frac{2}{3}}\,\text{tr}(\bar{\boldsymbol{\sigma}})\mathbb{p} - (\mathbf{I} \otimes \boldsymbol{\sigma}_{\mathbf{iso}} + \boldsymbol{\sigma}_{\mathbf{iso}} \otimes \mathbf{I})\right], \tag{2.42b}$$

where the scalar function $\tilde{p} = -(J\partial p/\partial J + p)$. The fictitious spatial elasticity tensor $\bar{\mathbb{c}}_{ijkl} = J^{-1}F_{iI}F_{jJ}F_{kK}F_{lL}\bar{\mathbb{C}}_{IJKL}$ is the inverse Piola transform of $\bar{\mathbb{C}} = 2J^{-\frac{4}{3}}\partial\bar{\mathbf{S}}/\partial\bar{\mathbf{C}}$ and the spatial trace operator $\text{tr}(\bullet) = (\bullet) : \mathbf{I}$ is used.

2.3 Lagrangian variational formulations of the problem

Remark – Developments presented in this chapter were made on the basis of the source code of FORGE® NXT software (mainly written in FORTRAN 90). FORGE® is a massively parallel commercial FE software developed at the laboratory and industrialized by TRANSVALOR company. The software was initially dedicated to the modeling of large plastic deformation for hot and cold–forming processes. Due to its core applications, FORGE® uses a mixed velocity–pressure formulation and not a displacement–pressure formulation which is much more suitable in the particular case of hyperelasticity since hyperelastic material models do not depend on strain rate. Moreover, the software is exclusively based on an updated Lagrangian approach in the framework of infinitesimal strain assumption meaning that the current discrete mechanical equations are integrated on the previous geometry configuration, assuming small body deformations between the two configurations. This assumption, that considerably simplifies the continuum mechanics' equations, is often used for the modeling of small elastic strain materials but is not suitable for soft materials that can undergo very large deformations. In the context of this work, the velocity–pressure formulation was adapted to the hyperelastic framework and an updated Lagrangian approach was implemented in finite strain.

This section introduces the formalism for the resolution of the mechanical problem in the large deformation framework. A two–field velocity–pressure variational formulation is presented to solve incompressible or quasi–incompressible problems. Our description is mainly based on A. Fortin et al. [2013].

2.3.1 Boundary conditions

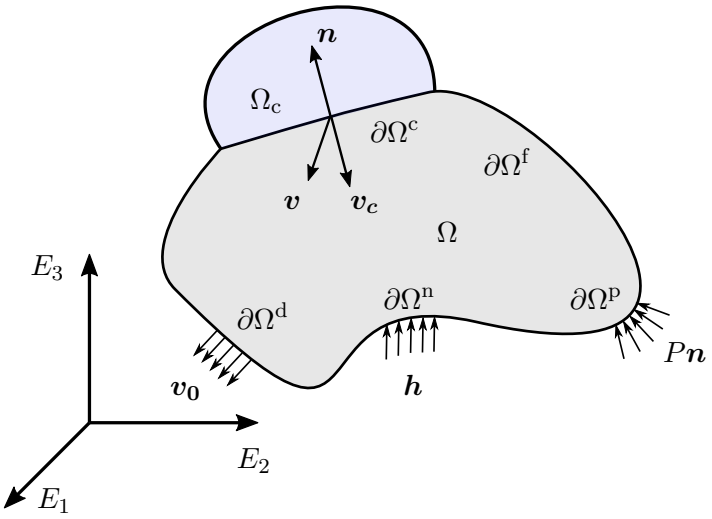

Fig. 2.3 – Illustration of the different types of boundary conditions

Boundary conditions apply on the outer surface $\partial\Omega$ of the domain volume Ω. The domain surface can be decomposed following $\partial\Omega = \partial\Omega^{\mathrm{f}} + \partial\Omega^{\mathrm{d}} + \partial\Omega^{\mathrm{n}} + \partial\Omega^{\mathrm{p}} + \partial\Omega^{\mathrm{c}}$ for the different types of boundary conditions with (fig. 2.3) :

1. the stress free boundary condition $\boldsymbol{\sigma} \cdot \boldsymbol{n} = \overrightarrow{0}$ on $\partial\Omega^{\mathrm{f}}$,

2. the prescribed velocity Dirichlet condition $\boldsymbol{v} = \boldsymbol{v_0}$ on $\partial\Omega^{\mathrm{d}}$ (or displacement $\boldsymbol{u} = \boldsymbol{u_0}$),

3. the Neumann load condition $\boldsymbol{\sigma} \cdot \boldsymbol{n} = \boldsymbol{h}$ on $\partial\Omega^{\mathrm{n}}$,

4. the normal pressure condition $\boldsymbol{\sigma} \cdot \boldsymbol{n} = P\boldsymbol{n}$ on $\partial\Omega^{\mathrm{p}}$ (particular case of 3),

5. the contact condition with or without friction $\boldsymbol{\sigma} \cdot \boldsymbol{n} = \sigma_n \boldsymbol{n} + \boldsymbol{\sigma_t}$ on $\partial\Omega^{\mathrm{c}}$, from another (deformable or undeformable) body or itself, where $\sigma_n \boldsymbol{n}$ is the normal stress vector and $\boldsymbol{\sigma_t}$ is the tangential stress vector. The non–penetration condition is ensured by the equations system

$$\begin{cases} (\boldsymbol{v} - \boldsymbol{v_c}) \cdot \boldsymbol{n} \leq 0, \\ \sigma_n = (\boldsymbol{\sigma} \cdot \boldsymbol{n}) \cdot \boldsymbol{n} \leq 0, \\ \sigma_n (\boldsymbol{v} - \boldsymbol{v_c}) \cdot \boldsymbol{n} = 0. \end{cases} \tag{2.43}$$

   The physics of contact is very complex as well as its numerical treatment, and will not be developed in this work.

2.3.2 Weak formulation of balance equations

The strong form of the momentum equilibrium equation in the deformed configuration Ω is

$$\boxed{-\nabla \cdot \boldsymbol{\sigma} = \boldsymbol{r} \text{ in } \Omega,} \tag{2.44}$$

where $\boldsymbol{r}$ represents the body forces. Multiplying equation (2.44) by the test function[1] $\boldsymbol{v}^*$ and integrating on the whole domain Ω using Green's theorem, it becomes :

$$\int_\Omega -(\nabla \cdot \boldsymbol{\sigma}) \cdot \boldsymbol{v}^* \mathrm{d}v = \int_\Omega \boldsymbol{\sigma} : \nabla \boldsymbol{v}^* \mathrm{d}v - \int_{\partial\Omega} (\boldsymbol{\sigma} \cdot \boldsymbol{n}) \cdot \boldsymbol{v}^* \mathrm{d}a = \int_\Omega \boldsymbol{r} \cdot \boldsymbol{v}^* \mathrm{d}v. \tag{2.45}$$

We subsequently use a quasi–static approach, which means that inertial terms are neglected. For sake of simplification, we do not consider hereinafter the free boundary and contact conditions in the formulation developments (respectively on $\partial\Omega^{\mathrm{f}}$ and $\partial\Omega^{\mathrm{c}}$). The strong form of the mechanical problem is then defined with the following set of equilibrium equations,

$$\begin{cases} -\nabla \cdot \boldsymbol{\sigma} = \overrightarrow{0} & \text{in } \Omega, \\ \boldsymbol{v} = \boldsymbol{v_0} & \text{on } \partial\Omega^{\mathrm{d}}, \\ \boldsymbol{\sigma} \cdot \boldsymbol{n} = \boldsymbol{h} & \text{on } \partial\Omega^{\mathrm{n}}, \\ \boldsymbol{\sigma} \cdot \boldsymbol{n} = P\boldsymbol{n} & \text{on } \partial\Omega^{\mathrm{p}}, \end{cases} \tag{2.46}$$

Equation (2.45) can be rewritten as :

$$\int_\Omega \boldsymbol{\sigma} : \nabla \boldsymbol{v}^* \mathrm{d}v - \int_{\partial\Omega} (\boldsymbol{\sigma} \cdot \boldsymbol{n}) \cdot \boldsymbol{v}^* \mathrm{d}a = 0. \tag{2.47}$$

with $\partial\Omega = \partial\Omega^{\mathrm{d}} + \partial\Omega^{\mathrm{n}} + \partial\Omega^{\mathrm{p}}$. Knowing that test functions $\boldsymbol{v}^*$ vanish on the boundary $\partial\Omega^{\mathrm{d}}$ of the Dirichlet conditions we get :

$$\int_\Omega \boldsymbol{\sigma} : \nabla \boldsymbol{v}^* \mathrm{d}v - \int_{\partial\Omega^{\mathrm{n}}} \boldsymbol{h} \cdot \boldsymbol{v}^* \mathrm{d}a - \int_{\partial\Omega^{\mathrm{p}}} P\boldsymbol{n} \cdot \boldsymbol{v}^* \mathrm{d}a = 0. \tag{2.48}$$

Using the decomposition (2.41) of the stress tensor $\boldsymbol{\sigma}$ into a deviatoric part $\boldsymbol{\sigma_{\mathrm{iso}}}$ and a volumetric part $\boldsymbol{\sigma_{\mathrm{vol}}} = -p\mathbf{I}$, the weak formulation becomes :

$$\int_\Omega \boldsymbol{\sigma_{\mathrm{iso}}} : \dot{\boldsymbol{\varepsilon}}(\boldsymbol{v}^*) \mathrm{d}v - \int_\Omega p(\nabla \cdot \boldsymbol{v}^*) \mathrm{d}v - \int_{\partial\Omega^{\mathrm{n}}} \boldsymbol{h} \cdot \boldsymbol{v}^* \mathrm{d}a - \int_{\partial\Omega^{\mathrm{p}}} P\boldsymbol{n} \cdot \boldsymbol{v}^* \mathrm{d}a = 0. \tag{2.49}$$

However, the use of a single–field varational principle is not always a good choice. In particular, in the incompressible case, equation (2.49) is not the most appropriate formulation to solve the mechanical problem. A suitable choice is to add another fundamental balance equation in order to write a two–field varational principle (see Simo et al. [1991]

[1] FORGE® uses a mixed velocity–pressure formulation (with velocity and pressure test functions).

for an example of a three–field varational principle).

The strong form of the mass conservation equation, assuming a body $\mathcal{B}$ that possesses a continuously distributed mass m in the current configuration Ω, is

$$\boxed{\frac{\partial \rho}{\partial t} + \nabla \cdot (\rho \boldsymbol{v}) = 0 \text{ in } \Omega,} \tag{2.50}$$

where ρ is the mass density. In the case of incompressibility, ρ does not depends on time so we obtain the equation

$$\nabla \cdot \boldsymbol{v} = 0. \tag{2.51}$$

We use a velocity–pressure mixed formulation, with an additional pressure test function p^*. Assuming incompressibility the equations system (2.46) becomes

$$\begin{cases} -\nabla \cdot \boldsymbol{\sigma} = \overrightarrow{0} \text{ in } \Omega, \\ \nabla \cdot \boldsymbol{v} = 0 \quad \text{in } \Omega, \\ \boldsymbol{v} = \boldsymbol{v_0} \quad \text{on } \partial\Omega^{\mathrm{d}}, \\ \boldsymbol{\sigma} \cdot \boldsymbol{n} = \boldsymbol{h} \quad \text{on } \partial\Omega^{\mathrm{n}}, \\ \boldsymbol{\sigma} \cdot \boldsymbol{n} = P\boldsymbol{n} \quad \text{on } \partial\Omega^{\mathrm{p}}, \end{cases} \tag{2.52}$$

and after multiplying equation (2.50) by the test function p^* as for (2.44), we finally obtain the weak mixed formulation

$$\begin{cases} \displaystyle\int_\Omega \boldsymbol{\sigma_{\mathrm{iso}}} : \dot{\boldsymbol{\varepsilon}}(\boldsymbol{v}^*)\mathrm{d}v - \int_\Omega p(\nabla \cdot \boldsymbol{v}^*)\mathrm{d}v - \int_{\partial\Omega^{\mathrm{n}}} \boldsymbol{h} \cdot \boldsymbol{v}^*\mathrm{d}a - \int_{\partial\Omega^{\mathrm{p}}} P\boldsymbol{n} \cdot \boldsymbol{v}^*\mathrm{d}a = 0, \\ \displaystyle\int_\Omega - p^*(\nabla \cdot \boldsymbol{v})\mathrm{d}v = 0, \\ \forall (\boldsymbol{v}^*, p^*) \in \mathcal{V}^* \times \mathscr{P}. \end{cases} \tag{2.53}$$

Solve the above equations means to find the couple $(\boldsymbol{v}, p) \in \mathcal{V} \times \mathscr{P}$ that satisfies equation (2.53). We define the spaces of kinematically admissible velocity field $\mathcal{V}$, $\mathcal{V}^*$, and the functional pressure space $\mathscr{P}$ as following

$$\mathcal{V} = \left[\boldsymbol{v} \in (\mathbf{H}^1(\Omega))^3, \boldsymbol{v} \mid_{\partial\Omega^{\mathrm{d}}} = \boldsymbol{v_0}\right], \tag{2.54}$$

$$\mathcal{V}^* = \left[\boldsymbol{v} \in (\mathbf{H}^1(\Omega))^3, \boldsymbol{v} \mid_{\partial\Omega^{\mathrm{d}}} = \overrightarrow{0}\right], \tag{2.55}$$

$$\mathscr{P} = \mathbf{L}^2(\Omega), \tag{2.56}$$

where $\mathbf{H}^1$ and $\mathbf{L}^2$ are respectively the Sobolev and the Lebesgue spaces.

2.3.3 Total Lagrangian formulation

The weak formulation (2.53) is expressed in the usually unknown deformed configuration. In practice, the use of this equation implies the small perturbation assumption[1] because $\boldsymbol{\sigma}$ is integrated on the last updated geometrical configuration. Thus, it is useful to rewrite the variational formulation in the reference frame Ω_0. Using tensor algebra and some of the relations between the initial and the current domain presented above, (2.53) can be expressed in the reference configuration using

$$\begin{cases} \displaystyle\int_{\Omega_0} \mathbf{S} : (\mathbf{F}^T \cdot \nabla_X \boldsymbol{v}^*) \mathrm{d}V - \int_{\partial\Omega_0^{\mathrm{n}}} \boldsymbol{H} \cdot \boldsymbol{v}^* \mathrm{d}A - \int_{\partial\Omega_0^{\mathrm{p}}} P\boldsymbol{v}^* \cdot (\mathbf{F}^{-T} \cdot \boldsymbol{N}) J \mathrm{d}A = 0, \\ \displaystyle\int_{\Omega_0} -p^*(J-1)\mathrm{d}V = 0, \end{cases} \tag{2.57}$$

where $\boldsymbol{H} = J_s \boldsymbol{h}$ with $J_s = \mathrm{d}a/\mathrm{d}A$ from equation (2.9). Notice that the mass conservation is expressed as $\rho_0 = J\rho$ leading to $J = 1$ in the case of incompressibility. Using the decomposition of the stress tensor $\mathbf{S}$ from equation (2.39) we obtain

$$\begin{cases} \displaystyle\int_{\Omega_0} \mathbf{S_{iso}} : (\mathbf{F}^T \cdot \nabla_X \boldsymbol{v}^*) \mathrm{d}V - \int_{\Omega_0} pJ\mathbf{F}^{-T} : \nabla_X \boldsymbol{v}^* \mathrm{d}V - \int_{\partial\Omega_0^{\mathrm{n}}} \boldsymbol{H} \cdot \boldsymbol{v}^* \mathrm{d}A \\ \qquad\qquad - \displaystyle\int_{\partial\Omega_0^{\mathrm{p}}} P\boldsymbol{v}^* \cdot (\mathbf{F}^{-T} \cdot \boldsymbol{N}) J \mathrm{d}A = 0, \\ \displaystyle\int_{\Omega_0} -p^*(J-1)\mathrm{d}V = 0. \end{cases} \tag{2.58}$$

Equation (2.58) is the total Lagrangian formulation, integrated on the initial domain Ω_0. The set of equilibrium equations (2.52) to be solved becomes

$$\begin{cases} -\nabla \cdot \mathbf{P} = \overrightarrow{0} & \text{in } \Omega_0, \\ J - 1 = 0 & \text{in } \Omega_0, \\ \boldsymbol{V} = \boldsymbol{V_0} & \text{on } \partial\Omega_0^{\mathrm{d}}, \\ \mathbf{P} \cdot \boldsymbol{N} = \boldsymbol{H} & \text{on } \partial\Omega_0^{\mathrm{n}}, \\ \mathbf{P} \cdot \boldsymbol{N} = PJ(\mathbf{F}^{-T} \cdot \boldsymbol{N}) & \text{on } \partial\Omega_0^{\mathrm{p}}. \end{cases} \tag{2.59}$$

2.3.4 Updated Lagrangian formulation

In the total Lagrangian formulation, results obtained on the current balanced configuration Ω are calculated from the initial reference configuration Ω_0. However, if the material undergoes very large deformations, it can be suitable to use intermediate deformed configurations for which the solution is known in order to avoid potential numerical problems.

[1] This assumption is made in the original solver of FORGE®.

In the updated Lagrangian formulation, an intermediate known configuration becomes the new reference configuration. Thus, at each step of the calculation the new solution is related to the transformation between the reference domain Ω_{m} and the current one Ω_{n}. Naturally, Ω_{m} not being stress free, it is necessary to take into account the history of the transformation. Total Lagrangian and updated Lagrangian formulations are intrinsically equivalent.

We consider, $\chi_{m\to n}$ the bijection of Ω_{m} on Ω_{n}. We denote $\boldsymbol{X_m}$ the material point coordinate in the configuration Ω_{m} and $\boldsymbol{U_{m\to n}}$ the displacement vector from Ω_{m} to Ω_{n}. Thus,

$$\begin{aligned}\chi_{m\to n}(\boldsymbol{X_m}) = \boldsymbol{x_n} &= \boldsymbol{X_m} + \boldsymbol{U_{m\to n}} \\ &= \boldsymbol{X_m} + \boldsymbol{U_{m\to m+1}} + \cdots + \boldsymbol{U_{n-1\to n}}.\end{aligned} \tag{2.60}$$

Rewriting equation (2.60) from the initial reference configuration Ω_0 :

$$\begin{aligned}\chi_{m\to n}(\boldsymbol{X_m}) = \boldsymbol{x_n} &= \boldsymbol{X} + \boldsymbol{U_{0\to n}} \\ &= \underbrace{\boldsymbol{X} + \boldsymbol{U_{0\to 1}} + \cdots + \boldsymbol{U_{m-1\to m}}}_{\boldsymbol{X_m}} + \underbrace{\boldsymbol{U_{m\to m+1}} + \cdots + \boldsymbol{U_{n-1\to n}}}_{\boldsymbol{U_{m\to n}}}.\end{aligned} \tag{2.61}$$

Moreover, following derivative rules, the deformation gradient $\mathbf{F_{m\to n}}$ between Ω_{m} and Ω_{n} can be decomposed as

$$\begin{aligned}\mathbf{F_{m\to n}} &= \frac{\partial \boldsymbol{x_n}}{\partial \boldsymbol{X_m}} \\ &= \frac{\partial \boldsymbol{x_n}}{\partial \boldsymbol{X_{n-1}}} \cdots \frac{\partial \boldsymbol{X_{m+2}}}{\partial \boldsymbol{X_{m+1}}} \frac{\partial \boldsymbol{X_{m+1}}}{\partial \boldsymbol{X_m}} \\ &= \mathbf{F_{n-1\to n}} \cdots \mathbf{F_{m+1\to m+2}} \cdot \mathbf{F_{m\to m+1}}.\end{aligned} \tag{2.62}$$

The determinant of $\mathbf{F_{m\to n}}$ can be decomposed similarly

$$J_{m\to n} = J_{n-1\to n} \cdots J_{m+1\to m+2} J_{m\to m+1}. \tag{2.63}$$

For clarity reasons, we subsequently consider three consecutive steps 0, 1 and 2. The total Lagrangian formulation (2.58) to go directly from the configuration Ω_0 to the configuration Ω_2 is

$$\begin{cases} \displaystyle\int_{\Omega_0} (\mathbf{S_{iso}})_{0\to2} : (\mathbf{F}_{0\to2}^T \cdot \nabla_{X_0} \boldsymbol{v}^*) \mathrm{d}V - \int_{\Omega_0} p J_{0\to2} \mathbf{F}_{0\to2}^{-T} : \nabla_{X_0} \boldsymbol{v}^* \mathrm{d}V \\ \qquad\qquad - \displaystyle\int_{\partial\Omega_0^{\mathrm{n}}} \boldsymbol{H}_0 \cdot \boldsymbol{v}^* \mathrm{d}A - \int_{\partial\Omega_0^{\mathrm{p}}} P\boldsymbol{v}^* \cdot (\mathbf{F}_{0\to2}^{-T} \cdot \boldsymbol{N}_0) J_{0\to2} \mathrm{d}A = 0, \\ \displaystyle\int_{\Omega_0} - p^* (J_{0\to2} - 1) \mathrm{d}V = 0, \end{cases} \tag{2.64}$$

where $\boldsymbol{N}_0$ is the normal vector of the domain Ω_0, $\mathbf{F}_{0\to2}$ and $J_{0\to2}$ are respectively the deformation gradient and the Jacobian of the transformation from Ω_0 to Ω_2 and $(\mathbf{S_{iso}})_{0\to2}$ the second Piola–Kirchhoff stress tensor evaluated using $\mathbf{C}_{0\to2} = \mathbf{F}_{0\to2}^T \cdot \mathbf{F}_{0\to2}$. However, assuming that it is difficult to move from Ω_0 to Ω_2 because of large deformations it is better to solve an updated Lagrangian problem instead of the total Lagrangian problem (2.64). In that case, the intermediate known configuration Ω_1 is used as reference configuration. To do this, the right Cauchy–Green tensor is decomposed following the rules presented above

$$\mathbf{C}_{0\to2} = \mathbf{F}_{0\to2}^T \cdot \mathbf{F}_{0\to2} = (\mathbf{F}_{1\to2} \cdot \mathbf{F}_{0\to1})^T \cdot (\mathbf{F}_{1\to2} \cdot \mathbf{F}_{0\to1}) = \mathbf{F}_{0\to1}^T \cdot \mathbf{C}_{1\to2} \cdot \mathbf{F}_{0\to1} \tag{2.65}$$

where $\boldsymbol{u}_{1\to2}$, therefore $\mathbf{F}_{1\to2}$ and $\mathbf{C}_{1\to2}$, are unknowns. Also notice that

$$\nabla_{X_m} \boldsymbol{v}^* = \nabla_{X_n} \boldsymbol{v}^* \cdot \mathbf{F}_{m\to n}. \tag{2.66}$$

Rewriting equation (2.64) using relations (2.65) and (2.66) on Ω_1 (see A. Fortin et al. [2013] for further developments), the mixed updated Lagrangian formulation is

$$\begin{cases} \displaystyle\int_{\Omega_1} (\tilde{\mathbf{S}}_{\mathbf{iso}})_{0\to2} : (\mathbf{F}_{1\to2}^T \cdot \nabla_{X_1} \boldsymbol{v}^*) \mathrm{d}V_1 - \int_{\Omega_1} p J_{1\to2} \mathbf{F}_{1\to2}^{-T} : \nabla_{X_1} \boldsymbol{v}^* \mathrm{d}V_1 \\ \qquad\qquad - \displaystyle\int_{\partial\Omega_1^{\mathrm{n}}} \boldsymbol{H}_1 \cdot \boldsymbol{v}^* \mathrm{d}A_1 - \int_{\partial\Omega_1^{\mathrm{p}}} P\boldsymbol{v}^* \cdot (\mathbf{F}_{1\to2}^{-T} \cdot \boldsymbol{N}_1) J_{1\to2} \mathrm{d}A_1 = 0, \\ \displaystyle\int_{\Omega_1} - p^* (J_{0\to2} - 1) J_{0\to1}^{-1} \mathrm{d}V_1 = 0, \end{cases} \tag{2.67}$$

where $(\tilde{\mathbf{S}}_{\mathbf{iso}})_{0\to2} = J_{0\to1}^{-1} \mathbf{F}_{0\to1} \cdot \mathbf{S_{iso}}(\mathbf{C}_{0\to2}) \cdot \mathbf{F}_{0\to1}^T$, the Neumann condition vector $\boldsymbol{H}_1 = (J_s)_{0\to1}^{-1} \boldsymbol{H}_0$ and the unit vector $\boldsymbol{N}_1 = J_{0\to1} (J_s)_{0\to1}^{-1} \mathbf{F}_{0\to1}^{-T} \cdot \boldsymbol{N}_0$. Finally, considering the arbitrary reference domain Ω_{m} and the unknown domain Ω_{n} we get

$$\begin{cases} \displaystyle\int_{\Omega_\mathrm{m}} (\tilde{\mathbf{S}}_{\mathbf{iso}})_{0\to n} : (\mathbf{F}^T_{m\to n} \cdot \nabla_{X_m} \boldsymbol{v}^*) \mathrm{d}V_m - \int_{\Omega_\mathrm{m}} p J_{m\to n} \mathbf{F}^{-T}_{m\to n} : \nabla_{X_m} \boldsymbol{v}^* \mathrm{d}V_m \\ \qquad\qquad - \displaystyle\int_{\partial\Omega^\mathrm{n}_\mathrm{m}} \boldsymbol{H}_m \cdot \boldsymbol{v}^* \mathrm{d}A_m - \int_{\partial\Omega^\mathrm{p}_\mathrm{m}} P \boldsymbol{v}^* \cdot (\mathbf{F}^{-T}_{m\to n} \cdot \boldsymbol{N}_m) J_{m\to n} \mathrm{d}A_m = 0, \\ \displaystyle\int_{\Omega_\mathrm{m}} - p^* (J_{0\to n} - 1) J^{-1}_{0\to m} \mathrm{d}V_m = 0. \end{cases} \tag{2.68}$$

2.3.5 Quasi–incompressiblility

Multi–field variational formulations can be insufficient to ensure unique solvability, convergence and robustness in the case of incompressibility, especially using low order finite elements, producing solutions which are locked by the incompressibility constraint. To overcome volumetric locking phenomena a penalty term can be added in order to approximate an incompressible material as slightly compressible. In that case, the volumetric strain–energy function becomes $W_{vol}(J) = \tau U(J)$ where penalty function $U(J)$ is mathematically motivated and the penalty parameter $\tau > 0$ is adjusted depending on the compressibility allowed. From a physical point of view $U(J)$ must fulfill an energy and stress free reference configuration, so that $U(1) = 0$ and $U'(1) = 0$ (global minimum). Furthermore, convexity (see 2.5.3) requires $U(J) \longrightarrow \infty$ for $J \longrightarrow 0$ and $J \longrightarrow \infty$.

Some penalty functions from the literature are summarized in tab. 2.1.

$U(J)$	$U'(J)$	$U''(J)$
$\frac{1}{2}(J-1)^2$	$J-1$	1
$\frac{1}{4}\left((J-1)^2 + (\ln J)^2\right)$	$\frac{1}{2}\left(J - 1 + \frac{1}{J}\ln J\right)$	$\frac{1}{2J^2}\left(1 + J^2 - \ln J\right)$
$\frac{1}{2}(\ln J)^2$	$\frac{1}{J}\ln J$	$\frac{1}{J^2}(1 - \ln J)$
$\frac{1}{4}\left(J^2 - 1 - 2\ln J\right)$	$\frac{1}{2}\left(J - \frac{1}{J}\right)$	$\frac{1}{2}\left(1 + \frac{1}{J^2}\right)$
$J - \ln J - 1$	$1 - \frac{1}{J}$	$\frac{1}{J^2}$
$J\ln J - J + 1$	$\ln J$	$\frac{1}{J}$

Tab. 2.1 – Some penalty functions of the literature [Hartmann et al. 2003]

The simplest penalty functions $U(J) = \frac{1}{2}(J-1)^2$, which is also the most used in practice was implemented in this work. The penalty parameter τ may be viewed as the bulk modulus

$$\tau = \frac{E}{3(1-2\upsilon)}, \tag{2.69}$$

where E and υ are respectively a fictive Young's modulus and Poisson's ratio. Notice that for $\tau \longrightarrow \infty$ the volumetric constraint is exactly enforced. The resulting volumetric strain–energy function is $W_{vol}(J) = \frac{\tau}{2}(J-1)^2$. This mathematical function does not respect the $U(0)$ limit but is sufficient in the case of nearly–incompressible materials. The hydrostatic pressure p is then simply obtained from

$$p = -\frac{\partial W_{vol}}{\partial J} = -\tau(J-1). \tag{2.70}$$

The unforced pressure Lagrangian weak equation becomes

$$\int_{\Omega_0} -p^* \left[(J-1) + \frac{p}{\tau}\right] \mathrm{d}V = 0. \tag{2.71}$$

Thus, the unforced updated Lagrangian formulation (2.68) is rewritten as

$$\begin{cases} \displaystyle\int_{\Omega_\mathrm{m}} (\tilde{\mathbf{S}}_{\mathbf{iso}})_{0\to n} : (\mathbf{F}^T_{m\to n} \cdot \nabla_{X_m} \boldsymbol{v}^*)\mathrm{d}V_m - \int_{\Omega_\mathrm{m}} pJ_{m\to n}\mathbf{F}^{-T}_{m\to n} : \nabla_{X_m}\boldsymbol{v}^*\mathrm{d}V_m \\ \qquad\qquad - \displaystyle\int_{\partial\Omega^\mathrm{n}_\mathrm{m}} \boldsymbol{H}_m \cdot \boldsymbol{v}^*\mathrm{d}A_m - \int_{\partial\Omega^\mathrm{p}_\mathrm{m}} P\boldsymbol{v}^* \cdot (\mathbf{F}^{-T}_{m\to n} \cdot \boldsymbol{N}_m)J_{m\to n}\mathrm{d}A_m = 0, \\ \displaystyle\int_{\Omega_\mathrm{m}} -p^* \left[(J_{0\to n} - 1) + \frac{p}{\tau}\right] J^{-1}_{0\to m}\mathrm{d}V_m = 0. \end{cases} \tag{2.72}$$

2.4 Finite element discretization

In this section the FE discretization is presented, with an application to the stabilized MINI–element used in this work. The Newton–Raphson algorithm is recalled and applied to the mechanical problem resolution.

2.4.1 Spatial discretization

Spatial discretization and stability

Equations (2.72) are solved using the FE method, firstly introduced in Courant [1943] but developed in a more proper sense in Argyris et al. [1954] and Turner [1956]. This is a widely used method for approximating solutions for partial differential or integral equations in a wide range of engineering problems. FE method implies a spatial discretization of the problem that consists in subdividing a large domain Ω into sub–domains (elements) Ω_e with $e \in \mathfrak{E} \subset \mathbb{N}$, where $\mathfrak{E}$ is the set of elements. Thus, we define the discretized domain

$$\Omega_\mathrm{h} = \bigcup_{e\in\mathfrak{E}} \Omega_\mathrm{e}, \tag{2.73}$$

where the h index is related to the mesh size. We write $(\boldsymbol{v_h}, p_h) \in \mathcal{V}_h \times \mathcal{P}_h$ the discretized velocity and pressure solutions of $(\boldsymbol{v}, p) \in \mathcal{V} \times \mathcal{P}$. The discrete spaces $\mathcal{V}_h$ and $\mathcal{P}_h$ are usually included into their solution spaces $\mathcal{V}$ and $\mathcal{P}$, thus

$$\begin{aligned} \mathcal{V}_h \subset \mathcal{V} \quad \text{with} \quad \lim_{h\to 0} \mathcal{V}_h = \mathcal{V}, \\ \mathcal{P}_h \subset \mathcal{P} \quad \text{with} \quad \lim_{h\to 0} \mathcal{P}_h = \mathcal{P}. \end{aligned} \tag{2.74}$$

The choice of approximation spaces $\mathcal{V}_h$ and $\mathcal{P}_h$ is directly related to the efficiency and accuracy of the velocity and pressure results from solving the discrete problem. Moreover, both interpolation spaces cannot be chosen independently and must verify the Brezzi–Babŭska [Babuska 1971] (also called "inf–sup") compatibility condition which insures the existence, uniqueness and stability of the solution :

$$\inf_{p_h \in \mathcal{P}_h} \sup_{\boldsymbol{v_h} \in \mathcal{V}_h} \frac{\int_{\Omega_h} p_h \nabla . \boldsymbol{v_h} \mathrm{d}\Omega_h}{\|p_h\|_{\mathcal{P}_h} \|\boldsymbol{v_h}\|_{\mathcal{V}_h}} \geqslant \alpha, \tag{2.75}$$

where $\alpha > 0$ is a constant. The non–compliance of this condition leads to huge numerical difficulties and unacceptable solutions, such as locking or oscillating solutions. For example the $P1/P1$ element, with both linear velocity (or displacement) and pressure unknowns, does not satisfy the inf–sup condition. However, a vast literature exits on stabilization methods in order to achieve the Brezzi–Babŭska condition for incompatible elements. The reader can refer among others to "bubble", Streamline–Upwind Petrov–Galerkin (SUPG) and Algebraic/Orthogonal Subgrid Scale (ASGS/OSGS) methods [Pierre 1988; Brezzi, Bristeau, et al. 1992; Hughes 1995].

The MINI–Element

Linear tetrahedron elements are very attractive because they are simple, which makes the mesh generation and mesh adaptation processes robust and fast even on complex geometries. In this work, the so–called MINI–element (or $P1^+/P1$ element) is used. The MINI–element was firstly introduced as a bidimensional (triangular) element in Arnold et al. [1984] for Stokes flow modeling, then extended to tridimensional problems (tetrahedron) in Coupez [1995] (fig. 2.4). It is a mixed linear element ($O(h)$). Two kinds of variables are defined on the element, P1 and P0. P1 variables are the unknowns of the mechanical problems (*i.e.* velocity and pressure in that case). They are computed and stored at the elements' nodes. P0 variables are calculated and stored at the center of the elements (stress tensor, velocity gradient, ...).

The pressure discretization is continuous and the velocity discretization is enriched with an additional degree of freedom in the center of the element in order to verify the Brezzi–Babŭska compatibility condition between velocity and pressure discretization spaces.

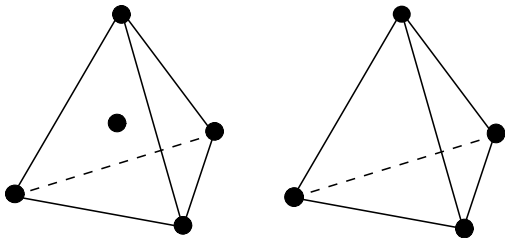

Fig. 2.4 – $P1^+/P1$ tetrahedron element with velocity (left) and pressure (right) degree of freedom

Thus, respectively 15 and 4 velocity and pressure degrees of freedom are available for each element in the tridimensional case. This small number of degrees of freedom makes it relatively computationally inexpensive but the counterpart of its minimalistic properties is its poor accuracy (smallest interpolation degree among the compatible elements).

The shape function of the additional velocity degree of freedom, commonly called "bubble", is equal to unity at element center and zero at element borders. The interpolated velocity field $\boldsymbol{v_h}$ on the $P1^+/P1$ element follows the unique decomposition

$$\boldsymbol{v_h} = \boldsymbol{v^l} + \boldsymbol{v^b}, \quad \text{with} \quad \boldsymbol{v_h} \in \mathcal{V}_h = \boldsymbol{\mathcal{L}_h} \oplus \boldsymbol{\mathcal{B}_h} \tag{2.76}$$

where $\boldsymbol{v^l}$ is the linear part of the velocity field $\boldsymbol{v_h}$ and $\boldsymbol{v^b}$ its bubble part. $\boldsymbol{\mathcal{L}_h}$ and $\boldsymbol{\mathcal{B}_h}$ are respectively the approximation spaces of the linear and bubble functions. The bubble interpolation function can be constructed in the reference (or canonical) element as a fourth–order polynomial [M. Fortin 1981],

$$N^b(\xi,\eta,\zeta) = 256(1-\xi-\eta-\zeta)\xi\eta\zeta, \tag{2.77}$$

where (ξ,η,ζ) is reference element space. However, following Coupez [1995] the $\boldsymbol{\mathcal{B}_h}$ space is defined with a piecewise linear function on four sub–tetrahedrons to avoid the difficulty in integrating a fourth–degree polynomial (fig. 2.5). Discrete spaces are defined as :

$$\begin{aligned}
\mathcal{V}_h &= \boldsymbol{\mathcal{L}_h} \oplus \boldsymbol{\mathcal{B}_h}, \\
\boldsymbol{\mathcal{L}_h} &= \left[\boldsymbol{v^l} \in (\mathbf{C}^0(\Omega_\mathrm{h}))^3, \boldsymbol{v^l} \mid_{\Omega_\mathrm{e}} \in (\mathbf{P}^1(\Omega_\mathrm{e}))^3, \boldsymbol{v^l} \mid_{\partial\Omega_\mathrm{e}} = \boldsymbol{v_0}, \forall e \in \mathcal{E}\right], \\
\boldsymbol{\mathcal{L}_h^*} &= \left[\boldsymbol{v^{l*}} \in \mathcal{V}^* \cap (\mathbf{C}^0(\Omega_\mathrm{h}))^3, \boldsymbol{v^{l*}} \mid_{\Omega_\mathrm{e}} \in (\mathbf{P}^1(\Omega_\mathrm{e}))^3, \boldsymbol{v^{l*}} \mid_{\partial\Omega_\mathrm{e}} = \overrightarrow{0}, \forall e \in \mathcal{E}\right], \\
\boldsymbol{\mathcal{B}_h} &= \left[\boldsymbol{v^b} \in (\mathbf{C}^0(\Omega_\mathrm{h}))^3, \boldsymbol{v^b} \mid_{\partial\Omega_\mathrm{e}} = \overrightarrow{0}, \boldsymbol{v^b} \mid_{\Omega_{\mathrm{e}_\mathrm{i}}} \in (\mathbf{P}^1(\Omega_{\mathrm{e}_\mathrm{i}}))^3, \forall e \in \mathcal{E}, i = 1,\ldots,4\right], \\
\boldsymbol{\mathcal{P}_h} &= \left[\mathbf{L}^2(\Omega_\mathrm{h}) \cap \mathbf{C}^0(\Omega_\mathrm{h}), p_h \mid_{\Omega_\mathrm{e}} \in (\mathbf{P}^1(\Omega_\mathrm{e}))^3, \forall e \in \mathcal{E}\right],
\end{aligned} \tag{2.78}$$

where $\mathbf{C}^0(\Omega_\mathrm{h})$ is the space of continuous functions on Ω_h and $\mathbf{P}^1(\Omega_\mathrm{e})$ is the space of linear functions on element Ω_e.

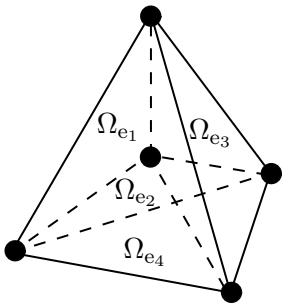

Fig. 2.5 – Decomposition of the $P1^+/P1$ element into 4 sub–tetrahedrons

At a material point $\boldsymbol{x}$, the velocity and pressure fields can be expressed as a function of the linear shape functions as

$$\begin{aligned} \boldsymbol{v_h}(\boldsymbol{x}) &= \sum_{i=1}^{\text{NbNo}} N_i^l(\boldsymbol{x})\boldsymbol{v_i^l} + \sum_{j=1}^{\text{NbElt}} N_j^b(\boldsymbol{x})\boldsymbol{v_j^b}, \\ p_h(\boldsymbol{x}) &= \sum_{i=1}^{\text{NbNo}} N_i^l(\boldsymbol{x})p_i, \end{aligned} \tag{2.79}$$

where NbNo is the number of nodes and NbElt is the number of elements. $N_i^l(\boldsymbol{x}) \in \boldsymbol{\mathcal{L}_h}$ with $i = 1, \ldots,$ NbNo are the interpolation functions of the linear velocity and pressure fields associated with each node i. $N_j^b(\boldsymbol{x}) \in \boldsymbol{\mathcal{B}_h}$ with $j = 1, \ldots,$ NbElt is the interpolation function of bubble velocity associated with the element j. $\boldsymbol{v_i^l}$, p_i and $\boldsymbol{v_j^b}$ are respectively the linear velocity, pressure and bubble velocity associed with node i and element j. From equations (2.79), velocity and pressure fields can be obtained for each element Ω_e following

$$\begin{aligned} \boldsymbol{v_h}(\boldsymbol{x}) &= \sum_{i=1}^{4} N_i^l(\boldsymbol{x})\boldsymbol{v_i^l} + N^b(\boldsymbol{x})\boldsymbol{v^b}, \\ p_h(\boldsymbol{x}) &= \sum_{i=1}^{4} N_i^l(\boldsymbol{x})p_i. \end{aligned} \tag{2.80}$$

The shape functions associated with the reference element are defined as

$$\begin{cases} N_1^l = \xi \\ N_2^l = \eta \\ N_3^l = \zeta \\ N_4^l = 1 - \xi - \eta - \zeta \end{cases} \quad \text{and} \quad \begin{cases} N^b = 4\xi & \text{in} \quad \Omega_{e_1} \\ N^b = 4\eta & \text{in} \quad \Omega_{e_2} \\ N^b = 4\zeta & \text{in} \quad \Omega_{e_3} \\ N^b = 4(1 - \xi - \eta - \zeta) & \text{in} \quad \Omega_{e_4} \end{cases} \tag{2.81}$$

The bubble has some useful properties as velocity $\boldsymbol{v^b} = \overrightarrow{0}$ on $\partial\Omega_e$, which allows eliminating the bubble on the borders. Another property is for all constant tensor $\mathbf{k}$

$$\int_{\Omega_\mathrm{h}} \mathbf{k} : \nabla \boldsymbol{v}^{\boldsymbol{b}} \mathrm{d}\Omega_\mathrm{h} = 0, \tag{2.82}$$

with in particular,

$$\int_{\Omega_\mathrm{h}} \nabla \boldsymbol{v}^{\boldsymbol{l}} : \nabla \boldsymbol{v}^{\boldsymbol{b}} \mathrm{d}\Omega_\mathrm{h} = 0, \tag{2.83}$$

$\forall (\boldsymbol{v}^{\boldsymbol{l}}, \boldsymbol{v}^{\boldsymbol{b}}) \in \boldsymbol{\mathcal{L}}_{\boldsymbol{\hbar}} \times \boldsymbol{\mathcal{B}}_{\boldsymbol{\hbar}}$, which is called orthogonal property [Aliaga 2000; Perchat 2000].

The problem (2.72) can be written on the discretized space Ω_{h_m}, using the decomposition (2.76) of $\boldsymbol{v_h}$ and the orthogonal property (2.83), as

$$\begin{cases} \displaystyle\int_{\Omega_{\mathrm{h_m}}} (\tilde{\mathbf{S}}_{\mathbf{iso}})_{0\to n} : (\mathbf{F}^T_{m\to n} \cdot \nabla_{X_m} \boldsymbol{v}^{\boldsymbol{l}*}) \mathrm{d}V_{h_m} - \int_{\Omega_{\mathrm{h_m}}} p_h J_{m\to n} \mathbf{F}^{-T}_{m\to n} : \nabla_{X_m} \boldsymbol{v}^{\boldsymbol{l}*} \mathrm{d}V_{h_m} \\ \qquad - \displaystyle\int_{\partial\Omega^{\mathrm{n}}_{\mathrm{h_m}}} \boldsymbol{H}_m \cdot \boldsymbol{v}^{\boldsymbol{l}*} \mathrm{d}A_{h_m} - \int_{\partial\Omega^{\mathrm{p}}_{\mathrm{h_m}}} P \boldsymbol{v}^{\boldsymbol{l}*} \cdot (\mathbf{F}^{-T}_{m\to n} \cdot \boldsymbol{N}_m) J_{m\to n} \mathrm{d}A_{h_m} = 0, \\ \displaystyle\int_{\Omega_{\mathrm{h_m}}} (\tilde{\mathbf{S}}_{\mathbf{iso}})_{0\to n} : (\mathbf{F}^T_{m\to n} \cdot \nabla_{X_m} \boldsymbol{v}^{\boldsymbol{b}*}) \mathrm{d}V_{h_m} \\ \qquad\qquad - \displaystyle\int_{\Omega_{\mathrm{h_m}}} p_h J_{m\to n} \mathbf{F}^{-T}_{m\to n} : \nabla_{X_m} \boldsymbol{v}^{\boldsymbol{b}*} \mathrm{d}V_{h_m} = 0, \\ \displaystyle\int_{\Omega_{\mathrm{h_m}}} - p^*_h \left[(J_{0\to n} - 1) + \frac{p_h}{\tau} \right] J^{-1}_{0\to m} \mathrm{d}V_{h_m} = 0, \\ \forall (\boldsymbol{v}^{\boldsymbol{l}*}, \boldsymbol{v}^{\boldsymbol{b}*}, p^*_h) \in \boldsymbol{\mathcal{L}}^*_{\boldsymbol{\hbar}} \times \boldsymbol{\mathcal{B}}_{\boldsymbol{\hbar}} \times \boldsymbol{\mathcal{P}}_{\boldsymbol{\hbar}}, \end{cases} \tag{2.84}$$

where $\tilde{\mathbf{S}}_{\mathbf{iso}}$ depends on the linear displacement $\boldsymbol{U}^{\boldsymbol{l}}$ and the bubble displacement $\boldsymbol{U}^{\boldsymbol{b}}$, that can be linked with the velocities $(\boldsymbol{v}^{\boldsymbol{l}}, \boldsymbol{v}^{\boldsymbol{b}}) \in \boldsymbol{\mathcal{L}}_{\boldsymbol{\hbar}} \times \boldsymbol{\mathcal{B}}_{\boldsymbol{\hbar}}$ through time. Due to the non–linearity of $\tilde{\mathbf{S}}_{\mathbf{iso}}$ and J, the system (2.84) is a coupled system of several unknown fields. By analogy to the subgrid–scale methods [Brezzi, L. P. Franca, et al. 1996; Hughes and Stewart 1996; Hughes 1995] and considering an interval time discretization Δt between increments m and n, a Taylor series expansion is used to keep only linear bubble terms. We note $\boldsymbol{U}^{\boldsymbol{l}}_{0\to n} = \boldsymbol{U}^{\boldsymbol{l}}_{0\to m} + \boldsymbol{v}^{\boldsymbol{l}} \Delta t$ and $\boldsymbol{U}^{\boldsymbol{b}}_{m\to n} = \boldsymbol{v}^{\boldsymbol{b}} \Delta t$ the displacements respectively for the linear and the bubble part. Following Hughes and Pister [1978] directional derivatives are used for the linearization, so that

$$\begin{aligned} \mathbf{S}(\boldsymbol{U}^{\boldsymbol{l}}_{0\to n} + \boldsymbol{U}^{\boldsymbol{b}}_{m\to n}) &\approx \mathbf{S}(\boldsymbol{U}^{\boldsymbol{l}}_{0\to n}) + \frac{d}{d\epsilon} \left[\mathbf{S}(\boldsymbol{U}^{\boldsymbol{l}}_{0\to n} + \epsilon \boldsymbol{U}^{\boldsymbol{b}}_{m\to n}) \right] \Big|_{\epsilon=0} \\ &= \mathbf{S}(\boldsymbol{U}^{\boldsymbol{l}}_{0\to n}) + \mathbb{C}_{0\to n} : \frac{d}{d\epsilon} \left[\mathbf{E}(\boldsymbol{U}^{\boldsymbol{l}}_{0\to n} + \epsilon \boldsymbol{U}^{\boldsymbol{b}}_{m\to n}) \right] \Big|_{\epsilon=0} \\ &= \mathbf{S}(\boldsymbol{U}^{\boldsymbol{l}}_{0\to n}) + \mathbb{C}_{0\to n} : \frac{1}{2} \left[(\nabla_X \boldsymbol{U}^{\boldsymbol{b}})^T \cdot \mathbf{F}_{0\to n} + \mathbf{F}^T_{0\to n} \cdot \nabla_X \boldsymbol{U}^{\boldsymbol{b}} \right] \\ &= \mathbf{S}(\boldsymbol{U}^{\boldsymbol{l}}_{0\to n}) + \mathbb{C}_{0\to n} : \left[\mathbf{F}^T_{0\to n} \cdot \nabla \boldsymbol{v}^{\boldsymbol{b}} \cdot \mathbf{F}_{0\to n} \right] \Delta t, \end{aligned} \tag{2.85}$$

where we used the minor symmetries of $\mathbb{C}_{0\to n} = \partial \mathbf{S}(\boldsymbol{U}^{\boldsymbol{l}}_{0\to n})/\partial \mathbf{E}(\boldsymbol{U}^{\boldsymbol{l}}_{0\to n})$ from (2.32) and (2.35). Also,

$$\begin{aligned} J(\boldsymbol{U}^{\boldsymbol{l}}_{0\to n} + \boldsymbol{U}^{\boldsymbol{b}}_{m\to n}) &\approx J(\boldsymbol{U}^{\boldsymbol{l}}_{0\to n}) + \frac{d}{d\epsilon}\left[J(\boldsymbol{U}^{\boldsymbol{l}}_{0\to n} + \epsilon \boldsymbol{U}^{\boldsymbol{b}}_{m\to n})\right]\Big|_{\epsilon=0} \\ &= J(\boldsymbol{U}^{\boldsymbol{l}}_{0\to n}) + J(\boldsymbol{U}^{\boldsymbol{l}}_{0\to n})\nabla\cdot\boldsymbol{v}^{\boldsymbol{b}}\Delta t. \end{aligned} \tag{2.86}$$

Residual equations (2.84) can be rewritten using linearizations (2.85) and (2.86), and the orthogonal property (2.83), into the compact form

$$\left\{\begin{array}{rcccccc} \boldsymbol{R}^{\boldsymbol{l}}_{\boldsymbol{e}} &=& \boldsymbol{R}^{\boldsymbol{ll}}_{\boldsymbol{e}} &+& \overrightarrow{0} &+& \boldsymbol{R}^{\boldsymbol{lp}}_{\boldsymbol{e}} &=& \overrightarrow{0}, \\ \boldsymbol{R}^{\boldsymbol{b}}_{\boldsymbol{e}} &=& \overrightarrow{0} &+& \boldsymbol{R}^{\boldsymbol{bb}}_{\boldsymbol{e}} &+& \boldsymbol{R}^{\boldsymbol{bp}}_{\boldsymbol{e}} &=& \overrightarrow{0}, \\ \boldsymbol{R}^{\boldsymbol{p}}_{\boldsymbol{e}} &=& \boldsymbol{R}^{\boldsymbol{pl}}_{\boldsymbol{e}} &+& \boldsymbol{R}^{\boldsymbol{pb}}_{\boldsymbol{e}} &+& \boldsymbol{R}^{\boldsymbol{pp}}_{\boldsymbol{e}} &=& \overrightarrow{0}, \end{array}\right. \tag{2.87}$$

where $\boldsymbol{R}^{\boldsymbol{l}}_{\boldsymbol{e}}$, $\boldsymbol{R}^{\boldsymbol{b}}_{\boldsymbol{e}}$ and $\boldsymbol{R}^{\boldsymbol{p}}_{\boldsymbol{e}}$ respectively are the linear velocity, bubble velocity and pressure residuals calculated at the element level, and

$$\begin{aligned} \boldsymbol{R}^{\boldsymbol{ll}}_{\boldsymbol{e}} = \int_{\Omega_{\mathrm{h_m}}} (\tilde{\mathbf{S}}_{\mathbf{iso}})_{0\to n} : \left(\mathbf{F}^{T}_{m\to n}\cdot\nabla_{X_m}\boldsymbol{v}^{\boldsymbol{l*}}\right)\mathrm{d}V_{h_m} - \int_{\partial\Omega^{\mathrm{n}}_{\mathrm{h_m}}} \boldsymbol{H}_m\cdot\boldsymbol{v}^{\boldsymbol{l*}}\mathrm{d}A_{h_m} \\ - \int_{\partial\Omega^{\mathrm{p}}_{\mathrm{h_m}}} P\boldsymbol{v}^{\boldsymbol{l*}}\cdot\left(\mathbf{F}^{-T}_{m\to n}\cdot\boldsymbol{N}_m\right)J_{m\to n}\mathrm{d}A_{h_m}, \end{aligned} \tag{2.88a}$$

$$\boldsymbol{R}^{\boldsymbol{lp}}_{\boldsymbol{e}} = -\int_{\Omega_{\mathrm{h_m}}} p_h J_{m\to n}\mathbf{F}^{-T}_{m\to n} : \nabla_{X_m}\boldsymbol{v}^{\boldsymbol{l*}}\mathrm{d}V_{h_m}, \tag{2.88b}$$

$$\boldsymbol{R}^{\boldsymbol{bb}}_{\boldsymbol{e}} = \int_{\Omega_{\mathrm{h_m}}} (\tilde{\mathbb{C}}_{\mathbb{iso}})_{0\to n} : \left[\mathbf{F}^{T}_{m\to n}\cdot\nabla\boldsymbol{v}^{\boldsymbol{b}}\cdot\mathbf{F}_{m\to n}\right]\Delta t : \left(\mathbf{F}^{T}_{m\to n}\cdot\nabla_{X_m}\boldsymbol{v}^{\boldsymbol{b*}}\right)\mathrm{d}V_{h_m}, \tag{2.88c}$$

$$\boldsymbol{R}^{\boldsymbol{bp}}_{\boldsymbol{e}} = -\int_{\Omega_{\mathrm{h_m}}} p_h J_{m\to n}\nabla\cdot\boldsymbol{v}^{\boldsymbol{b}}\Delta t\left(\mathbf{F}^{-T}_{m\to n} : \nabla_{X_m}\boldsymbol{v}^{\boldsymbol{b*}}\right)\mathrm{d}V_{h_m}, \tag{2.88d}$$

$$\boldsymbol{R}^{\boldsymbol{pl}}_{\boldsymbol{e}} = -\int_{\Omega_{\mathrm{h_m}}} p^*_h(J_{0\to n}-1)J^{-1}_{0\to m}\mathrm{d}V_{h_m}, \tag{2.88e}$$

$$\boldsymbol{R}^{\boldsymbol{pb}}_{\boldsymbol{e}} = -\int_{\Omega_{\mathrm{h_m}}} p^*_h J_{m\to n}\Delta t\nabla\cdot\boldsymbol{v}^{\boldsymbol{b}}\mathrm{d}V_{h_m}, \tag{2.88f}$$

$$\boldsymbol{R}^{\boldsymbol{pp}}_{\boldsymbol{e}} = -\int_{\Omega_{\mathrm{h_m}}} p^*_h\frac{p_h}{\tau}J^{-1}_{0\to m}\mathrm{d}V_{h_m}, \tag{2.88g}$$

where $(\tilde{\mathbb{C}}_{\mathbb{iso}})_{0\to n} = J^{-1}_{0\to m}\chi^{\star}_{0\to m}\left((\mathbb{C}_{\mathbb{iso}})_{0\to n}\right)$ and $(\mathbb{C}_{\mathbb{iso}})_{0\to n} = \dfrac{\partial(\mathbf{S}_{\mathbf{iso}})_{0\to n}}{\partial\mathbf{E}_{0\to n}}$. The standard Galerkin method is adopted, where the shape functions are identical to the test functions, using (2.79) and

$$\nabla \boldsymbol{v}^{\boldsymbol{l}}_{xy} = \sum_{i=1}^{\mathrm{NbNo}} \frac{\partial N^l_i}{\partial x_y} \boldsymbol{v}^{\boldsymbol{l}}_{x,i}, \tag{2.89}$$

$$\nabla \boldsymbol{v}^{\boldsymbol{b}}_{xy} = \frac{\partial N^b}{\partial x_y} \boldsymbol{v}^{\boldsymbol{b}}_{x}, \tag{2.90}$$

where $i \in \{1, \dots, 4\}$ is the node number and $x, y \in \{1, 2, 3\}$ are vector components index.

For further details, a vast literature exists on the bubble concept and its similarities with other stabilization methods [Pierre 1988; Brezzi, L. P. Franca, et al. 1996; Brezzi, Bristeau, et al. 1992; Hughes and Stewart 1996; Hughes 1995; Hughes, Feijoo, et al. 1998]. Also, Franca et *al.* highlight bubble limitations in some specific cases [Leopoldo P. Franca et al. 1994; Leopoldo P. Franca et al. 1995].

2.4.2 Temporal discretization

The Newton–Raphson method

Due to non–linearities of the mechanical problem, an iterative method is required to solve the system (2.87). The Newton–Raphson method is used to reduce the residual terms $\boldsymbol{R}$ to zero and to reach the equilibrium between internal and external forces. We subsequently consider a time discretization between $[t, t + \Delta t]$ corresponding to the consecutive increments n and $n + 1$. At the instant t, the problem is supposed to be at equilibrium. The Newton–Raphson method uses the first order Taylor series expansion to linearize the equations and find the velocity and pressure fields that respect the equilibrium at the instant $t + \Delta t$ when updating the external forces (see fig. 2.6). Knowing a solution $\boldsymbol{x}_n$,

$$\boldsymbol{R}(\boldsymbol{x}_n + \boldsymbol{\delta x}) \approx \boldsymbol{R}(\boldsymbol{x}_n) + \left.\frac{d\boldsymbol{R}}{d\boldsymbol{x}_n}\right|_{\boldsymbol{x}_n} \cdot \boldsymbol{\delta x} = \overrightarrow{0}. \tag{2.91}$$

We define the tangent stiffness matrix (or Hessian matrix) as

$$\mathbf{H} = \left.\frac{d\boldsymbol{R}}{d\boldsymbol{x}_n}\right|_{\boldsymbol{x}_n}. \tag{2.92}$$

The system to be solved becomes

$$\mathbf{H}(\boldsymbol{x}_n) \cdot \boldsymbol{\delta x} = -\boldsymbol{R}(\boldsymbol{x}_n). \tag{2.93}$$

Notice that $\boldsymbol{\delta x}$ is an iterative correction of the solution field, $\boldsymbol{x}_{n+1} = \boldsymbol{x}_n + \boldsymbol{\delta x}$.

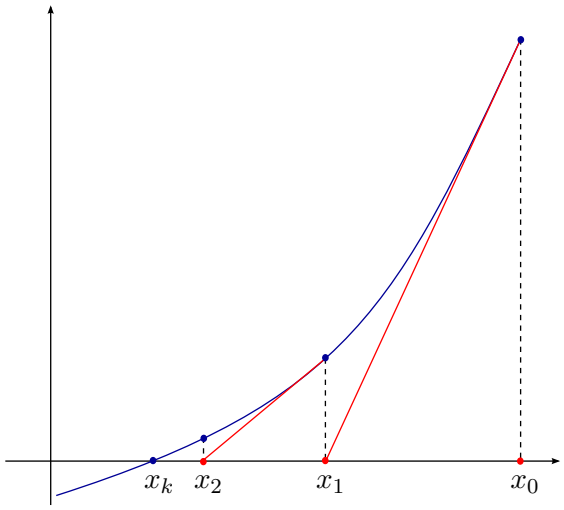

Fig. 2.6 – Illustration of the Newton–Raphson algorithm where $x_0 = x_n$ is the initial (known) solution at t and $x_k = x_{n+1}$ is the converged solution at $t + \Delta t$

Application of the Newton–Raphson method

From equations (2.87), (2.92) and (2.93), the linear system to be solved at each Newton–Raphson iteration takes the form

$$\begin{pmatrix} \mathbf{H_e^{ll}} & \mathbf{0} & \mathbf{H_e^{lp}} \\ \mathbf{0} & \mathbf{H_e^{bb}} & \mathbf{H_e^{bp}} \\ \mathbf{H_e^{pl}} & \mathbf{H_e^{pb}} & \mathbf{H_e^{pp}} \end{pmatrix} \begin{pmatrix} \boldsymbol{\delta v_e^l} \\ \boldsymbol{\delta v_e^b} \\ \boldsymbol{\delta p_{he}} \end{pmatrix} = - \begin{pmatrix} \boldsymbol{R_e^l} \\ \boldsymbol{R_e^b} \\ \boldsymbol{R_e^p} \end{pmatrix} \tag{2.94}$$

with

$$\mathbf{H_e^{xy}} = \frac{\partial \boldsymbol{R_e^x}}{\partial \alpha_y}, \tag{2.95}$$

where $(xy) \in \{(ll), (lp), (bb), (bp), (pl), (pb), (pp)\}$ and $\alpha_y \in \{\boldsymbol{v_e^l}, \boldsymbol{v_e^b}, p_{he}\}$. The Hessian matrix is generally symmetric, so that $\mathbf{H_e^{pl}} = (\mathbf{H_e^{lp}})^T$ and $\mathbf{H_e^{pb}} = (\mathbf{H_e^{bp}})^T$. Notice that for an incompressible material $\mathbf{H_e^{pp}} = \mathbf{0}$.

The Hessian matrix

The Hessian matrix terms can be obtained from (2.88) and (2.95). However, for implementation purpose, only the following derivatives were considered

$$\mathbf{H_e^{ll}} = \frac{\partial \boldsymbol{R_e^{ll}}}{\partial \boldsymbol{v_e^l}}, \quad \mathbf{H_e^{lp}} = \frac{\partial \boldsymbol{R_e^{lp}}}{\partial p_{he}}, \quad \mathbf{H_e^{bb}} = \frac{\partial \boldsymbol{R_e^{bb}}}{\partial \boldsymbol{v_e^b}}, \quad \mathbf{H_e^{bp}} = \frac{\partial \boldsymbol{R_e^{bp}}}{\partial p_{he}},$$
$$\mathbf{H_e^{pl}} = \frac{\partial \boldsymbol{R_e^{pl}}}{\partial \boldsymbol{v_e^l}}, \quad \mathbf{H_e^{pb}} = \frac{\partial \boldsymbol{R_e^{pb}}}{\partial \boldsymbol{v_e^b}}, \quad \mathbf{H_e^{pp}} = \frac{\partial \boldsymbol{R_e^{pp}}}{\partial p_{he}}.$$

For instance, $\frac{\partial \boldsymbol{R}_e^{lp}}{\partial \boldsymbol{v}_e^{l}}$ and $\frac{\partial \boldsymbol{R}_e^{bp}}{\partial \boldsymbol{v}_e^{b}}$ were not taken into account in the Hessian matrix, respectively in the $\mathbf{H}_\mathbf{e}^{\mathbf{ll}}$ and $\mathbf{H}_\mathbf{e}^{\mathbf{bb}}$ terms. Hence,

$$\begin{aligned}
\mathbf{H}_\mathbf{e}^{\mathbf{ll}} = &\int_{\Omega_{\mathrm{h_n}}} (\tilde{\mathbb{C}}_{\mathbb{iso}})_{0\to n+1} : \left(\mathbf{F}_{n\to n+1}^{T} \cdot \frac{\partial \nabla \boldsymbol{v}^{\boldsymbol{l}}}{\partial \boldsymbol{v}^{\boldsymbol{l}}} \Delta t \right) : \left(\mathbf{F}_{n\to n+1}^{T} \cdot \nabla_{X_n} \boldsymbol{v}^{\boldsymbol{l}*} \right) \mathrm{d}V_{h_n} \\
&+ \int_{\Omega_{\mathrm{h_n}}} (\tilde{\mathbf{S}}_{\mathbf{iso}})_{0\to n+1} : \left[\left(\frac{\partial \nabla \boldsymbol{v}^{\boldsymbol{l}}}{\partial \boldsymbol{v}^{\boldsymbol{l}}} \right)^{T} \Delta t \cdot \nabla_{X_n} \boldsymbol{v}^{\boldsymbol{l}*} \right] \mathrm{d}V_{h_n} \\
&- \int_{\partial\Omega_{\mathrm{h_n}}^{\mathrm{p}}} P\boldsymbol{v}^{\boldsymbol{l}*} \cdot \left[\mathbf{F}_{n\to n+1}^{-T} \cdot \frac{\partial \nabla \boldsymbol{v}^{\boldsymbol{l}}}{\partial \boldsymbol{v}^{\boldsymbol{l}}} \Delta t \right] \cdot \left(\mathbf{F}_{n\to n+1}^{-T} \cdot \boldsymbol{N}_n \right) J_{n\to n+1} \mathrm{d}A_{h_n} \\
&+ \int_{\partial\Omega_{\mathrm{h_n}}^{\mathrm{p}}} P\boldsymbol{v}^{\boldsymbol{l}*} \cdot \left[\mathbf{F}_{n\to n+1}^{-T} \cdot \left(\frac{\partial \nabla \boldsymbol{v}^{\boldsymbol{l}}}{\partial \boldsymbol{v}^{\boldsymbol{l}}} \right)^{T} \Delta t \cdot \mathbf{F}_{n\to n+1}^{-T} \cdot \boldsymbol{N}_n \right] J_{n\to n+1} \mathrm{d}A_{h_n}, \qquad (2.96a)
\end{aligned}$$

$$\mathbf{H}_\mathbf{e}^{\mathbf{lp}} = -\int_{\Omega_{\mathrm{h_n}}} J_{n\to n+1} \mathbf{F}_{n\to n+1}^{-T} : \nabla_{X_n} \boldsymbol{v}^{\boldsymbol{l}*} \mathrm{d}V_{h_n}, \qquad (2.96b)$$

$$\begin{aligned}
\mathbf{H}_\mathbf{e}^{\mathbf{bb}} = &\int_{\Omega_{\mathrm{h_n}}} (\tilde{\mathbb{C}}_{\mathbb{iso}})_{0\to n+1} : \left[\mathbf{F}_{n\to n+1}^{T} \cdot \frac{\partial \nabla \boldsymbol{v}^{\boldsymbol{b}}}{\partial \boldsymbol{v}^{\boldsymbol{b}}} \cdot \mathbf{F}_{n\to n+1} \right] \Delta t \\
&: \left(\mathbf{F}_{n\to n+1}^{T} \cdot \nabla_{X_n} \boldsymbol{v}^{\boldsymbol{b}*} \right) \mathrm{d}V_{h_n}, \qquad (2.96c)
\end{aligned}$$

$$\mathbf{H}_\mathbf{e}^{\mathbf{bp}} = -\int_{\Omega_{\mathrm{h_n}}} J_{n\to n+1} \nabla \cdot \boldsymbol{v}^{\boldsymbol{b}} \Delta t \left(\mathbf{F}_{n\to n+1}^{-T} : \nabla_{X_n} \boldsymbol{v}^{\boldsymbol{b}*} \right) \mathrm{d}V_{h_n}, \qquad (2.96d)$$

$$\mathbf{H}_\mathbf{e}^{\mathbf{pl}} = -\int_{\Omega_{\mathrm{h_n}}} p_h^* J_{n\to n+1} \Delta t \left(\mathbf{F}_{n\to n+1}^{-T} : \frac{\partial \nabla \boldsymbol{v}^{\boldsymbol{l}}}{\partial \boldsymbol{v}^{\boldsymbol{l}}} \right) \mathrm{d}V_{h_n}, \qquad (2.96e)$$

$$\mathbf{H}_\mathbf{e}^{\mathbf{pb}} = -\int_{\Omega_{\mathrm{h_n}}} p_h^* J_{n\to n+1} \Delta t \frac{\partial \nabla \cdot \boldsymbol{v}^{\boldsymbol{b}}}{\partial \boldsymbol{v}^{\boldsymbol{b}}} \mathrm{d}V_{h_n}, \qquad (2.96f)$$

$$\mathbf{H}_\mathbf{e}^{\mathbf{pp}} = -\int_{\Omega_{\mathrm{h_n}}} p_h^* \frac{1}{\tau} J_{0\to n}^{-1} \mathrm{d}V_{h_n}, \qquad (2.96g)$$

where

$$\frac{\partial \nabla \boldsymbol{v}_{xy}^{\boldsymbol{l}}}{\partial \boldsymbol{v}_{z}^{\boldsymbol{l}}} = \sum_{i=1}^{\mathrm{NbNo}} \frac{\partial N_i^l}{\partial x_y} \delta_{xz}, \qquad (2.97)$$

$$\frac{\partial \nabla \boldsymbol{v}_{xy}^{\boldsymbol{b}}}{\partial \boldsymbol{v}_{z}^{\boldsymbol{b}}} = \frac{\partial N^b}{\partial x_y} \delta_{xz}, \qquad (2.98)$$

with $i \in \{1, \ldots, 4\}$ is the node number, $x, y, z \in \{1, 2, 3\}$ are vector components index and δ the Kronecker delta. The reader can refer to A. Fortin et al. [2013] for additional information.

Bubble elimination

Since the bubble is locally defined, it is possible to reduce the system (2.94) using the well known static condensation process. From (2.94), one can obtain

$$\boldsymbol{\delta v}_e^b = -(\mathbf{H}_\mathbf{e}^{\mathbf{bb}})^{-1} \cdot (\boldsymbol{R}_e^b + \mathbf{H}_\mathbf{e}^{\mathbf{bp}} \cdot \boldsymbol{\delta p}_{he}). \tag{2.99}$$

Replacing (2.99) in (2.94), and after some manipulations, the system becomes

$$\begin{pmatrix} \mathbf{H}_\mathbf{e}^{\mathbf{ll}} & \mathbf{H}_\mathbf{e}^{\mathbf{lp}} \\ (\mathbf{H}_\mathbf{e}^{\mathbf{lp}})^T & \mathbf{H}_\mathbf{e}^{\mathbf{pp}} - (\mathbf{H}_\mathbf{e}^{\mathbf{bp}})^T (\mathbf{H}_\mathbf{e}^{\mathbf{bb}})^{-1} \mathbf{H}_\mathbf{e}^{\mathbf{bp}} \end{pmatrix} \begin{pmatrix} \boldsymbol{\delta v}_e^l \\ \boldsymbol{\delta p}_{he} \end{pmatrix} = - \begin{pmatrix} \boldsymbol{R}_e^l \\ \boldsymbol{R}_e^p - (\mathbf{H}_\mathbf{e}^{\mathbf{bp}})^T (\mathbf{H}_\mathbf{e}^{\mathbf{bb}})^{-1} \boldsymbol{R}_e^b \end{pmatrix}.$$

The terms $\boldsymbol{R}_e^{bb}$, $\boldsymbol{R}_e^{pb}$ beeing linear with respect to the bubble velocity and $\boldsymbol{R}_e^{bp}$ linear with respect to the pressure, one can write $\boldsymbol{R}_e^{bb} = \mathbf{H}_\mathbf{e}^{\mathbf{bb}} \cdot \boldsymbol{v}_e^b$, $\boldsymbol{R}_e^{pb} = (\mathbf{H}_\mathbf{e}^{\mathbf{bp}})^T \cdot \boldsymbol{v}_e^b$ and $\boldsymbol{R}_e^{bp} = \mathbf{H}_\mathbf{e}^{\mathbf{bp}} \cdot \boldsymbol{p}_{he}$, so that

$$\begin{aligned} \boldsymbol{R}_e^b &= \mathbf{H}_\mathbf{e}^{\mathbf{bb}} \cdot \boldsymbol{v}_e^b + \mathbf{H}_\mathbf{e}^{\mathbf{bp}} \cdot \boldsymbol{p}_{he}, \\ \boldsymbol{R}_e^p &= \boldsymbol{R}_e^{pl} + \boldsymbol{R}_e^{pp} + (\mathbf{H}_\mathbf{e}^{\mathbf{bp}})^T \cdot \boldsymbol{v}_e^b. \end{aligned} \tag{2.100}$$

Finally, defining $\mathbf{C}_\mathbf{e} = (\mathbf{H}_\mathbf{e}^{\mathbf{bp}})^T \cdot (\mathbf{H}_\mathbf{e}^{\mathbf{bb}})^{-1} \cdot \mathbf{H}_\mathbf{e}^{\mathbf{bp}}$, the system to be solved at each iteration becomes

$$\begin{pmatrix} \mathbf{H}_\mathbf{e}^{\mathbf{ll}} & \mathbf{H}_\mathbf{e}^{\mathbf{lp}} \\ (\mathbf{H}_\mathbf{e}^{\mathbf{lp}})^T & \mathbf{H}_\mathbf{e}^{\mathbf{pp}} - \mathbf{C}_\mathbf{e} \end{pmatrix} \begin{pmatrix} \boldsymbol{\delta v}_e^l \\ \boldsymbol{\delta p}_{he} \end{pmatrix} = - \begin{pmatrix} \boldsymbol{R}_e^l \\ \boldsymbol{R}_e^{pl} + \boldsymbol{R}_e^{pp} - \mathbf{C}_\mathbf{e} \cdot \boldsymbol{p}_{he} \end{pmatrix}. \tag{2.101}$$

Using PETSc[1] (Portable Extensible Toolkit for Scientific Computation) library, the linear system (2.101) is preconditioned with an incomplete LU factorization and solved with a conjugate residual method. A relative residual is used $\|\boldsymbol{R} - \mathbf{H} \cdot \boldsymbol{\delta x}\| \leqslant \alpha \|\boldsymbol{R}\|$ with the tolerance criterion α set to 10^{-8}.

2.5 Material models

In this section, two different approaches for the modeling of hyperelastic fiber reinforced materials are presented, the Angular Integration (AI) and the Generalized Structure Tensors (GST). Three material transversely isotropic models belonging to these categories were implemented in the context of this work. They are detailed and we briefly explain the concept of polyconvexity of the strain energy function.

2.5.1 Fiber distribution

As shown in chapter 1, the collagen fiber network is the main component providing the mechanical properties of the tissues. However, if collagen fibers are loaded under

[1] http://mcs.anl.gov/petsc

tension, they buckle under compression. Therefore, to capture the right behavior of the tissue, only the stiffness of each individual fiber in tension should be taken into account depending on the fibers orientations, their waviness and the loading conditions. In soft tissue constitutive modeling, due to the complexity of the fibers organization, simplified orientations and traction–compression switch are usually considered using a statistical distribution of fibers. Two main constitutive frameworks are commonly used in order to take into account this statistical distribution, the Angular Integration (AI) and the Generalized Structure Tensors (GST).

We consider an arbitrary fiber orientation represented by the unit vector $\boldsymbol{M}$, with $\|\boldsymbol{M}\| = 1$, in the reference configuration Ω_0. The fibers orientation are defined into the current configuration with $\boldsymbol{m} = \mathbf{F} \cdot \boldsymbol{M}$, and the stretch in the direction of the fiber is $\lambda = \|\boldsymbol{m}\|$. In both method, AI and GST, the relative density of fibers in a specific direction is described by the orientation distribution function $\rho(\boldsymbol{N})$ assumed to fulfill the normalization condition

$$\frac{1}{4\pi}\int_{\omega}\rho(\boldsymbol{N})\mathrm{d}\omega = 1 \quad \text{with} \quad \boldsymbol{N} = \begin{pmatrix} \sin\theta\cos\phi \\ \sin\theta\sin\phi \\ \cos\theta \end{pmatrix} \tag{2.102}$$

where $\theta \in [0, \pi]$ and $\phi \in [0, 2\pi]$ are Eulerian angles according to fig. 2.7, $\|\boldsymbol{N}\| = 1$, ω is the unit sphere and $\mathrm{d}\omega = \sin(\theta)\mathrm{d}\theta\mathrm{d}\phi$. Furthermore, $\rho(\boldsymbol{N}) \equiv \rho(-\boldsymbol{N})$ for symmetry requirement. In that case, we consider the current vector $\boldsymbol{n} = \mathbf{F} \cdot \boldsymbol{N}$ and the stretch ratio $\lambda = \|\boldsymbol{N}\|$ in the direction of the fiber. Basically, $\boldsymbol{N}$ represents the direction of an infinitesimal fraction of fibers and $\rho(\boldsymbol{N})$ give the probability to find a fiber aligned with the direction $\boldsymbol{N}$. We subsequently assume fibers distributed with rotational symmetry with respect to the preferred fiber direction $\boldsymbol{N}$ according to Gasser et al. [2006] and Federico et al. [2010] for example. Holzapfel, Niestrawska, et al. [2015] recently introduced a non–symmetric fiber dispersion model in order to capture more complex structural behaviors.

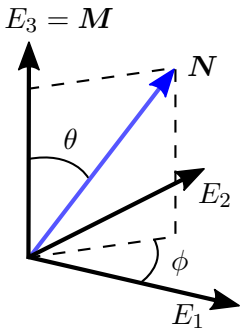

Fig. 2.7 – Characterization of the fiber direction vector in the tree–dimensional Cartesian coordinate system $\{E_1, E_2, E_3\}$

Angular Integration

In the first approach, the fiber distribution is obtained by angular integration of infinitesimal fractions of fibers. From a numerical point of view, the distributed fiber orientation is implemented by summing the individual fibers contribution in all directions. This method was originally introduced by Lanir [Lanir 1983], then followed by others (see for instance Billiar et al. [2000a] and Driessen [2006] with application to valvular tissues and Federico et al. [2010] with application to articular cartilages).

In this method, the strain–energy function of the fibers W^f takes the form

$$W^f = \int_\omega \rho(\boldsymbol{N}) W^{fi} \mathrm{d}\omega, \tag{2.103}$$

where W^{fi} is the strain–energy function of a single fiber of a bundle of fibers.

Thus, the total strain–energy function results from the independent contribution of all individual fibers. The method leads to relatively accurate results but requires a large number of calculations to evaluate the angular integration.

Generalized Structure Tensors

In the GST approach, the fiber distribution is represented by a second order (symmetric) generalized structure tensor $\mathbf{H}$ introduced in Gasser et al. [2006] and also used in Gizzi et al. [2014] for instance. The structure tensor is assumed to represent the three–dimensional distribution of fibers and takes the form

$$\mathbf{H} = \frac{1}{4\pi} \int_\omega \rho(\boldsymbol{N}) \boldsymbol{N} \otimes \boldsymbol{N} \mathrm{d}\omega. \tag{2.104}$$

According to Gasser et al. [2006], in the transversely isotropic case, $\mathbf{H}$ is given by the compact form

$$\mathbf{H} = \kappa \mathbf{I} + (1 - 3\kappa) \boldsymbol{M} \otimes \boldsymbol{M} \tag{2.105}$$

where the dispersion parameter κ represents the "degree of anisotropy".

The GST method is computationally efficient and easy to implement in a FE framework. However this method is less accurate than the AI approach, because based on an average of stretch of all fibers rather than the actual stretch of each fiber depending on its orientation. This simplification leads to important errors in some cases, especially in the case of non–tensile loading. A comparison of both approaches can be found in Cortes et al. [2010] and Skacel et al. [2014] for example.

2.5.2 Strain–energy functions

From previous assumption, we consider an hyperelastic material reinforced by one family of fibers. Fibers are embedded in an isotropic matrix and deform affinely with this matrix. The strain–energy function W for a transversaly isotropic material is

$$W = W(\mathbf{C}, \boldsymbol{M} \otimes \boldsymbol{M}) = W(I_1, I_2, I_3, I_4, I_5) \tag{2.106}$$

where I_1, I_2, I_3 are the three first invariants and I_4, I_5 are pseudo–invariants related to the anisotropic behavior. They are defined as

$$I_1 = \operatorname{tr} \mathbf{C}, \quad I_2 = \frac{1}{2}\left[(\operatorname{tr} \mathbf{C})^2 - \operatorname{tr} \mathbf{C}^2\right], \quad I_3 = \det \mathbf{C}, \tag{2.107a}$$

$$I_4 = \mathbf{C} : \boldsymbol{M} \otimes \boldsymbol{M}, \quad I_5 = \mathbf{C}^2 : \boldsymbol{M} \otimes \boldsymbol{M}. \tag{2.107b}$$

In order to obtain the second Piola–Kirchhoff stress tensor $\mathbf{S}$, equation (2.32) is used :

$$\mathbf{S} = 2\frac{\partial W}{\partial \mathbf{C}} = 2\sum_{i=1}^{5} \frac{\partial W}{\partial I_i}\frac{\partial I_i}{\partial \mathbf{C}}, \tag{2.108}$$

and from (2.28)

$$\boldsymbol{\sigma} = 2J^{-1}\mathbf{F}\sum_{i=1}^{5} \frac{\partial W}{\partial I_i}\frac{\partial I_i}{\partial \mathbf{C}}\mathbf{F}^T. \tag{2.109}$$

The invariants derivative with respect to $\mathbf{C}$ have the forms

$$\frac{\partial I_1}{\partial \mathbf{C}} = \mathbf{I}, \quad \frac{\partial I_2}{\partial \mathbf{C}} = I_1\mathbf{I} - \mathbf{C}, \quad \frac{\partial I_3}{\partial \mathbf{C}} = I_3\mathbf{C}^{-1}, \tag{2.110a}$$

$$\frac{\partial I_4}{\partial \mathbf{C}} = \boldsymbol{M} \otimes \boldsymbol{M}, \quad \frac{\partial I_5}{\partial \mathbf{C}} = \mathbf{C} \cdot (\boldsymbol{M} \otimes \boldsymbol{M}) + (\boldsymbol{M} \otimes \boldsymbol{M}) \cdot \mathbf{C}. \tag{2.110b}$$

Finally, equations (2.108) and (2.109) can be rewritten with respect to the invariants :

$$\begin{cases} \mathbf{S} = 2[W_1 I + W_2(I_1\mathbf{I} - \mathbf{C}) + W_3 I_3 \mathbf{C}^{-1} + W_4 \boldsymbol{M} \otimes \boldsymbol{M} \\ \qquad\qquad + W_5(\mathbf{C} \cdot (\boldsymbol{M} \otimes \boldsymbol{M}) + (\boldsymbol{M} \otimes \boldsymbol{M}) \cdot \mathbf{C})] \\ \boldsymbol{\sigma} = 2J^{-1}[W_1\mathbf{b} + W_2(I_1\mathbf{b} - \mathbf{b}^2) + W_3 I_3 \mathbf{I} + W_4 \boldsymbol{m} \otimes \boldsymbol{m} \\ \qquad\qquad + W_5(\boldsymbol{m} \otimes \mathbf{b} \cdot \boldsymbol{m} + \mathbf{b} \cdot \boldsymbol{m} \otimes \boldsymbol{m})] \end{cases} \tag{2.111}$$

where $W_i = \dfrac{\partial W}{\partial I_i}$ for $i = \{1, 2, \ldots, 5\}$.

The material elasticity tensor $\mathbb{C} = 2\partial\mathbf{S}/\partial\mathbf{C} = 4\partial^2 W/\partial\mathbf{C}^2$ is obtained from

$$\mathbb{C} = 4\sum_{\substack{i=1\\j=1}}^{5} \frac{\partial^2 W}{\partial I_i \partial I_j} \frac{\partial I_i}{\partial \mathbf{C}} \otimes \frac{\partial I_j}{\partial \mathbf{C}}. \tag{2.112}$$

Using the decoupled form of the elastic strain–energy function from (2.37), equation (2.106) is simply rewritten as

$$W = W(\mathbf{C}, \boldsymbol{M} \otimes \boldsymbol{M}) = W_{vol}(J) + W_{iso}(\bar{I}_1, \bar{I}_2, \bar{I}_4, \bar{I}_5), \tag{2.113}$$

where $\bar{I}_i$ are obtained by replacing $\mathbf{C}$ by $\bar{\mathbf{C}}$ in (2.107b). Thus, respectively from equations (2.108) and (2.109) we obtain

$$\mathbf{S_{iso}} = 2\frac{\partial W_{iso}}{\partial \mathbf{C}} = 2\left[\sum_{\substack{i=1\\i\neq 3}}^{5} \frac{\partial W_{iso}}{\partial \bar{I}_i} \frac{\partial \bar{I}_i}{\partial \bar{\mathbf{C}}}\right] : \frac{\partial \bar{\mathbf{C}}}{\partial \mathbf{C}}, \tag{2.114}$$

and

$$\boldsymbol{\sigma}_{\mathbf{iso}} = 2J^{-1}\bar{\mathbf{F}} \cdot \left[\left(\sum_{\substack{i=1\\i\neq 3}}^{5} \frac{\partial W_{iso}}{\partial \bar{I}_i} \frac{\partial \bar{I}_i}{\partial \bar{\mathbf{C}}}\right) : \frac{\partial \bar{\mathbf{C}}}{\partial \mathbf{C}}\right] \cdot \bar{\mathbf{F}}^T, \tag{2.115}$$

with $\partial\bar{\mathbf{C}}/\partial\mathbf{C} = J^{-\frac{2}{3}}\left(\mathbb{I} - \frac{1}{3}\bar{\mathbf{C}} \otimes \bar{\mathbf{C}}^{-1}\right)$. $\mathbf{S_{vol}}$ and $\boldsymbol{\sigma}_{\mathbf{vol}}$ are respectively obtained with equations (2.39) and (2.41). According to Holzapfel [2006b], the isochoric and volumetric parts $\mathbb{C}_{\mathbb{iso}} = 2\partial\mathbf{S_{iso}}/\partial\mathbf{C}$ and $\mathbb{C}_{\mathbb{vol}} = 2\partial\mathbf{S_{vol}}/\partial\mathbf{C}$ of the material elasticity tensor are

$$\begin{aligned}\mathbb{C}_{\mathbb{iso}} = \mathbb{P} : \bar{\mathbb{C}} : \mathbb{P}^T - \frac{2}{3}\Bigg[J^{-\frac{2}{3}}(\bar{\mathbf{S}} : \mathbf{C})\left(\frac{\partial \mathbf{C}^{-1}}{\partial \mathbf{C}} + \frac{1}{3}\mathbf{C}^{-1} \otimes \mathbf{C}^{-1}\right)\\ + \mathbf{C}^{-1} \otimes \mathbf{S_{iso}} + \mathbf{S_{iso}} \otimes \mathbf{C}^{-1}\Bigg],\end{aligned} \tag{2.116a}$$

$$\mathbb{C}_{\mathbb{vol}} = 2\mathbf{C}^{-1} \otimes \left(p\frac{\partial J}{\partial \mathbf{C}} + J\frac{\partial p}{\partial \mathbf{C}}\right) + 2Jp\frac{\partial \mathbf{C}^{-1}}{\partial \mathbf{C}}, \tag{2.116b}$$

with

$$\bar{\mathbf{S}} = 2\sum_{\substack{i=1\\i\neq 3}}^{5} \frac{\partial W_{iso}}{\partial \bar{I}_i} \frac{\partial \bar{I}_i}{\partial \bar{\mathbf{C}}} \quad \text{and} \quad \bar{\mathbb{C}} = 4J^{-\frac{4}{3}} \sum_{\substack{i,j=1\\i,j\neq 3}}^{5} \frac{\partial^2 W_{iso}}{\partial \bar{I}_i \partial \bar{I}_j} \frac{\partial \bar{I}_i}{\partial \bar{\mathbf{C}}} \otimes \frac{\partial \bar{I}_j}{\partial \bar{\mathbf{C}}}. \tag{2.117}$$

Finally the spatial elasticity tensors $\mathbb{c}_{\mathbb{iso}}$ and $\mathbb{c}_{\mathbb{vol}}$ result from equations (2.42) using (2.115) and (2.117). One can refer to Weiss et al. [1995] for further details. In the following, three strain energy functions from the literature were selected and implemented.

Weisbecker (AI model)

The material model introduced in Weisbecker et al. [2015] is a structurally motivated constitutive law that captures three different scales : a single collagen fiber, a bundle of collagen fibers and the collagen network within the tissue. It belongs to the family of AI models. As the collagen fibers are crimped in the reference configuration, they do not carry load until they are stretched. Thus, when a fiber is uncrimped, one can say that it becomes active and contributes to the strain–energy function. The potential W_{iso}^{fi} of a fiber is defined as

$$W_{iso}^{fi} = \frac{c_f}{2}\left(\bar{\lambda} - \lambda_r\right)^2, \tag{2.118}$$

where $\bar{\lambda} = \sqrt{\bar{\boldsymbol{C}} : \boldsymbol{N} \otimes \boldsymbol{N}}$ and λ_r are respectively the stretch and the recruitment stretch of a particular fiber. c_f is a material parameter. When $\bar{\lambda} < \lambda_r$ the fibers are crimped or in compression and c_f is set to zero. Considering a bundle composed of several fibers with varying waviness, a probability density function for the recruitment stretch ρ_r is used. The potential W_{iso}^{b} of a bundle of fibers is then defined as

$$W_{iso}^{b} = \int_1^{\bar{\lambda}} \rho_r(\lambda_r) W_{iso}^{fi}(\bar{\lambda}, \lambda_r) \mathrm{d}\lambda_r \tag{2.119}$$

with

$$\rho_r(\lambda_r) = \frac{(\lambda_r - \lambda_1)^{a_1 - 1}(\lambda_2 - \lambda_r)^{a_2 - 1}}{\beta(a_1, a_2)(\lambda_2 - \lambda_1)^{a_1 + a_2 - 1}}. \tag{2.120}$$

ρ_r is a modified beta distribution, where $\beta(a_1, a_2)$ is a beta function and a_1 and a_2 are shape parameters whose values allow to take into account symmetric and non–symmetric distributions (fig. 2.8). Equation (2.120) is defined on the interval $\lambda_1 \leq \lambda_r \leq \lambda_2$, where λ_1 and λ_2 are the stretches at which respectively the first and the last fibers are recruited. Parameters a_1, a_2, λ_1 and λ_2 must be experimentally determined or identified using an inverse approach.

Assuming a biphasic material with only collagen and elastin, the total strain–energy for the collagen fibers per unit of reference volume is

$$W_{iso}^{f} = \nu \int_\Omega \rho(\boldsymbol{N}) W_{iso}^{b}(\bar{\lambda}) \mathrm{d}\Omega, \tag{2.121}$$

where ν is the volume fraction of the fiber bundles and $\rho(\boldsymbol{N})$ is the orientation distribution function in the direction $\boldsymbol{N}$. A suitable function to describe the orientation distribution $\rho(\boldsymbol{N})$ is the von Mises distribution also used in Gasser et al. [2006] and Federico et al. [2010] for instance. Furthermore, for a transversely isotropic probability distribution with respect to $\boldsymbol{M}$, $\rho(\boldsymbol{N}(\theta, \phi))$ simplifies into $\rho(\theta)$. The normalized (2.102) and π–periodic

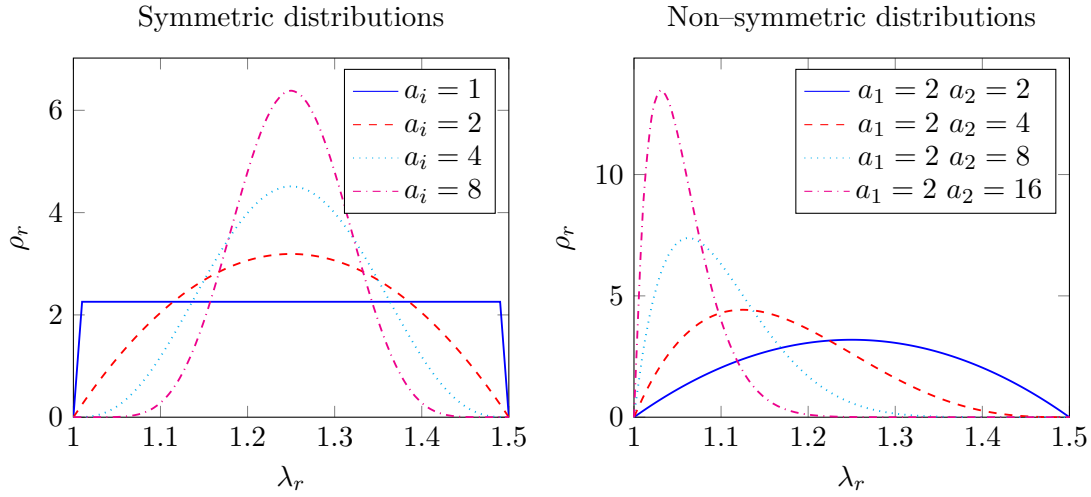

Fig. 2.8 – Examples of probability density functions ρ_r for $1 < \lambda_r < 1.5$

von Mises distribution centered at $\theta = 0$ is

$$\rho(\theta) = 4\sqrt{\frac{b}{2\pi}}\frac{\mathrm{e}^{b(\cos(2\theta)+1)}}{\mathrm{erfi}(\sqrt{2b})}, \tag{2.122}$$

where $b \in]0, \infty[$ is the concentration parameter, and $\mathrm{erfi}(x) = -i\ \mathrm{erf}(ix)$ denotes the imaginary error function at x, with the error function erf defined as

$$\mathrm{erf}(x) = \frac{2}{\sqrt{\pi}}\int_0^x \mathrm{e}^{-t^2}\mathrm{d}t. \tag{2.123}$$

Notice that $b \longrightarrow 0$ represents isotropy with fibers equally distributed in all directions and $b \longrightarrow \infty$ describes fibers all aligned in one direction. Following the additive decomposition of the strain–energy function into a (neo–Hookean) matrix contribution and a fibers contribution, the material strain–energy function W_{iso} becomes

$$W_{iso} = (1-\nu)c_g(\bar{I}_1 - 3) + \nu\int_\Omega \rho(\boldsymbol{N})W^b_{iso}(\bar{\lambda})\mathrm{d}\Omega, \tag{2.124}$$

where $c_g = \dfrac{\mu_g}{2}$ is the groundmatrix material parameter (μ_g is the matrix bulk modulus). See appendix B for further details. Finally, adding the volumetric strain energy function from subsection 2.3.5, the total strain–energy function is $W = W_{iso} + \dfrac{\tau}{2}(J-1)^2$.

From an implementation point of view, integrals of a function f on the interval $[a, b]$ are evaluated using a trapezoidal rule

$$\int_a^b f(x)\mathrm{d}x \approx \frac{b-a}{n}\left[\frac{f(a)+f(b)}{2} + \sum_{k=1}^{n-1} f\left(a + k\frac{b-a}{n}\right)\right], \tag{2.125}$$

with n the number of intervals determined recursively. To solve integrals over the unit sphere surface $\mathbb{S}^2$, an efficient method suggested in Weisbecker et al. [2015] and initially proposed in Bazant et al. [1986] was used. In this method, the integral of a tensor–valued function $\mathbf{A}(\boldsymbol{N})$ is approximated with the formula

$$\int_{\mathbb{S}^2} \mathbf{A}(\boldsymbol{N}) \mathrm{d}S \approx 4\pi \sum_{k=1}^{n} \mathbf{A}(\boldsymbol{N_k}) q_k, \tag{2.126}$$

where $\boldsymbol{N_k}$ are vectors in specific directions of the sphere and q_k their associated integration weights, with $k = \{1, \ldots, n\}$. Choosing $n = 42$, only 21 weights are required due to the symmetry of the integration scheme multiplying the weights by two. Values of $\boldsymbol{N_k}$ and q_k can be found in Bazant et al. [1986]. The beta function is computed using Stirling's approximation given by the formula

$$\beta(a_1, a_2) \approx \sqrt{2\pi} \frac{a_1^{a_1 - \frac{1}{2}} a_2^{a_2 - \frac{1}{2}}}{(a_1 + a_2)^{a_1 + a_2 - \frac{1}{2}}}, \tag{2.127}$$

and the imaginary error function with the locals power series developments at 0,

$$\operatorname{erfi}(x) = \frac{2}{\sqrt{\pi}} \left(x + \frac{x^3}{3} + \frac{x^5}{10} + \frac{x^7}{42} + \frac{x^9}{216} + O(x^{11}) \right), \tag{2.128}$$

and at ∞,

$$\operatorname{erfi}(x) = \frac{\mathrm{e}^{x^2}}{\sqrt{\pi}} \left(x^{-1} + \frac{1}{2} x^{-3} + \frac{3}{4} x^{-5} + \frac{15}{8} x^{-7} + \frac{105}{16} x^{-9} + O(x^{-11}) \right). \tag{2.129}$$

The algorithm is illustrated in alg. 1.

Algorithm 1 FE implementation of the Weisbecker model

procedure WEISBECKER($\boldsymbol{M}$, $\bar{\mathbf{F}}$, c_g, c_f, ν, b)
  $\tilde{\mathbf{S}}_{\mathbf{iso}} \leftarrow$ initialization
  $\tilde{\mathbb{C}}_{\mathbb{iso}} \leftarrow$ initialization
  load spherical design $\boldsymbol{N_k}$ with $k = \{1, \ldots, 21\}$
  for all direction k **do**
    compute fiber direction $\boldsymbol{n_k}$
    compute isochoric stretch $\bar{\lambda}_k$
    compute angle θ_k
    if $\bar{\lambda}_k \geq \lambda_1$ **then**
      compute fiber bundle strain energy derivative $(W^b_{iso_k})'$ ▷ trapezoidal rule
      compute orientation density ρ_k
      compute stress tensor $(\tilde{\mathbf{S}}_{\mathbf{iso}})_k$ ▷ sphere integration
      compute elasticity tensor $(\tilde{\mathbb{C}}_{\mathbb{iso}})_k$ ▷ sphere integration
    $\tilde{\mathbf{S}}_{\mathbf{iso}} \leftarrow \tilde{\mathbf{S}}_{\mathbf{iso}} + (\tilde{\mathbf{S}}_{\mathbf{iso}})_k$
    $\tilde{\mathbb{C}}_{\mathbb{iso}} \leftarrow \tilde{\mathbb{C}}_{\mathbb{iso}} + (\tilde{\mathbb{C}}_{\mathbb{iso}})_k$

Holzapfel Gasser Ogden (GST model)

The Holzapfel Gasser Ogden (HGO) model was introduced first in Holzapfel, Gasser, et al. [2000] for the description of the mechanical response of arterial tissues. It was then extended to distributed fiber orientations in Gasser et al. [2006] using a GST formulation. This is a transversely isotropic model defined in terms of the invariants $\bar{I}_1$ and $\bar{I}_4$ and its strain–energy function W results from the superposition of the isotropic potential W^g_{iso} of the non–collagenous groundmatrix and the transversely isotropic potential W^f_{iso} of the embedded collagen fibers. Hence,

$$W_{iso} = W^g_{iso} + W^f_{iso} \tag{2.130}$$

and from subsection 2.3.5

$$W = W_{iso} + \frac{\tau}{2}(J-1)^2 \tag{2.131}$$

with $\tau \longrightarrow \infty$ for an incompressible material. The non–collagenous groundmatrix is modeled by mean of an incompressible neo–Hookean model $W^g_{iso} = c_0(I_1 - 3)$, with $c_0 = \dfrac{\mu_g}{2}$ where μ_g is the bulk modulus of the groundmatrix. For the fibers contribution, Gasser et al. [2006] replaced the classical structure tensor $\boldsymbol{M} \otimes \boldsymbol{M}$ of the HGO model [Holzapfel, Gasser, et al. 2000] by the generalized structure tensor (2.105). Thus, $\bar{I}_4 - 1 = \boldsymbol{M} \otimes \boldsymbol{M} : \bar{\mathbf{C}} - 1$ becomes $\mathbf{H} : \bar{\mathbf{C}} - 1$, which characterize the strain of the fibers in the principal orientation $\boldsymbol{M}$:

$$W^f_{iso} = \frac{c_1}{2c_2}\left[\mathrm{e}^{c_2\left(\kappa\bar{I}_1 + (1-3\kappa)\bar{I}_4 - 1\right)^2} - 1\right]. \tag{2.132}$$

Finally, the isochoric contribution of the strain–energy function is

$$W_{iso} = c_0(\bar{I}_1 - 3) + \frac{c_1}{2c_2}\left[\mathrm{e}^{c_2\left(\kappa\bar{I}_1 + (1-3\kappa)\bar{I}_4 - 1\right)^2} - 1\right], \tag{2.133}$$

where c_i with $i = \{0, 1, 2\}$ are positive material parameters and $\kappa \in \left[0, \dfrac{1}{3}\right]$ is the fiber structure dispersion parameter as defined in Gasser et al. [2006], to be obtained from experimental data. In the transversely isotropic case,

$$\kappa = \frac{1}{4}\int_0^{\pi} \rho(\theta)\sin^3(\theta)\mathrm{d}\theta \tag{2.134}$$

where $\rho(\theta)$ is the same normalized π–periodic von Mises distribution as defined previously (2.122). Using equations (2.134) and (2.122) and the trigonometric function $\cos(2\theta) = 1 - 2\sin^2(\theta)$, we obtain the relation between κ and b

$$\kappa = \sqrt{\frac{b}{2\pi}} \frac{\mathrm{e}^{2b}}{\mathrm{erfi}(\sqrt{2b})} \int_0^{\pi} \mathrm{e}^{-2b\sin^2(\theta)} \sin^3(\theta) \mathrm{d}\theta$$
$$= \frac{1}{2} + \frac{1}{8b} - \frac{1}{4b}\sqrt{\frac{2b}{\pi}} \frac{\mathrm{e}^{2b}}{\mathrm{erfi}(\sqrt{2b})}. \tag{2.135}$$

The relation between the dispersion and the concentration parameters is plotted on fig. 2.9.

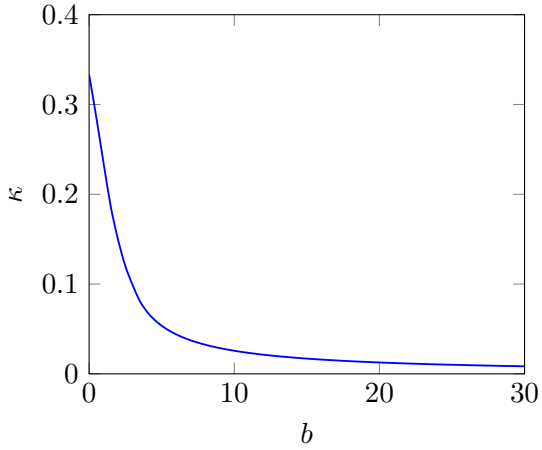

Fig. 2.9 – Relation between κ and b according to equation (2.135)

Notice that $\kappa = 1/3$ corresponds to isotropy (*i.e.* $b \longrightarrow 0$) with fibers equally distributed in all directions and $\kappa = 0$ corresponds to the case where fibers are all aligned in one direction (*i.e.* $b \longrightarrow \infty$). Representations of fibers orientations and fibers distributions are respectively shown on fig. 2.10 and fig. 2.11 for several κ values.

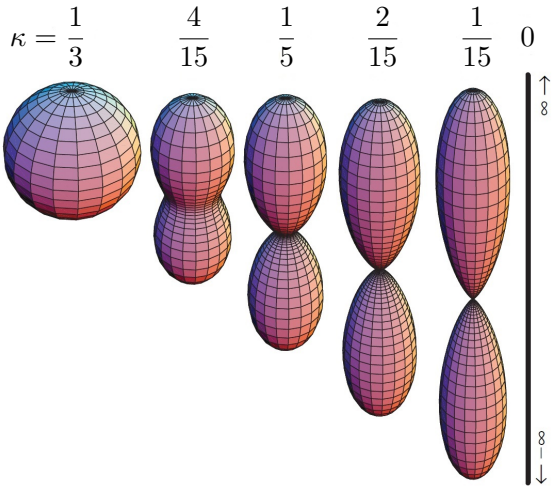

Fig. 2.10 – Three–dimensional graphical representation of the collagen fibers orientation for several κ values [Gasser et al. 2006]

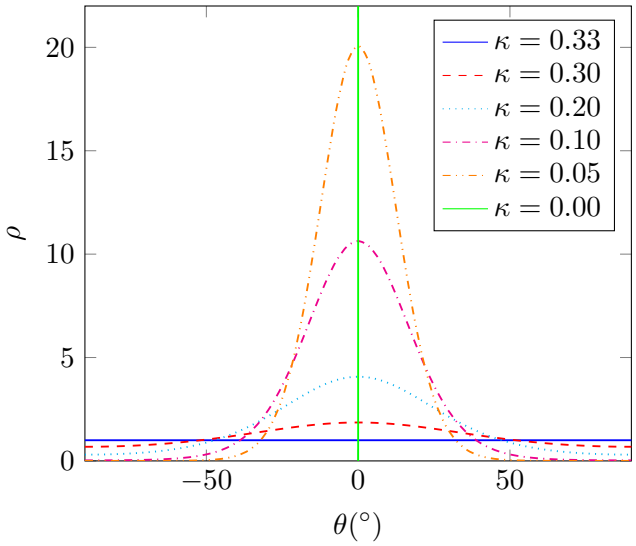

Fig. 2.11 – Two–dimensional representation of the distribution $\rho(\theta)$ of the collagen fibers for several κ values

From the physically and numerically (stability) motivated assumption that collagen fibers cannot support any compressive load, the anisotropic part contributes only if the strain in the direction $\boldsymbol{M}$ is positive *i.e.* $\mathbf{H} : \bar{\mathbf{C}} > 1$. Otherwise, the parameter c_1 is set to zero.

Using above equations, the spatial stress and elasticity tensors can be computed using an efficient FE implementation. One can refer to appendix B for further details.

Modified Holzapfel Gasser Ogden (GST model)

A slightly modified transversely isotropic HGO model was also implemented. The neo–Hookean matrix potential W_{iso}^{g} was remplaced by Fung type exponential strain–energy function in order to better capture high non–linearity groundmatrix behavior. Thus,

$$W_{iso}^{g} = \frac{c_0}{c_1}\left[\mathrm{e}^{c_1(\bar{I}_1-3)} - 1\right] \tag{2.136}$$

and

$$W_{iso} = \frac{c_0}{c_1}\left[\mathrm{e}^{c_1(\bar{I}_1-3)} - 1\right] + \frac{c_2}{2c_3}\left[\mathrm{e}^{c_3\left(\kappa\bar{I}_1+(1-3\kappa)\bar{I}_4-1\right)^2} - 1\right] \tag{2.137}$$

where c_i with $i = \{0, \ldots, 3\}$ are positive material parameters and $\kappa \in \left[0, \frac{1}{3}\right]$ is the fiber structure dispersion parameter like for the HGO model presented above. This constitutive law was for example used in Wang et al. [2014] for the modeling of the human left ventricle in diastole. One can refer to appendix B for further details.

2.5.3 Polyconvexity

Polyconvexity, in the sense of Ball [Ball 1976], is a very important concept for hyperelastic constitutive models in order to guarantee the existence of minimizers of the potential (while strict convexity implies the existence of an unique global minimum). In other words, polyconvexity of a strain–energy function implies material stability. A vast literature exists on polyconvexity. For definitions and several important results on polyconvexity for hyperelastic anisotropy, see for instance Balzani et al. [2006], Schröder, P. Neff, et al. [2005], Schröder and Patrizio Neff [2003], Itskov et al. [2004], and Hartmann et al. [2003] for nearly–incompressibility. One can also refer to the work of Ebbing [Edding 2010] on the design of polyconvex energy functions for anisotropic materials for definitions and remarks about the generalized convexity conditions. However, a general proof of convexity for AI and GST approaches in the case of complex orientation distributions remains to be provided.

2.5.4 Fibers orientation

Principal collagen fibers orientations are assumed to be correlated with the models macroscopic directions of anisotropy. In order to reproduce the planar tissue network in the FE model, a vector anisotropy $\boldsymbol{M}$ has to be defined on each element from experimental measurements of a locally averaged collagen orientations. Confocal laser scanning microscope images of the collagen fibers in the fibrosa layer were used to identify this local preferred orientation as well as the local fiber distribution parameter (chapter 1). Since the material is assumed locally transversely isotropic, only one direction of anisotropy oriented in the focal plan, and one fiber distribution parameter, were identified for each picture. The confocal measurements were firstly pre–treated to be projected on a 3D FE mesh as initial (*i.e.* unloaded) fiber configuration as shown on fig. 2.12.

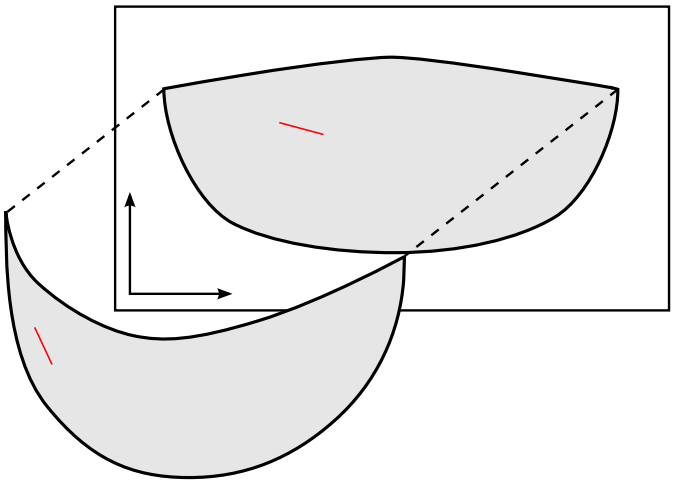

Fig. 2.12 – Illustration of the projection of a fiber direction (in red) from a 2D measurement to a 3D geometry

Knowing the image planar coordinates from a reference point of the sample, anisotropy directions and fiber distribution parameters are interpolated and extrapolated on a fine regular grid. A cubic polynomial function was used for the interpolation while the extrapolation, if required, was linear. To easily link the sample to the model geometry, the coordinates of the interpolation grid points are normalized between 0 and 1 taking the reference point as origin.

A Dijkstra's algorithm was implemented in order to compute the minimum distance between the reference element (corresponding to the reference point of the sample) and all other elements barycenter by finding the shortest paths on the FE mesh. The element barycenter $\mathbf{\Gamma}$ is defined as

$$\mathbf{\Gamma} = \frac{1}{\mathrm{NbNo}} \sum_{i}^{\mathrm{NbNo}} \boldsymbol{x}_i. \tag{2.138}$$

where NbNo is the number of nodes of an element. In order to use the Dijkstra's algorithm, the table of neighbors was built considering element's faces (*i.e.* maximum of four neighbors per element). Knowing the neighborhood of each element, the mesh can be seen as a graph where the elements barycenter are nodes. Hence, the minimum distance was computed on the mesh, through the other elements in order to give not a real but a relative value of the distance (fig. 2.13).

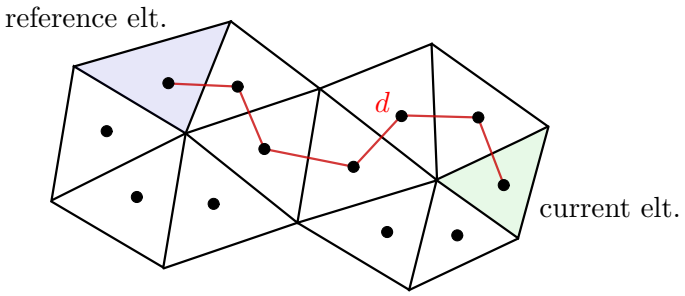

Fig. 2.13 – Illustration of the Djikstra's algorithm on a 2D mesh to compute a minimum distance d between the reference and current elements

The geometry, is then virtually "unfolded" in order to project elements' barycenter coordinates into a plan. In other words, for each element the computed distance is virtually stretched into a plane defined by two vectors, a predefined vector of the Cartesian coordinate system and the vector from the reference element to the current element. The projection is made along the latter direction (fig. 2.14). Hence, coordinates corresponding to elements' barycenter are obtained in a plane. These coordinates were normalized with respect to the reference element in order to be linked with the geometrically closest experimental interpolated grid values. Note that the geometry has to be open.

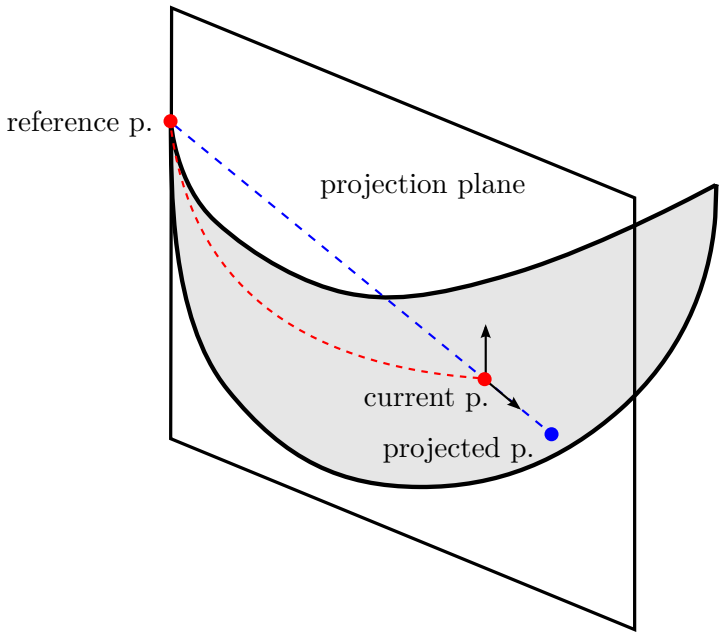

Fig. 2.14 – Illustration of the projection method from a 3D geometry into a plane

Finally, a rotation was applied to the anisotropy vectors defined on the elements to make them perpendicular to the closest outward normal surface vector. Thus, fibers vectors and fibers distribution parameters in the unloaded configuration obtained from confocal microscope images are reproduced on the FE model. A brief summary of the finite element algorithm is illustrated in alg. 2.

Algorithm 2 Initial anisotropy directions from experimental data

```
procedure ORIENT(reference element, experimental normalized grid)
    initialization
    build elements neighbors table
    for all element do
        compute element barycenter
        compute shortest distance between element barycenter and reference element
                                                          ▷ Dijkstra's algorithm
        store distance
    build planar grid from elements barycenter 3D coordinates
    normalize FE grid coordinates
    link FE and experimental normalized grids
    for all element do
        interpolate closest experimental value and FE grid
        find element closest outward normal vector from surface geometry
        compute rotation matrix
        rotate anisotropy vector in the tissue plan
```

2.6 Solver validation

In this section the convergence and stability of the hyperelastic solver is discussed, as well as the accuracy of the material models implementation.

2.6.1 Convergence and stability

Pressure field

In order to make sure that the bubble is correctly implemented ensuring a stable element, a compression test was performed on FORGE®. It has been observed that compression loadings are more subjected to numerical instabilities in case of incompatible elements. A deformable cube with a length of 10 mm was modeled using 0.5 mm structured tetrahedral mesh. A pressure of 1 kPa along the vertical direction was applied on a 5 mm × 5 mm area at the center of the deformable body (fig. 2.15). Both incompressible and quasi–incompressible formulations were used with a neo–Hookean material model. The material parameter was set to $c_0 = 100$ kPa. In the quasi–incompressible case, the fictive Young's modulus was defined following $E = 4c_0(1 + \upsilon)$ and the fictive Poisson's ratio was set to $\upsilon = 0.4995$. On fig. 2.16, a comparison of the pressure field in the quasi–incompressible case for both non–stabilized ($P1/P1$) and stabilized ($P1^+/P1$) elements is shown. It clearly appears that the $P1/P1$ element presents a noisy pressure field accountable to non–consistent interpolation while it is significantly smoother for the $P1^+/P1$ element. This phenomenon is highlighted in the fully incompressible case with non–stabilized elements while it is very similar to the quasi–incompressible case using MINI–elements (fig. 2.17). Thus, the bubble formulation proposed in section 2.4 is suitable for dealing with incompressibility and quasi–incompressibility using linear tetrahedral elements.

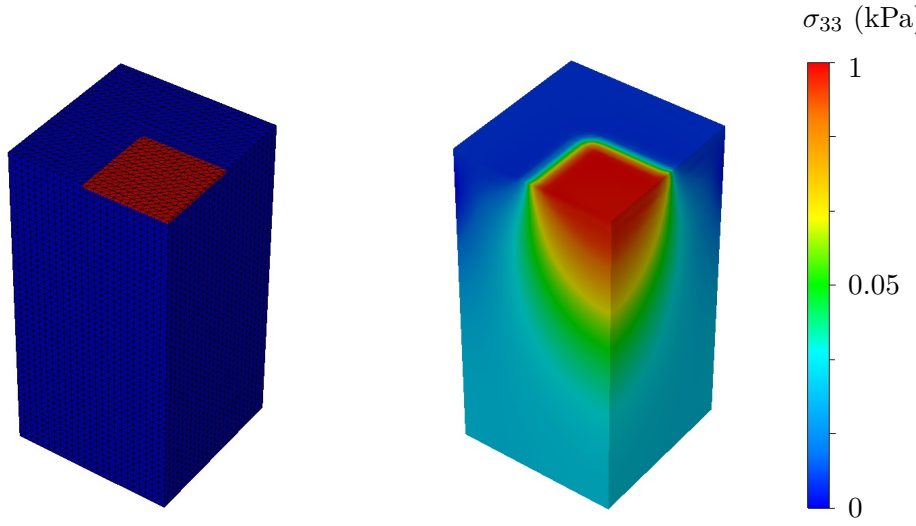

(a) σ_{33} boundary condition area in red **(b)** σ_{33} field

Fig. 2.15 – Pressure applied on one–fourth of the geometry

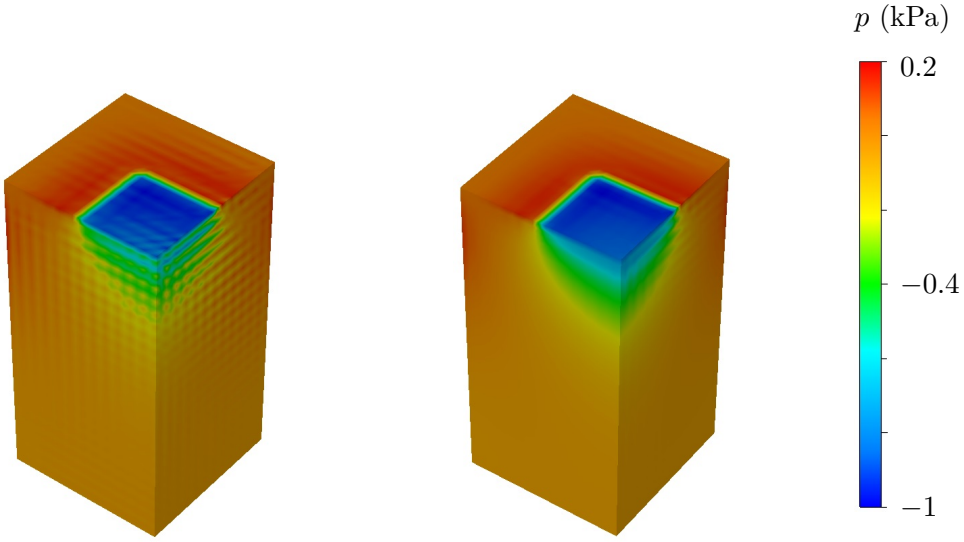

(a) No stabilization **(b)** Bubble stabilization

Fig. 2.16 – Pressure field in the quasi–incompressible case without and with stabilization

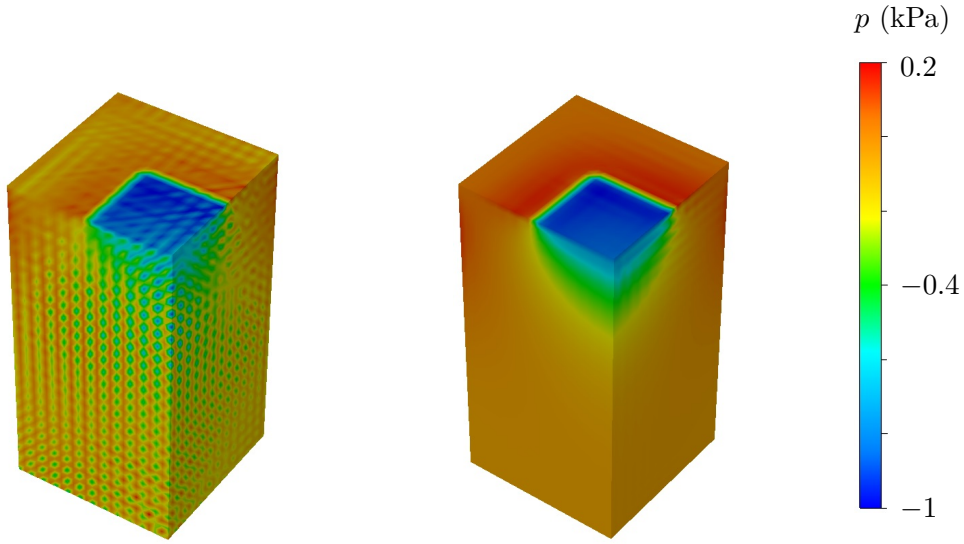

(a) No stabilization **(b)** Bubble stabilization

Fig. 2.17 – Pressure field in the incompressible case without and with stabilization

Volume conservation

The volume conservation accuracy of the implemented formulation was checked in both incompressibility and quasi–incompressibility cases. Similar geometry and material parameters as presented above were used. In this example, the geometry was submitted to a compression loading with a compression ratio ranging from 0 to 80%. On fig. 2.18 is shown the evolution of the normalized volume during the compression. The volume is perfectly preserved in the case of the fully incompressible formulation, while a slight but

expected loss is observed with the quasi–incompressible formulation.

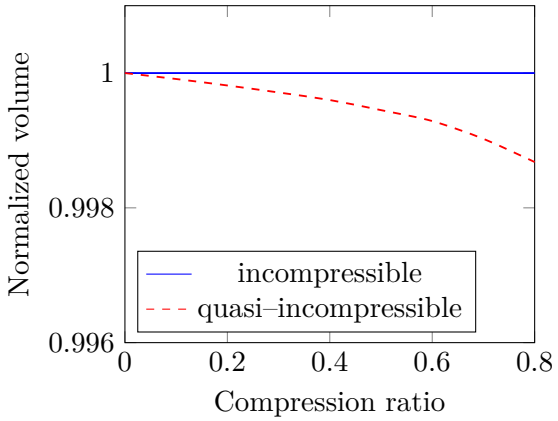

Fig. 2.18 – Evolution of the normalized volume with compression in incompressible and quasi–incompressible formulations

2.6.2 Models implementation

Validation on isotropic cases

The models implementation was validated on isotropic analytic cases. Results are presented on fig. 2.19a and fig. 2.19b. Like before, a 10 mm width cube geometry with a 0.5 mm structured tetrahedral mesh was used.

On these figures, the uniaxial tension in the direction E_3 until 400% stretch is respectively shown for a neo–Hookean model with $c_0 = 100$ kPa (isotropic part of HGO and Weisbecker models) and a Fung–Demiray model with $c_0 = 10$ kPa and $c_1 = 0.1$ (isotropic part of the modified HGO model). In both cases the material was considered as fully incompressible.

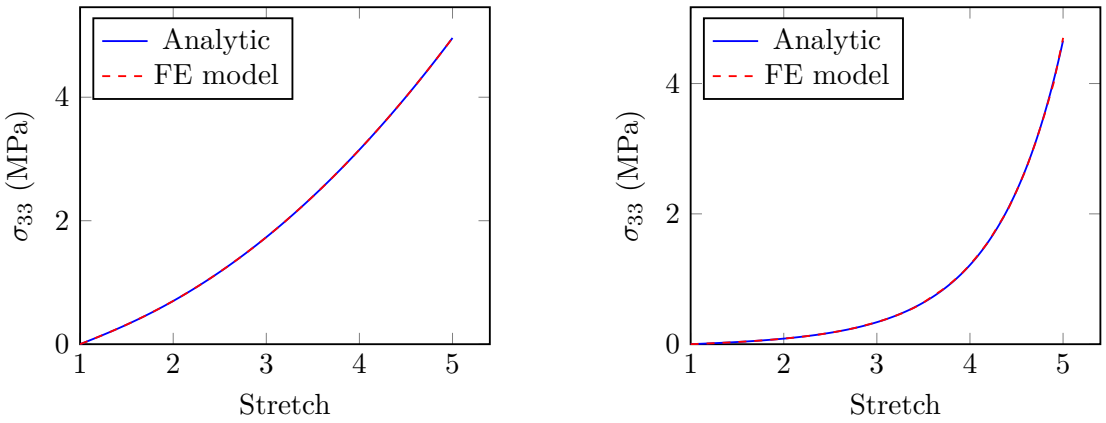

(a) Neo–Hookean model validation

(b) Fung–Demiray model validation

Fig. 2.19 – Isotropic models validation on uniaxial tension tests

For the neo–Hookean model the analytic equation of the stress along E_3 is given by

$$\sigma_{33} = 2c_0 \left(\lambda^2 - \frac{1}{\lambda}\right), \tag{2.139}$$

and for the Fung–Demiray model by

$$\sigma_{33} = 2c_0 \left(\lambda^2 - \frac{1}{\lambda}\right) \mathrm{e}^{c_1\left(\frac{2}{\lambda}+\lambda^2-3\right)}, \tag{2.140}$$

where $\lambda = 1 + \dfrac{\Delta l}{l_0}$ with $l_0 = 10$ mm. A perfect agreement was found between the FE implementation and the analytical results.

Anisotropy

To illustrate the anisotropy effect of the fibers, an inflation test of a spherical balloon with circumferentially arranged fibers subjected to an internal pressure was performed (fig. 2.20). The pressure evolves linearly from 0 to 0.1 kPa. Since the problem is axisymmetric, one–eighth of the structure was modeled and mirror symmetries were used. The sphere has a radius of 10 mm and a thickness of 0.5 mm. A 0.25 mm unstructured mesh was used. In the following example, an HGO material model was used with $c_0 = 1$ kPa, $c_1 = 10$ kPa, $c_2 = 1$. Several values for the fibers dispersion parameter κ were tested, $\kappa = 0.333$ (isotropic), $\kappa = 0.2$ and $\kappa = 0$ (transversely isotropic). After inflation, the initially spherical balloon took an elongated shape for $\kappa \neq 0.333$ due to the circumferential fibers stiffness and stayed spherical for $\kappa = 0.333$ (fig. 2.21).

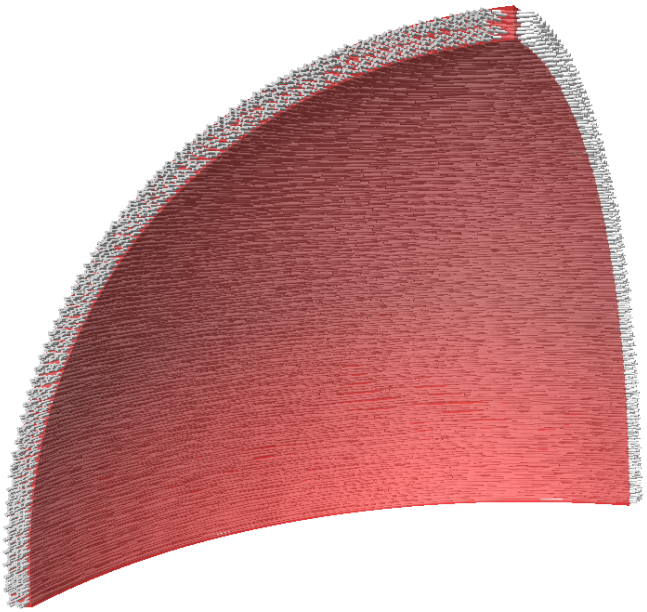

Fig. 2.20 – Circular fiber arrangement on one–eighth of a spherical balloon (arrows indicate the orientation of the fibers)

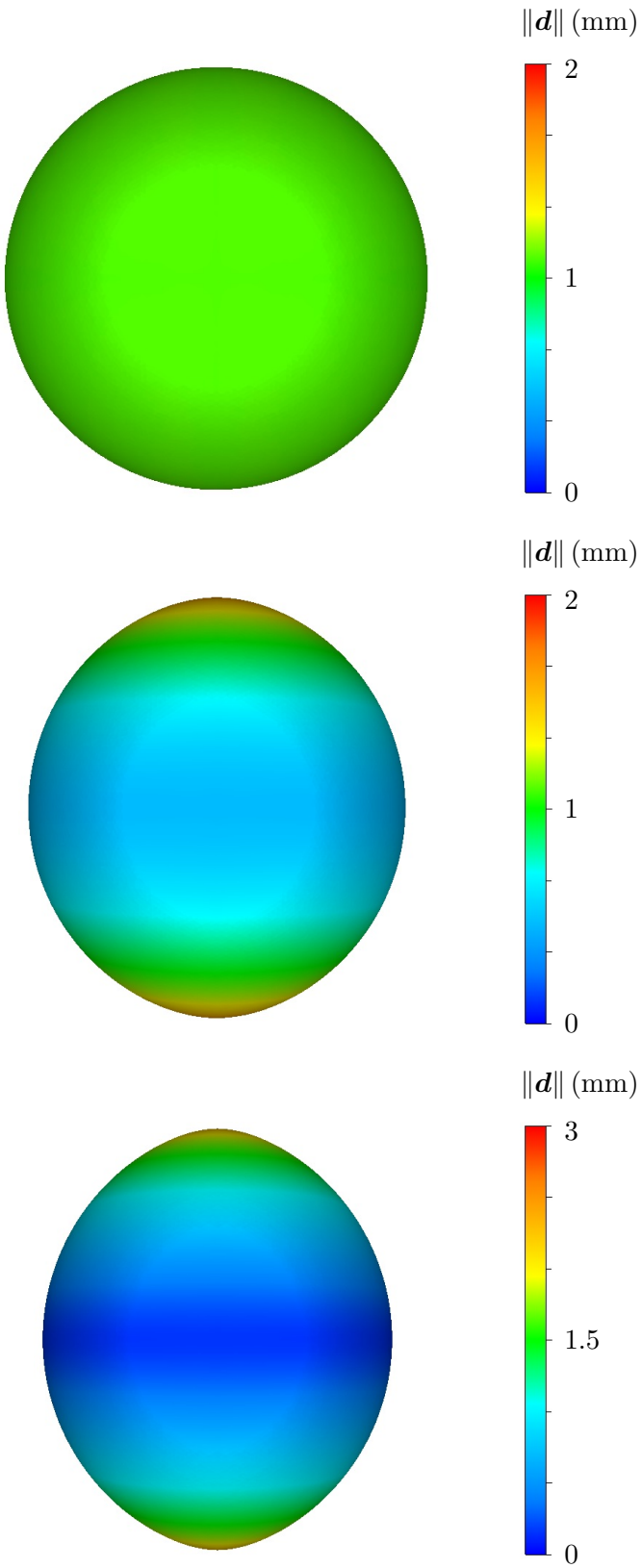

Fig. 2.21 – Inflation of the spherical balloon submitted to internal pressure with $\kappa = 0.333$, $\kappa = 0.2$ and $\kappa = 0$ from top to bottom (the norm of the displacement field $\|\boldsymbol{d}\|$ is shown)

Quasi–static energy conservation and full recovery

To check the energy conservation, the elastic springback was tested in two cases. In the first case (fig. 2.22), a normal pressure was applied at the free tip of an embedded beam (50 mm × 10 mm × 10 mm with a 1 mm structured mesh). The normal pressure evolved linearly with time from 0 to 1 kPa. When the threshold value is reached, the normal pressure is removed. In the second case (fig. 2.23), the deformation was induced by a rigid (undeformable) object assuming a free–slip contact. The indentation of a 10 mm width cube (0.5 mm structured mesh) using a spherical rigid object with a radius of 2.5 mm was modeled. The spherical object goes down to a fixed depth of 3 mm and then goes back to its initial position. In both cases, an incompressible hyperelastic neo–Hookean model with $c_0 = 100$ kPa was used. After unloading the deformed meshes return to their original shape showing that the energy is conserved. However, the remaining displacement is higher in the second case due to the large elements deformation locally induced by the sphere.

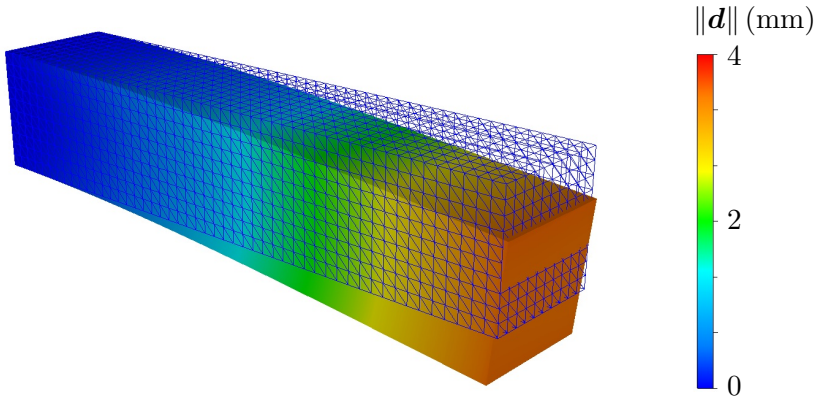

(a) Initial mesh with deformed geometry

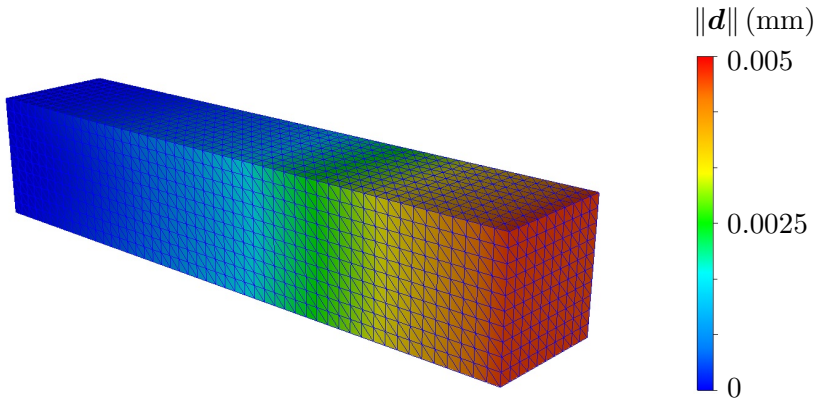

(b) Initial mesh with final geometry after elastic springback

Fig. 2.22 – Energy conservation on a bending test (the norm of the displacement field $\|\boldsymbol{d}\|$ is shown)

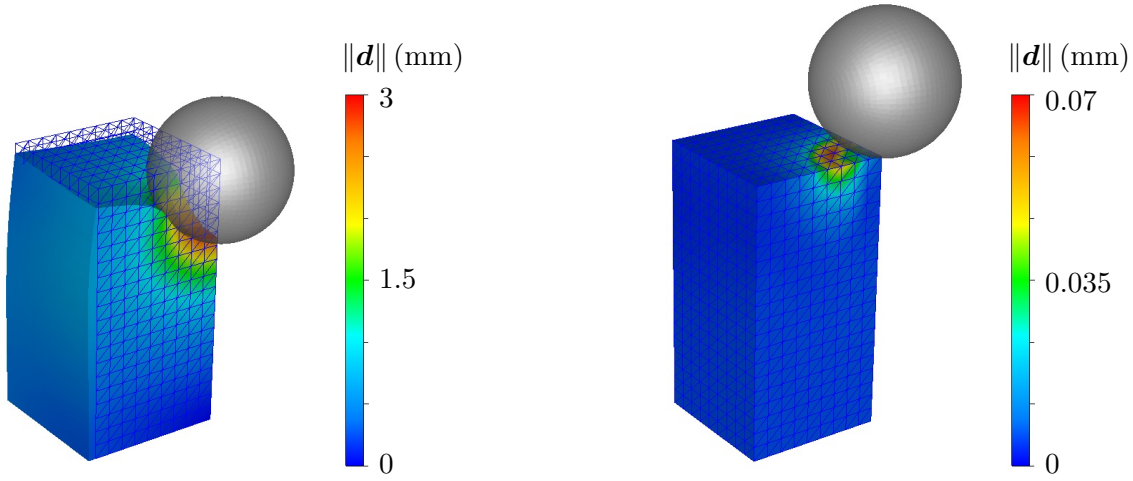

(a) Initial mesh with deformed geometry

(b) Initial mesh with final geometry after elastic springback

Fig. 2.23 – Energy conservation during an indentation test on one–fourth of the deformable cube (the norm of the displacement field $\|\boldsymbol{d}\|$ is shown)

2.6.3 Fibers orientation algorithm

Fibers orientation

The fibers orientation algorithm was tested on artificial data. A sinusoidal fibers angle distribution was used to be interpolated on a fine planar grid. The interpolated values were then projected on a planar FE mesh in the software to be used as initial fibers angle distribution (fig. 2.24). Results show a good accuracy between the interpolated and the projected orientation values. However, this accuracy directly depends on the mesh size that must be adapted to the complexity of the distribution (*i.e.* a fine mesh is required in the areas of complex fibers distribution).

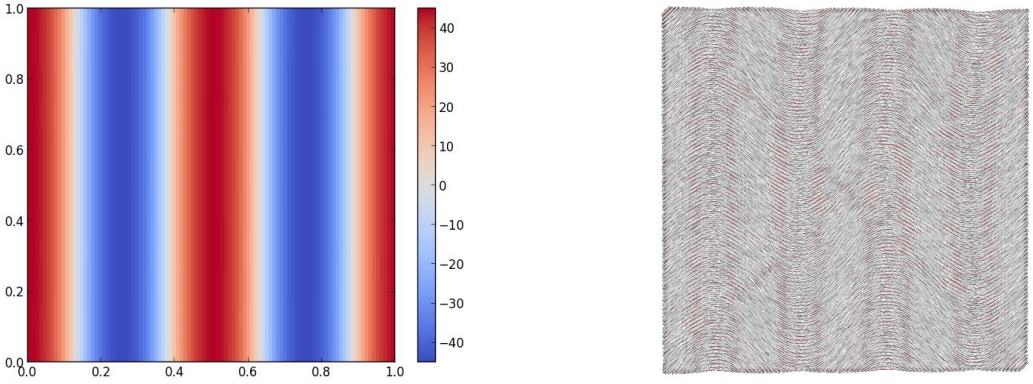

(a) Interpolation on a normalized fine grid

(b) Projection on a planar mesh

Fig. 2.24 – Example of sinusoidal θ (°) interpolation and projection corresponding to fiber orientation vectors

To qualitatively demonstrate the proper functioning of the algorithm on a complex three–dimensional geometry, the same distribution was projected on a bimaterial prosthetic aortic valve geometry (fig. 2.25). On fig. 2.25, the leaflet tissues are represented in red while the rigid support structure is in blue. Once again, a good accuracy was found.

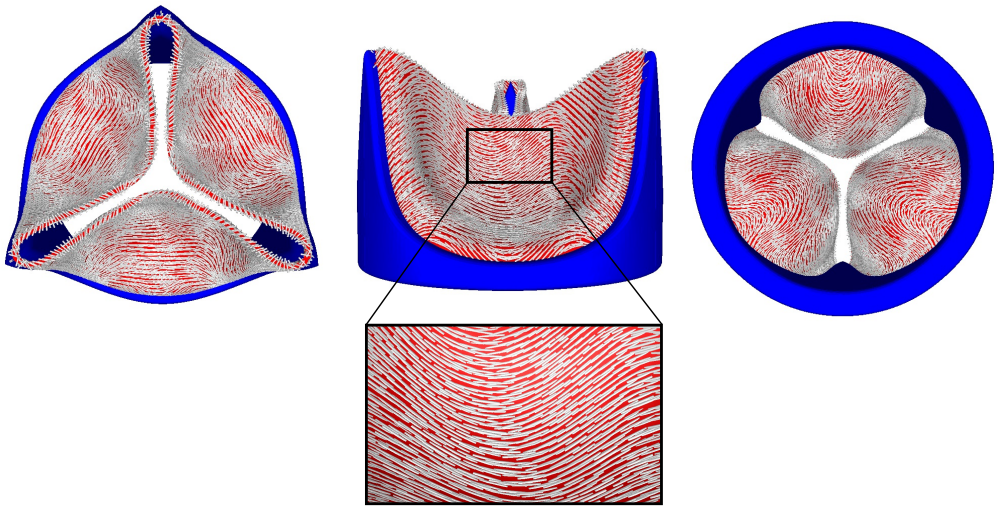

Fig. 2.25 – Orientation projection on a complex 3D geometry of prosthetic valve (from left to right : top, side and bottom views)

Fibers dispersion or concentration

As for the fibers angle distribution, fiber dispersion (or concentration) parameter interpolation and projection was checked. A random $\kappa \in \left[0, \frac{1}{3}\right]$ distribution was chosen. The projection of the interpolated random κ distribution on a planar FE mesh and on a prosthetic aortic valve geometry are respectively shown on fig. 2.26 and fig. 2.27. Similarly to above observations, results were satisfying.

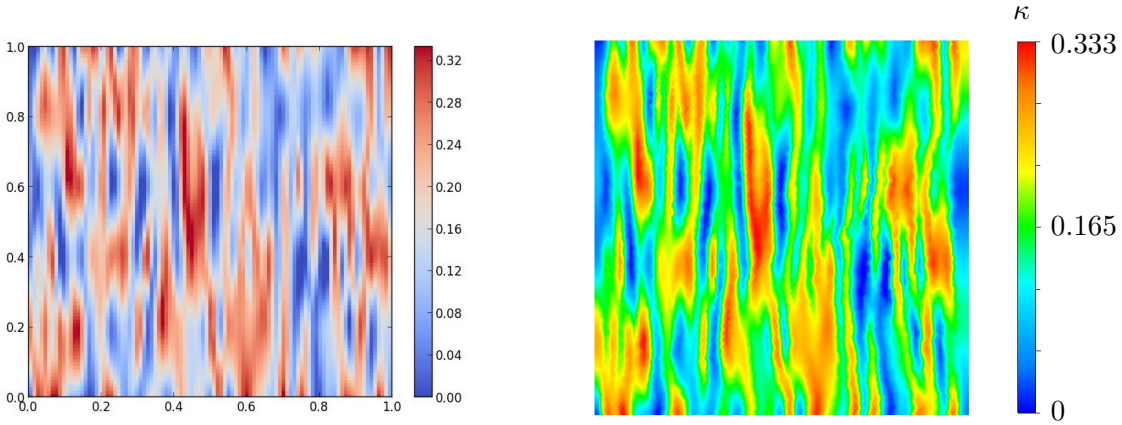

(a) Interpolation on a normalized fine grid **(b)** Projection on a planar mesh

Fig. 2.26 – Example of random κ interpolation and projection

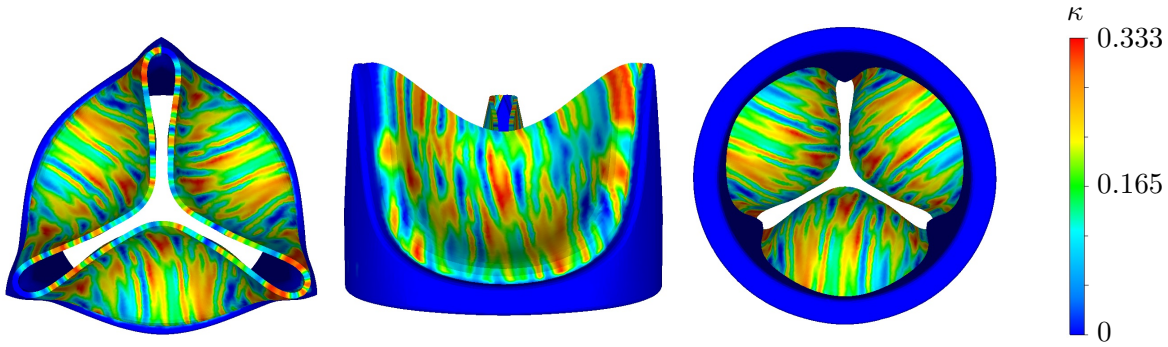

Fig. 2.27 – κ on a complex 3D geometry of prosthetic valve (from left to right : top, side and bottom views)

2.7 Summary of Chapter 2

According to the literature, mechanical tensile tests presented in chapter 1 highlighted the hyperelastic anisotropic behavior of aortic valves tissues. Hence, the modeling of such materials requires the implementation of relevant numerical methods and models. Developments were made in a custom laboratory version of the finite element software FORGE®. Due to the software constraints, an hyperelastic solver in mixed velocity–pressure formulation was implemented. The assumption of infinitesimal strains used in FORGE® was not made in this work. An updated Lagrangian method in the finite strain framework, more suitable for the modeling of soft tissues, was developed. Moreover, both incompressible and quasi–incompressible formulations were implemented. Since the software uses linear tetrahedron elements with bubble stabilization, the bubble was also adapted to the hyperelastic framework.

Three hyperelastic orthotropic material models from the literature were implemented. A phenomenological approach was chosen in order to model the tissues at the valve's scale. However, these models are able to take into account some structural information, like a local statistical fibers distribution that confer anisotropic properties to the material. Assuming that local principal fibers orientations can be correlated to the macroscopic directions of anisotropy of the models, an algorithm was developed to transpose orientations measured by confocal microscopy in the chapter 1 to a complex finite element mesh. Thus, this algorithm used at the beginning of the finite element computation allows to define an initial direction of anisotropy and a dispersion (or concentration) parameter on each element from experimental data.

Finally, the stability and accuracy of the implementation were checked through several numerical tests.

2.8 Résumé en français

Les essais mécaniques présentés dans le chapitre 1 ont montré, en accord avec la littérature, que les tissus de valves aortiques ont un comportement hyperélastique anisotrope. La modélisation numérique de tels matériaux nécessite donc le choix d'une méthode de résolution et l'implémentation de modèles de comportement adaptés. Les développements ont été réalisés dans une version laboratoire du logiciel éléments finis FORGE®. En raison de contraintes inhérentes au logiciel, un solveur hyperélastique en formulation mixte vitesse–pression a été implémenté. L'hypothèse des déformations infinitésimales utilisée dans FORGE® n'a pas été choisie pour ce travail. Une méthode Lagrangienne actualisée dans le formalisme des grandes déformations, plus adaptée à la modélisation des tissus mous, a été développée. En outre, une formulation incompressible et une formulation quasi–incompressible ont été implémentées. Le logiciel utilisant des éléments tétraédriques linéaires avec une stabilisation bulle, celle–ci a aussi été adaptée au formalisme hyperélastique.

Trois modèles de comportement hyperélastiques orthotropes de la littérature ont été implémentés. Une approche phénoménologique a été choisie de manière à pouvoir modéliser les tissus à l'échelle de la valve. Ces modèles sont néanmoins capables de prendre en compte un certain nombre d'informations structurelles, notamment une distribution statistique locale de fibres de collagène conférant son anisotropie au matériau. En supposant que les orientations préférentielles locales des fibres de collagène puissent être corrélées aux directions d'anisotropies macroscopiques des modèles, un algorithme a été développé afin de transposer les orientations mesurées par microscopie confocale dans le chapitre 1 à un maillage éléments finis de géométrie complexe. Cet algorithme utilisé au début du calcul éléments finis, permet de définir la direction initiale d'anisotropie ainsi que la valeur du paramètre de dispersion (ou concentration) des fibres pour chaque élément à partir de données expérimentales.

Finalement, la stabilité et la validité de l'implémentation ont été vérifiées à travers plusieurs tests numériques.

Chapter 3

Inverse analysis procedure

Contents

3.1 Introduction 90
3.2 Inverse analysis approach 91
3.2.1 Generalities on inverse analysis 91
3.2.2 Inverse analysis method 93
3.2.3 Fibers dispersion and concentration parameters 93
3.2.4 Numerical setup and inverse analysis procedure 94
3.3 Inverse analysis results 99
3.3.1 Models comparison 99
3.3.2 Influence of input data 101
3.3.3 Limitations of the inverse analysis procedure 105
3.4 Summary of Chapter 3 105
3.5 Résumé en français 106

3.1 Introduction

Identification of physical models parameters allowing to reproduce experimental observations has been an important research area for a long time, with a wide range of applications in many fields. An accurate parameter identification on a proper model calibrated on proper experiments should confer a good consistency and predictability. In order to find these parameters, an inverse analysis procedure is often used. It usually involves the minimization of an objective function, also called error or cost function, that ensures the agreement between experimental data and theoretical model results. In other words, an experiment is simulated and the model parameters are adjusted until the model matches the experiment.

In the mechanical field, inverse analysis is based on mechanical experiments where the reference state, the deformed state, and the applied boundary conditions are known and can be numerically reproduced. Thus, material parameters identification requires robust inverse analysis procedures conducted on relevant material models and an accurate modeling of the experimental boundary conditions, while containing experimental error within acceptable limits. In case of complex materials such as biomaterials, the inverse analysis procedure may deal with additional practical difficulties such as for instance multi–scale properties, non–linearity, anisotropy, remodeling, complex geometries and local heterogeneity (regionally varying stiffness, fiber reorientation, ...).

A vast literature exists on inverse analysis applied to biomaterials. Readers can refer for instance to Harb et al. [2014] who introduced a method based on genetic algorithms and analytical optimization for complex models with numerous material parameters. Another approach based on a successive response surface method was used in Einstein et al. [2005] to fit hyperelastic anisotropic constitutive equations on aortic wall and AV tissue properties. Kroon et al. [2009] proposed an inverse method applied to non–linear elastic membrane such as cerebral aneurysms. Krishnamurthy et al. [2008] used finite element inverse analysis to find material properties of mitral valve leaflets based on *in vivo* experiments involving tracking of miniature radiopaque markers. Abbasi et al. [2016] used inverse analysis on planar biaxial tensile tests of bioprosthetic valve tissues followed by a second–step optimization on a 3D finite element model coupled with *in vitro* experiments for validation. One can also refer to Fehervary et al. [2016] who proposed a parameter optimization procedure improving fitting results on soft tissue planar biaxial tests using rakes.

In this chapter, biaxial experiments results and fibrous structure information from chapter 1 were used together with finite element models implemented in chapter 2 to setup an inverse analysis procedure. In section 3.2, we first remind some concepts of inverse analysis and briefly introduce two optimization algorithms. Then, our inverse analysis software

and strategy are presented. In section 3.3 the inverse analysis results are discussed and the different implemented constitutive models are compared to determine which one better fits AV tissues behavior. Finally, a summary concludes the chapter (section 3.4).

3.2 Inverse analysis approach

In this section we present generalities on optimization, as well as the inverse analysis strategy used to identify material models' parameters from experimental observations.

3.2.1 Generalities on inverse analysis

An inverse problem is a constrained non–linear optimization problem that seeks to minimize an objective function $f(\boldsymbol{x})$ where $\boldsymbol{x}$ is the vector of the optimization variables x_i. For a n dimensional optimization problem $\boldsymbol{x} \in \Psi$ with $\Psi \subset \mathbb{R}^n$ the optimization domain. The inverse problem is the process of computing from a set of observations the causal factors that produced them. It is called "inverse" because it starts from the output results and then calculate input parameters. Non–linear inverse problems are often solved using either gradient or evolutionary optimization methods.

Gradient methods

Gradient descent is the most used procedure among gradient methods. It is a first–order iterative optimization algorithm based on the gradient of objective function ∇f with $f \in \mathbf{C}^0(\Psi)$. $\mathbf{C}^0(\Psi)$ is the space of continuous functions on the optimization domain Ψ. Thus, the optimal solution condition is $\nabla f = 0$. This optimal solution is achieved using

$$d \cdot \nabla f < 0, \tag{3.1}$$

where d is the descent direction. One can refer for instance to Roux [2011] for more information about the choice of d and the resolution methods.

These algorithms are widely used but suffer from two major drawbacks : the objective function must be continuous on Ψ, and the optimal solution found do not ensure convergence to the global solution but only to a local minimum (except if f is convex). Hence, the optimal solution depends on the initial values of the optimization variables.

Evolutionary algorithms

Evolutionary algorithms are inspired by the evolution theory, using mechanisms such as selection, recombination and mutation for instance. Since the sixties, they experienced a wide development in the optimization field. These algorithms are usually robust and efficient for all types of problems because they do not make any assumption but are

generally more time consuming than gradient methods. In evolutionary algorithms, an initial population is generated in the optimization domain Ψ. This generation can be random or follow specific rules. The population is then evaluated and a selection allows best individuals to reproduce for next generation using recombinations (information exchange between individuals) and mutations (permanent alteration). The process is repeated as long as the convergence criterion is not reach. Thus, evolutionary algorithms can efficiently solve complex (non convex) optimization problems avoiding convergence towards local minima. Two types of evolutionary algorithms are commonly used in optimization problems :

1. genetic algorithms, initially introduced in Holland [1962] and Holland [1975], are often based on a binary representation of the individuals ;

2. evolution strategies, introduced in Rechenberg [1965], are quite similar to genetic algorithms but based on a real valued representation of the individuals.

A functional diagram of these algorithms is illustrated on fig. 3.1. Further information on genetic operators like selection, crossing, mutation and recombination, can be found in Roux [2011] for instance.

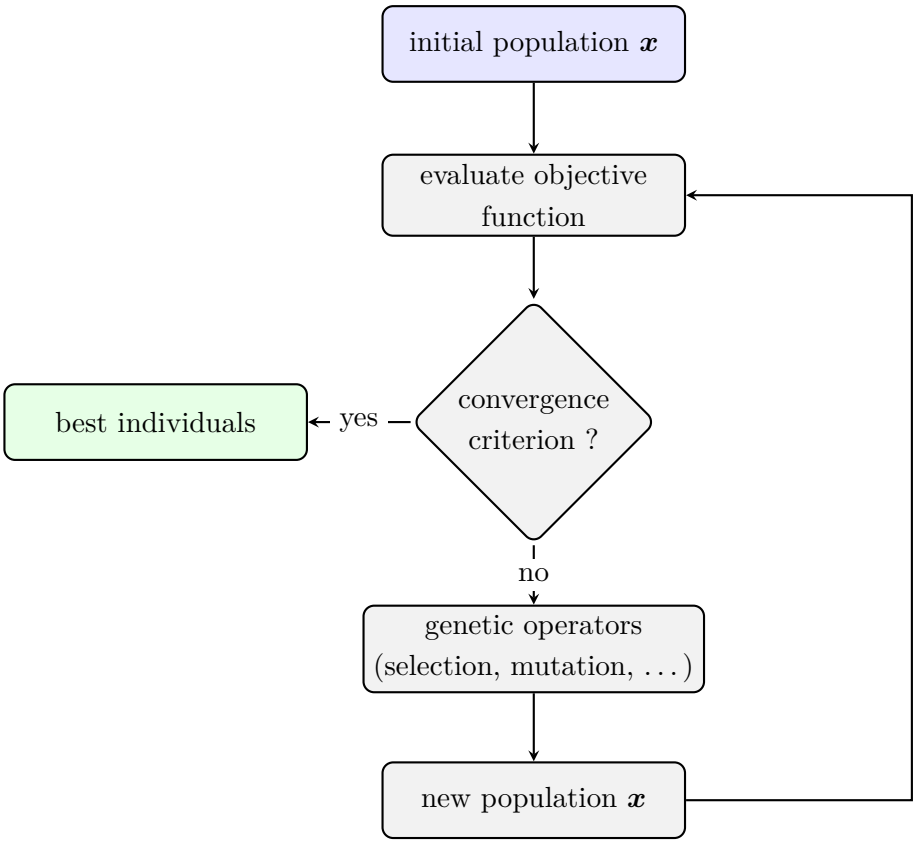

Fig. 3.1 – Evolutionary algorithm diagram

3.2.2 Inverse analysis method

The Levenberg—Marquardt algorithm, which uses a modified gradient descent approach, is often used to solve non–linear least squares problems in biomechanics. However, this method can encounter numerical difficulties and sometimes require to be combined with a multi–step approach decomposing the initial problem in smaller ones. This gradual procedure allows to progressively determine all the material parameters but is time consuming and requires adapted experiments (see for instance Holzapfel [2006a]). On the other hand, global stochastic methods have demonstrated their robustness for solving complex optimization problems and should perform well in single–step inverse analysis. Thus, we decided to use a metamodel–assisted evolutionary algorithm based on the latter procedure. The algorithm, developed in our laboratory, is called MOOPI for MOdular software dedicated to Optimization and Parameters Identification [Roux 2011]. The MOOPI platform was coupled with the FE software FORGE®.

MOOPI uses a kriging metamodel for the construction and the exploitation of the response surface. The metamodel gives an estimate of an unknown solution based on observations of previous ones. It allows to quickly obtain an approximation of the objective function at every points of the (continuous) optimization domain Ψ. Another important aspect is to ensure the global nature of the optimum search exploring unknown areas of the domain in order to iteratively enrich the solutions database. Thus, MOOPI uses an evolution strategy optimization algorithm that maximize the "expected improvement" criterion introduced in Jones et al. [1998]. The objective function f to minimize is defined as a least mean squares function following the equation

$$f(\boldsymbol{x}) = \sqrt{\frac{\sum_{i=1}^{m} \left(y_i^{exp} - y_i^{num}(\boldsymbol{x})\right)^2}{\sum_{i=1}^{m} \left(y_i^{exp}\right)^2}}. \tag{3.2}$$

We denote m the number of experimental points, y_i^{exp} the experimental points values and y_i^{num} the corresponding (interpolated) numerical values. In counterpart of their robustness, global methods requires a large number of evaluation of the objective function. For further information on MOOPI the reader can refer to Roux [2011].

3.2.3 Fibers dispersion and concentration parameters

Fully automated methods for quantification of the local fiber dispersion (or concentration) parameters from two–dimensional collagen fibers images are increasingly popular. For instance, Schriefl et al. [2012] used an automated fitting process based on Fourier power spectrum analysis to find preferred fibers directions and fibers dispersion on multiphoton images. However, from section 1.4 we consider a series of k independent angle

measurements θ_i with $i = \{1, \dots, k\}$. According to Banerjee et al. [2005], the maximum likelihood estimate of b can be obtain following the equations

$$\bar{\mathrm{R}} = \frac{I_{\frac{d}{2}}(b)}{I_{\frac{d}{2}-1}(b)} = \frac{1}{k}\left\|\sum_{i=1}^{k}\theta_i\right\|, \tag{3.3}$$

and

$$b \approx \frac{\bar{\mathrm{R}}(d - \bar{\mathrm{R}}^2)}{1 - \bar{\mathrm{R}}^2}, \tag{3.4}$$

where $d = 2$ is the dimension and $I_n(b)$ is the modified Bessel function of the first kind defined as

$$I_n(b) = \frac{1}{\pi}\int_0^{\pi} \mathrm{e}^{b\cos(\theta)}\cos(n\theta)\mathrm{d}\theta. \tag{3.5}$$

The dispersion parameter κ is then computed from (2.135).

3.2.4 Numerical setup and inverse analysis procedure

For the inverse analysis procedure, experimental data from the representative fresh sample presented in section 1.4 were used. Thus, both mechanical behavior and collagen fiber information, were known on a same specimen. The numerical setup reproduces the biaxial experiment on a 5×5 mm^2 area between the rakes. Fiber orientations and dispersion (or concentration) parameters obtained from fibers confocal measurements presented in section 1.4 were transposed to the finite element mesh (0.25 mm structured mesh) using alg. 2 in order to approximate the actual fibrous structure of the sample (fig. 3.2).

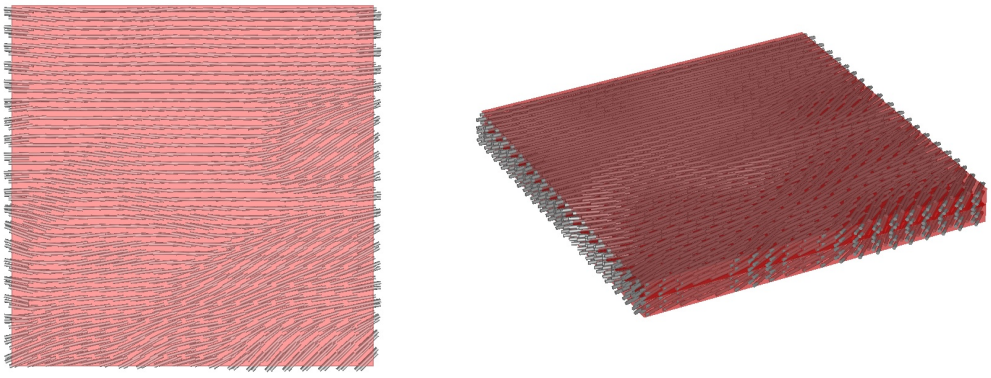

Fig. 3.2 – Interpolation of measured fibers directions on the undeformed finite element mesh

Some assumptions were made for the numerical modeling of the sample. First, an homogeneous thickness of 0.5 mm was chosen. In practice, a thickness of 0.25 mm was used with a mirror symmetry. Secondly, material parameters are assumed to be homogeneous in the tissue while structural parameters are locally imposed. The local concentration

parameters b on the sample were obtained from equations (3.3) and (3.4) where θ_i are the measured angles on each confocal image. The dispersion parameters κ were obtained using b and (2.135). Finally, dispersion and concentration parameters were interpolated using the algorithm presented in subsection 2.5.4. Results are shown on fig. 3.3.

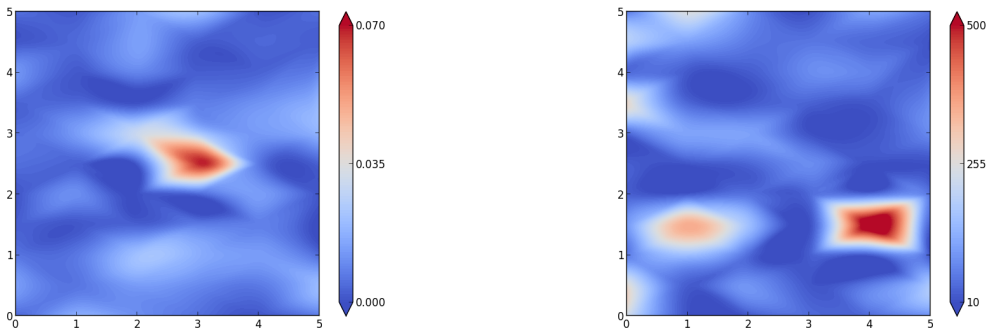

(a) b interpolation **(b)** κ interpolation

Fig. 3.3 – Interpolation on the sample of the local concentration and dispersion parameters

Since the numerical modeling of the experiments must be accurately reproduced, displacements measured from DIC (virtual extensometers) at the 5×5 mm^2 area boundaries were imposed. Hooks were not modeled. Hence, only the area of interest was represented and area borders stay straight during deformation as illustrated on fig. 3.4. Radial and circumferential axes of tension as defined in chapter 1 are recalled on fig. 3.5. The optimization was made on force data versus time. Displacements and forces measurements for all the experimental protocol loadings on a representative fresh sample are presented on fig. 3.6, fig. 3.7, fig. 3.8 and fig. 3.9. An inverse analysis procedure was performed on each implemented material model (see chapter 2) in order to select the most relevant one. The influence of the number of loading conditions and fiber orientation angles (free or imposed) on the inverse analysis results were also investigated.

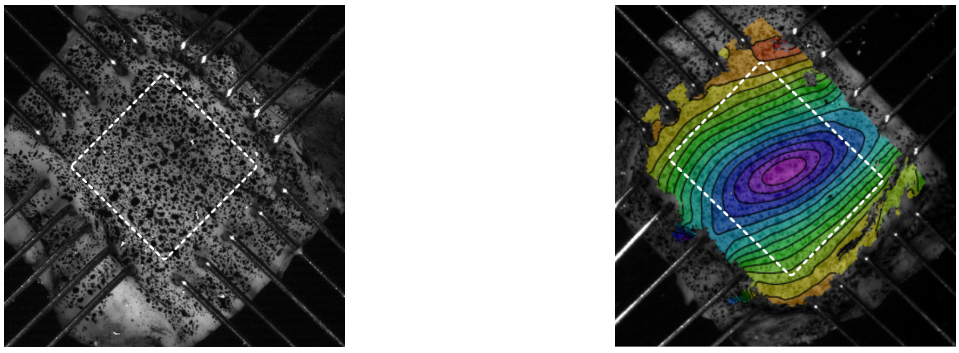

(a) Initial area **(b)** Deformed area

Fig. 3.4 – Illustration of the modeled area at the initial and deformed states

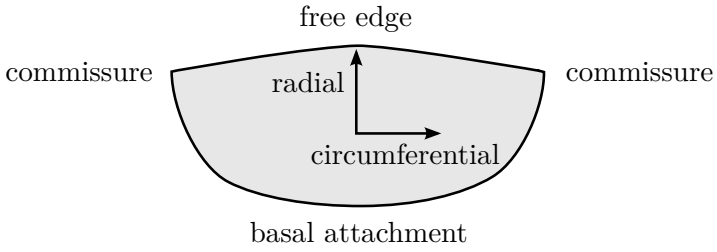

Fig. 3.5 – Scheme of an excised AV leaflet with radial and circumferential axes definition

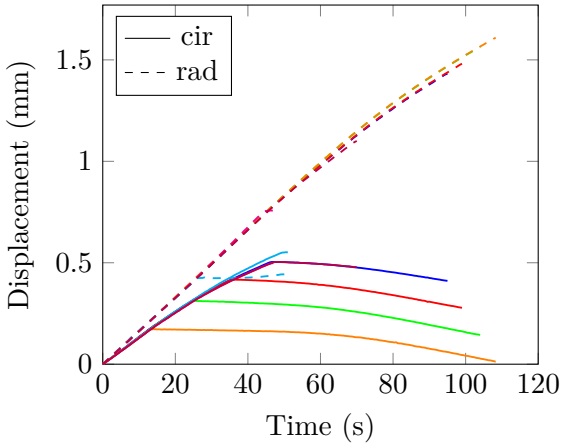

Fig. 3.6 – Superposition of displacements from all the experimental loading conditions on a representative fresh sample (DIC measurements)

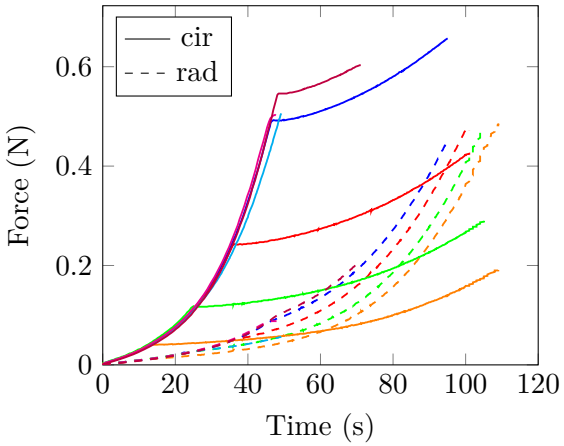

Fig. 3.7 – Superposition of forces from all the experimental loading conditions on a representative fresh sample

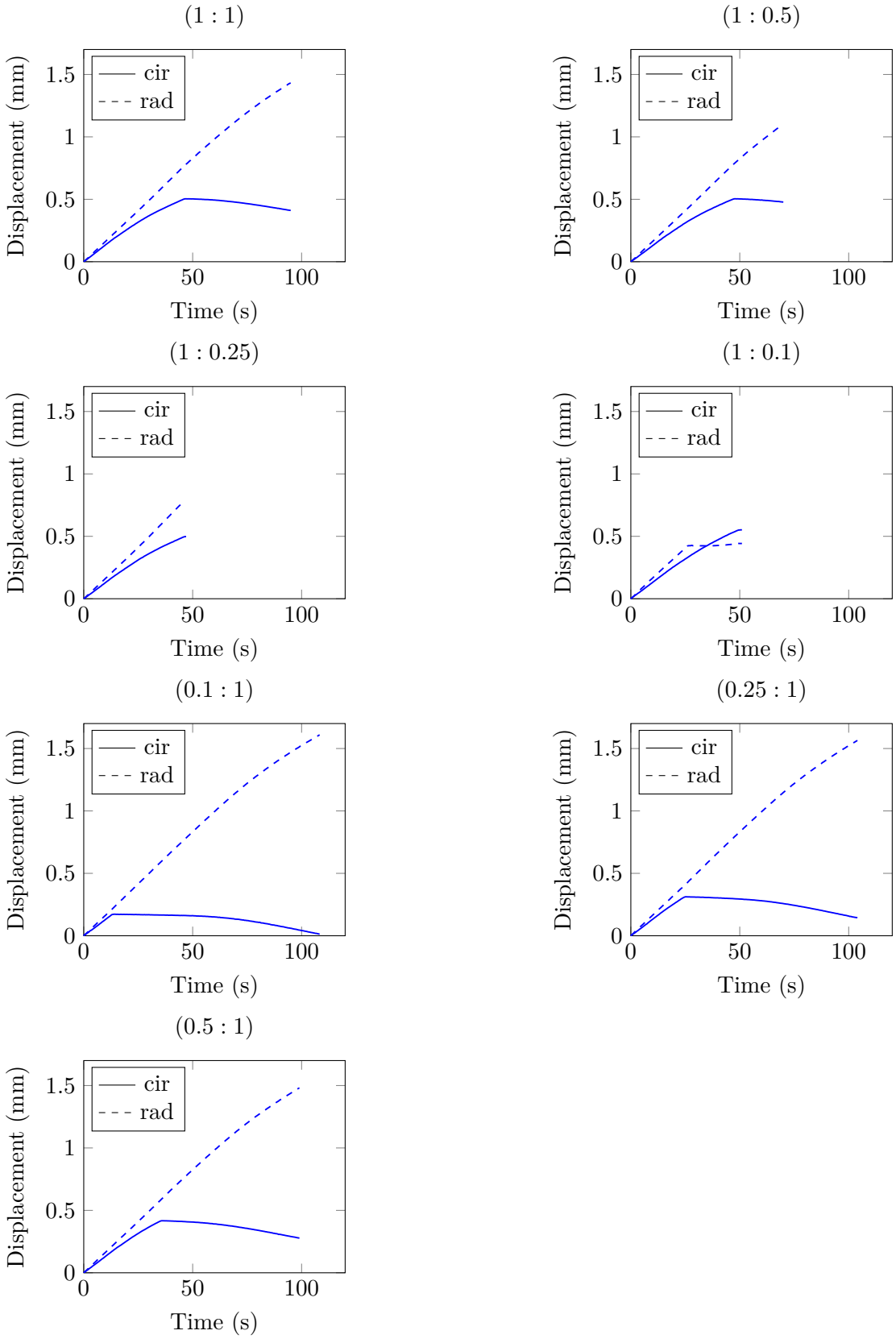

Fig. 3.8 – Displacements from DIC measurements imposed on the modeled geometry

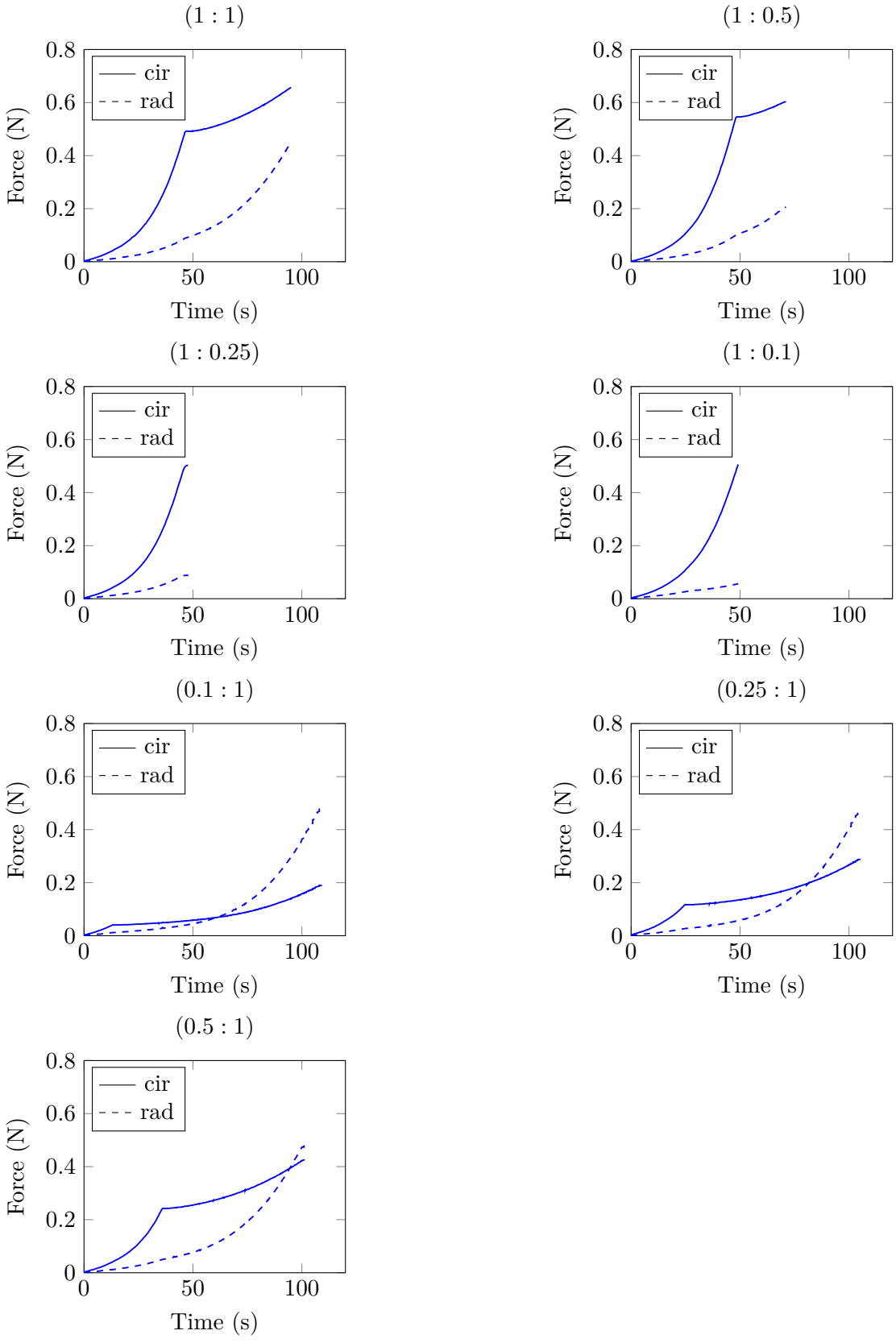

Fig. 3.9 – Forces from experimental measurements to be compered to computed results

3.3 Inverse analysis results

In this section we present inverse analysis results with a comparison of the three implemented material models. Influence of input data, such as the number of observables or information on fibers orientations, on parameters identification is also discussed.

3.3.1 Models comparison

As presented in section 2.5, hyperelastic anisotropic strain–energy function are usually a sum of two terms : an isotropic potential for the groundmatrix behavior and a transversaly isotropic potential for the collagen fibers response. In first instance this study aims to select among the implemented models the one that best fits biaxial experiments results presented in section 1.4, in both circumferential and radial directions. Since several observables are used for each evaluation step of the inverse analysis procedure, a mean objective function was used, defined as

$$\bar{f}(\boldsymbol{x}) = \frac{1}{\text{obs}} \sum_{i=1}^{\text{obs}} f_i(\boldsymbol{x}), \tag{3.6}$$

where obs is the number of observables. It is equal for instance to 14 in case of a complete experimental protocol, which corresponds to 7 loading conditions and 2 axes each. However, for determining which of the models best fits the experimental results, only the $(1:1)$ loading was used. At this stage, the idea was to check the ability of the models to reproduce the shape of the experimental curves, not to identify accurate sets of parameters. In the particular case of the Weisbecker model, a symmetric recruitment stretch distribution was assumed, so that $a_1 = a_2$ from equation (2.120). The stretch λ_1 at which the first fiber is activated was set to 1 and fiber volume fraction ν to 0.5 [Weisbecker et al. 2015; Billiar et al. 2000b]. For all models, the fictive Poisson ratio v was set to 0.4995 considering the material as quasi–incompressible. Large admissible optimization domains were defined for all other models parameters. Depending on the number of unknowns, from 32 to 64 sets of parameters were initially generated. Models with many unknown parameters require a large initial population in order to ensure an optimization search toward a global optimum. Each new generation was composed of four offspring. The inverse analysis procedure was stopped once the objective function reached an arbitrary convergence criterion set to 0.01 or if no improvement was observed after more than 10 consecutive generations. Results are presented on fig. 3.10 and tab. 3.1. For both, Weisbecker and HGO models, the neo–Hookean contribution of the groundmatrix behavior seems not to be able to capture the tissue non–linearity, leading to inaccurate inverse analysis results. On the other hand, the modified HGO model composed of two exponential strain–energy functions gave satisfying fitting results both in radial and circumferential directions. Hence, only the latter model was used for parameters identification.

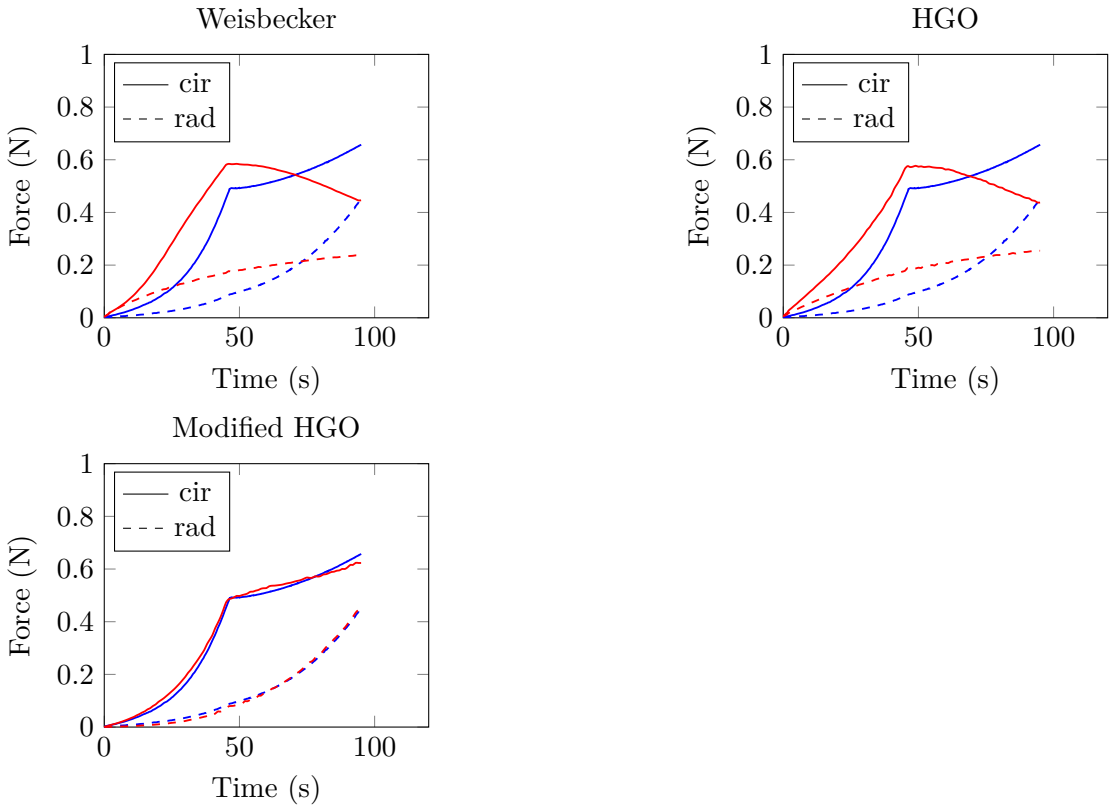

Fig. 3.10 – Forces from experimental $(1:1)$ result (blue) and inverse analysis results (red) for each model

	Weisbecker	HGO	Modified HGO
c_0/c_g	65 kPa	55.3 kPa	2.5 kPa
c_1/c_f	220 kPa	210.7 kPa	10.3
c_2	–	26	190 kPa
c_3	–	–	29.7
$a_1 = a_2$	2.6	–	–
λ_1	1	–	–
λ_2	1.2	–	–
ν	0.5	–	–
v	0.4995	0.4995	0.4995
$\bar{f}$	0.379	0.307	0.036

Tab. 3.1 – Sets of parameters identified by inverse analysis on the $(1:1)$ experiment

3.3.2 Influence of input data

One experimental loading is usually not enough for a relevant inverse analysis procedure. The uniqueness of the identified set of parameters can be insured by increasing the quantity of experimental data. On tab. 3.2 are shown several parameters identification results depending on the number of loading conditions used (on a modified HGO model). For these parameters identifications, force threshold ratios ($F_x : F_y$) are respectively :

- $\{(1:1)\}$ for the 1 loading protocol ;
- $\{(1:1), (1:0.25), (0.25:1)\}$ for the 3 loadings protocol ;
- $\{(1:1), (1:0.5), (1:0.25), (0.25:1), (0.5:1)\}$ for the 5 loadings protocol ;
- $\{(1:1), (1:0.5), (1:0.25), (1:0.1), (0.1:1), (0.25:1), (0.5:1)\}$ for the 7 loadings protocol.

It can be seen from the model's mathematical function (2.137) that c_0 and c_2 are scaling parameters multiplying the exponential functions while c_1 and c_3 are parameters of this exponential functions. Thus, parameters $\{c_0, c_1\}$ and $\{c_2, c_3\}$ are respectively coupled, and each couple evolve independently as a function of the loading conditions applied in the inverse analysis procedure.

Modified HGO	1 loading	3 loadings	5 loadings	7 loadings
c_0	2.5 kPa	6.2 kPa	5.5 kPa	5.9 kPa
c_1	10.3	7.9	8.3	8
c_2	190 kPa	152 kPa	145.6 kPa	131 kPa
c_3	29.7	33.2	34	34.7
v	0.4995	0.4995	0.4995	0.4995
$\bar{f}$	0.036	0.087	0.078	0.1

Tab. 3.2 – Modified HGO model parameters identification depending on the number of experimental loading conditions used

The complete experimental protocol was chosen as reference. Results of the inverse analysis procedure are shown on fig. 3.11. The model with identified parameters was able to efficiently reproduce most of experimental observations. Globally similar results quality were obtained for the other inverse analysis procedures on their respective loading conditions. However, identified parameters considerably evolved from the single loading inverse analysis procedure with respect to the reference one. In order to assess the predictability of the model depending on the number of observables available for the parameters identification, the model responses for the $(1:0.1)$ and $(0.1:1)$ loading conditions were superimposed for all identified set of parameters (fig. 3.12).

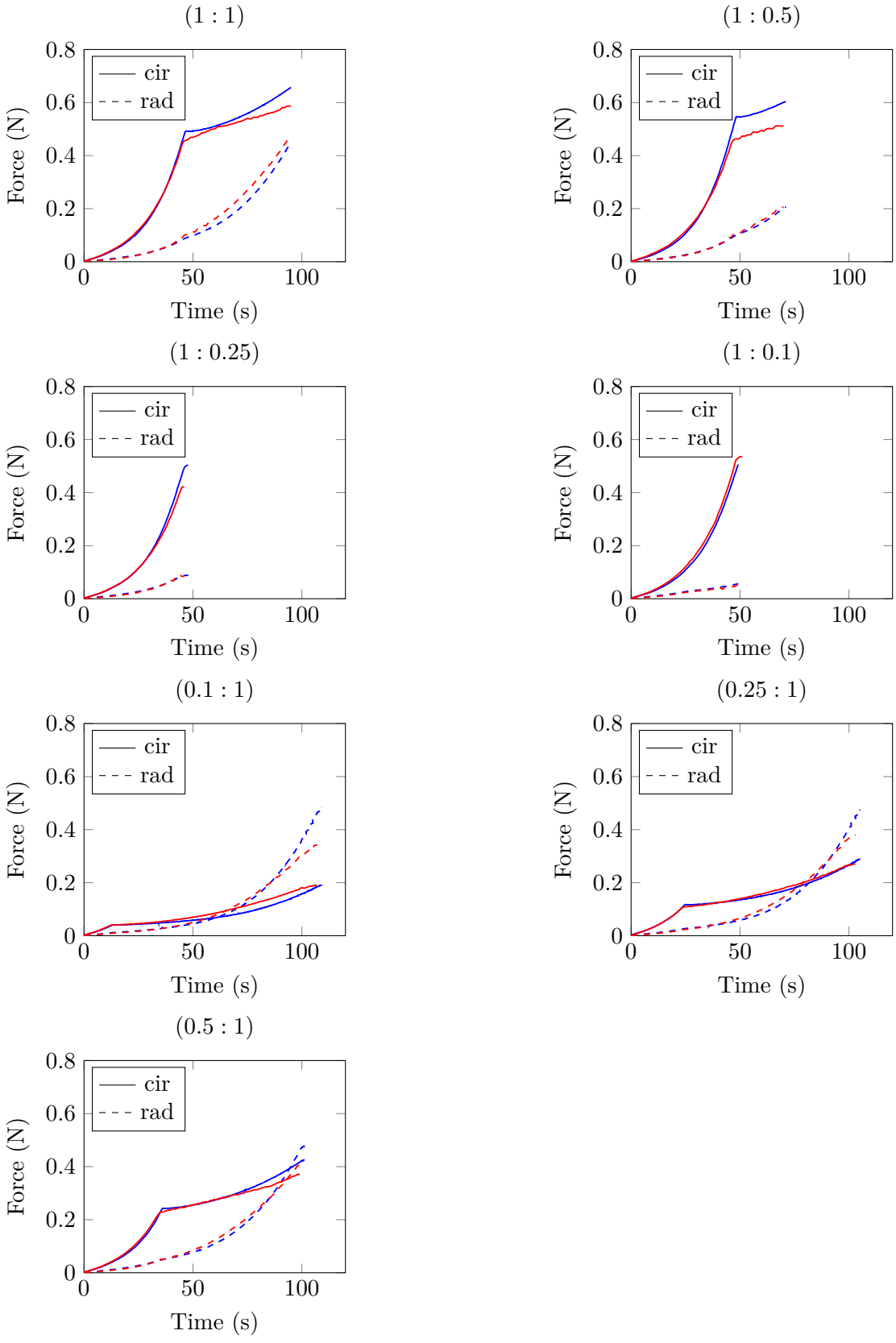

Fig. 3.11 – Forces from experimental (blue) and inverse analysis (red) results with fixed angles

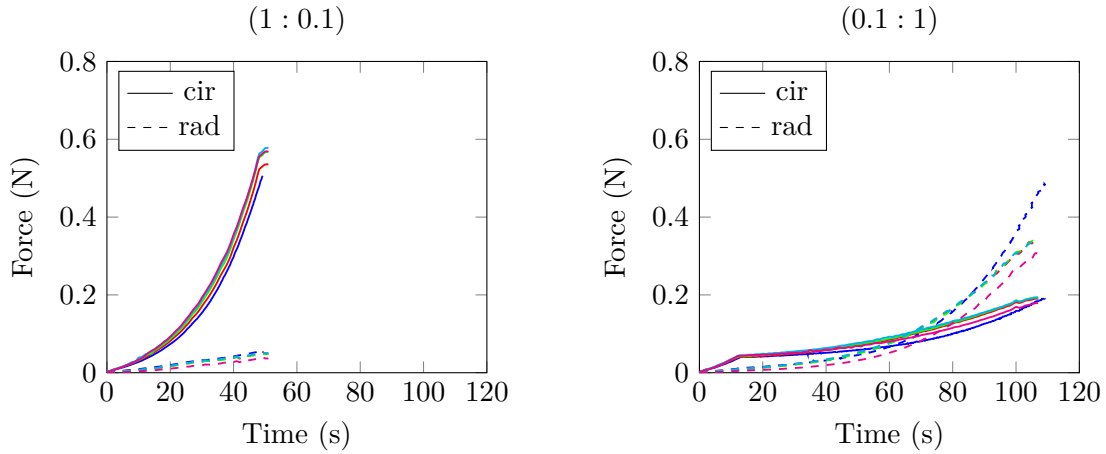

Fig. 3.12 – Forces from experimental results (blue), 7 loadings identification (red), 5 loadings identification (green), 3 loadings identification (cyan) and 1 loading identification (magenta)

As expected, results accuracy increases with the number of observables used. Nevertheless, if one loading condition is clearly insufficient, the improvement between the 3 and 5 loading conditions is quite low. The complete inverse analysis procedure, with $(1:0.1)$ and $(0.1:1)$ loading conditions as observables, gave the best results. This observation confirms the need to perform inverse analysis procedure on a large experimental database in order to get a reliable predictability for complex materials.

A second inverse analysis procedure on a 7 loading conditions protocol was carried out, letting free the fiber orientation angle in the tissue plan. The fiber dispersion parameter κ was set to 0 everywhere assuming perfectly aligned fibers. Hence, four material parameters and a global fiber orientation θ were identified. Results are presented on tab. 3.3 and fig. 3.13.

Modified HGO	7 loadings	7 loadings (ref.)
c_0	4 kPa	5.9 kPa
c_1	9.6	8
c_2	138 kPa	131 kPa
c_3	29.4	34.7
θ	13.1°	–
v	0.4995	0.4995
$\bar{f}$	0.124	0.1

Tab. 3.3 – Modified HGO model parameters identification with unknown fibers orientation

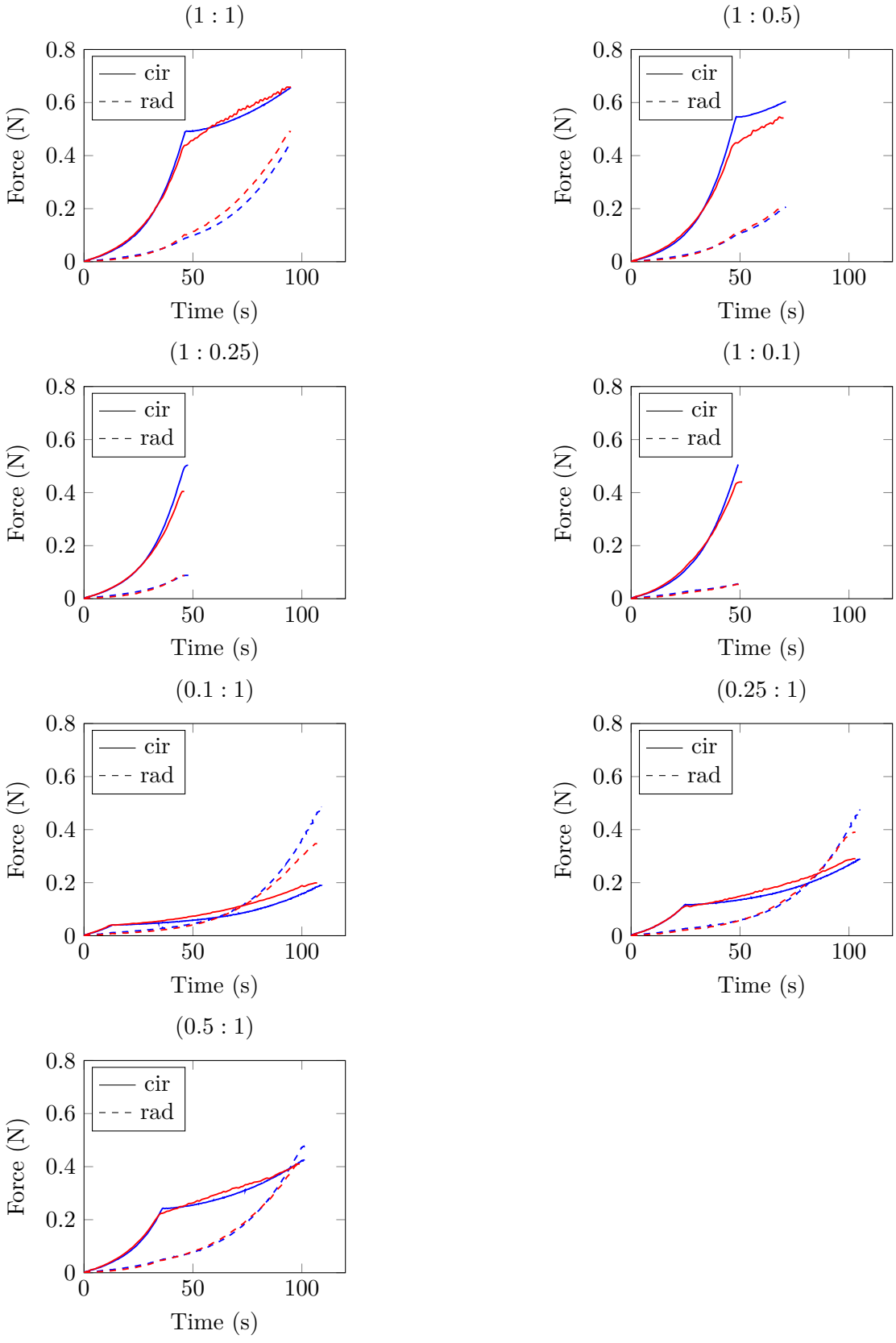

Fig. 3.13 – Forces from experimental (blue) and inverse analysis (red) results with free angles

Once again, the model was able to efficiently reproduce the tissue mechanical response. However, the modeled area have a relatively distinct preferred fibers direction along the circumferential direction (fig. 3.2) and a global fiber orientation seems to not disrupt the fitting process. A less arranged fibrous structure may significantly affect the inverse analysis results.

3.3.3 Limitations of the inverse analysis procedure

The inverse analysis was carried out on a geometry corresponding to a perfect monolayer material with an homogeneous thickness and a simplified fibrous structure. Moreover, the displacements imposed on the mesh boundaries come from an average of three virtual extensometers for each axis. Hence, these displacements are homogeneous on the mesh sides and borders stay straight during the deformation. These assumptions produce errors on the tension and strain computation in comparison to the experimental measurements. A comparison of the numerical and experimental tension–strain results for the $(1:1)$ loading condition using identified modified HGO parameters is shown on fig. 3.14. An overestimation of both strain and tension can be observed, especially in the circumferential direction. However, on this figure the numerical strain is not averaged in a circular area like it is experimentally done, but computed on a single node located at the center of the mesh.

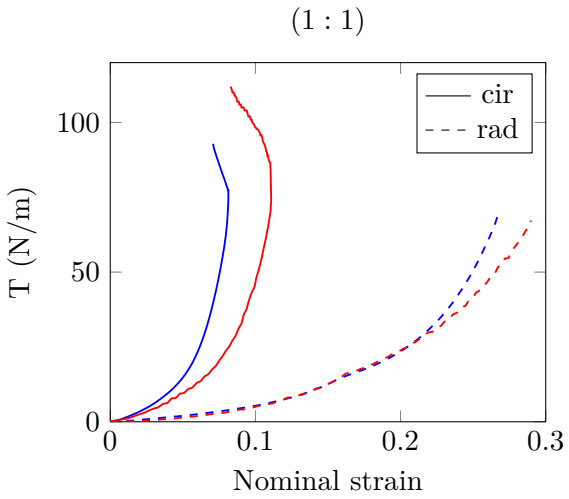

Fig. 3.14 – Comparison of the experimental (blue) and numerical (red) tension curves for a $(1:1)$ loading condition

3.4 Summary of Chapter 3

An inverse analysis procedure was carried out in order to select and calibrate a material model among those implemented in the chapter 2 using experimental data from chapter 1. A kriging metamodel–assisted evolutionary algorithm developed at the laboratory was

used. Hence, a biaxial tensile test was numerically reproduced with a simplified geometry of the central area of a sample. Local principal orientations and dispersion (or concentration) parameters of the fibers, obtained by treatment of the confocal microscopy images, were interpolated and transposed on the finite element mesh. Displacements measured with the digital image correlation system were imposed as boundary conditions and the inverse analysis procedure was made on the measured force on each axis.

A first inverse analysis procedure performed on a single loading condition allowed to select a model among the three implemented (the modified HGO model). Then, several other inverse analysis procedures were carried out on the selected model to evaluate the influence of the number of observables on the results. In each case, a good correlation was obtained between numerical and experimental results despite important variations of the identified parameters. However, in accordance with the literature, an improvement of the predictability of the model was noticed while increasing the number of observables.

3.5 Résumé en français

Afin de sélectionner et de calibrer l'un des modèles de comportement implémentés dans le chapitre 2 à partir des données expérimentales du chapitre 1, une méthode d'analyse inverse a été mise en place. L'algorithme utilisé pour le problème d'optimisation a été développé au laboratoire. Il s'agit d'un algorithme évolutionnaire faisant appel à une méthode de krigeage. Un essai de traction biaxiale a donc été reproduit numériquement en utilisant une géométrie simplifiée de la zone utile de l'échantillon. Les orientations principales ainsi que les paramètres de dispersion (ou concentration) locaux des fibres de collagène obtenus à partir des images de microscopie confocale ont été interpolés et transposés sur le maillage éléments finis. Les déplacements mesurés avec le système de corrélation d'images ont été imposés comme conditions aux limites du modèle numérique et l'analyse inverse a été effectuée sur la force mesurée pour chaque axe.

Une première analyse inverse sur un chargement a permis de selectionner un modèle numérique parmis les trois implémentés (le modèle de HGO modifié). Plusieurs analyses inverses ont ensuite été menées sur le modèle retenu afin d'évaluer l'influence du nombre d'observables sur les résultats. Les résultats des identifications ont systématiquement montré une bonne corrélation entre résultats numériques et expérimentaux malgré d'importantes variations des paramètres optimaux. Néanmoins, en accord avec la littérature, une amélioration de la prédictibilité du modèle a été constatée avec l'augmentation du nombre d'observables.

Chapter 4

Toward fluid–structure interaction

Contents

4.1 Introduction . . . 108
4.2 Governing equations . . . 109
4.2.1 Navier–Stokes equations for incompressible flows . . . 109
4.2.2 Boundary conditions . . . 110
4.3 SPH : method and implementation . . . 111
4.3.1 Generalities on SPH . . . 111
4.3.2 SPH interpolation . . . 112
4.3.3 First order differential operators . . . 114
4.3.4 Second order differential operator . . . 116
4.3.5 Accuracy of SPH differential operators . . . 116
4.3.6 Definition of the kernel function . . . 117
4.3.7 Fluid discretization . . . 120
4.3.8 Incompressible SPH . . . 122
4.3.9 Boundary conditions treatment . . . 125
4.3.10 Time–stepping and numerical stability . . . 127
4.3.11 Reduction of the computational time . . . 127
4.4 SPH–FE coupling . . . 129
4.4.1 FSI algorithm . . . 129
4.4.2 Interface coupling . . . 130
4.5 Solver validation . . . 131
4.5.1 SPH implementation validation . . . 131
4.5.2 SPH–FE coupling validation . . . 134
4.6 Summary of Chapter 4 . . . 137
4.7 Résumé en français . . . 137

4.1 Introduction

Fluid—Structure Interaction (FSI) formulations are increasingly used in biomechanics. One of the most challenging FSI problem in the body is the heart valves dynamics when submitted to blood pressure variations during diastole and systole. The complex material behavior of both, blood and valvular tissues, coupled with complex topological change with self–contact of leaflets during opening and closing, makes the problem extremely difficult to model. However, several methods have been proposed in the literature. The most common one is the FE Arbitrary Lagrangian–Eulerian (ALE) formulation. But this method suffers from numerical issues in case of large displacements or deformations because of degenerate (ill–shaped) elements without adaptive meshing and numerical diffusion due to interpolation errors with adaptive meshing. Readers can for instance refer to De Hart, Peters, et al. [2003] and De Hart, Baaijens, et al. [2003] who worked on the three–dimensional FSI modeling of AVs using a combined fictitious domain/ALE formulation. One can also cite the Immersed Boundary Method (IBM) that involves Eulerian and Lagrangian variables, linked by the Dirac delta function [Peskin 2002]. Eulerian variables are computed on a fixed mesh and Lagrangian variables on a moving curvilinear one. Borazjani [2013] used a FE solver with an anisotropic Fung–type non–linear constitutive law coupled with a sharp–interface IBM for the FSI modeling of bioprosthetic heart valves. Hsu et al. [2014] used an hybrid ALE/immersed–boundary approach, also for the FSI modeling of bioprosthetic heart valves.

Another promising possibility for FSI modeling is the use of meshfree particle methods, like for instance Smoothed Particle Hydrodynamics (SPH) or Immersed Particle Method (IPM). They differ from FE formulations in that the fluid model is Lagrangian with a domain subdivided into a set of particles without connectivity. Consequently, these methods can easily handle large fluid–structure interface displacement and deformation as the particles move with the flow. One can refer for instance to the work of Z. Li et al. [2015] on an SPH–FE methods for transient FSI problems with large interface motion.

Another major difficulty is the blood rheology modeling itself. Blood is a complex non–Newtonian fluid composed of various cellular constituents and active substances reacting to biomechanical and chemical stimuli from their environment. These constituents are mainly plasma, red blood cells, white blood cells and platelets. Hence, the flow behavior can be significantly affected by properties change at the cellular level. Various computational methods have been applied to blood flow modeling, from a macroscopic to a multiscale point of view. Among these, Lagrangian particle–based methods have been widely used for mesoscopic hemodynamics. With such methods, plasma which is essentially an aqueous solution is modeled as a Newtonian fluid using particles and cells components as solid deformable aggregate of particles. Reader can refer for instance to

Yamaguchi et al. [2010] and Fedosov et al. [2014] for reviews on multiscale blood flow modeling.

However, as a first approximation and as far as a macroscopic modeling is acceptable, a continuum approach can be chosen even if it is not sufficient to capture the complex blood flow behavior. An incompressible Newtonian fluid was considered in this chapter. Blood flow is usually laminar in the body and was considered as such in this study. Nevertheless, depending on the location, the size and shape of the blood vessels, it can become turbulent (*e.g.* in the case of aneurysm) especially in the ascending aorta due to its high flow rate. The process is also assumed to be adiabatic, so that no heat transfer occurs. In this chapter, a 3D–SPH solver was implemented and coupled with our FE hyperelastic solver (chapter 2). In section 4.2, we first remind governing equations of incompressible flows. In section 4.3, the SPH method and its implementation are introduced. Then, first developments of a fluid–structure coupling are explained (section 4.4) and the overall implementation is validated and discussed (section 4.5). Finally, a summary concludes the chapter (section 4.6).

4.2 Governing equations

This section aims to introduce Navier—Stokes equations in the particular case of incompressible flows.

4.2.1 Navier–Stokes equations for incompressible flows

Navier–Stokes equations are governing equations that describe the motion of viscous fluids. It consists of two equations, the continuity and the momentum equations. We adopt the Eulerian configuration and define the domain $\Omega \in \mathbb{R}^d$ with $d = \{1, 2, 3\}$ the dimension. The continuity equation which represents the mass conservation in the domain Ω can be written in its most general form as

$$\boxed{\frac{\partial \rho}{\partial t} + \nabla \cdot (\rho \boldsymbol{v}) = 0,} \tag{4.1}$$

where ρ denotes the density of the fluid, $\boldsymbol{v}$ the velocity of the fluid and t the time. Furthermore, the Cauchy momentum equation is

$$\boxed{\frac{\partial \boldsymbol{v}}{\partial t} + (\boldsymbol{v} \cdot \nabla)\, \boldsymbol{v} = \frac{1}{\rho} \nabla \cdot \boldsymbol{\sigma} + \boldsymbol{g},} \tag{4.2}$$

where $\boldsymbol{\sigma}$ represents the Cauchy stress tensor and $\boldsymbol{g}$ the body accelerations per unit mass acting on the continuum (gravity for instance). In the particular case of an incompressible Newtonian fluid, $\boldsymbol{\sigma}$ can be expressed as

$$\boldsymbol{\sigma} = 2\mu\dot{\boldsymbol{\varepsilon}} - p\mathbf{I}, \tag{4.3}$$

where μ is the dynamic viscosity, p the hydrostatic pressure and $\dot{\boldsymbol{\varepsilon}}$ denotes the strain rate tensor as defined in 2.2. Thus, $\nabla \cdot \boldsymbol{\sigma} = \mu\nabla^2\boldsymbol{v}$ and (4.2) becomes

$$\frac{\partial \boldsymbol{v}}{\partial t} + (\boldsymbol{v} \cdot \nabla)\,\boldsymbol{v} = \nu\nabla^2\boldsymbol{v} - \frac{1}{\rho}\nabla p + \boldsymbol{g}, \tag{4.4}$$

where $\nu = \dfrac{\mu}{\rho}$ is the kinematic viscosity and $\nabla^2(\bullet)$ is the Laplacian operator. Also, since the fluid is incompressible its density remains constant with time and equation (4.1) simplifies into

$$\nabla \cdot \boldsymbol{v} = 0. \tag{4.5}$$

Equation (4.4) can be written in the Lagrangian configuration. The system to be solved becomes

$$\begin{cases} \nabla \cdot \boldsymbol{v} = 0, \\ \dfrac{\mathrm{D}\boldsymbol{v}}{\mathrm{D}t} = \nu\nabla^2\boldsymbol{v} - \dfrac{1}{\rho}\nabla p + \boldsymbol{g}, \\ \dfrac{\mathrm{D}\boldsymbol{x}}{\mathrm{D}t} = \boldsymbol{v}, \end{cases} \tag{4.6}$$

where

$$\frac{\mathrm{D}(\bullet)}{\mathrm{D}t} = \frac{\partial(\bullet)}{\partial t} + \boldsymbol{v} \cdot \nabla(\bullet), \tag{4.7}$$

denotes the material time derivative of a spatial field with $\boldsymbol{v} \cdot \nabla(\bullet)$ the advection term (for an incompressible flow).

4.2.2 Boundary conditions

In order to solve the system (4.6), boundary conditions must be considered. These boundary conditions can be of three types : free–surface, walls and inflow–outflow. Thus, the boundary $\partial\Omega$ of the domain Ω can be decomposed as $\partial\Omega = \partial\Omega^{\mathrm{f}} + \partial\Omega^{\mathrm{w}} + \partial\Omega^{\mathrm{i}} + \partial\Omega^{\mathrm{o}}$ (fig. 4.1). For free–surface boundary conditions (on $\partial\Omega^{\mathrm{f}}$) the external environment (air for instance) and the surface tension have to be taken into account. The pressure boundary condition on $\partial\Omega^{\mathrm{f}}$ should be $p = p_{atm}$ with p_{atm} the atmospheric pressure (often chosen null). The position of the free–surface is an unknown of the problem. Wall boundary conditions (on $\partial\Omega^{\mathrm{w}}$) can be of two kinds : free–slip (inviscid flow) or no–slip (viscous flow) conditions. Considering a viscous flow, the velocity Dirichlet condition imposed on $\partial\Omega^{\mathrm{w}}$ is $\boldsymbol{v} = \boldsymbol{v_w}$ with $\boldsymbol{v_w}$ the velocity of the wall. Finally, inflow–outflow conditions (acting on $\partial\Omega^{\mathrm{i}}$ and $\partial\Omega^{\mathrm{o}}$) consist of imposing desired velocity or pressure at the inlet or outlet boundaries. Usually, a velocity Dirichlet condition is imposed on $\partial\Omega^{\mathrm{i}}$ as $\boldsymbol{v} = \boldsymbol{v_i}$

with $\boldsymbol{v_i}$ the inlet velocity, and a pressure boundary condition is imposed on $\partial\Omega^{\mathrm{o}}$ through $p = p_o$ with p_o the outlet pressure.

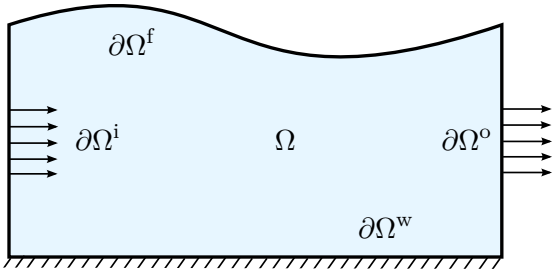

Fig. 4.1 – Illustration of the different boundary conditions

4.3 SPH : method and implementation

Remark – The SPH solver presented below was implemented from scratch for the purpose of this work as a preliminary step to FSI modeling in our FE software FORGE®. The code is written in FORTRAN 90 for straightforward compatibility with the FE solver. A VTK format is used for output data allowing a visualization of the results using ParaView[1] software.

[1] http://paraview.org

In this section SPH method and its implementation are presented. The reader can refer to Liu et al. [2010] for a more detailed review of SPH method and developments.

4.3.1 Generalities on SPH

SPH is a numerical technique used to model a large variety of mechanical problems. It is a Lagrangian meshless method initially developed by Gingold et al. [1977] and Lucy [1977] for astrophysical problems. Over the years SPH method has evolved, being extended to the simulation of a wide range of mechanical and thermodynamical phenomena. Its main applications are currently the dynamics of continua in fluid and solid mechanics.

In the mechanical field, SPH method approximates numerical solutions of the continuum equations by discretizing the material domain into a set of particles without fixed topological connectivity. These particles form interpolation points where the physical properties of the material can be calculated using a kernel estimation technique to derive continuum equations. The initial applications were the modeling of gas dynamic problems and incompressible flow problems by treating them as slightly compressible with an appropriate pressure equation of state [Monaghan 1994]. Nowadays the scope of mature applications

of SPH in continuum mechanics is relatively wide, from turbulent free–surface flows problems to dynamic fracture. Another benefit of this method is its (often) trivial treatment of interface problems and its ability to intrinsically handle complex topological changes. Thus, multi–phase or free–surface problems do not require explicit interface tracking due to particles motion. Moreover, advection is treated implicitly since particles carry their properties with them and the formulation can be exactly conservative (*i.e.* guarantees conservation of momentum and energy).

Disadvantages of the approach mostly concern accuracy and stability issues partly due to the fact that particles are not constrained in a well ordered configuration.

4.3.2 SPH interpolation

Continuous interpolation

We consider an arbitrary scalar field f defined on the domain $\Omega \subset \mathbb{R}^d$, with $d = \{1, 2, 3\}$ the dimension of the problem. An exact estimation of the function f at a point can be obtained through the convolution between this function and the delta Dirac distribution. The value of f at position $\boldsymbol{x}$ is given by the equation

$$f(\boldsymbol{x}) = \int_\Omega f(\boldsymbol{x'})\delta(\boldsymbol{x} - \boldsymbol{x'})\mathrm{d}\boldsymbol{x'}, \tag{4.8}$$

where δ is the Dirac distribution and $\boldsymbol{x'}$ is an arbitrary position. We remind the following property of the Dirac delta function

$$\delta(\boldsymbol{x}) = \prod_i \delta(x_i) \tag{4.9}$$

and for a scalar x,

$$\delta(x) = \begin{cases} +\infty, & x = 0 \\ 0, & x \neq 0 \end{cases} \tag{4.10}$$

with

$$\int_{-\infty}^{+\infty} \delta(x)\mathrm{d}x = 1. \tag{4.11}$$

As Dirac distribution can not be defined numerically we introduce a so–called smoothing kernel function w with a characteristic width h (or smoothing length) such that

$$\lim_{h\to 0} w(\boldsymbol{x}, h) = \delta(\boldsymbol{x}). \tag{4.12}$$

Thus, smoothing kernel function is defined on a non–null interval of space and the smoothing length h can be seen as a measure of the domain of influence of a point

$\boldsymbol{x}$. Consequently, f is evaluated at $\boldsymbol{x}$ through a continuous interpolation that involves its values at surrounding points. The continuous kernel estimation of f from (4.8) is obtained following

$$f_c(\boldsymbol{x}) = \int_{\Omega_\mathrm{h}} f(\boldsymbol{x'}) w(\boldsymbol{x} - \boldsymbol{x'}, h) \mathrm{d}\boldsymbol{x'}. \tag{4.13}$$

where Ω_h is the domain of finite support around a point $\boldsymbol{x}$. The smoothing kernel function should satisfy some other conditions as the normalization condition

$$\int_{\Omega_\mathrm{h}} w(\boldsymbol{x} - \boldsymbol{x'}, h) \mathrm{d}\boldsymbol{x'} = 1, \tag{4.14}$$

so that the area under the curve is unity, and the zero mean condition

$$\int_{\Omega_\mathrm{h}} (\boldsymbol{x} - \boldsymbol{x'}) w(\boldsymbol{x} - \boldsymbol{x'}, h) \mathrm{d}\boldsymbol{x'} = 0. \tag{4.15}$$

In the literature most of the kernel approximations are of second order accuracy. This observation can be obtained by expanding equation (4.13) as a Taylor series. Hence, $f(\boldsymbol{x}) = f_c(\boldsymbol{x}) + O(h^2)$. Readers can refer for instance to Liu et al. [2010] for more details.

Discrete interpolation

In order to discretize the continuous equations, the domain Ω_h is decomposed into $n \in \mathbb{N}$ particles. The continuous interpolation is then approximated by a discrete sum over the particles. Rewriting equation (4.13) as

$$f_c(\boldsymbol{x}) = \int_{\Omega_\mathrm{h}} \frac{f(\boldsymbol{x'})}{\rho(\boldsymbol{x'})} w(\boldsymbol{x} - \boldsymbol{x'}, h) \rho(\boldsymbol{x'}) \mathrm{d}\boldsymbol{x'}, \tag{4.16}$$

and noting that an element of mass $m = \rho(\boldsymbol{x'})\mathrm{d}\boldsymbol{x'}$, one can obtain the discretized form

$$f_d(\boldsymbol{x}) = \sum_i^n f(\boldsymbol{x_i}) w(\boldsymbol{x} - \boldsymbol{x_i}, h) V_i, \tag{4.17}$$

where $V_i = m_i/\rho_i$ is the volume of a particle i, m_i its mass and ρ_i its density. For a specific particle i the scalar field f is obtained by summing on the surrounding particles $j \in \boldsymbol{n} \subset \mathbb{N}$ where $\boldsymbol{n}$ is the set of neighbors fluid particles, so that

$$f_d(\boldsymbol{x_i}) = \sum_{j \in \boldsymbol{n}} f(\boldsymbol{x_j}) w(\boldsymbol{x_i} - \boldsymbol{x_j}, h) V_j. \tag{4.18}$$

4.3.3 First order differential operators

Gradient

In order to solve the system (4.6) it is necessary to build discrete differential operators. The gradient of a scalar field f is given by

$$\nabla f_c(\boldsymbol{x}) = \int_{\Omega_\mathrm{h}} \nabla f(\boldsymbol{x'}) w(\boldsymbol{x} - \boldsymbol{x'}, h) \mathrm{d}\boldsymbol{x'}. \tag{4.19}$$

Using an integration by part, equation (4.19) becomes

$$\nabla f_c(\boldsymbol{x}) = \int_{\Omega_\mathrm{h}} \nabla \left(f(\boldsymbol{x'}) w(\boldsymbol{x} - \boldsymbol{x'}, h) \right) \mathrm{d}\boldsymbol{x'} - \int_{\Omega_\mathrm{h}} f(\boldsymbol{x'}) \nabla w(\boldsymbol{x} - \boldsymbol{x'}, h) \mathrm{d}\boldsymbol{x'}. \tag{4.20}$$

Then, applying the Stokes–Cartan theorem one can obtain

$$\nabla f_c(\boldsymbol{x}) = \int_{\partial\Omega_\mathrm{h}} \left(f(\boldsymbol{x'}) w(\boldsymbol{x} - \boldsymbol{x'}, h) \right) \boldsymbol{n} \mathrm{d}S - \int_{\Omega_\mathrm{h}} f(\boldsymbol{x'}) \nabla w(\boldsymbol{x} - \boldsymbol{x'}, h) \mathrm{d}\boldsymbol{x'}, \tag{4.21}$$

where $\boldsymbol{n}$ is the normal vector to $\partial\Omega_\mathrm{h}$ pointing outward. Since the kernel function w is null $\forall \boldsymbol{x'} \in \partial\Omega_\mathrm{h}$, equation (4.21) becomes

$$\nabla f_c(\boldsymbol{x}) = -\int_{\Omega_\mathrm{h}} f(\boldsymbol{x'}) \nabla w(\boldsymbol{x} - \boldsymbol{x'}, h) \mathrm{d}\boldsymbol{x'} \tag{4.22}$$

if the support domain is not truncated. Finally, knowing that the kernel gradient is antisymmetric

$$\frac{\partial w(\boldsymbol{x} - \boldsymbol{x'}, h)}{\partial \boldsymbol{x'}} = -\frac{\partial w(\boldsymbol{x} - \boldsymbol{x'}, h)}{\partial \boldsymbol{x}} \tag{4.23}$$

one can obtain

$$\nabla f_c(\boldsymbol{x}) = \int_{\Omega_\mathrm{h}} f(\boldsymbol{x'}) \nabla w(\boldsymbol{x} - \boldsymbol{x'}, h) \mathrm{d}\boldsymbol{x'}, \tag{4.24}$$

and its discretized form

$$\nabla f_d(\boldsymbol{x_i}) = \sum_{j \in \boldsymbol{n}} f(\boldsymbol{x_j}) \nabla w(\boldsymbol{x_i} - \boldsymbol{x_j}, h) V_j. \tag{4.25}$$

Applied to a vector field $\boldsymbol{f}$, equation (4.25) becomes

$$\nabla \boldsymbol{f_d}(\boldsymbol{x_i}) = \sum_{j \in \boldsymbol{n}} \boldsymbol{f}(\boldsymbol{x_j}) \otimes \nabla w(\boldsymbol{x_i} - \boldsymbol{x_j}, h) V_j. \tag{4.26}$$

From previous results, one can notice that the gradient of a field can be approximated directly from the field values themselves and the derivative of a kernel function which is computationally effective since no $\nabla f(\boldsymbol{x_j})$ (or $\nabla \boldsymbol{f}(\boldsymbol{x_j})$) evaluation is required. However, the gradient of a constant field is not null using equation (4.25) (or (4.26)). Hence,

following Monaghan [1992] another estimator commonly used in the literature arises from the expression

$$\nabla f = \frac{1}{\rho}\left[\nabla(\rho f) - f\nabla\rho\right], \tag{4.27}$$

yielding to

$$\nabla f_d(\boldsymbol{x_i}) = \frac{1}{\rho_i}\sum_{j\in\boldsymbol{n}} m_j(f(\boldsymbol{x_j}) - f(\boldsymbol{x_i}))\nabla w(\boldsymbol{x_i} - \boldsymbol{x_j}, h). \tag{4.28}$$

Equation (4.28) is often used in SPH to compute velocity gradient for instance, ensuring a better stability. However, this formulation of the gradient is no longer antisymmetric which is a required property to ensure conservation of momentum (*i.e.* opposite mutual action–reaction forces induced by particles i and j). Thus, using the expression from Monaghan [1992]

$$\nabla f = \rho\nabla\left(\frac{f}{\rho}\right) + \frac{f}{\rho}\nabla\rho, \tag{4.29}$$

the following antisymmetric gradient estimator can be obtained

$$\nabla f_d(\boldsymbol{x_i}) = \rho_i\sum_{j\in\boldsymbol{n}} m_j\left(\frac{f(\boldsymbol{x_i})}{\rho_i^2} + \frac{f(\boldsymbol{x_j})}{\rho_j^2}\right)\nabla w(\boldsymbol{x_i} - \boldsymbol{x_j}, h). \tag{4.30}$$

Equation (4.30) is often used in SPH to evaluate pressure gradient. Like for (4.26), equations (4.28) and (4.30) can be applied to vector fields.

Divergence

Using the same method as for the gradient, the discrete divergence estimator of a vector field $\boldsymbol{f}$ is

$$\nabla\cdot\boldsymbol{f_d}(\boldsymbol{x_i}) = \sum_{j\in\boldsymbol{n}}\boldsymbol{f}(\boldsymbol{x_j})\cdot\nabla w(\boldsymbol{x_i} - \boldsymbol{x_j}, h)V_j. \tag{4.31}$$

From equations (4.27) and (4.29), one can respectively obtain the following additional expressions

$$\nabla\cdot\boldsymbol{f_d}(\boldsymbol{x_i}) = \frac{1}{\rho_i}\sum_{j\in\boldsymbol{n}} m_j(\boldsymbol{f}(\boldsymbol{x_j}) - \boldsymbol{f}(\boldsymbol{x_i}))\cdot\nabla w(\boldsymbol{x_i} - \boldsymbol{x_j}, h), \tag{4.32}$$

and

$$\nabla\cdot\boldsymbol{f_d}(\boldsymbol{x_i}) = \rho_i\sum_{j\in\boldsymbol{n}} m_j\left(\frac{\boldsymbol{f}(\boldsymbol{x_i})}{\rho_i^2} + \frac{\boldsymbol{f}(\boldsymbol{x_j})}{\rho_j^2}\right)\cdot\nabla w(\boldsymbol{x_i} - \boldsymbol{x_j}, h). \tag{4.33}$$

4.3.4 Second order differential operator

The discrete Laplacian operator can also be estimated following the same approach by differentiating twice equation (4.25). Thus, one can obtain for a scalar field f

$$\nabla^2 f_d(\boldsymbol{x_i}) = \sum_{j \in \boldsymbol{n}} f(\boldsymbol{x_j}) \nabla^2 w(\boldsymbol{x_i} - \boldsymbol{x_j}, h) V_j. \tag{4.34}$$

However, this formulation that involves second derivative of the kernel function presents numerical issues like a high sensitivity to particle disorder or may switch sign on its support domain inducing a poor estimation [Monaghan 1992]. Several improved Laplacian estimators have been proposed in the literature. Among other, readers can refer for instance to Shao et al. [2003] or Colin et al. [2006]. A formulation commonly used was proposed in Morris et al. [1997a] and follows

$$\nabla^2 f_d(\boldsymbol{x_i}) = 2 \sum_{j \in \boldsymbol{n}} (f(\boldsymbol{x_i}) - f(\boldsymbol{x_j})) \frac{\boldsymbol{x_i} - \boldsymbol{x_j}}{\|\boldsymbol{x_i} - \boldsymbol{x_j}\|^2} \cdot \nabla w(\boldsymbol{x_i} - \boldsymbol{x_j}, h) V_j. \tag{4.35}$$

Applied to a vector field $\boldsymbol{f}$, one can obtain

$$\nabla^2 \boldsymbol{f_d}(\boldsymbol{x_i}) = 2 \sum_{j \in \boldsymbol{n}} (\boldsymbol{f}(\boldsymbol{x_i}) - \boldsymbol{f}(\boldsymbol{x_j})) \frac{\boldsymbol{x_i} - \boldsymbol{x_j}}{\|\boldsymbol{x_i} - \boldsymbol{x_j}\|^2} \cdot \nabla w(\boldsymbol{x_i} - \boldsymbol{x_j}, h) V_j. \tag{4.36}$$

Notice that only the first derivative of the kernel function is used in order to avoid stability issues. In counterpart, if this formulation conserves exactly the linear momentum, the angular momentum is not fully conserved.

4.3.5 Accuracy of SPH differential operators

Accuracy of discrete operators presented above directly depends on the particle distribution. SPH estimation improves increasing the number of particles within the smoothing kernel but also reducing the smoothing length according to equation (4.12). Hence, a balance between computational efficiency and accuracy must be found.

Moreover, SPH discrete differential operators are not first–order accurate. It is possible to increase their order of accuracy through a renormalization method initially proposed in Randles et al. [1996]. In order to reach first–order consistency for gradient and divergence operators, the following equality must be verified

$$-\sum_{j \in \boldsymbol{n}} V_j (\boldsymbol{x_i} - \boldsymbol{x_j}) \otimes (\mathbf{L_i} \cdot \nabla w(\boldsymbol{x_i} - \boldsymbol{x_j}, h)) = \mathbf{I}, \tag{4.37}$$

where $\mathbf{L_i}$ is the renormalization matrix of size $d \times d$ for a particle i and $\mathbf{I}$ the second order identity tensor. This matrix is given by

$$\mathbf{L_i} = \left[\sum_{j \in n} V_j (\boldsymbol{x_j} - \boldsymbol{x_i}) \otimes \nabla w(\boldsymbol{x_i} - \boldsymbol{x_j}, h) \right]^{-T}. \tag{4.38}$$

Finally, the renormalized kernel gradient becomes

$$\tilde{\nabla} w(\boldsymbol{x_i} - \boldsymbol{x_j}, h) = \mathbf{L_i} \cdot \nabla w(\boldsymbol{x_i} - \boldsymbol{x_j}, h). \tag{4.39}$$

Hereinafter, the renormalized kernel gradient $\tilde{\nabla} w$ is used but to make notation less cluttered the tilde symbol is dropped. Several other methods can be found in the literature to improve accuracy of first and second order differential operators. Readers can refer for instance to Fatehi et al. [2011] who proposed an improved second derivative scheme. However, they are usually computationally expensive and were not considered in this work.

4.3.6 Definition of the kernel function

Kernel functions are usually bell–shaped functions that monotonically decrease with the distance to the interpolation point, so that the interpolation is smooth (fig. 4.2). By analogy with FE method, kernel functions can be seen as shape functions without connectivity. They must be at least $\mathbf{C}^1$, where $\mathbf{C}^1$ is the space of continuously differentiable functions, in order to compute interpolation of the fields derivatives. In SPH method both kernel function with infinite and finite (or compact) support can be used. However, for computational efficiency reasons only kernels with compact support are considered in practice. The size of the compact support Ω_h is defined by the smoothing length h. Thus kernels are locally defined and for two points $\boldsymbol{x}$ and $\boldsymbol{x'}$, $w(\boldsymbol{x} - \boldsymbol{x'}, h) = 0$ for $\|\boldsymbol{x} - \boldsymbol{x'}\| \geqslant kh$ where $k \in \mathbb{R}$. They are also radial $w(\boldsymbol{x} - \boldsymbol{x'}, h) = w(\|\boldsymbol{x} - \boldsymbol{x'}\|, h)$ and symmetric $w(\boldsymbol{x} - \boldsymbol{x'}, h) = w(\boldsymbol{x'} - \boldsymbol{x}, h)$. This means in practice that particles from same distance but different positions have equal effect on a given particle.

Fig. 4.2 – Example of bell–shaped function

On fig. 4.3, a two–dimensional scheme of kernel compact support of radius kh for a particle i is shown. We denote $x_{ij} = \|\boldsymbol{x_i} - \boldsymbol{x_j}\|$ the distance from the particle i to its neighbor j.

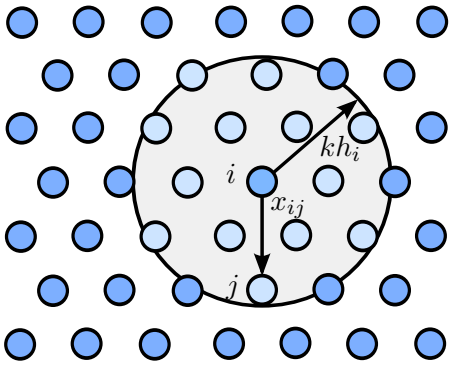

Fig. 4.3 – Neighbors of a particle i with its kernel support

We define the following notations

$$w(x,h) = \frac{\alpha}{h^d}\psi(q) \quad \text{with} \quad q = \frac{\|\boldsymbol{x} - \boldsymbol{x'}\|}{h}, \tag{4.40}$$

where α is a normalization constant and, for the record, $d = \{1, 2, 3\}$ is the dimension of the problem. One of the first and most intuitive choice for the kernel was the Gaussian function, such that

$$\psi(q) = \begin{cases} \mathrm{e}^{-q^2}, & 0 \leqslant q \leqslant 3 \\ 0, & q > 3 \end{cases} \tag{4.41}$$

and $\alpha = \dfrac{1}{\pi^{\frac{d}{2}}}$.

The Gaussian kernel is not a exactly compact support kernel because even approaching zero rapidly, it never becomes null theoretically. Hence, in practice its compact support is usually fixed to $3h$ ($k = 3$). A modified Gaussian function with compact support, called super–Gaussian, also exists in the literature [Liu et al. 2010]. However, it is also possible to build polynomial functions having the required properties and a lower computational cost. One of the most used polynomial kernel is the cubic spline kernel introduced in Monaghan [1992] as

$$\psi(q) = \begin{cases} 1 - \dfrac{3}{2}q^2 + \dfrac{3}{4}q^3, & 0 \leqslant q \leqslant 1 \\ \dfrac{1}{4}(2-q)^3, & 1 < q \leqslant 2 \\ 0, & q > 2 \end{cases} \tag{4.42}$$

and $\alpha = \left\{\dfrac{2}{3}, \dfrac{10}{7\pi}, \dfrac{1}{\pi}\right\}$ respectively for $d = \{1, 2, 3\}$.

The compact support size is $2h$ ($k = 2$). However, the second derivative of the cubic spline is a piecewise linear function, and consequently the stability properties can be inferior to those of smoother kernels. Thus, higher order polynomial functions, as quartic

and quintic, approximate more closely the Gaussian function and are more stable [Morris 1995]. In particular the quintic spline kernel is defined as

$$\psi(q) = \begin{cases} (3-q)^5 - 6(2-q)^5 + 15(1-q)^5, & 0 \leqslant q \leqslant 1 \\ (3-q)^5 - 6(2-q)^5, & 1 < q \leqslant 2 \\ (3-q)^5, & 1 < q \leqslant 2 \\ 0, & q > 2 \end{cases} \tag{4.43}$$

and $\alpha = \left\{ \frac{1}{120}, \frac{7}{478\pi}, \frac{3}{359\pi} \right\}$ respectively for $d = \{1, 2, 3\}$.

The compact support size is $3h$ ($k = 3$). Many other kernel functions exist in the literature. Several kernel functions were implemented in this work including Gaussian and cubic spline but we exclusively use in the following the 5^{th} order Wendland kernel introduced in Wendland [1995]. This kernel function is defined as

$$\psi(q) = \begin{cases} \left(1 - \frac{q}{2}\right)^4 (1 + 2q), & 0 \leqslant q \leqslant 2 \\ 0, & q > 2 \end{cases} \tag{4.44}$$

and $\alpha = \left\{ \frac{3}{4}, \frac{7}{4\pi}, \frac{21}{16\pi} \right\}$ respectively for $d = \{1, 2, 3\}$.

The compact support size is $2h$ ($k = 2$). The quintic Wendland kernel is known to be computationally efficient and shows very good performances and stability [Dehnen et al. 2012].

The derivative of a kernel function is defined following

$$\nabla w(\boldsymbol{x} - \boldsymbol{x'}, h) = \frac{\partial w(\boldsymbol{x} - \boldsymbol{x'}, h)}{\partial \boldsymbol{x}} = \frac{\boldsymbol{x} - \boldsymbol{x'}}{\|\boldsymbol{x} - \boldsymbol{x'}\|} \frac{\alpha}{h^d} \frac{\partial \psi(q)}{\partial q}. \tag{4.45}$$

For the above Wendland function we obtain

$$\frac{\partial \psi(q)}{\partial q} = \begin{cases} -5q \left(1 - \frac{q}{2}\right)^3, & 0 \leqslant q \leqslant 2 \\ 0. & q > 2 \end{cases} \tag{4.46}$$

Plots of the non–normalized 5^{th} order Wendland kernel and its first derivative are shown on fig. 4.4.

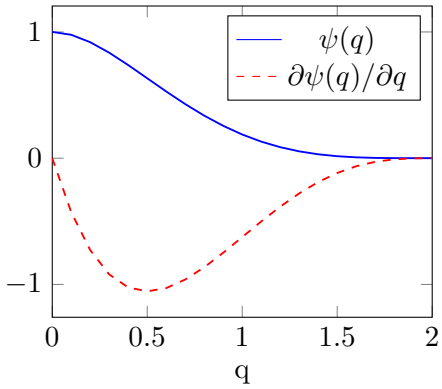

Fig. 4.4 – Plot of the non–normalized 5$^{\text{th}}$ order Wendland kernel and its derivative

4.3.7 Fluid discretization

In order to make notation less cluttered we denote hereinafter for two particles i and j, $x_{ij} = \|\boldsymbol{x_i} - \boldsymbol{x_j}\|$, $w_{ij} = w(\boldsymbol{x_i} - \boldsymbol{x_j}, h)$, $\nabla w_{ij} = \nabla w(\boldsymbol{x_i} - \boldsymbol{x_j}, h)$ and for any scalar or vector field respectively $f_{ij} = f_i - f_j$ and $\boldsymbol{f_{ij}} = \boldsymbol{f_i} - \boldsymbol{f_j}$.

Smoothing length

Smoothing length can be constant and equal for all particles or vary with time and location. In case of a variable smoothing length, h is usually symmetrized according to Benz [1990] such as, for two particles i and j

$$h_{ij} = \frac{1}{2}(h_i + h_j), \tag{4.47}$$

with the smoothing kernel which becomes $w_{ij} = w(\boldsymbol{x_{ij}}, h_{ij})$. Another approach, computationally more expensive because it involves the evaluation of two kernel functions, would be $w_{ij} = \frac{1}{2}(w(\boldsymbol{x_{ij}}, h_i) + w(\boldsymbol{x_{ij}}, h_j))$. The smoothing length h_i is obtained from

$$\frac{4}{3}\pi h_i^3 \rho_i = \bar{n}\bar{m}, \tag{4.48}$$

where $\bar{m}$ is the average particle mass and $\bar{n}$ the number of expected neighbors to be defined. Using variable smoothing length, time derivative of h may be incorporated for exact energy and entropy conservation. Readers can for instance refer to Benz [1990] for further information. However, a constant smoothing length was used in this work since fluid density is constant.

Density

The fluid density can be computed directly from the continuum equations using the mass conservation (4.1) and the divergence estimator (4.32). The time derivative of the

density for a particle i gives

$$\frac{\partial \rho_i}{\partial t} = \sum_{j \in \boldsymbol{n}} m_j \boldsymbol{v_{ij}} \cdot \nabla w_{ij}. \tag{4.49}$$

This equation, that can be approximated using a finite difference scheme in a time step interval, does not exactly conserve mass due to numerical errors. Density can also be approximated directly from SPH interpolation (4.18). Hence, one can obtain the simple expression

$$\rho_i = \sum_{j \in \boldsymbol{n}} m_j w_{ij}. \tag{4.50}$$

However, this equation suffers from major issues close to fluid interfaces and especially to free surface, induced by the truncated kernel support (*i.e.* lack of neighbors particles in the kernel support). In case of a truly incompressible fluid, density computation may be avoided.

Viscous stress

The viscous stress term for a particle i can be obtained from the Laplacian estimator (4.36), which gives

$$\nu \nabla^2 \boldsymbol{v_i} = \frac{2\mu}{\rho_i} \sum_{j \in \boldsymbol{n}} \boldsymbol{v_{ij}} \frac{\boldsymbol{x_{ij}}}{x_{ij}^2} \cdot \nabla w_{ij} V_j. \tag{4.51}$$

Another approach avoiding the low accuracy Laplacian estimation can be used by applying directly the divergence operator to gradient operator since $\nabla^2(\bullet) = \nabla \cdot (\nabla(\bullet))$, so that using equation (4.33)

$$\nu \nabla^2 \boldsymbol{v_i} = \mu \sum_{j \in \boldsymbol{n}} m_j \left(\frac{\nabla \boldsymbol{v_i}}{\rho_i^2} + \frac{\nabla \boldsymbol{v_j}}{\rho_j^2} \right) \cdot \nabla w_{ij}, \tag{4.52}$$

with the velocity gradient that can be obtained from (4.28). However, this method involves two sums over the neighbors which is computationally expensive. For a multiphase flow or more generally a varying viscosity, μ should be replaced by $\dfrac{\mu_i + \mu_j}{2}$.

Pressure gradient

The pressure gradient can be computed from the symmetric expression (4.30) as

$$\frac{\nabla p_i}{\rho_i} = \sum_{j \in \boldsymbol{n}} m_j \left(\frac{p_i}{\rho_i^2} + \frac{p_j}{\rho_j^2} \right) \nabla w_{ij}. \tag{4.53}$$

4.3.8 Incompressible SPH

Two incompressible SPH schemes were implemented, with an implicit and an explicit resolution of the pressure Poisson equation.

Semi–implicit

The classical ISPH (Incompressible SPH) scheme was initially proposed by Cummins et al. [1999]. ISPH uses a projection method introduced by Chorin [1968] to solve the discretized equations and keep a divergence–free velocity. The projection method is divided into two parts, a prediction step and a correction step. The prediction step computes the viscous and body forces when the correction step corrects them adding the pressure force. We subsequently consider a time discretization between $[t, t+\Delta t]$ corresponding to the consecutive increments n and $n+1$. The intermediate fields corresponding to the prediction step are denoted $(\bullet)^*$. A general form of the algorithm is given by alg. 3. The predictor–corrector scheme is based on Euler method, so that

$$\frac{\boldsymbol{v}^{n+1} - \boldsymbol{v}^*}{\Delta t} = -\frac{1}{\rho}\nabla p^{n+1}, \tag{4.54}$$

and by applying the divergence operator using the incompressiblity condition $\nabla\cdot\boldsymbol{v}^{n+1} = 0$,

$$\nabla \cdot \left(\frac{1}{\rho}\nabla p^{n+1}\right) = \frac{\nabla \cdot \boldsymbol{v}^*}{\Delta t}. \tag{4.55}$$

From equation (4.35), the Laplacian operator of the pressure Poisson equation (4.55) can be discretized for all particles i following

$$\nabla^2 p_i^{n+1} = 2\sum_{j\in\boldsymbol{n}} \frac{\boldsymbol{x_{ij}}}{x_{ij}^2}\cdot\nabla w_{ij} p_{ij} V_j. \tag{4.56}$$

Algorithm 3 ISPH solver at increment n

procedure ISPH($\boldsymbol{x}^n$, $\boldsymbol{v}^n$, p^n)
  while $t < t_{end}$ **do**
    $\boldsymbol{v}^* \leftarrow \boldsymbol{v}^n + \Delta t(\nu\nabla^2\boldsymbol{v}^n + \boldsymbol{g})$ ▷ using (4.51)
    $\boldsymbol{x}^* \leftarrow \boldsymbol{x}^n + \Delta t\boldsymbol{v}^n$
    $p^{n+1} \leftarrow$ from equation (4.55) ▷ using (4.56)
    $\boldsymbol{v}^{n+1} \leftarrow \boldsymbol{v}^* - \dfrac{\Delta t}{\rho}\nabla p^{n+1}$ ▷ using (4.53)
    $\boldsymbol{x}^{n+1} \leftarrow \boldsymbol{x}^n + \dfrac{\Delta t}{2}(\boldsymbol{v}^{n+1} + \boldsymbol{v}^n)$
    $t \leftarrow t + \Delta t$
    $n \leftarrow n + 1$
  return $\boldsymbol{x}^{n+1}$, $\boldsymbol{v}^{n+1}$, p^{n+1}

The linear system to solve can be written as

$$\mathbf{M}\boldsymbol{p} = \boldsymbol{R}, \tag{4.57}$$

where $\mathbf{M}$ is the system matrix, $\boldsymbol{p}$ is the pressure vector of unknowns and $\boldsymbol{R}$ is the residual vector. From equation (4.56), one can obtain the following matrix terms

$$\begin{cases} M_{ii} = 2\sum\limits_{j\in\boldsymbol{n}} \dfrac{\boldsymbol{x_{ij}}}{x_{ij}^2} \cdot \nabla w_{ij} V_j, \\ M_{ij} = -2\dfrac{\boldsymbol{x_{ij}}}{x_{ij}^2} \cdot \nabla w_{ij} V_j. \end{cases} \tag{4.58}$$

According to (4.55) and using the divergence operator (4.32), the residual vector terms are obtained from

$$R_i = \frac{1}{\Delta t}\sum_{j\in\boldsymbol{n}} m_j \boldsymbol{v^*_{ji}} \cdot \nabla w_{ij}. \tag{4.59}$$

The matrix $\mathbf{M}$ is built using a compressed sparse row format in order to save processing time and storage memory. The system (4.57) is preconditioned with an incomplete LU factorization (ILU(0) preconditioner) and solved iteratively with a generalized minimal residual method. A relative residual is used with a tolerance criterion set to 10^{-6}. The use of ISPH scheme requires an explicit treatment of boundary conditions and especially free–surface in order to avoid instabilities and ill conditioned matrix (see subsection 4.3.9). The ISPH scheme presented by alg. 3 is the most commonly used method, but other schemes can be found in the literature. Readers can refer for instance to Xu et al. [2009].

Explicit

The EISPH scheme for Explicit Incompressible SPH, initially introduced by Barcarolo [2013], has shown a good stability and computational efficiency [Nomeritae et al. 2016]. EISPH is very similar to the ISPH scheme, with however an explicit evaluation of the pressure Poisson equation (4.55) using a Jacobi method. According to Barcarolo [2013], using the pressure Laplacian estimator (4.56) and divergence operator (4.32) of the field $\boldsymbol{v}^*$, the pressure of a particle i can be obtained from

$$p_i^{n+1} = \frac{R_i - \sum\limits_{j\in\boldsymbol{n}} M_{ij} p_j^n}{-\sum\limits_{j\in\boldsymbol{n}} M_{ij}} \tag{4.60}$$

with M_{ij} and R_i as defined respectively in (4.58) and (4.59). Instead of the classical first–order Euler numerical procedure, a Velocity Verlet method which is one order better was chosen. A general form of the algorithm is given by alg. 4.

Algorithm 4 EISPH solver at increment n

procedure EISPH($\boldsymbol{x}^n$, $\boldsymbol{v}^n$, $\boldsymbol{a}^n$, p^n)
  while $t < t_{end}$ **do**
    $\boldsymbol{a}^* \leftarrow \nu\nabla^2\boldsymbol{v}^n + \boldsymbol{g}$ ▷ using (4.51)
    $\boldsymbol{v}^* \leftarrow \boldsymbol{v}^n + \dfrac{\Delta t}{2}(\boldsymbol{a}^n + \boldsymbol{a}^*)$
    $\boldsymbol{x}^{n+1} \leftarrow \boldsymbol{x}^n + \Delta t\boldsymbol{v}^n + \dfrac{\Delta t^2}{2}\boldsymbol{a}^n$
    $p^{n+1} \leftarrow$ from equation (4.55) ▷ using (4.56)
    $\boldsymbol{a}^{n+1} \leftarrow \boldsymbol{a}^* - \dfrac{\nabla p^{n+1}}{\rho}$ ▷ using (4.53)
    $\boldsymbol{v}^{n+1} \leftarrow \boldsymbol{v}^n + \dfrac{\Delta t}{2}(\boldsymbol{a}^{n+1} + \boldsymbol{a}^n)$
    $t \leftarrow t + \Delta t$
    $n \leftarrow n + 1$
  return $\boldsymbol{x}^{n+1}$, $\boldsymbol{v}^{n+1}$, $\boldsymbol{a}^{n+1}$, p^{n+1}

Since the pressure Poisson equation is explicitly solved using a Jacobi–like approach, several iterations are needed to converge through a stable solution. However, explicit formulations present some advantages in comparison to semi–implicit ones. Indeed, EISPH does not require the resolution of a large linear system, saving computational time, and can automatically handle free–surface conditions (subsection 4.3.9).

Displacement correction

It is known that irregular particles arrangement is responsible for numerical errors, causes instabilities and can lead to non–physical predictions. Several methods exist in the literature to improve the uniformity of the particle distribution. Two of them were implemented in this work. In the approach proposed by Monaghan [1989], the velocity of a particle i is corrected taking into account velocity of the neighboring particles such as

$$\frac{\mathrm{d}\boldsymbol{x_i}}{\mathrm{d}t} = \boldsymbol{v_i} + 2\epsilon\sum_{j\in\boldsymbol{n}}\frac{m_j}{\rho_i + \rho_j}\boldsymbol{v_{ji}}w_{ij}, \tag{4.61}$$

where ϵ is a constant parameter to be calibrated (usually between 0.01 and 1). At the end of a time increment the velocity field is updated using (4.61). Another method has been propped in Xu et al. [2009] based on shifting projection. In this method, a variable ϕ is corrected by the Taylor series expansion such as

$$\phi_i^{t+\delta t} = \phi_i^t + \delta\boldsymbol{x_i}\cdot\nabla\phi_i + O(\delta\boldsymbol{x_i}^2), \tag{4.62}$$

where $\delta\boldsymbol{x_i}$ is the distance vector between the particle's i old and new positions, respectively at time t and $t + \delta t$. The distance $\delta\boldsymbol{x_i}$ is obtained from

$$\delta \boldsymbol{x_i} = \epsilon \delta t \, \|\boldsymbol{v_{max}}\| \sum_{j \in \boldsymbol{n}} \frac{\tilde{x}_i^2}{x_{ij}^2} \boldsymbol{n_{ij}}, \tag{4.63}$$

with

$$\tilde{x}_i = \frac{1}{n_i} \sum_{j \in \boldsymbol{n}} x_{ij}. \tag{4.64}$$

ϵ is a constant parameter to be calibrated (usually between 0.01 and 0.1), δt is the time interval, $\|\boldsymbol{v_{max}}\|$ is the maximum particle velocity, $\boldsymbol{n_{ij}}$ is the normalized distance vector between two particles i and j, and n_i is the number of neighbors of i. The shifting distance must be correctly calibrated in order to prevent instability or inaccuracy that could be induced by a too small or a too large value. This value is always much lower than the smoothing length h [Xu et al. 2009]. At the end of a time increment the particles are shifted by equation (4.63) and the velocity field is corrected by equation (4.62).

4.3.9 Boundary conditions treatment

Near the boundaries particles' kernel support domain is truncated and properties (4.14) and (4.15) are not satisfied. Hence, errors are introduced and inconsistencies or penetration of fluid particles into the solid domain may occur.

Wall boundary conditions

Several methods exist in the literature for wall boundary treatment. Three main techniques are commonly used : ghost particles, repulsive force and dynamic particles (fig. 4.5).

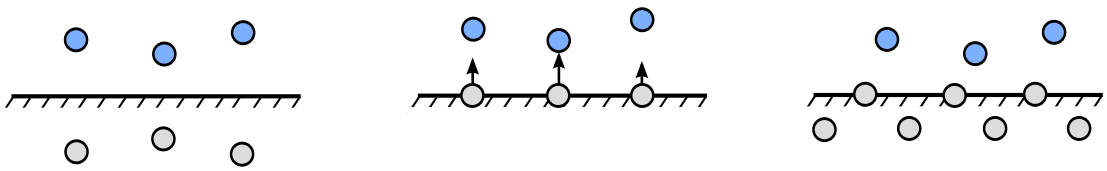

Fig. 4.5 – Illustration of three classic wall boundary conditions with from left to right : ghost particles, repulsive force and dynamic particles boundaries

The ghost (or mirror) particles method was introduced in Takeda et al. [1994]. Readers can also refer to Randles et al. [1996], Morris et al. [1997b] and more recently Bierbrauer et al. [2009], for instance. In this method, when a fluid particle is sufficiently close to a boundary to have its kernel truncated, a mirror virtual particle with same density and pressure is generated. This particle is placed at the same distance to the boundary but outside the domain, so that the kernel of the particles near the walls is not truncated anymore. Moreover, free–slip and no–slip conditions can be exactly enforced by imposing respectively an identical and an opposite velocity to the mirror particle (fig. 4.6). The

implementation of this method is however complicated since the number of mirror particles varies at each time step and complex geometries are very difficult to model.

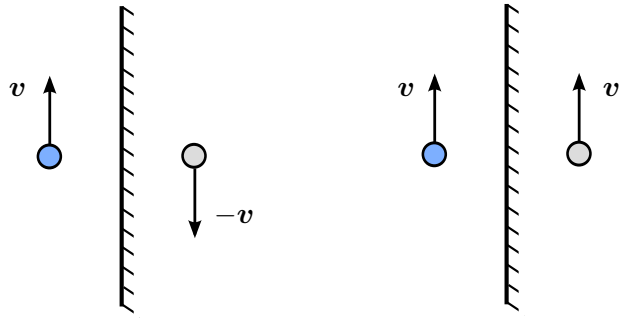

Fig. 4.6 – No–slip and free–slip wall boundary conditions from left to right

The repulsive force method was initially proposed by Monaghan [1994] in order to prevent fluid particles from penetrating walls. In this method one layer of regularly distributed solid particles with identical physical properties to the fluid part is used to model the boundaries. These wall particles exert an artificial repulsive force on the fluid particles proportional to the distance between them and in the normal direction to the solid boundary. However, if this method is computationally efficient and easy to implement even for complex geometries, kernel truncation of the fluid particles is not corrected and it is not possible to exactly enforce slipping conditions.

The dynamic particles method was introduced by Dalrymple et al. [2001]. In this method several layers of particles are used to model the walls. These additional layers allow to fill, at least partially, the truncated kernel support domain of boundary fluid particles and improve SPH interpolation consistency. Solid particles generally behave like fluid particles, with same physical properties (reference density, ...), but their position remains unchanged or is externally imposed. Thus, solving the pressure Poisson equation for all the particles generates a repulsive force near the walls. This method is also very attractive for its simplicity and computational efficiency since solid particles can be treated in same loops than fluid particles. However the number of particles increases, and once again, it is not possible to exactly enforce slipping conditions using dynamic particles.

Several improvements of these methods can be found in the literature. This list of classic wall boundary conditions is not exhaustive. Other methods exist like dummy particles (see for instance Adami et al. [2012]) or more recently boundary integrals which are semi–analytical methods to complete the kernel support domain near boundaries (one can for instance refer to Ferrand et al. [2013]). In this work dynamic boundary conditions were used due to the simplicity and efficiency of the method.

Free–surface boundary conditions

In the particular case of free–surface flow, truncation of the kernel support domain also occurs for boundary particles. Moreover, using an ISPH scheme, free–surface detection algorithms are required since a null pressure must be imposed (when the air effect and surface tension are not considered) on fluid particles belonging to the surface in order to solve the pressure Poisson equation. The main approach commonly used in the literature is to detect the free–surface by evaluating the particles density that drops due to the kernel support truncation. Thus, a density fluctuation over 1% below inner fluid value is often used as threshold (see for instance Shao et al. [2003]). Some other methods exit, like for instance a surface detection algorithm simply depending on the number of neighboring particles or more sophisticated approaches as proposed by Marrone et al. [2010] involving a level–set function.

In this work two surface detection algorithms were implemented, depending on the number of neighboring particles (in comparison to the maximum number of neighbors) and on the divergence of the position vectors [E. S. Lee et al. 2008; Bøckmann et al. 2012]. In the last method the divergence, which is evaluated by

$$\nabla \cdot \boldsymbol{x_i} = \frac{1}{\rho_i} \sum_{j \in \boldsymbol{n}} m_j \boldsymbol{x_{ji}} \cdot \nabla w_{ij}, \tag{4.65}$$

will be smaller near the surface. Thus, a particle j belongs to the surface if $\nabla \cdot \boldsymbol{x_j} < \alpha \max(\nabla \cdot \boldsymbol{x_i})$ with $\alpha \in]0,1[$ a constant parameter to be calibrated.

4.3.10 Time–stepping and numerical stability

The choice of a relevant time–step in an important numerical stability condition. The time–step can be constant in case of constant smoothing length but is usually computed following

$$\Delta t = \min \left(c_{cfl} \frac{h}{\|\boldsymbol{v_{max}}\|}, c_{visq} \frac{h^2}{\nu} \right), \tag{4.66}$$

where c_{cfl} is the parameter of the Courant–Friedrichs–Lewy condition (usually around 0.1) and c_{visq} is the parameter due to viscous diffusion constraint (also around 0.1) [Shao et al. 2003].

4.3.11 Reduction of the computational time

In order to improve the computational efficiency a multi–list data structure in which the SPH particles are stored is of prime importance. The SPH algorithm needs to find and browse nearby particles of each particle to compute its variables. The objective of multi–list data structures is to easily access to each particle spatial neighborhood and

keep the memory used clustered together to improve performance. Most of the 3D–SPH code use tree structures such as octree or k–d tree (short for k–dimensional tree). These tree structures are used at the beginning of each time increment to build tables containing neighboring particles j related to each particle i (*i.e.* if $\|r_{ij}\| < kh$). For n particles, tree structures have performance which scales as $O(n \log n)$, in comparison with the $O(n^2)$ complexity without any list–like structure.

In this work a k–d tree algorithm was implemented. This is a binary tree firstly introduced in Bentley [1975] in which every node is k–dimensional, representing a subdivision of the space. The space is split using lines in 2D or planes in 3D, along one axis initially and changing the axis in a cyclic way at each level of depth. Optimally, each subdivision step should split the previous space into two subspaces containing the same number of particles in order to build a globally balanced tree. Hence, splitting entities are chosen with a normal vector corresponding to one axis of the coordinate system and going through the median of the current subspace of particles. The median is computed using particles' coordinates in the splitting entity normal direction. For each subdivision step, a signed distance from each particle to the splitting entity is computed in the normal direction to the splitting entity. All particles on one side of a splitting entity (negative signed distance) will be placed in a left subtree, and all nodes on the other side (positive signed distance) in a right subtree from the current node. Thus, each node contains a splitting entity and two subtrees. The tree is built recursively until one of the two subtrees contains the other on each branch. An example of a simple k–d tree is shown on fig. 4.7.

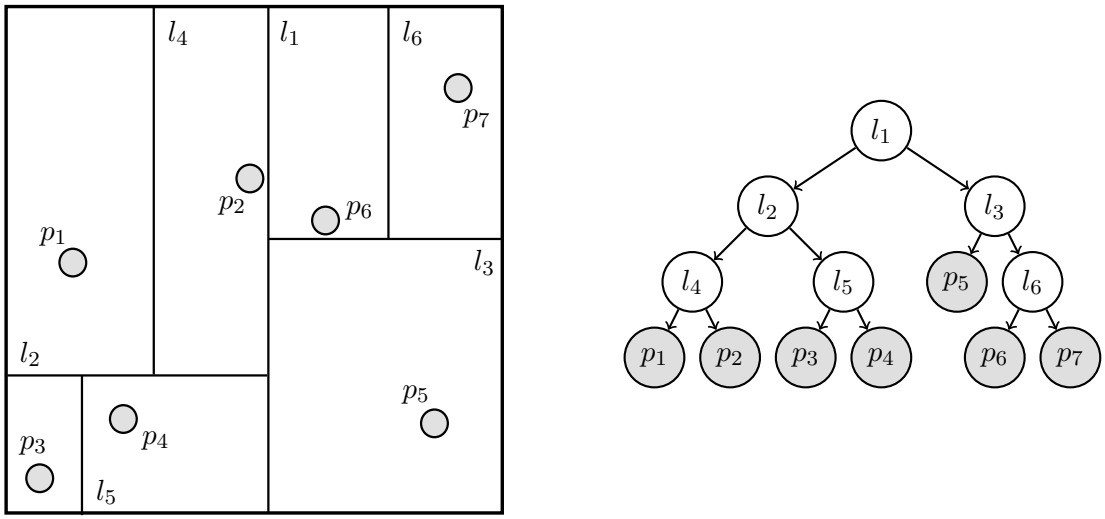

Fig. 4.7 – Illustration of k–d tree algorithm functioning in 2D where l_i represents the splitting lines and p_i the particles

Using tree properties, nearest neighbor particles can be found efficiently by quickly eliminating large areas of the search space. Reading the tree, related neighbors of each particle, *i.e.* particles located in a kh radius, are stored in lists (squared distances are used to avoid computing square roots). The neighbor search for each particle moves down the tree recursively from the root. The signed distance from current node to the stored splitting entity is computed. If the distance is lower than $-kh$, search back in the left subtree and if it is greater than kh, search back in the right subtree. Since particles located on the splitting entity are in both left and right subtrees, duplicates can occur. A recursive quicksort algorithm ($O(n \log n)$ complexity) is used to classify neighbor particles and remove duplicates choosing the middle index of the neighbor list as pivot. The tree is built at the beginning and destroyed at the end of each time increment.

Massively parallel implementation that allows to divide the domain into several subdomains affected to different CPUs (Central Processing Unit) was not considered here. However, parallelization cannot be avoided in order to perform high resolution simulations using a large number of particles and should be implemented in a future work.

4.4 SPH–FE coupling

In this section a first attempt of SPH–FE coupling between the SPH solver presented in this chapter and the FE solver of chapter 2 is introduced.

4.4.1 FSI algorithm

Considering a viscous flow and according to 4.3.9, the following Dirichlet and Neumann conditions at fluid–structure interface $\partial\Omega^{\mathrm{w}}$ must be satisfied

$$\boldsymbol{v} = \boldsymbol{v_w}, \tag{4.67a}$$

$$\boldsymbol{\sigma} \cdot \boldsymbol{n} = \boldsymbol{\sigma_{\mathbf{w}}} \cdot \boldsymbol{n}, \tag{4.67b}$$

where $\boldsymbol{n}$ is the interface outward normal vector. FSI modeling may be categorized into "monolithic" approaches and "partitioned" approaches [Hou et al. 2012]. In the monolithic approach, fluid and solid computations are made from a single system of equations solved simultaneously for the whole problem. However, even if potentially very accurate this method presents substantial implementation difficulties such as the definition of an efficient global preconditioner, and especially in an existing structural FE code since the formulation must be completely changed. In the partitioned approach, fluid and solid are treated separately by two distinct algorithms and interface information are explicitly exchanged between fluid and solid solutions. This approach offers much more flexibility

and scalability but is usually less accurate. Since, in our case, two different numerical methods are used for the FSI modeling and for feasibility reason, the latter approach was chosen.

One can also distinguish strongly and weakly coupled algorithms. If equations (4.67) are exactly satisfied at each time step the method is strongly coupled. If they are not, the method is weakly coupled. Monolithic approaches are strongly coupled while partitioned approaches often use a weakly coupled scheme, but they can also enforce equations (4.67) by using multiple sub–iterations. In case of a weakly coupled scheme, the FSI problem is explicitly solved and only a first order accuracy can be reached independently of the accuracy of the distinct solvers. Due to the explicit resolution, numerical stability highly depends on the time step and energy conservation is not ensured. However, a weakly coupled scheme was chosen in the first instance for simplicity reasons. The general principle of the implemented FSI is presented by alg. 5.

Algorithm 5 SPH–FE weak coupling

```
procedure FSI
    while t < t_end do
        generate dynamic boundary particles from solid FE mesh
        compute fluid and move particles
        transfer forces from fluid computation to surface FE
        compute solid and move FE mesh
        t ← t + Δt
        n ← n + 1
```

4.4.2 Interface coupling

Since no specific interface algorithm has been implemented, FE nodes are directly used as boundary particles locations for the SPH computation (fig. 4.8). This operation requires to generate a finite element mesh with an (almost) equivalent size to the fluid initial inter–particle distance. Hence, high resolution FSI modeling would lead to prohibitive computational time since the number of both particles and finite elements increases simultaneously. Another problem may appear in case of large solid deformation (without remeshing) due to the increasing node spacing. These issues must be addressed in a future work.

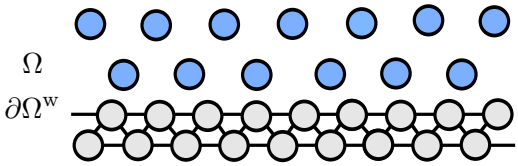

Fig. 4.8 – 2D illustration of FSI interface with fluid particles (blue) and dynamic boundary particles generated from finite element nodes (gray)

4.5 Solver validation

In this section the SPH solver implementation and its coupling with the FE hyperelastic solver presented in chapter 2 is validated and discussed.

4.5.1 SPH implementation validation

Hydrostatic pressure

In order to make sure that pressure calculation is correctly implemented on both ISPH and EISPH solvers, the pressure in a still water column was checked. Dimensions of the rectangular fluid part were 5 mm × 5 mm × 10 mm with a 0.25 mm initial particle spacing. The fluid was composed of approximately 17600 regularly arranged particles. Since the fluid was supposed to be water, a constant density $\rho = 1000$ kg.m^{-3} and a dynamic viscosity $\mu = 1.002$ mPa.s were used. The hydrostatic pressure can be simply calculated according to formula

$$p = \rho g z + p_0, \tag{4.68}$$

where g is the gravitational acceleration along the vertical direction, z is the height of water above (from the surface) and p_0 is the surface pressure. In the example presented fig. 4.9, g was set to 1 m.s^{-2} and $p_0 = 0$. We denote $H = 10$ mm the total height of the liquid column. The pressure at $z = 10$ mm as a function of time and the pressure at $t = 1$ s as a function of depth are respectively shown on fig. 4.10 and fig. 4.11. For both ISPH and EISPH solvers, a good agreement with the theoretical solution was found at the end of the simulation. However, the pressure explicitly computed in the EISPH solver needs more iterations to stabilize as it can be seen on fig. 4.10.

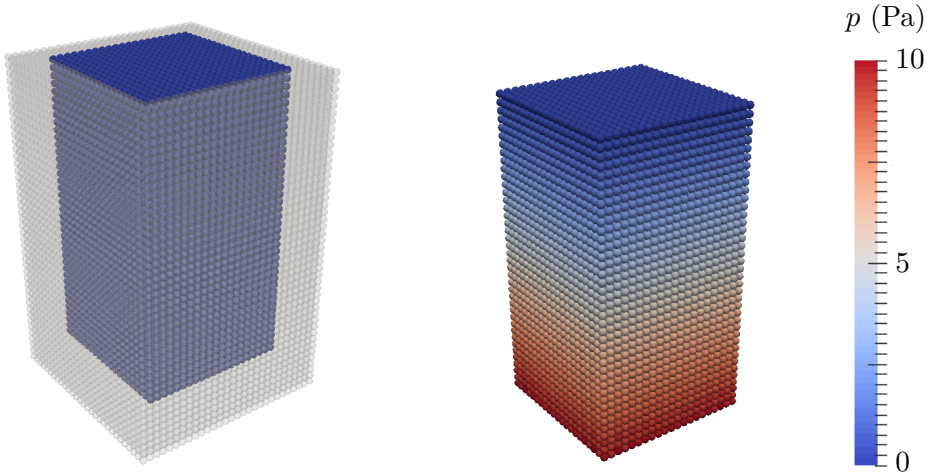

(a) Initial configuration **(b)** Pressure gradient at $t = 1$ s

Fig. 4.9 – Illustration of the hydrostatic pressure in a water column (dynamic boundary particles are represented in transparent gray)

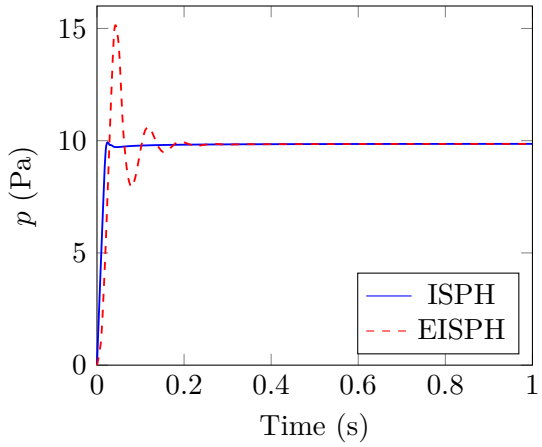

Fig. 4.10 – Evolution of the hydrostatic pressure versus time for $z = 10$ mm

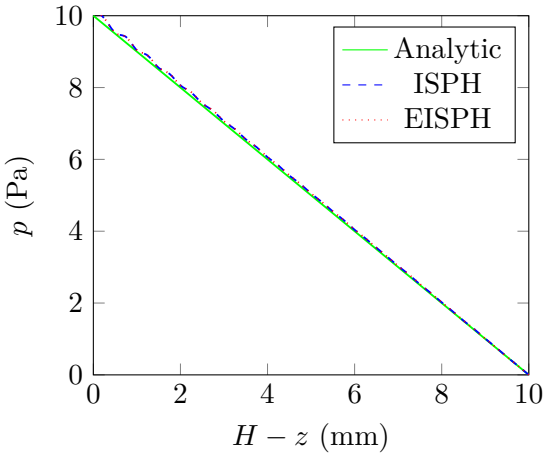

Fig. 4.11 – Evolution of the pressure along the vertical direction

Poiseuille flow

The velocity calculation was checked considering a Poiseuille flow. A portion of tube of 5 mm length and with an internal diameter of 5 mm too was modeled. The fluid part was composed of 6500 regularly arranged particles with an initial particle spacing of 0.25 mm. Same fluid properties as presented above were chosen. The laminar flow through a pipe was induced by a constant body force g oriented along the tube axis. The steady velocity field as a function of the radius is given by the formula

$$v = \frac{1}{4\mu}\frac{\Delta p}{\Delta z}(R^2 - r^2), \tag{4.69}$$

where R is the pipe radius and $r \in [0, R]$ the radius of the lamina from the center of the tube. One can notice that $v = v_{max}$ for $r = 0$. The imposed body force g was defined as a function of the Reynolds number following

$$g = \frac{8\mu^2 \mathrm{Re}}{\rho^2 R^3}, \tag{4.70}$$

where $\mathrm{Re} = \dfrac{\rho l \bar{v}}{\mu}$ is the Reynolds number with $\bar{v}$ the mean flow velocity and l the characteristic length. In the case of a Poiseuille flow, $\bar{v} = \dfrac{v_{max}}{2}$ and $l = R$. An illustration of the Poiseuille flow modeling is presented on fig. 4.12 showing the norm of the velocity field for $\mathrm{Re} = 0.5$. An example of the evolution of the maximum velocity as a function of time is presented on fig. 4.13. In that example, position of fluid particles was not actualized at the end of each time step since only a small portion of tube is modeled. A comparison of the analytic and computed steady velocity profiles is shown fig. 4.14 for several Reynolds numbers. ISPH and EISPH solvers showed similar results and a good agreement with the theoretical solution at the end of the simulation.

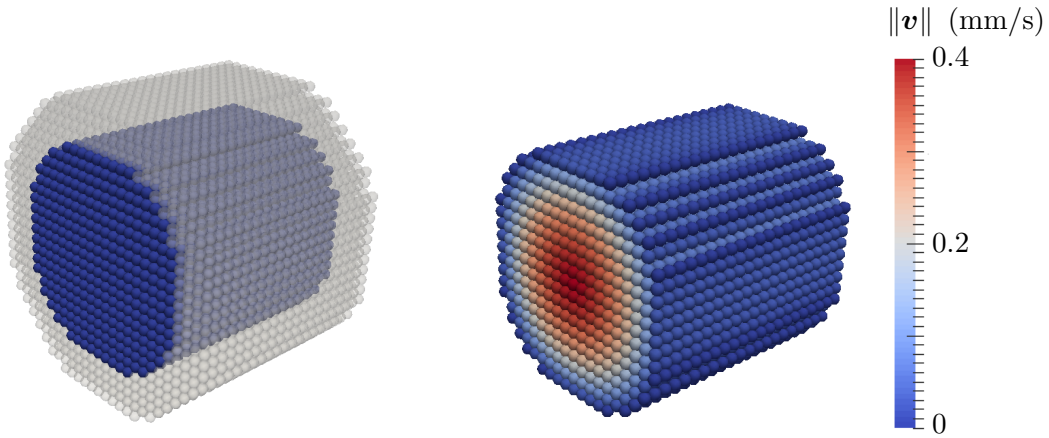

(a) Initial configuration **(b)** Velocity profile at $t = 10$ s

Fig. 4.12 – Illustration of a Poiseuille flow for $\mathrm{Re} = 0.5$ (dynamic boundary particles are represented in transparent gray)

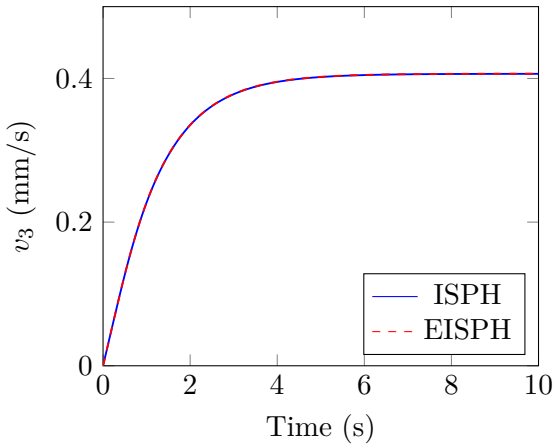

Fig. 4.13 – Evolution of the maximum Poiseuille velocity flow along E_3 versus time for $\mathrm{Re} = 0.5$

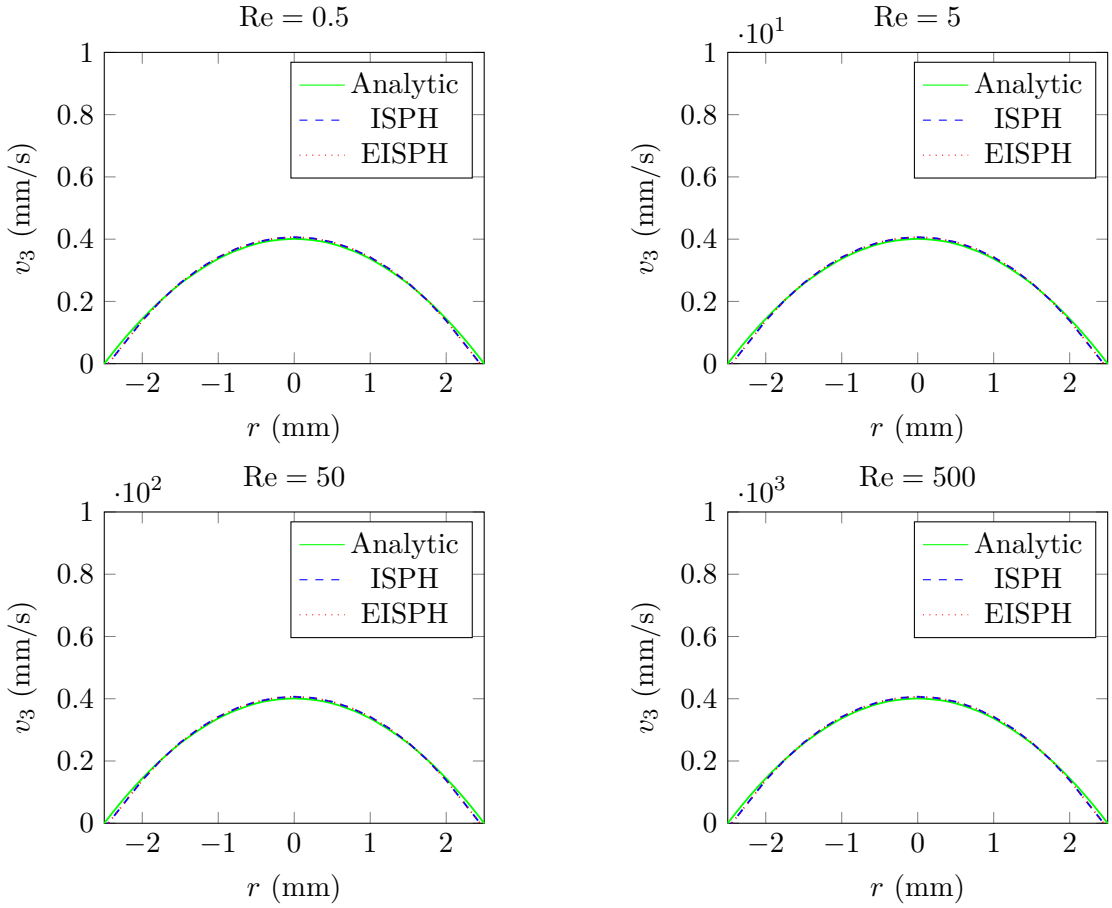

Fig. 4.14 – Velocity profiles for a Poiseuille flow at several Re and comparison with the theoretical solution

4.5.2 SPH–FE coupling validation

The convergence of the FSI modeling was tested on a simple case. In this simulation, blood flows in a deformable artery modeled with a pipe geometry containing a strip in the middle (supposed to represent a kind of leaflet). The pipe has a diameter of 20 mm, a length of 50 mm and a thickness of 2 mm. The strip has a length and width of 10 mm and a thickness of 2 mm. Both were modeled with 0.5 mm elements. For the solid part, a quasi–incompressible neo–Hookean constitutive model was used with a material parameter set to $c_0 = 2$ kPa and a fictive Poisson's ratio to $\upsilon = 0.4995$. Blood, in its initial position was modeled using a cylinder with a diameter of 20 mm and a length of 24 mm. The fluid was discretized using about $5 \cdot 10^4$ particles with an initial particle spacing of 0.5 mm. A Newtonian fluid was used with a density of 1060 kg.m^{-3} and a viscosity of 3 mPa.s which is a reasonable approximation for large arteries [J. K. J. Li 1988; Borazjani 2013]. The flow was assumed with a Reynolds number of 1553 as indicated in J. K. J. Li

[1988] for a man of 70 kg. The fluid was initially positioned on one side of the strip (fig. 4.15). Hence, when blood flows, the strip deforms under fluid pressure. The EISPH solver was used for its simplified treatment of free–surface conditions. For each solid time step Δt, a constant number of 100 sub–iterations was chosen in the fluid solver (*i.e.* with a time step of $\Delta t \cdot 10^{-2}$). Moreover, despite the loss of accuracy, only a single layer of elements nodes was used as solid dynamic boundary particles in order to reduce the computational time (corresponding to about 28000 particles). Steps of the FSI simulation are shown on fig. 4.16 and fig. 4.17, respectively at $t = 0.4$ s and $t = 0.6$ s.

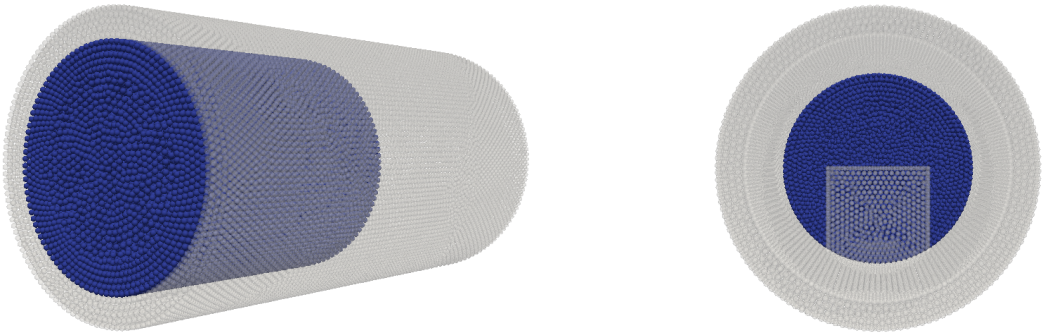

(a) Oblique view **(b)** Front view

Fig. 4.15 – Representation of the initial configuration with blood particles in blue and dynamic boundary particles in transparent gray

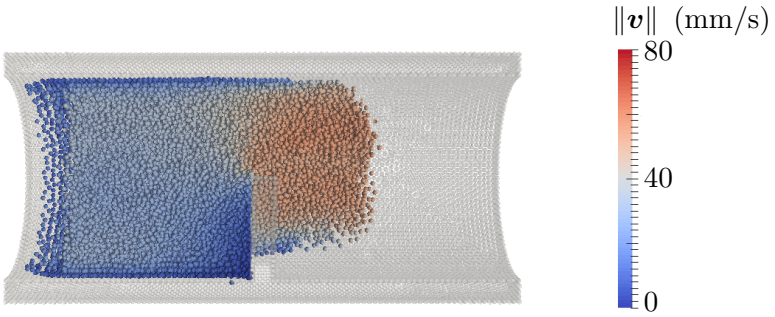

(a) Norm of the fluid velocity field $\|\boldsymbol{v}\|$

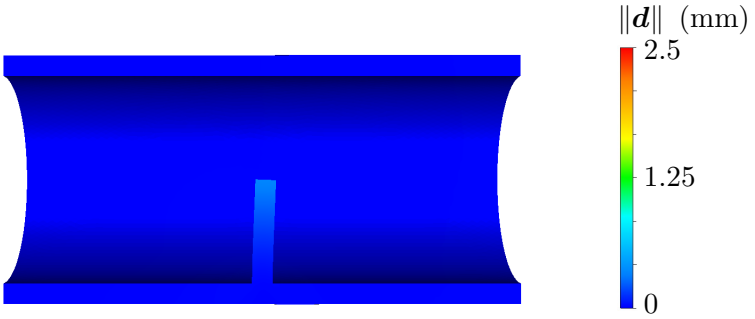

(b) Norm of the solid displacement field $\|\boldsymbol{d}\|$

Fig. 4.16 – FSI illustration at $t = 0.4$ s (longitudinal cutting plane view)

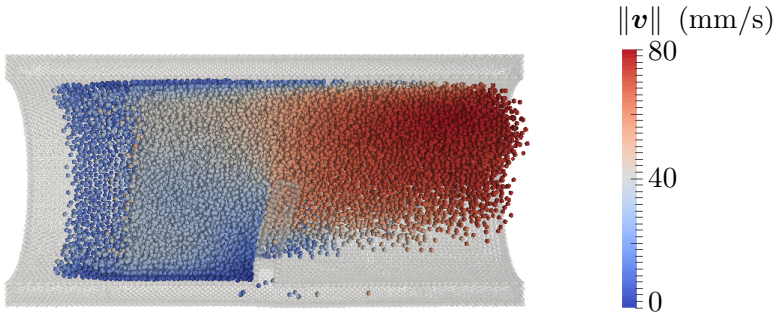

(a) Norm of the fluid velocity field $\|\boldsymbol{v}\|$

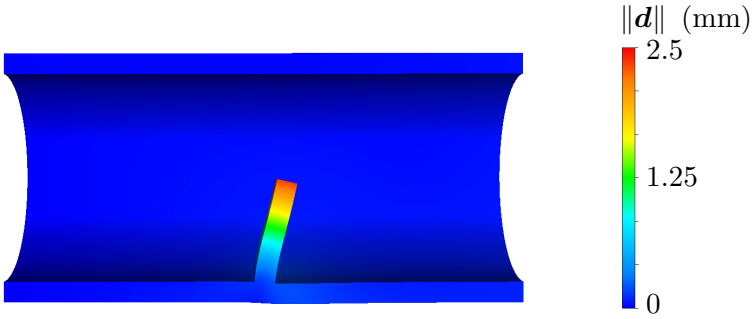

(b) Norm of the solid displacement field $\|\boldsymbol{d}\|$

Fig. 4.17 – FSI illustration at $t = 0.6$ s (longitudinal cutting plane view)

Due to the monolayer dynamic boundary, penetration of fluid particles into the solid domain occurs in areas with high particle concentration and pressure as shown on fig. 4.18. This issue should be addressed by adding solid particles layers in order to increase the wall repulsive force.

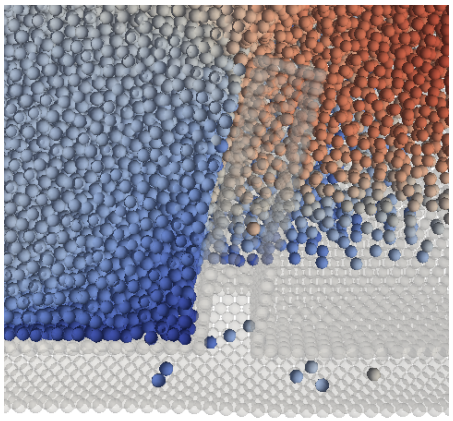

Fig. 4.18 – Fluid–structure interface issues

4.6 Summary of Chapter 4

In order to simulate the opening and closing kinetic of a prosthetic heart valve, the blood flow must be accurately modeled. Thus, a fluid solver was implemented and coupled to the finite element solver presented in chapter 2. A Lagrangian meshless method, called Smoothed Particle Hydrodynamics (SPH), was chosen for its relative simplicity and its flexibility. In this method, the domain is discretized into a set of particles where the physical properties are estimated using a kernel function. The solver presented in this chapter is dedicated to the modeling of incompressible Newtonian fluids and laminar flows. Two formulations of the literature were implemented, a semi–implicit formulation (ISPH) and an explicit formulation (EISPH). Finally, the fluid and solid solvers were weakly coupled and the implementation was checked trough several numerical tests.

However, this work is a preliminary study that should be improved and enriched in the future. In particular, even though a data structure (k–d tree) was implemented to optimize the neighbor search and to reduce computational time, it remains prohibitive due to the sequential implementation of the SPH solver. High computational time requires to decrease the number of particles and consequently to decrease resolution of the modeling. Hence, a parallelization of the existing code is necessary. Another limitation is the fluid–structure coupling formulation that should be improved to ensure a better energy conservation and computational robustness.

Due to these limitations, the modeling of a complete valve prosthesis subjected to a blood flow could not be carried out. Nevertheless, most of the necessary elements are now available.

4.7 Résumé en français

Afin de simuler la cinétique d'ouverture et de fermeture d'une prothèse de valve cardiaque en fonctionnement, le flux sanguin doit être modélisé. Ainsi, un solveur fluide a été implémenté et couplé au solveur éléments finis présenté dans le chapitre 2. Le choix s'est porté sur une méthode sans maillage Lagrangienne appelée Smoothed Particle Hydrodynamics (SPH) pour sa relative simplicité et sa grande flexibilité. Dans cette méthode, le domaine modélisé est discrétisé en particules sur lesquelles les propriétés physiques sont estimées à l'aide d'un noyau. Le solveur présenté dans ce chapitre est dédié à la modélisation des fluides Newtoniens incompressibles en écoulement laminaire. Deux formulations de la littérature ont été implémentées, l'une semi–implicite (ISPH) et l'autre explicite (EISPH). Finalement, un couplage faible a été réalisé entre les solveurs fluide et solide et l'implémentation a été vérifiée à travers plusieurs tests numériques.

Ce travail demeure néanmoins un travail préliminaire et devra être amélioré et enrichi par la suite. En particulier, bien qu'une structure de données (arbre k–d) ait été implémentée pour optimiser la recherche de voisins et ainsi diminuer les temps de calcul, ceux–ci restent prohibitifs du fait de l'implémentation séquentielle du solveur SPH. Les temps de calcul trop importants imposent de diminuer le nombre de particules avec pour conséquence de baisser la résolution de la modélisation. Ainsi, une parallélisation du code existant s'impose. Une autre limitation est le couplage fluide–structure dont la formulation devra être améliorée afin d'assurer une meilleure conservation de l'énergie à l'interface et une plus grande robustesse.

Ces limitations font que la modélisation d'une prothèse de valve complète soumise à un flux sanguin n'a pas pu être réalisée. Néanmoins, la plupart des éléments nécessaires pour y parvenir sont à présent disponibles.

Conclusions and outlook

Achievements

This work aims to develop experimental and numerical tools for the mechanical characterization and the numerical modeling of aortic valve tissues. These tools are intended to be used for the development of new biomimetic polymeric films for prosthetic valves. Experimental tools are necessary to better understand the mechanical behavior of valvular tissues at a macroscopic level in order to be able to produce adapted synthetic materials, while numerical tools are intended to assist the design phase of new implants by predicting their mechanical in–use properties. To reach these objectives, several tasks were achieved.

Mechanical characterization Treated porcine valvular tissues are commonly used for biological prostheses and have proven their excellent hemodynamic properties despite their limited durability. Hence, mechanical properties of engineered polymeric films should tend toward natural ones improving durability in comparison to treated tissues. The first part of this work aims to provide an experimental protocol and relevant tissue–level results for future developments. Biaxial mechanical tensile tests are performed on six frozen and six fresh porcine aortic valve leaflets using a custom device designed at the laboratory for the purpose of this study. The experiments are associated to a digital image correlation system for full–field surface measurements on samples excised from the central region of the leaflets. In accordance with the literature, results show an anisotropic hyperelastic mechanical behavior with a strong coupling between the tensile axes (*i.e.* circumferential and radial). Measured strain fields are highly heterogeneous near the rakes but relatively homogeneous in the 25% central area of the samples. Moreover, freezing appears to substantially damage the tissues with a meaningful impact on their mechanical properties. Hence, the rest of this work focuses on fresh leaflets.

Fibers orientation measurement The second part of this work aims to provide microstructural information to be related to the macroscopic behavior of the tissues. According to the literature, the stiffness of the tissues is mainly induced by the collagen structure. Thus, collagen fibers arrangement is of prime importance to better understand

the overall tissue behavior and for the development of biomimetic materials. Collagen fibers from the fibrosa layer, which is the main layer responsible for the mechanical behavior of the leaflet, are observed using a confocal microscope. The study is made at the Hubert Curien laboratory (Saint–Étienne, France). A series of images are taken at several locations on two samples. The highly aligned fibrous arrangement allows to extract a preferred fibers orientation in the tissue plane for each picture. These measurements are then interpolated on the whole surface. In accordance with the literature, collagen fibers in the fibrosa are found mainly oriented along the circumferential direction with however large local disparities.

Structure solver The first requirement for the modeling of valvular tissues is the implementation of relevant numerical methods and constitutive models. Developments are made in a custom laboratory version of the finite element software FORGE®. An hyperelastic solver is implemented using an updated Lagrangian method in the finite strain framework and a mixed velocity–pressure formulation. Moreover, the bubble stabilization of the linear tetrahedron elements is adapted to the hyperelastic framework. Three hyperelastic orthotropic material models of the literature are implemented and validated. These models are able to take into account some structural information, like a local statistical fibers distribution that confers anisotropic properties to the material. Both incompressible and quasi–incompressible formulations are also available.

Orientation algorithm The proper modeling of complex materials requires an accurate modeling of its fibrous structure. Assuming that observed local principal fibers orientations can be correlated to the anisotropy directions of the models, an algorithm is developed to transpose measured planar orientations to a complex 3D finite element mesh. This algorithm is used at the beginning of the finite element computation to define an initial (*i.e.* in the unloaded state) statistical fibers distribution on each element from experimental measurements.

Parameters identification In order to assess the ability of the implemented models to reproduce the mechanical response of valvular tissues, an inverse analysis procedure is carried out using a kriging metamodel–assisted evolutionary algorithm developed at the laboratory. Thus, the biaxial tensile test is modeled using a simplified geometry of a sample. The fibers distribution measured from confocal images is transposed on the finite element mesh using the orientation algorithm. Finally, displacements obtained from digital image correlation are imposed at the boundary conditions and the inverse analysis procedure is carried out on measured forces on each axis. A first inverse analysis procedure is conducted to select the most relevant model. A second one studies the influence of the number of observables on the model calibration and predictability. The proposed constitutive model demonstrate its ability to fit a large number of experimental

loadings, and therefore its ability to model such materials.

Fluid solver The simulation of the opening and closing kinetics of prosthetic valves is intended to predict their mechanical response in operation. Hence, this part aims to provide a fluid solver for modeling blood flow. A smoothed particle hydrodynamics Lagrangian meshless method is chosen for its relative simplicity and its flexibility. This method is particularly interesting for its ability to intrinsically handle complex interface problems, such as leaflets opening and closing movements. As a first approximation, blood is supposed to be an incompressible Newtonian fluid and blood flow is assumed to be laminar. Two formulations of the literature, a semi–implicit and an explicit one, are implemented and validated.

Fluid–structure interaction In the last part of this work, a first attempt of fluid–structure interaction is proposed with the coupling of the implemented solvers. For feasibility reasons, a weakly coupled approach is chosen. Fluid–structure interaction results are obtained but several improvements remain to be done for the modeling of a whole prosthetic heart valve subjected to blood flow.

Future work

Several improvements of the present work should be considered. Some possible perspectives are subsequently proposed. These suggestions do not pretend to be exhaustive.

Short–term suggestions Several aspects should be improved to be able to simulate a prosthetic valve in–use. In particular, the inflow–outflow conditions of the smoothed particle hydrodynamics solver require improvements, especially the application of pressure conditions. Indeed, pressure conditions from the Wiggers diagram should be imposed at inlet–outlet boundaries to accurately model the blood stream into an artery. Another important aspect is the fluid–structure interaction formulation that should be enhanced to ensure a better energy conservation and computational robustness. Moreover, the implementation of the fluid solver is currently sequential and must be parallelized to improve computational efficiency and allow large scale computation.

Mid–term suggestions An interesting prospect, in the case of mimetic development of polymeric materials, would be the implementation of multiscale material models. Multiscale approaches require the definition of a representative elementary volume, which is very challenging with natural tissues but could be potentially easier with engineered ones. Such physically based methods could considerably improve the modeling accuracy and predictability if coupled with relevant homogenization techniques. Another suggestion would be the modeling of multilayer materials inspired from natural tissues. However,

if a multilayer modeling do not requires additional developments, it requires a deeper understanding of valvular tissues and to perform additional experiments for mechanical characterization of each layer. Finally, a non–Newtonian blood rheology should be implemented in order to better capture its complex behavior.

Appendix A

Device protocol

A.1 Introduction

This appendix explains the mounting of a tissue sample on the biaxial tensile test device presented in chapter 1.

A.2 Protocol

An aortic valve leaflet is excised from a porcine heart and immersed into 0.9% isotonic saline (NaCl) during the preparation of the experiment (fig. A.1a). Shortly before the experiment the sample is taken out of the isotonic saline. The surface of the sample is quickly dried with a jet of compressed air and black ink is sprayed using an airbrush at low pressure (0.5 bar with a 0.5 mm pipe) until the speckle pattern uniformly covers the surface (fig. A.1b). The specimen is then dried for less than five minutes at ambient air before being mounted on the biaxial device.

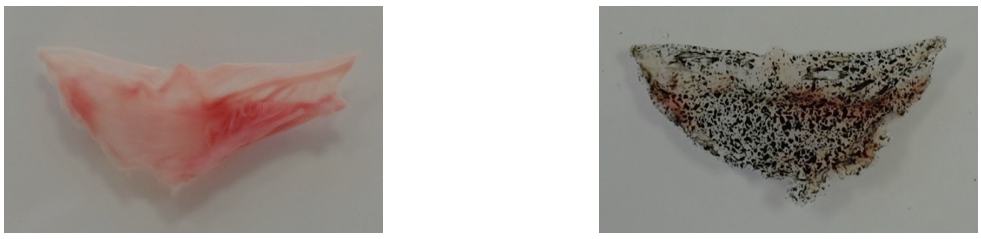

(a) Excised leaflet **(b)** Speckle pattern

Fig. A.1 – Leaflet excision and application of the ink

For each leaflet, a square sample of about 10 mm side length was isolated from the central region. The sample was placed on a support device to be mounted on the device (fig. A.2). The support is composed of four comb–shaped guides for rakes positioning and a foam stand.

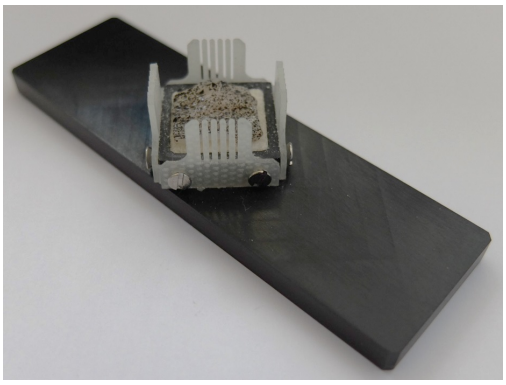

Fig. A.2 – Positioning of the sample on the support device

The sample is then positioned on the biaxial tensile test device using the support and hooked with the rakes thanks to a piston system which makes it possible to move vertically the tray (fig. A.3).

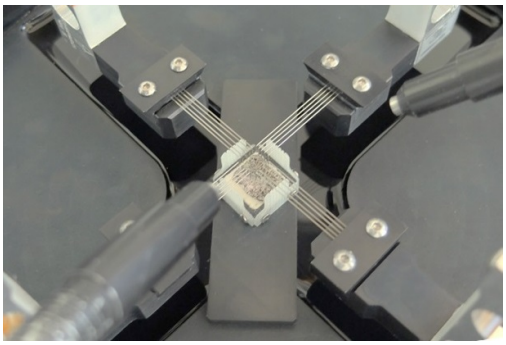

Fig. A.3 – Mounting of the sample on the biaxial device

Finally, the support is removed without damaging the sample using the same piston system. The sample is then immersed into a 0.9% isotonic saline bath at room temperature (fig. A.4). After a few minutes, the tissue is rehydrated and the experiment can start.

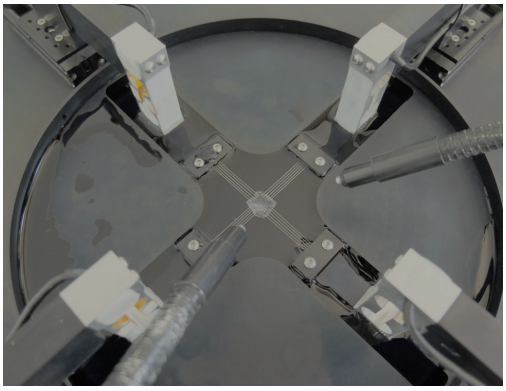

Fig. A.4 – Sample mounted on the biaxial device

Appendix B

Material models derivatives

B.1 Introduction

This appendix details the implementation of the hyperelastic models presented in chapter 2, with in particular the calculations of derivatives of the isochoric strain–energy functions. First derivatives are used for the stress tensors calculation, while second derivative are used for the elasticity tensors calculation, using equations presented in subsection 2.5.2.

B.2 Weisbecker model

As a remainder, the isochoric contribution of the Weisbecker strain–energy function is

$$W_{iso} = (1-\nu)c_g(\bar{I}_1 - 3) + \nu\int_\Omega \rho(\boldsymbol{N})\int_1^{\bar{\lambda}} \rho_r(\lambda_r)\frac{c_f}{2}(\bar{\lambda}-\lambda_r)^2 \mathrm{d}\lambda_r \mathrm{d}\Omega, \tag{B.1}$$

where $c_g = \dfrac{\mu_g}{2}$ is the groundmatrix material parameter (μ_g is the matrix bulk modulus), ρ_r is a modified beta distribution and $\bar{\lambda} = (\bar{\mathbf{C}} : \boldsymbol{N}\otimes\boldsymbol{N})^{\frac{1}{2}}$, λ_r and c_f are respectively the stretch, the recruitment stretch and a material parameter of a particular fiber. From equation (B.1) and using (2.120) introduced in chapter 2, one can obtain

$$W_{iso} = (1-\nu)c_g(\bar{I}_1 - 3) + \nu\int_\Omega \rho(\boldsymbol{N})\int_1^{\bar{\lambda}} \varphi \mathrm{d}\lambda_r \mathrm{d}\Omega, \tag{B.2}$$

with φ defined as

$$\varphi = \gamma(\lambda_r - \lambda_1)^{a_1-1}(\lambda_2-\lambda_r)^{a_2-1}(\bar{\lambda}-\lambda_r)^2, \tag{B.3}$$

and the constant γ as

$$\gamma = \frac{c_f}{2\beta(a_1,a_2)(\lambda_2-\lambda_1)^{a_1+a_2-1}}, \tag{B.4}$$

where $\beta(a_1, a_2)$ is a beta function and a_1 and a_2 are shape parameters. λ_1 and λ_2 are the stretches at which respectively the first and the last fibers are recruited. The first derivative of W_{iso} with respect to the invariant $\bar{I}_1$ is

$$\frac{\partial W_{iso}}{\partial \bar{I}_1} = (1-\nu)c_g. \tag{B.5}$$

Moreover, one can obtain

$$\frac{\partial}{\partial \bar{\mathbf{C}}} \int_1^{\bar{\lambda}} \varphi \mathrm{d}\lambda_r = \frac{\partial}{\partial \bar{\lambda}} \int_1^{\bar{\lambda}} \varphi \mathrm{d}\lambda_r \cdot \frac{\partial \bar{\lambda}}{\partial \bar{\mathbf{C}}}, \tag{B.6}$$

yielding to

$$\frac{\partial}{\partial \bar{\mathbf{C}}} \int_1^{\bar{\lambda}} \varphi \mathrm{d}\lambda_r = \int_1^{\bar{\lambda}} \frac{\partial \varphi}{\partial \bar{\lambda}} \mathrm{d}\lambda_r \cdot \frac{1}{2} \boldsymbol{N} \otimes \boldsymbol{N} \cdot \bar{\lambda}^{-\frac{1}{2}}. \tag{B.7}$$

Hence, the first derivative of φ with respect to the stretch $\bar{\lambda}$ is

$$\frac{\partial \varphi}{\partial \bar{\lambda}} = 2\gamma(\lambda_r - \lambda_1)^{a_1 - 1}(\lambda_2 - \lambda_r)^{a_2 - 1}(\bar{\lambda} - \lambda_r). \tag{B.8}$$

The second derivative of φ with respect to the stretch $\bar{\lambda}$ is

$$\frac{\partial^2 \varphi}{\partial \bar{\lambda} \partial \bar{\lambda}} = 2\gamma(\lambda_r - \lambda_1)^{a_1 - 1}(\lambda_2 - \lambda_r)^{a_2 - 1}. \tag{B.9}$$

B.3 Holzapfel Gasser Ogden model

As a remainder, the isochoric contribution of the Holzapfel Gasser Ogden strain–energy function is

$$W_{iso} = c_0(\bar{I}_1 - 3) + \frac{c_1}{2c_2}\left[\mathrm{e}^{c_2\left(\kappa \bar{I}_1 + (1-3\kappa)\bar{I}_4 - 1\right)^2} - 1\right], \tag{B.10}$$

where c_i with $i = \{0, 1, 2\}$ are positive material parameters and $\kappa \in \left[0, \frac{1}{3}\right]$ is the fiber structure dispersion parameter. The first derivatives of W_{iso} with respect to the invariant $\bar{I}_1$ and the pseudo–invariant $\bar{I}_4$ are

$$\frac{\partial W_{iso}}{\partial \bar{I}_1} = c_0 + c_1\kappa\left(\kappa \bar{I}_1 + (1-3\kappa)\bar{I}_4 - 1\right)\mathrm{e}^{c_2\left(\kappa \bar{I}_1 + (1-3\kappa)\bar{I}_4 - 1\right)^2}, \tag{B.11}$$

$$\frac{\partial W_{iso}}{\partial \bar{I}_4} = c_1(1-3\kappa)\left(\kappa \bar{I}_1 + (1-3\kappa)\bar{I}_4 - 1\right)\mathrm{e}^{c_2\left(\kappa \bar{I}_1 + (1-3\kappa)\bar{I}_4 - 1\right)^2}. \tag{B.12}$$

The second derivatives are

$$\frac{\partial^2 W_{iso}}{\partial \bar{I}_1 \partial \bar{I}_1} = c_1\kappa^2 \left[1 + 2c_2 \left(\kappa\bar{I}_1 + (1-3\kappa)\bar{I}_4 - 1\right)^2\right] \mathrm{e}^{c_2\left(\kappa\bar{I}_1+(1-3\kappa)\bar{I}_4-1\right)^2}, \tag{B.13}$$

$$\frac{\partial^2 W_{iso}}{\partial \bar{I}_1 \partial \bar{I}_4} = c_1\kappa(1-3\kappa) \left[1 + 2c_2 \left(\kappa\bar{I}_1 + (1-3\kappa)\bar{I}_4 - 1\right)^2\right] \mathrm{e}^{c_2\left(\kappa\bar{I}_1+(1-3\kappa)\bar{I}_4-1\right)^2}, \tag{B.14}$$

$$\frac{\partial^2 W_{iso}}{\partial \bar{I}_4 \partial \bar{I}_4} = c_1(1-3\kappa)^2 \left[1 + 2c_2 \left(\kappa\bar{I}_1 + (1-3\kappa)\bar{I}_4 - 1\right)^2\right] \mathrm{e}^{c_2\left(\kappa\bar{I}_1+(1-3\kappa)\bar{I}_4-1\right)^2}. \tag{B.15}$$

B.4 Modified Holzapfel Gasser Ogden model

As a remainder, the isochoric contribution of the modified Holzapfel Gasser Ogden strain–energy function is

$$W_{iso} = \frac{c_0}{c_1}\left[\mathrm{e}^{c_1(\bar{I}_1-3)} - 1\right] + \frac{c_2}{2c_3}\left[\mathrm{e}^{c_3\left(\kappa\bar{I}_1+(1-3\kappa)\bar{I}_4-1\right)^2} - 1\right] \tag{B.16}$$

where c_i with $i = \{0, \ldots, 3\}$ are positive material parameters and $\kappa \in \left[0, \frac{1}{3}\right]$ is the fiber structure dispersion parameter. The first derivatives of W_{iso} with respect to the invariant $\bar{I}_1$ and the pseudo–invariant $\bar{I}_4$ are

$$\frac{\partial W_{iso}}{\partial \bar{I}_1} = c_0\mathrm{e}^{c_1(\bar{I}_1-3)} + c_2\kappa\left(\kappa\bar{I}_1 + (1-3\kappa)\bar{I}_4 - 1\right)\mathrm{e}^{c_3\left(\kappa\bar{I}_1+(1-3\kappa)\bar{I}_4-1\right)^2}, \tag{B.17}$$

$$\frac{\partial W_{iso}}{\partial \bar{I}_4} = c_2(1-3\kappa)\left(\kappa\bar{I}_1 + (1-3\kappa)\bar{I}_4 - 1\right)\mathrm{e}^{c_3\left(\kappa\bar{I}_1+(1-3\kappa)\bar{I}_4-1\right)^2}. \tag{B.18}$$

The second derivatives are

$$\frac{\partial^2 W_{iso}}{\partial \bar{I}_1 \partial \bar{I}_1} = c_0c_1\mathrm{e}^{c_1(\bar{I}_1-3)} + c_2\kappa^2\left[1 + 2c_3\left(\kappa\bar{I}_1 + (1-3\kappa)\bar{I}_4 - 1\right)^2\right] \mathrm{e}^{c_3\left(\kappa\bar{I}_1+(1-3\kappa)\bar{I}_4-1\right)^2}, \tag{B.19}$$

$$\frac{\partial^2 W_{iso}}{\partial \bar{I}_1 \partial \bar{I}_4} = c_2\kappa(1-3\kappa)\left[1 + 2c_3\left(\kappa\bar{I}_1 + (1-3\kappa)\bar{I}_4 - 1\right)^2\right] \mathrm{e}^{c_3\left(\kappa\bar{I}_1+(1-3\kappa)\bar{I}_4-1\right)^2}, \tag{B.20}$$

$$\frac{\partial^2 W_{iso}}{\partial \bar{I}_4 \partial \bar{I}_4} = c_2(1-3\kappa)^2\left[1 + 2c_3\left(\kappa\bar{I}_1 + (1-3\kappa)\bar{I}_4 - 1\right)^2\right] \mathrm{e}^{c_3\left(\kappa\bar{I}_1+(1-3\kappa)\bar{I}_4-1\right)^2}. \tag{B.21}$$

Bibliography

[**Abbasi et al. 2016**]
Abbasi, M., M. S. Barakat, K. Vahidkhah, and A. N. Azadani (09/2016). "Characterization of three-dimensional anisotropic heart valve tissue mechanical properties using inverse finite element analysis". *Journal of the Mechanical Behavior of Biomedical Materials* 62, pp. 33–44.

[**Adami et al. 2012**]
Adami, S., X. Y. Hu, and N. A. Adams (2012). "A generalized wall boundary condition for smoothed particle hydrodynamics". *Journal of Computational Physics* 231 (21), pp. 7057–7075.

[**Aliaga 2000**]
Aliaga, C. (2000). "Simulation numérique par éléments finis en 3D du comportement thermomécanique au cours du traitement thermique d'aciers: application à la trempe de pièces forgées ou coulées". PhD thesis. CEMEF: Ecole Nationale Supérieure des Mines de Paris. 197 pp.

[**Amoroso et al. 2012**]
Amoroso, N. J. et al. (2012). "Microstructural manipulation of electrospun scaffolds for specific bending stiffness for heart valve tissue engineering". *Acta Biomaterialia.*

[**Argyris et al. 1954**]
Argyris, J. H. and S. Kelsey (1954). *Energy Theorems and Structural Analysis.* DOI: 10.1007/978-1-4899-5850-1. Boston, MA: Springer US.

[**Arnold et al. 1984**]
Arnold, D. N., F. Brezzi, and M. Fortin (1984). "A stable finite element for the Stokes equations". *Calcolo* 21 (4), pp. 337–344.

[**Babuska 1971**]
Babuska, I. (1971). "Error-Bounds for Finite Element Method". *Numer. Math.* 16, pp. 322–333.

[**Badel et al. 2012**]
Badel, P., S. Avril, S. Lessner, and M. A. Sutton (01/2012). "Mechanical identification of layer-specific properties of mouse carotid arteries using 3D-DIC and a hyperelastic anisotropic constitutive model". *Computer Methods in Biomechanics and Biomedical Engineering* 15 (1), pp. 37–48.

[**Ball 1976**]
Ball, J. M. (1976). "Convexity conditions and existence theorems in nonlinear elasticity". *Archive for rational mechanics and Analysis* 63 (4), pp. 337–403.

[**Balzani et al. 2006**]
Balzani, D., P. Neff, J. Schröder, and G. A. Holzapfel (2006). "A polyconvex framework for

soft biological tissues. Adjustment to experimental data". *International Journal of Solids and Structures* 43 (20), pp. 6052–6070.

[**Banerjee et al. 2005**]
Banerjee, A., I. S. Dhillon, J. Ghosh, and S. Sra (2005). "Clustering on the unit hypersphere using von Mises-Fisher distributions". *Journal of Machine Learning Research* 6 (Sep), pp. 1345–1382.

[**Barcarolo 2013**]
Barcarolo, D. A. (2013). "Improvement of the precision and the efficiency of the SPH method: theoretical and numerical study". PhD thesis. Ecole Centrale de Nantes (ECN).

[**Bazant et al. 1986**]
Bazant, Z. P. and B. H. Oh (1986). "Efficient Numerical Intégration on the Surface of a Sphere". *Math. u. Mech.* Pp. 37–49.

[**Bentley 1975**]
Bentley, J. L. (1975). "Multidimensional binary search trees used for associative searching". *Communications of the ACM* 18 (9), pp. 509–517.

[**Benz 1990**]
Benz, W. (1990). "Smooth particle hydrodynamics: a review". *The numerical modelling of nonlinear stellar pulsations.* Springer, pp. 269–288.

[**Bezuidenhout et al. 2013**]
Bezuidenhout, D. and P. Zilla (2013). "Flexible Leaflet Polymeric Heart Valves". *Cardiovascular and Cardiac Therapeutic Devices.* Ed. by T. Franz. Vol. 15. Berlin, Heidelberg: Springer Berlin Heidelberg, pp. 93–129.

[**Bierbrauer et al. 2009**]
Bierbrauer, F., P. Bollada, and T. Phillips (09/2009). "A consistent reflected image particle approach to the treatment of boundary conditions in smoothed particle hydrodynamics". *Computer Methods in Applied Mechanics and Engineering* 198 (41), pp. 3400–3410.

[**Billiar et al. 1997**]
Billiar, K. L. and M. S. Sacks (1997). "A method to quantify the fiber kinematics of planar tissues under biaxial stretch". *Journal of biomechanics* 30 (7), pp. 753–756.

[**Billiar et al. 2000a**]
Billiar, K. L. and M. S. Sacks (2000a). "Biaxial Mechanical Properties of the Native and Glutaraldehyde-Treated Aortic Valve Cusp: Part II - A Structural Constitutive Model". *Journal of Biomechanical Engineering* 122 (1), pp. 327–335.

[**Billiar et al. 2000b**]
Billiar, K. L. and M. S. Sacks (2000b). "Biaxial mechanical properties of the natural and glutaraldehyde treated aortic valve cusp : Part I - Experimental results". *Journal of Biomechanical Engineering* 122 (1), pp. 23–30.

[**Bøckmann et al. 2012**]
Bøckmann, A., O. Shipilova, and G. Skeie (08/2012). "Incompressible SPH for free surface flows". *Computers & Fluids* 67, pp. 138–151.

[**Borazjani 2013**]
Borazjani, I. (2013). "Fluid–structure interaction, immersed boundary-finite element method simulations of bio-prosthetic heart valves". *Computer Methods in Applied Mechanics and Engineering* 257, pp. 103–116.

[**Borghi et al. 2013**]
Borghi, A., S. E. New, A. H. Chester, P. M. Taylor, and M. H. Yacoub (2013). "Time-dependent mechanical properties of aortic valve cusps: Effect of glycosaminoglycan depletion". *Acta Biomaterialia* 9, pp. 4645–4652.

[**Boyce et al. 2008**]
Boyce, B. L., J. M. Grazier, R. E. Jones, and T. D. Nguyen (10/2008). "Full-field deformation of bovine cornea under constrained inflation conditions". *Biomaterials* 29 (28), pp. 3896–3904.

[**Brezzi et al. 1992**]
Brezzi, F., M.-O. Bristeau, L. P. Franca, M. Mallet, and G. Rogé (1992). "A relationship between stabilized finite element methods and the Galerkin method with bubble functions". *Computer Methods in Applied Mechanics and Engineering* 96, pp. 117–129.

[**Brezzi et al. 1996**]
Brezzi, F., L. P. Franca, T. J. R. Hughes, and A. Russo (1996). "b = integal(g)". *Comput. Methods Appl. Mech. Engrg.* 145, pp. 329–339.

[**Buchanan et al. 2013**]
Buchanan, R. M. and M. S. Sacks (2013). "Interlayer micromechanics of the aortic heart valve leaflet". *Biomechanics and modeling in mechanobiology,* pp. 1–14.

[**Candau et al. 2016**]
Candau, N., C. Pradille, J.-L. Bouvard, and N. Billon (12/2016). "On the use of a four-cameras stereovision system to characterize large 3D deformation in elastomers". *Polymer Testing* 56, pp. 314–320.

[**Chorin 1968**]
Chorin, J. (1968). "Numerical Solution of the Navier-Stokes Equation". *Mathematics of computation* 22 (104), pp. 745–762.

[**Colin et al. 2006**]
Colin, F., R. Egli, and F. Y. Lin (2006). "Computing a null divergence velocity field using smoothed particle hydrodynamics". *Journal of Computational Physics* 217 (2), pp. 680–692.

[**Cortes et al. 2010**]
Cortes, D. H., S. P. Lake, J. A. Kadlowec, L. J. Soslowsky, and D. M. Elliott (2010). "Characterizing the mechanical contribution of fiber angular distribution in connective tissue: comparison of two modeling approaches". *Biomechanics and modeling in mechanobiology* 9 (5), pp. 651–658.

[**Coupez 1995**]
Coupez, T. (1995). "Stable-stabilized finite element for 3D forming calculation". *CEMEF Internal report.*

[**Courant 1943**]
Courant, R. (1943). "Variational methods for the solution of problems of equilibrium and vibrations". *Lecture Notes in Pure and Applied Mathematics,* pp. 1–1.

[**Courtney et al. 2006**]
Courtney, T., M. S. Sacks, J. Stankus, J. Guan, and W. R. Wagner (2006). "Design and analysis of tissue engineering scaffolds that mimic soft tissue mechanical anisotropy". *Biomaterials* 27 (19), pp. 3631–3638.

[**Cummins et al. 1999**]
Cummins, S. J. and M. Rudman (1999). "An SPH Projection Method". *Journal of Computational Physics* 152, pp. 584–607.

[**Dalrymple et al. 2001**]
Dalrymple, R. A. and O. Knio (2001). "SPH modelling of water waves". *Coastal Dynamics' 01,* pp. 779–787.

[**De Hart et al. 2003**]
De Hart, J., F. P. T. Baaijens, G. W. M. Peters, and P. J. G. Schreurs (2003). "A computational fluid-structure interaction analysis of a fiber-reinforced stentless aortic valve". *Journal of biomechanics* 36 (5), pp. 699–712.

[**De Hart et al. 2003**]
De Hart, J., G. W. M. Peters, P. J. G. Schreurs, and F. P. T. Baaijens (2003). "A three-dimensional computational analysis of fluid–structure interaction in the aortic valve". *Journal of biomechanics* 36 (1), pp. 103–112.

[**Dehnen et al. 2012**]
Dehnen, W. and H. Aly (2012). "Improving convergence in smoothed particle hydrodynamics simulations without pairing instability". *Monthly Notices of the Royal Astronomical Society* 425 (2), pp. 1068–1082.

[**Deplano et al. 2016**]
Deplano, V. et al. (07/2016). "Biaxial tensile tests of the porcine ascending aorta". *Journal of Biomechanics* 49 (10), pp. 2031–2037.

[**Driessen 2006**]
Driessen, N. J. B. (2006). *Modeling and remodeling of the collagen architecture in cardiovascular tissues.*

[**Eckert et al. 2013**]
Eckert, C. E. et al. (2013). "On the biomechanical role of glycosaminoglycans in the aortic heart valve leaflet". *Acta Biomaterialia* 9, pp. 4653–4660.

[**Edding 2010**]
Edding, V. (2010). "Design of Polyconvex Energy Functions for All Anisotropy Classes". PhD thesis. Universität Duisburg-Essen. 223 pp.

[**Einstein et al. 2005**]
Einstein, D. R., A. D. Freed, N. Stander, B. Fata, and I. Vesely (2005). "Inverse parameter fitting of biological tissues: a response surface approach". *Annals of biomedical engineering* 33 (12), pp. 1819–1830.

[**Fatehi et al. 2011**]
Fatehi, R. and M. T. Manzari (2011). "Error estimation in smoothed particle hydrodynamics and a new scheme for second derivatives". *Computers & Mathematics with Applications* 61 (2), pp. 482–498.

[**Federico et al. 2010**]
Federico, S. and T. C. Gasser (2010). "Nonlinear elasticity of biological tissues with statistical fibre orientation". *Journal of the Royal Society Interface* 7 (47), pp. 955–966.

[**Fedosov et al. 2014**]
Fedosov, D. A., H. Noguchi, and G. Gompper (04/2014). "Multiscale modeling of blood flow: from single cells to blood rheology". *Biomechanics and Modeling in Mechanobiology* 13 (2), pp. 239–258.

[**Fehervary et al. 2016**]
Fehervary, H., M. Smoljkić, J. Vander Sloten, and N. Famaey (08/2016). "Planar biaxial

testing of soft biological tissue using rakes: A critical analysis of protocol and fitting process". *Journal of the Mechanical Behavior of Biomedical Materials* 61, pp. 135–151.

[**Ferrand et al. 2013**]
Ferrand, M., D. R. Laurence, B. D. Rogers, D. Violeau, and C. Kassiotis (02/10/2013). "Unified semi-analytical wall boundary conditions for inviscid, laminar or turbulent flows in the meshless SPH method". *International Journal for Numerical Methods in Fluids* 71 (4), pp. 446–472.

[**A. Fortin et al. 2013**]
Fortin, A. and A. Garon (2013). *Les éléments finis : de la théorie à la pratique.*

[**M. Fortin 1981**]
Fortin, M. (1981). "Old and new finite elements for incompressible flows". *International Journal for numerical methods in fluids* 1 (4), pp. 347–364.

[**Leopoldo P. Franca et al. 1994**]
Franca, L. P. and C. Farhat (1994). "On the limitations of bubble functions". *Comput. Methods Appl. Mech. Engrg* 117, pp. 225–230.

[**Leopoldo P. Franca et al. 1995**]
Franca, L. P. and C. Farhat (1995). "Bubble functions prompt unusual stabilized finite element methods". *Comput. Methods Appl. Mech. Engrg.* 123, pp. 299–308.

[**Freed et al. 2005**]
Freed, A. D., D. R. Einstein, and I. Vesely (2005). "Invariant formulation for dispersed transverse isotropy in aortic heart valves". *Biomechanics and modeling in mechanobiology* 4 (2), pp. 100–117.

[**Gasser et al. 2006**]
Gasser, T. C., R. W. Ogden, and G. A. Holzapfel (2006). "Hyperelastic modelling of arterial layers with distributed collagen fibre orientations". *Journal of the royal society interface* 3 (6), pp. 15–35.

[**Genovese et al. 2011**]
Genovese, K., Y. U. Lee, and J. D. Humphrey (2011). "Novel optical system for in vitro quantification of full surface strain fields in small arteries: II. Correction for refraction and illustrative results". *Comput Methods Biomech Biomed Engin.* 14 (3), pp. 227–237.

[**Ghanbari et al. 2009**]
Ghanbari, H. et al. (06/2009). "Polymeric heart valves: new materials, emerging hopes". *Trends in Biotechnology* 27 (6), pp. 359–367.

[**Gingold et al. 1977**]
Gingold, R. A. and J. J. Monaghan (1977). "Smoothed particle hydrodynamics: theory and application to non-spherical stars". *Monthly notices of the royal astronomical society* 181 (3), pp. 375–389.

[**Gizzi et al. 2014**]
Gizzi, A., M. Vasta, and A. Pandolfi (2014). "Modeling collagen recruitment in hyperelastic biomaterial models with statistical distribution of the fiber orientation". *International Journal of Engineering Science* 78, pp. 48–60.

[**Grillo et al. 2014**]
Grillo, A., G. Wittum, A. Tomic, and S. Federico (2014). "Remodelling in statistically oriented fibre-reinforced materials and biological tissues". *Mathematics and Mechanics of Solids* XX(X) (210), pp. 1–23.

[**Gross et al. 1931**]
Gross, L. and M. A. Kugel (1931). "Topographic anatomy and histology of the valves in the human heart". *The American journal of pathology* 7 (5), p. 445.

[**Harb et al. 2014**]
Harb, N., N. Labed, M. Domaszewski, and F. Peyraut (2014). "Optimization of material parameter identification in biomechanics". *Structural and Multidisciplinary Optimization* 49 (2), pp. 337–349.

[**Hartmann et al. 2003**]
Hartmann, S. and P. Neff (2003). "Polyconvexity of generalized polynomial-type hyperelastic strain energy functions for near-incompressibility". *International Journal of Solids and Structures* 40 (11), pp. 2767–2791.

[**Holland 1962**]
Holland, J. H. (1962). "Outline for a logical theory of adaptative systems". *Journal of the association of computing machinery* 9, pp. 297–314.

[**Holland 1975**]
Holland, J. H. (1975). *Adaptation in natural and artificial system.* The University of Michigan Press.

[**Holzapfel 2006a**]
Holzapfel, G. A. (2006a). "Determination of material models for arterial walls from uniaxial extension tests and histological structure". *Journal of Theoretical Biology* 238 (2), pp. 290–302.

[**Holzapfel 2006b**]
Holzapfel, G. A. (2006b). *Nonlinear solid mechanics: a continuum approach for engineering.* Wiley.

[**Holzapfel et al. 2000**]
Holzapfel, G. A., T. C. Gasser, and R. W. Ogden (2000). "A new constitutive framework for arterial wall mechanics and a comparative study of material models". *Journal of elasticity and the physical science of solids* 61 (1), pp. 1–48.

[**Holzapfel et al. 2015**]
Holzapfel, G. A., J. A. Niestrawska, R. W. Ogden, A. J. Reinisch, and A. J. Schriefl (04/15/2015). "Modelling non-symmetric collagen fibre dispersion in arterial walls". *Journal of The Royal Society Interface* 12 (106), pp. 20150188–20150188.

[**Holzapfel et al. 2015**]
Holzapfel, G. A. and R. W. Ogden (2015). "On the tension-compression switch in soft fibrous solids". *European Journal of Mechanics A/Solids* 49, pp. 561–569.

[**Hou et al. 2012**]
Hou, G., J. Wang, and A. Layton (08/2012). "Numerical Methods for Fluid-Structure Interaction — A Review". *Communications in Computational Physics* 12 (2), pp. 337–377.

[**Hsu et al. 2014**]
Hsu, M.-C., D. Kamensky, Y. Bazilevs, M. S. Sacks, and T. J. R. Hughes (2014). "Fluid–structure interaction analysis of bioprosthetic heart valves: significance of arterial wall deformation". *Computational mechanics* 54 (4), pp. 1055–1071.

[**Hughes 1995**]
Hughes, T. J. R. (1995). "Multiscale phenomena: Green's functions, the Dirichlet-to-Neumann

formulation, subgrid scale models, bubbles and the origins of stabilized method". *Comput. Methods Appl. Mech. Engrg.* 127, pp. 387–401.

[**Hughes et al. 1998**]
Hughes, T. J. R., G. R. Feijoo, L. Mazzei, and J.-B. Quincy (1998). "The variational multiscale method - a paradigm for computational mechanics". *Comput. Methods Appl. Mech. Engrg.* 166, pp. 3–24.

[**Hughes et al. 1978**]
Hughes, T. J. R. and K. S. Pister (1978). "Consistent linearization in mechanics of solids and structures". *Computer & Structures* 8, pp. 391–397.

[**Hughes et al. 1996**]
Hughes, T. J. R. and J. R. Stewart (1996). "A space-time formulation for multiscale phenomena". *Journal of Computational and Applied Mathematics* 74, pp. 217–229.

[**Itskov et al. 2004**]
Itskov, M. and N. Aksel (2004). "A class of orthotropic and transversely isotropic hyperelastic constitutive models based on a polyconvex strain energy function". *International journal of solids and structures* 41 (14), pp. 3833–3848.

[**Jones et al. 1998**]
Jones, D. R., M. Schonlau, and W. J. Welch (1998). "Efficient global optimization of expensive black-box functions". *Journal of Global optimization* 13 (4), pp. 455–492.

[**Karšaj et al. 2009**]
Karšaj, I., C. Sansour, and J. Sorić (2009). "The modelling of fibre reorientation in soft tissue". *Biomechanics and modeling in mechanobiology* 8 (5), pp. 359–370.

[**Ke et al. 2008**]
Ke, X., M. A. Sutton, S. M. Lessner, and M. Yost (08/01/2008). "Robust stereo vision and calibration methodology for accurate three-dimensional digital image correlation measurements on submerged objects". *The Journal of Strain Analysis for Engineering Design* 43 (8), pp. 689–704.

[**Kidane et al. 2009**]
Kidane, A. G. et al. (09/2009). "A novel nanocomposite polymer for development of synthetic heart valve leaflets". *Acta Biomaterialia* 5 (7), pp. 2409–2417.

[**Krishnamurthy et al. 2008**]
Krishnamurthy, G. et al. (06/20/2008). "Material properties of the ovine mitral valve anterior leaflet in vivo from inverse finite element analysis". *AJP: Heart and Circulatory Physiology* 295 (3), H1141–H1149.

[**Kroon et al. 2009**]
Kroon, M. and G. A. Holzapfel (2009). "Elastic properties of anisotropic vascular membranes examined by inverse analysis". *Computer Methods in Applied Mechanics and Engineering* 198 (45), pp. 3622–3632.

[**Kuhl et al. 2007**]
Kuhl, E. and G. A. Holzapfel (2007). "A continuum model for remodeling in living structures". *Journal of Materials Science* 42 (21), pp. 8811–8823.

[**Lanir 1979**]
Lanir, Y. (1979). "A structural theory for the homogeneous biaxial stress-strain relationships in flat collagenous tissus". *Journal of biomechanics* 12, pp. 423–436.

[**Lanir 1983**]
Lanir, Y. (1983). "Constitutive equations for fibrous connective tissues". *Journal of biomechanics* 16, pp. 1–12.

[**Laurent et al. 1992**]
Laurent, M., G. Johannin, H. Guyader, and A. Fleury (1992). "Confocal scanning optical microscopy and three-dimensional imaging". *Biology of the Cell* 76 (1), pp. 113–124.

[**E. S. Lee et al. 2008**]
Lee, E. S. et al. (09/2008). "Comparisons of weakly compressible and truly incompressible algorithms for the SPH mesh free particle method". *Journal of Computational Physics* 227 (18), pp. 8417–8436.

[**T. C. Lee et al. 2001**]
Lee, T. C., R. J. Midura, V. C. Hascall, and I. Vesely (2001). "The effect of elastin damage on the mechanics of the aortic valve". *Journal of biomechanics* 34 (2), pp. 203–210.

[**J. K. J. Li 1988**]
Li, J. K. J. (1988). "Laminar and turbulent flow in the mammalian aorta: Reynolds number". *Journal of theoretical biology* 135 (3), pp. 409–414.

[**Z. Li et al. 2015**]
Li, Z., J. Leduc, J. Nunez-Ramirez, A. Combescure, and J.-C. Marongiu (04/2015). "A non-intrusive partitioned approach to couple smoothed particle hydrodynamics and finite element methods for transient fluid-structure interaction problems with large interface motion". *Computational Mechanics* 55 (4), pp. 697–718.

[**Liao et al. 2007**]
Liao, J., L. Yang, J. Grashow, and M. S. Sacks (2007). "The relation between collagen fibril kinematics and mechanical properties in the mitral valve anterior leaflet". *Journal of Biomechanical Engineering* 129 (1), p. 78.

[**Liu et al. 2010**]
Liu, M. B. and G. R. Liu (03/2010). "Smoothed Particle Hydrodynamics (SPH): an Overview and Recent Developments". *Archives of Computational Methods in Engineering* 17 (1), pp. 25–76.

[**Lovekamp et al. 2006**]
Lovekamp, J. J. et al. (2006). "Stability and function of glycosaminoglycans in porcine bioprosthetic heart valves". *Biomaterials* 27 (8), pp. 1507–1518.

[**Lucy 1977**]
Lucy, L. B. (1977). "A numerical approach to the testing of the fission hypothesis". *The astronomical journal* 82, pp. 1013–1024.

[**Luyckx et al. 2014**]
Luyckx, T. et al. (2014). "Digital image correlation as a tool for three-dimensional strain analysis in human tendon tissue". *Journal of experimental orthopaedics* 1 (1), p. 1.

[**Marrone et al. 2010**]
Marrone, S., A. Colagrossi, D. Le Touzé, and G. Graziani (2010). "Fast free-surface detection and level-set function definition in SPH solvers". *Journal of Computational Physics* 229 (10), pp. 3652–3663.

[**Martin et al. 2012**]
Martin, C. and W. Sun (2012). "Biomechanical characterization of aortic valve tissue in

humans and common animal models". *Journal of Biomedical Materials Research Part A* 100A (6), pp. 1591–1599.

[**Martufi et al. 2011**]
Martufi, G. and T. C. Gasser (2011). "A constitutive model for vascular tissue that integrates fibril, fiber and continuum levels with application to the isotropic and passive properties of the infrarenal aorta". *Journal of biomechanics* 44 (14), pp. 2544–2550.

[**Merryman et al. 2006**]
Merryman, W. D., S. H.-Y. Huang, F. J. Schoen, and M. S. Sacks (2006). "The effects of cellular contraction on aortic valve leaflet flexural stiffness". *Journal of biomechanics* 39 (1), pp. 88–96.

[**Misfeld et al. 2007**]
Misfeld, M. and H.-H. Sievers (2007). "Heart valve macro-and microstructure". *Philosophical Transactions of the Royal Society B: Biological Sciences* 362 (1484), pp. 1421–1436.

[**Mohammadi et al. 2011**]
Mohammadi, H. and K. Mequanint (2011). "Prosthetic aortic heart valves: modeling and design". *Medical engineering & physics* 33 (2), pp. 131–147.

[**Monaghan 1989**]
Monaghan, J. J. (1989). "On the problem of penetration in particle methods". *Journal of Computational physics* 82 (1), pp. 1–15.

[**Monaghan 1992**]
Monaghan, J. J. (1992). "Smoothed particle hydrodynamics". *Annual review of astronomy and astrophysics* 30, pp. 543–574.

[**Monaghan 1994**]
Monaghan, J. J. (1994). "Simulating free surface flows with SPH". *Journal of Computational Physics* 110, pp. 399–406.

[**Morris 1995**]
Morris, J. P. (1995). "A study of the stability properties of SPH". *arXiv preprint astro-ph/9503124*.

[**Morris et al. 1997a**]
Morris, J. P., P. J. Fox, and Y. Zhu (1997a). "Modeling Low Reynolds Number Incompressible Flows Using SPH". *Journal of Computational Physics* 136, pp. 214–226.

[**Morris et al. 1997b**]
Morris, J. P., P. J. Fox, and Y. Zhu (1997b). "Modeling Low Reynolds Number Incompressible Flows Using SPH". *Journal of Computational Physics* 136, pp. 214–226.

[**Mulholland et al. 1997**]
Mulholland, D. L. and A. I. Gotlieb (1997). "Cardiac valve interstitial cells: regulator of valve structure and function". *Cardiovascular Pathology* 6 (3), pp. 167–174.

[**Nomeritae et al. 2016**]
Nomeritae, E. Daly, S. Grimaldi, and H. H. Bui (11/2016). "Explicit incompressible SPH algorithm for free-surface flow modelling: A comparison with weakly compressible schemes". *Advances in Water Resources* 97, pp. 156–167.

[**Oomen et al. 2016**]
Oomen, P. et al. (2016). "Age-dependent changes of stress and strain in the human heart valve and their relation with collagen remodeling". *Acta Biomaterialia* 29, pp. 161–169.

[**Oren et al. 2013**]
Oren, T. et al. (2013). "Analytical and numerical analyses of the micromechanics of soft fibrous connective tissues". *Biomechanics and modeling in mechanobiology* 12 (1), pp. 151–166.

[**Pandolfi et al. 2012**]
Pandolfi, A. and M. Vasta (2012). "Fiber distributed hyperelastic modeling of biological tissues". *Mechanics of Materials* 44, pp. 151–162.

[**Pence et al. 2012**]
Pence, T. J. and A. Wineman (2012). "On some connections between equivalent single material and mixture theory models for fiber reinforced hyperelastic materials". *International Journal of Non-Linear Mechanics* 47 (2), pp. 285–292.

[**Perchat 2000**]
Perchat, E. (2000). "MINI-Elément et factorisations incomplètes pour la parallélisation d'un solver de Stokes 2D. Application au forgeage." PhD thesis. CEMEF: Ecole Nationale Supérieure des Mines de Paris. 154 pp.

[**Peskin 2002**]
Peskin, C. S. (01/2002). "The immersed boundary method". *Acta Numerica* 11.

[**Pham et al. 2017**]
Pham, T., F. Sulejmani, E. Shin, D. Wang, and W. Sun (2017). "Quantification and comparison of the mechanical properties of four human cardiac valves". *Acta Biomaterialia* 54, pp. 345–355.

[**Pibarot et al. 2009**]
Pibarot, P. and J. G. Dumesnil (02/09/2009). "Prosthetic Heart Valves: Selection of the Optimal Prosthesis and Long-Term Management". *Circulation* 119 (7), pp. 1034–1048.

[**Pierre 1988**]
Pierre, R. (1988). "Simple C0 approximations for the computation of incompressible flows". *Computer Methods in Applied Mechanics and Engineering* 68 (2), pp. 205–227.

[**Randles et al. 1996**]
Randles, P. W. and L. D. Libersky (1996). "Smoothed particle hydrodynamics: some recent improvements and applications". *Computer methods in applied mechanics and engineering* 139 (1), pp. 375–408.

[**Rechenberg 1965**]
Rechenberg, I. (1965). "Cybernetic solution path of an experimental problem". *Technical report, Royal Air Force Establishment.*

[**Roger et al. 2012**]
Roger, V. L. et al. (2012). "Executive summary: heart disease and stroke statistics - 2015 update a report from the American Heart Association". *Circulation* 125 (1), pp. 188–197.

[**Rong Fan et al. 2013**]
Rong Fan et al. (2013). "Optimal elastomeric scaffold leaflet shape for pulmonary heart valve leaflet replacement". *JournalofBiomechanics* 46, pp. 662–669.

[**Roux 2011**]
Roux, É. (2011). "Assemblage mécanique : stratégies d'optimisation des procédés et d'identification des comportements mécaniques des matériaux". PhD thesis. École Nationale Supérieure des Mines de Paris.

[**Sacks 1999**]
Sacks, M. S. (1999). "A Method for planar biaxial mechanical testing that includes in-plane shear". *Journal of Biomechanical Engineering* 121, pp. 551–555.

[**Sacks 2003**]
Sacks, M. S. (2003). "Incorporation of experimentally-derived fiber orientation into a structural constitutive model for planar collagenous tissues". *Journal of Biomechanical Engineering* 125, pp. 280–287.

[**Sacks et al. 2009**]
Sacks, M. S., W. David Merryman, and D. E. Schmidt (2009). "On the biomechanics of heart valve function". *Journal of biomechanics* 42 (12), pp. 1804–1824.

[**Schenke-Layland et al. 2009**]
Schenke-Layland, K. et al. (09/02/2009). "Cardiomyopathy is associated with structural remodelling of heart valve extracellular matrix". *European Heart Journal* 30 (18), pp. 2254–2265.

[**Schriefl et al. 2012**]
Schriefl, A. J., A. J. Reinisch, S. Sankaran, D. M. Pierce, and G. A. Holzapfel (2012). "Quantitative assessment of collagen fibre orientations from two-dimensional images of soft biological tissues". *Journal of The Royal Society Interface* 9 (76), pp. 3081–3093.

[**Schröder et al. 2005**]
Schröder, J., P. Neff, and D. Balzani (2005). "A variational approach for materially stable anisotropic hyperelasticity". *International journal of solids and structures* 42 (15), pp. 4352–4371.

[**Schröder et al. 2003**]
Schröder, J. and P. Neff (2003). "Invariant formulation of hyperelastic transverse isotropy based on polyconvex free energy functions". *International journal of solids and structures* 40 (2), pp. 401–445.

[**Shao et al. 2003**]
Shao, S. and E. Y. Lo (07/2003). "Incompressible SPH method for simulating Newtonian and non-Newtonian flows with a free surface". *Advances in Water Resources* 26 (7), pp. 787–800.

[**Simionescu 2004**]
Simionescu, D. T. (2004). "Prevention of calcification in bioprosthetic heart valves: challenges and perspectives". *Expert opinion on biological therapy* 4 (12), pp. 1971–1985.

[**Simo et al. 1991**]
Simo, J. C. and R. L. Taylor (1991). "Quasi-incompressible finite elasticity in principal stretches. Continuum basis and numerical algorithmsF". *Computer Methods in Applied Mechanics and Engineering* 85, pp. 273–310.

[**Skacel et al. 2014**]
Skacel, P. and J. Bursa (2014). "Comparison of constitutive models of arterial layers with distributed collagen fibre orientations". *Acta of Bioengineering and Biomechanics* 16 (3).

[**Stella et al. 2007**]
Stella, J. A., J. Liao, and M. S. Sacks (2007). "Time-dependent biaxial mechanical behavior of the aortic heart valve leaflet". *Journal of biomechanics* 40 (14), pp. 3169–3177.

[**Stella et al. 2007**]
Stella, J. A. and M. S. Sacks (2007). "On the biaxial mechanical properties of the layers of the aortic valve leaflet". *Journal of Biomechanical Engineering* 129, pp. 757–766.

[**Stephens et al. 2009**]
Stephens, E. H., N. de Jonge, M. P. McNeill, C. A. Durst, and K. J. Grande-Allen (2009). "Age-related changes in material behavior of porcine mitral and aortic valves and correlation to matrix composition". *Tissue Engineering Part A* 16 (3), pp. 867–878.

[**Sun et al. 2005**]
Sun, W., M. S. Sacks, and M. J. Scott (2005). "Effects of boundary conditions on the estimation of the planar biaxial mechanical properties of soft tissues". *Journal of Biomechanical Engineering* 127, pp. 709–715.

[**Sutton et al. 2008**]
Sutton, M. A., X. Ke, et al. (01/2008). "Strain field measurements on mouse carotid arteries using microscopic three-dimensional digital image correlation". *Journal of Biomedical Materials Research Part A* 84A (1), pp. 178–190.

[**Sutton et al. 1999**]
Sutton, M. A. and C. McFadden (1999). "Development of a methodology for non-contacting strain measurements in fluid environments using computer vision". *Optics and Lasers in Engineering* 32 (4), pp. 367–377.

[**Sutton et al. 2009**]
Sutton, M. A., J.-J. Orteu, and H. W. Schreier (2009). "Practical Considerations for Accurate Measurements with DIC". Schreier, H., J.-J. Orteu, and M. A. Sutton. *Image Correlation for Shape, Motion and Deformation Measurements.* Boston, MA: Springer US, pp. 1–24.

[**Takeda et al. 1994**]
Takeda, H., S. M. Miyama, and M. Sekiya (1994). "Numerical simulation of viscous flow by smoothed particle hydrodynamics". *Progress of Theoretical Physics* 92 (5), pp. 939–960.

[**Taylor et al. 2003**]
Taylor, P. M., P. Batten, N. J. Brand, P. S. Thomas, and M. H. Yacoub (2003). "The cardiac valve interstitial cell". *The international journal of biochemistry & cell biology* 35 (2), pp. 113–118.

[**Turner 1956**]
Turner, M. J. (09/1956). "Stiffness and Deflection Analysis of Complex Structures". *Journal of the Aeronautical Sciences* 23 (9), pp. 805–823.

[**Vesely 1997**]
Vesely, I. (1997). "The role of elastin in aortic valve mechanics". *Journal of biomechanics* 31 (2), pp. 115–123.

[**Wang et al. 2014**]
Wang, H. M. et al. (2014). "A modified Holzapfel-Ogden law for a residually stressed finite strain model of the human left ventricle in diastole". *Biomechanics and modeling in mechanobiology* 13 (1), pp. 99–113.

[**Weisbecker et al. 2015**]
Weisbecker, H., M. J. Unterberger, and G. A. Holzapfel (03/18/2015). "Constitutive modelling of arteries considering fibre recruitment and three-dimensional fibre distribution". *Journal of The Royal Society Interface* 12 (105), pp. 20150111–20150111.

[**Weiss et al. 1995**]
Weiss, J. A., B. N. Maker, and S. Govindjee (1995). "Finite element implementation of incompressible, transversely isotropic hyperelasticity". *Comput. Methods Appl. Mech. Engrg* 135, pp. 107–128.

[**Wendland 1995**]
Wendland, H. (1995). "Piecewise polynomial, positive definite and compactly supported radial functions of minimal degree". *Advances in computational Mathematics* 4 (1), pp. 389–396.

[**Xu et al. 2009**]
Xu, R., P. Stansby, and D. Laurence (2009). "Accuracy and stability in incompressible SPH (ISPH) based on the projection method and a new approach". *Journal of Computational Physics* 228 (18), pp. 6703–6725.

[**Yamaguchi et al. 2010**]
Yamaguchi, T. et al. (03/2010). "Particle-Based Methods for Multiscale Modeling of Blood Flow in the Circulation and in Devices: Challenges and Future Directions: Sixth International Bio-Fluid Mechanics Symposium and Workshop March 28–30, 2008 Pasadena, California". *Annals of Biomedical Engineering* 38 (3), pp. 1225–1235.

[**D. Zhang et al. 2004**]
Zhang, D. and D. D. Arola (2004). "Applications of digital image correlation to biological tissues". *Journal of Biomedical Optics* 9 (4), pp. 691–699.

[**W. Zhang et al. 2015**]
Zhang, W., S. Ayoub, J. Liao, and M. S. Sacks (2015). "A meso-scale layer-specific structural constitutive model of the mitral heart valve leaflets". *Acta biomaterialia.*

Résumé

L'objectif de cette thèse de doctorat est de développer des outils expérimentaux et numériques pour la caractérisation mécanique et la modélisation des tissus, naturels ou artificiels, de valve aortique. Ces outils sont destinés à être utilisés pour l'élaboration de nouveaux implants biomimétiques en matériaux polymères. Chaque année, près de 300 000 prothèses de valves sont implantées à travers le monde. Ces implants peuvent être de deux types : mécaniques ou biologiques. Les deux solutions souffrent cependant d'inconvénients majeurs. Dans ce contexte, les prothèses en matériaux polymères représentent une alternative prometteuse même si elles ne disposent pas encore de propriétés mécaniques suffisantes. Dans ce travail, un protocole expérimental combinant essais de traction biaxiale, mesure de champs et microscopie confocale est proposé. La mise au point de nouveaux implants peut aussi largement bénéficier de la modélisation numérique afin d'étudier leur comportement mécanique. Ainsi, un solveur structure et un solveur fluide ont été implémentés et couplés. À partir des résultats expérimentaux, les modèles de comportements ont été calibrés en utilisant une procédure d'analyse inverse.

Mots Clés

Valve aortique, mesure de champs, hyperélasticité, analyse inverse

Abstract

This PhD thesis aims to develop experimental and numerical tools for the mechanical characterization and the numerical modeling of natural or artificial aortic valve tissues. These tools are intended to be used for the development of new biomimetic polymeric implants. Nowadays, almost 300 000 prosthetic valves are implanted every year worldwide. Two families of prosthetic valves are currently available : mechanical and biological prostheses. However, both solutions suffer from major drawbacks. In this context, polymeric prostheses represent a promising alternative but currently suffer from insufficient material properties to be suitable for a long–lasting implantation. In this work, an experimental protocol using biaxial tensile tests together with full–field surface measurement and confocal microscopy is proposed. Since numerical simulation is intended to assist the design phase of new implants by predicting their mechanical behavior, a structure and a fluid solver are developed and coupled. Using experimental results, implemented constitutive models are calibrated through an inverse analysis procedure.

Keywords

Aortic valve, full–field measure, hyperelasticity, inverse analysis